CRANFIELD UNIVERSITY

S. ALHAJRAF

NUMERICAL SIMULATION OF DRIFTING SAND

SCHOOL OF MECHANICAL ENGINEERING

Ph.D. THESIS

CRANFIELD UNIVERSITY

SCHOOL OF MECHANICAL ENGINEERING

Ph.D. THESIS
Academic Year 2000-2001

Salem ALHAJRAF

Numerical simulation of drifting sand

Supervisor: P. RUBINI

December 2000

This thesis is submitted in partial fulfilment of the requirements for the degree of Doctor of Philosophy

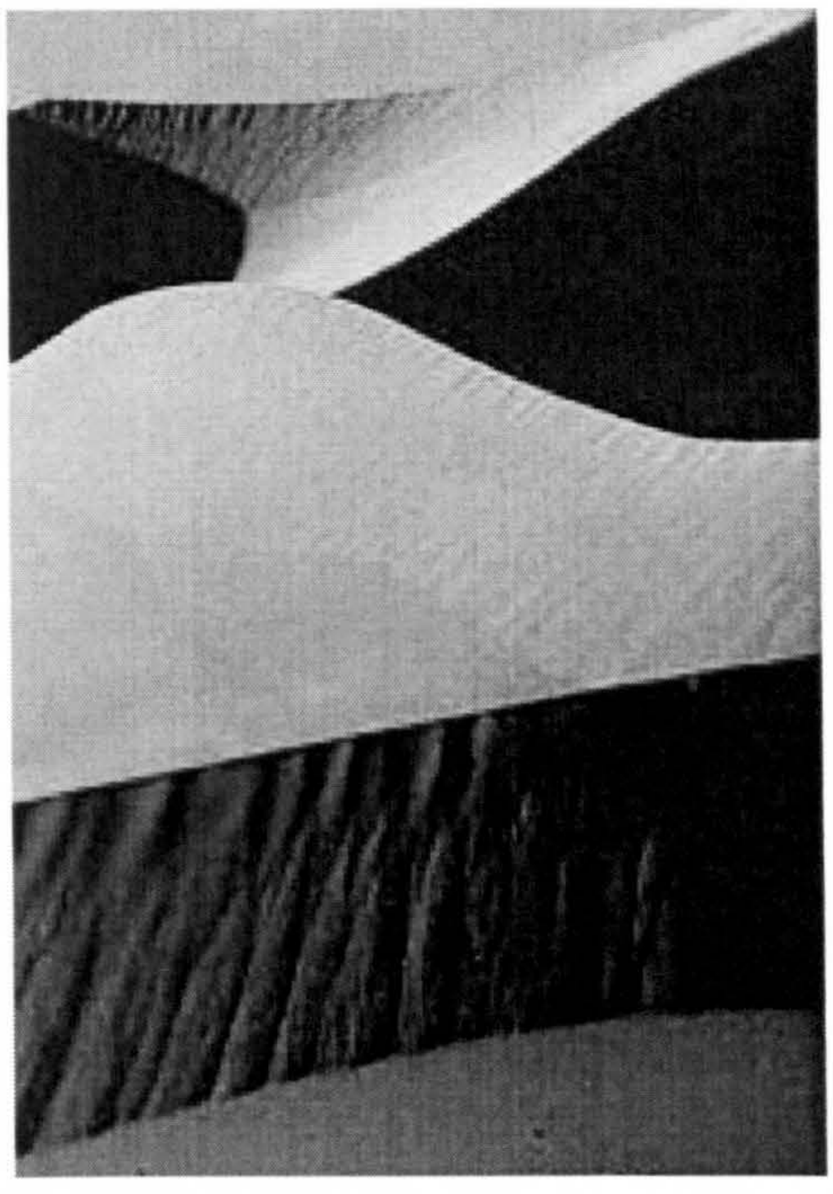

Wind and sand create majestic dunes
that are constant but ever changing.
They move across the deserts,
sing to the wind and
inspire our creativity!

Wayne P. Armstrong

Abstract

Two-phase flows are involved in many industrial and natural flow phenomena varying from as specific as the transport of crude oil in pipelines to as general as the dispersion of pollutants in the atmosphere. Numerical modelling based on Computational Fluid Dynamics (CFD), has attracted the attention of scientists and engineers from a wide range of backgrounds over recent decades during which these models have been extensively developed, analysed and applied to many practical applications.

Wind blown particles such as sand or snow and their resulting accumulation around buildings, roads, oil field installations and security fences causes severe structural and design problems. These are traditionally addressed based on previous experience, full-scale field investigation or using scale model wind tunnel experiments, all of which incur high cost.

In this study, wind blown particles are considered as a two-phase flow system. A finite volume based CFD code is developed using two-phase flow theory and is employed to numerically simulate the drifting of sand and snow around obstacles of different geometry. The model solves the governing transport equations in three dimensional space. Three different approaches are investigated to represent and solve the secondary flow phase, particles, within the flow field; a particle tracking model, based on a Lagrangian reference frame and the homogenous and the mixture models, based on an Eulerian reference frame. The capabilities and limitations of each of these models are investigated for flow fields involving drifting particles around obstacles of different geometry.

Particles transported by wind both in suspension and saltation are modelled based on the physical characteristic and the threshold condition of the particle. Their effect on the flow field is incorporated through separate source terms contributing to the particle transport equation.

The Eulerian based models are coupled with the Fractional Area/Volume Obstacle Representation (FAVOR) as a mean of representing the solid

boundary formed by deposited particles separating the flow field from the accumulation zones. The FAVOR treatment allows the flow field to respond to the changes in the geometry of the deposition regions and further calculations take into account the erosion and deposition processes that have previously occurred.

The model can be calibrated to match specific flow conditions through several controlling parameters. These controlling parameters are identified and analysed for four distinct case studies. Model results are compared with field and wind tunnel observations available in the literature and with field measurements conducted as a part of this study in the desert of the State of Kuwait. Qualitatively good agreement between the model and the observations is obtained in two as well as three dimensions.

Although the mixture and particle tracking models show the potential capability to simulate such flow systems, the homogenous model is found to be the most appropriate model due to its relative simplicity compared to the mixture model and its lower computational cost compared to the Lagrangian particle-tracking model.

In conclusion, a practical CFD tool has been developed and validated, incorporating novel physical and numerical models. The tool can be utilised by scientists and engineers to further understand the real world problem of drifting sand and snow in urban and industrial environments.

Acknowledgement

I would like to express my gratitude and appreciation to all people who have made this work possible.

Firstly I would like to thank my supervisor Dr. P. Rubini, for his guidance, encouragement and support throughout the duration of this research, for which I am deeply grateful.

I am grateful to my employer Kuwait Institute for Scientific Research (KISR) for the sponsorship and financial support. I also thank all my colleagues at KISR-Environmental and Earth Science Division whom gave me the support and valuable advises during my study.

Thank must go to V. Sanderson for the tremendous help and support during the write up stage of this work. Thanks also go to members of the computational group with whom I had valuable discussions, and in particular Prof. B. Moss and Dr. A Perrira.

Also thanks must go to Dr. A. Elenzi, Dr. A. Aldosarry, H. Ali and Salah for their help and advise during the field experiment and measurements in the desert of the State of Kuwait.

Finally, to my parents, wife and children from whom I gained the trust in the past, the confidence in the present and the hope in the future, the best thanks and gratitude must go.

Nomenclature

Alpha-Numeric

A	Threshold parameter
A_{fi}	Area fraction vectors
c	Particle concentration
c_k	Phase mass fraction
C_D	Drag force coefficient.
d	Distance.
D_P	Particle diameter
e_n	Normal coefficient of restitution
e_t	Tangential coefficient of restitution
F	Force
F_{Drag}	Drag force
F_{Lift}	Lift Force
g	Gravity
h	Saltation height
H	Fence or wall height
J	Jacobian determinant
k	Turbulent kinetic energy
l_e	Eddy length scale
L	Saltation length
m_g	Particle mass.
M_k	Averaged interface momentum source
P_k	Phase pressure
$P(u')$	Probability Density Function
Q	Mass flow rate
Q_k	Interfacial mass transfer of phases i
Q_{Salt}	Saltation mass flow rate
Q_{Susp}	Suspension mass flow rate
Re	Reynolds number
S_ϕ	Source term for variable ϕ
Re_p	Particle threshold Reynolds number
t	Time
T	Current time of the deposition stage
Te	Time required to achieve the equilibrium deposition state
u	Continuous phase velocity
u_D	Diffusion velocity
u_m	Average mixture velocity
u_p	Dispersed phase velocity

$u_{Rel.}$	Relative velocity
u^*	Friction velocity
u_t^*	Threshold friction velocity
u_{Pi}, v_{Pi}, w_{Pi}	Initial particle velocity
u', v', w'	Velocity fluctuation components
U_R^*	Normalised friction velocity ratio term
U	Average velocity magnitude
v_f	Free falling velocity
V	Grid cell volume
V_f	Volume fraction
V_p	Particle volume
W	Weight
y	Height from surface
y_o	Surface roughness
x, y, z	Cartesian coordinates
x_{Pi}, y_{Pi}, z_{Pi}	Initial particle position

Greek letters

α_k	i^{th} phase volume fraction
α	Continuous phase volume fraction
α_{pm}	Maximum volume fraction
α_p	Dispersed phase volume fraction
β^{mj}	Co-factor of the coordinate transformation
β_{Salt}	Saltation source term coefficient
β_{Susp}	Suspension source term coefficient
κ	Von Karman's constant
ϕ	Dependent variable
τ_D	Averaged diffusion stress tensors
τ_{fL}	Eddy life time scale
τ_k	Averaged viscous stress tensors
τ_{kT}	Averaged turbulent stress tensors
τ_p	Particle relaxation time.
τ_w	Wall shear stress
Γ_i	Diffusion coefficient of phase i
μ	Dynamic molecular viscosity
μ_m	Mixture dynamic viscosity
μ_p	Dispersed phase dynamic viscosity
μ_t	Turbulent eddy viscosity

ν	Kinematic viscosity
ρ	Continuous phase density
ρ_m	Mixture density
ρ_p	Dispersed phase density
ε	Turbulent dissipation rate
η,ξ,ζ	General curvilinear coordinates
ξ	Gaussian random variable

Acronyms

CFD	Computational Fluid Dynamics
DDM	Deterministic Dispersion model
FAVOR	Fractional Area/Volume Obstacle Representation
KISR	Kuwait Institute for Scientific Research
PDF	Probability Density Function
SOFIE	Simulation Of Fire In Enclosures
SSF	Stochastic Separated Flow Model

Content

List of Figures

List of Tables

Chapter 1

Introduction

1.1 Why wind blown particles?

Wind is one of the two key natural phenomena, the other being running water, that are responsible for the movement of hundreds of tonnes of soil, sand and snow particles all over the surface of the Earth.

Gradually, as the wind velocity over a surface of loose particles (e.g. sand) increases, particle movement is initiated when the wind velocity reaches a certain value at which the aerodynamic forces applied on the particle become higher than those resisting the movement.

The wind then exerts a momentum on the particle driving it in the direction of the flow. The particle will then be transported in one of three different modes, *rolling or surface creep*, *saltating or bouncing* and *suspension*. After some distance and under a certain minimum aerodynamic conditions where the resisting forces exceed the forces applied by the wind the particle will finally settle back to the ground.

These three processes of particles being drifted by the wind: erosion, transportation and then deposition are known as the *Aeolian process*, derived from the Greek god of wind *Aeolus*. Each of these processes can have a negative effect on human life, on animal life, the vegetation cover and on agricultural lands.

Engineers, mathematicians and scientists from a wide range of backgrounds have shown great interest in the effects of the Aeolian process on health, environment, roads, farms, building structure, oil field installations, etc. From the engineering point view, the accumulation and build up of snow, in the cold

regions, or sand, in the arid regions, on and around installations was the main cause of several structural, safety and security problems.

In order to understand and possibly prevent such deposition from occurring, an accurate prediction of the location and the amount of the expected deposition would be highly advantageous.

Equally, desertification in arid regions and global warming in the cold regions are of great concern to environmentalists and earth scientists. It was very clearly observed that the desert has expanded during the last few decades, Pye and Tsoar (1990) and Cooke et al. (1993), to cover thousands of acres of agricultural land. Moreover, due to global warming, there is a great concern about the mass of snow particles that can be blown by wind. Thus, a tremendous effort has been made by cold region scientists in order to gain a better knowledge of the dynamics of wind blown snow particles in order to help in estimating the mass balance between incoming snow and melted or drifted snow, Dover (1993).

1.2 Drifting problem and control measures

Sand drift and sand dune development around obstacles causes common problems that threatens those who are living in the desert and along sandy coasts. Similarly, snow drifts cause seasonal problems for those living in the cold regions. The negative effects of these problems include:

- Blocked roads or development of small dunes in the middle of roads that may cause severe accidents.

- Visibility reduction on motorways and airfields.

- Blocking oil and water wells and reservoirs, figure 1.1.

- Burial of security fences, pipelines and blocking of camp gates.

- Erosion of soil and abrasion damage to crops.

Efforts to stop or at least limit the damage caused by drifting problems have a long history; whether these particles are sand, snow or soil. There are different approaches, which have been employed to reduce problems associated with the drifting particles:

- Stopping or reducing the amount of particles that can be eroded at the sources of the particles.

- Controlling the aerodynamical structure of the flow field around the area of interest either by enhancing the wind capability to divert blown particles away from that area or by taking the problem into account during the early stages of the aerodynamical design of the installation itself.

- Trapping the incoming particles at a safe distance upstream of the area of interest either by using biological (e.g. trees or vegetation) or mechanical measures (e.g. walls, fences or trenches).

- Stabilising, dissipating or manually removing the deposited particles.

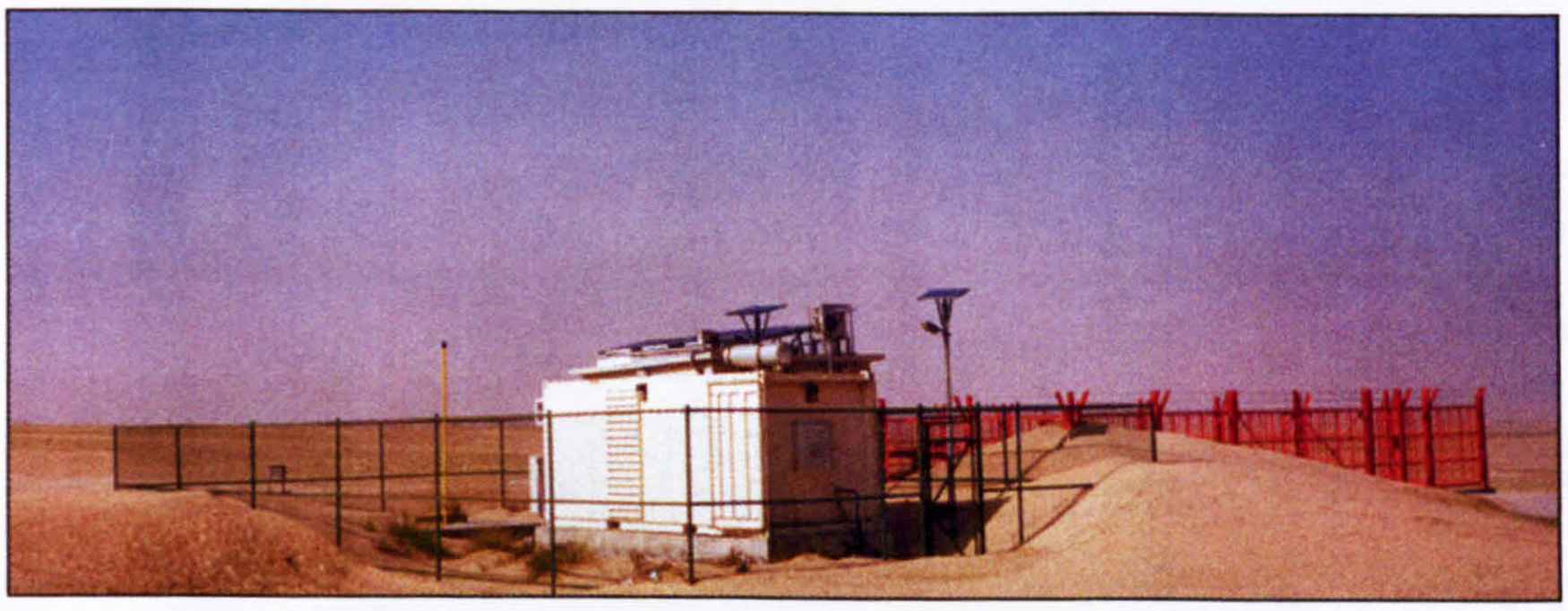

Figure 1.1: Sand drift at electricity transformation pint in the desert of the State of Kuwait. Photograph by author in December 1999.

1.3 Simulation and modelling of drifting particles

As early as 1885, trials to protect certain areas from sand and snow drift were conducted in field studies. Examples of these are the rock wall used in 1868 to protect the railroad in Southeast Wyoming from snow drift, figure 1.2. Fences are also used to protect installations from the drifting sand and to stabilise coastal sand dunes in many areas in the world, an example of that is the

brushwood fence used to stabilise coastal sand at Merseyside, UK, figure 1.3, Pye and Tsoar (1990).

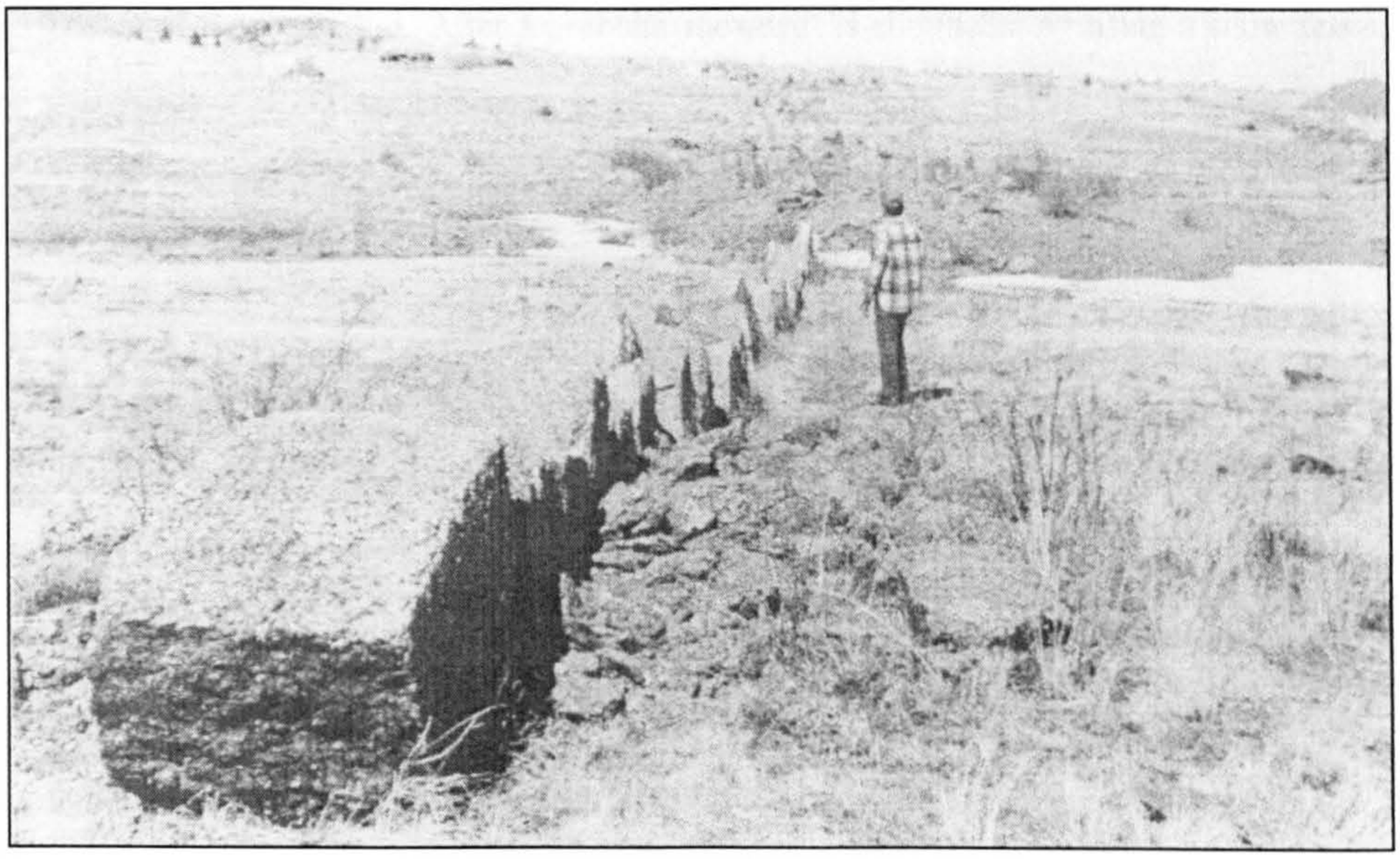

Figure 1.2: Southeast Wyoming rock-row fence was probably built in 1868 to protect railroad. From Tabler (1986).

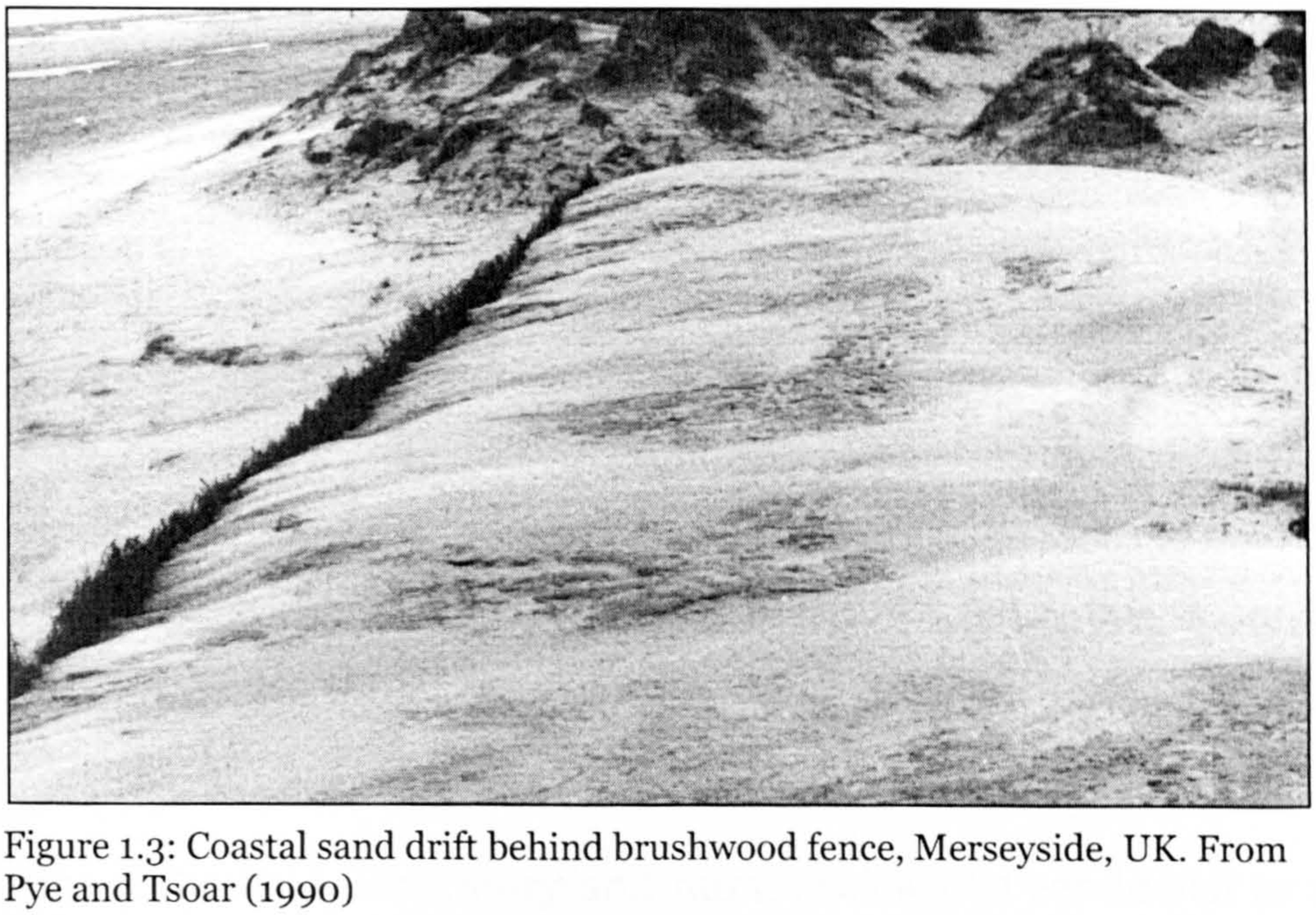

Figure 1.3: Coastal sand drift behind brushwood fence, Merseyside, UK. From Pye and Tsoar (1990)

From the early decades of the twentieth century, many laboratory experiments using atmospheric boundary layer wind tunnels were conducted seeking better understanding of the physics behind wind blown particles. Bagnold (1938)

conducted a leading field study while serving as an engineer with the British army during World War I in the Egyptian-Libyan desert. He then began a comprehensive investigation of the physics of wind blown sand using a wind tunnel located at Imperial College in London. His work resulted in the novel book "*The Physics of Blown Sand and Sand Dunes*", first published in 1941, which is considered as a standard textbook for the study of wind blown sand.

Following Bagnold's pioneering work, a series of field, wind tunnel and mathematical and numerical studies have been conducted covering many aspects of wind blown particles. These have been conducted at both micro and macro scales for a single and group of particles driven by wind. Research carried out during the last few decades has been compiled in conference proceedings and edited volumes, for example [Brookfield & Ahlbrandt (1983), Nickling (1986), El-baz & Hassan (1986), Nordstrom et al. (1990) and Pye and Tsoar (1990)].

Field and wind tunnel measurements give a more accurate and better understanding of the physics behind particle behaviour in the flow. These measurements involve high costs associated with equipment, manpower and time, all at high cost.

The existence of the theoretical background and the availability of powerful computational resources enable numerical techniques to be exploited. These techniques are based on solving the governing equations for flow containing two or more fluids of different physical properties. During recent decades these techniques have been developed, solved and tested for many engineering and environmental purposes. However, the application to problems associated with drifting particles is not yet common.

The majority of the field, laboratory and numerical works conducted to study wind blown particles have focused on:

- Better understanding of the particle threshold condition, particle trajectories and deposition conditions.

- Prediction of particle mass flow rate and the relationship between the mass flux and the different particle transport modes.

- Protection of roads, farms and buildings from drifting problems.

- Observation of global desertification in arid regions and sand dune emigration.

- Observation of the amount of eroded and drifted snow particles and its relation to global warming.

1.3.1 Field and wind tunnel studies

In the present work, several existing field and wind tunnel studies have been used to validate the numerical model as compared to the observations. Benchmark studies such as sand or snow drift at solid and porous fences were used first to compare simulation with both field and wind tunnel measurements, [Tabler (1994), Iversen (1981), Tsoar (1983) and Phillips and Willits (1979)].

Field measurements of sand drift at the twelve-year-old multiple raw porous fence experiment conducted in the Kuwait desert were used also to validate the simulated drift taking into account the full-scale flow dimensions.

Finally, a field experiment of sand drift around an open gate was conducted in the Kuwaiti desert; this provided a further case study to validate the model in a three-dimensional domain.

1.3.2 Numerical modelling

The numerical models used to simulate general gas-particle flow regime are based on solving the fluid flow governing equations.

Kawamura et al. (1999), Sundsbϕ (1997) and Uematsu et al. (1991), presented numerical models based on solving the field flow governing equations, well known as the *Navier-Stokes equations*, and employed them to simulate snow

drift around obstacles. Wipperman (1986) used the same basic theory to simulate the emigration of sand dunes over flat surfaces.

Wipperman (1986) and Kawamura et al. (1999), both solved the Navier-Stokes equations to predict the airflow velocity field while the predictions of the particle mass flux relied on an empirical expressions.

Uematsu et al. (1991), solved an extra equation for the concentration of suspended particles in a similar manner to the way the Navier-Stokes equations are solved. He involved the contribution of saltating particles through an empirical expression of the mass flow rate.

Sundsbϕ (1997) applied the same idea as Uematsu to the prediction of particle concentration. He included the contribution from both suspension and saltation by dividing the computational domain into four sub regions: suspension, saltation-erosion, saltation-deposition and deposition regions where the particle transport equation has a different form for each region.

In general, there are two fundamentally different theoretical approaches utilized to predict the dispersed phase properties in two-phase flows: Particle Tracking model (Lagrangian-Eulerian approach) and Continuum Two-Phase flow Model (Eulerian-Eulerian approach).

A. Particle Tracking Model or (Lagrangian-Eulerian)

The particle-tracking model is based on solving the particle equation of motion to track a single or a group of particles within the flow field. The air phase is considered as the continuum fluid phase, which is solved in a Eulerian reference frame, while the particle is considered as the discrete phase and solved based on the Lagrangian reference frame.

B. Continuum Two-Phase flow Model or (Eulerian-Eulerian)

In this approach the fluid phase as well as the particle phase are both considered as two different continuum solved in the Eulerian reference frame. The two-fluid model is the leading numerical model, which can handle a system

of multi-phase flows. This is classified as the most accurate but most complicated model since it is based on solving two sets of the conservation equations, one for each phase. Simplification of two-fluid model could lead to a less complicated model that may give a degree of accuracy that is acceptable from the engineering point of view. Examples of these simplified models are the mixture and homogenous models.

In the Mixture model, mixture properties such as mixture density, viscosity and the mixture velocity components, are predicted by solving the mixture flow conservation equations. Contributions from all phases are involved according to the phase volume fraction in a specific volume in space.

The Homogenous model is considered as the simplest two-phase flow model since the secondary phase is assumed to have the same local velocity as that of the primary fluid over an infinitesimal volume in space.

According to many authors, there are advantages and disadvantages for each approach. The proper approach for one application may not be the suitable one to another, [Faeth(1983), Durst(1984), Mostafa(1987), Shirolkar(1996), Crowe(1996)].

The Lagrangian approach has the advantage of being able to handle diluted particles with initial size, velocity, position and temperature distributions. It tracks individual particles as they move through the continuous flow field. However, this needs to be evaluated for a huge number of discrete particles, which is time and memory consuming.

Since the discrete phase is treated as another pseudo fluid the Eulerian approach is computationally efficient for a single particle size. Although the behaviour of the individual particles is not modelled, as with the Lagrangian model, the Eulerian model provides more practically useful and convenient results when a large number of particles are involved.

However, one of the limitations of the Eulerian approach is that, for particles of different physical properties (e.g. size and density), one extra transport equation

is required for every particle with a different physical property. This consumes considerable computer memory and CPU time.

Both Lagrangian and Eulerian approaches were implemented and analysed in the present study prior to choosing the most suitable approach in the context of the objectives of this work.

1.4 The aim and synopsis of this work

This research study aims to develop a computer code, based on a Computational Fluid Dynamics (CFD) modelling approach to multi-phase flow, to simulate drifting sand and sand dune development around obstacles of different geometry. The code is intended to be a powerful and convenient design tool for engineers, environmentalist and those who are dealing with daily problems caused by the accumulation of particles around structures.

The model considers both suspension and saltation modes of particle transportation, in the particle transport equation, as individual contributions to the overall momentum balance. The model also takes into account the growing interface boundary between the deposited particles and the flow field by introducing an interface boundary as a solid surface that is allowed to grow or contract according to the wind condition and the particle concentration near that boundary.

The remainder of this thesis is divided in to seven chapters as follow:

- Chapter 2 discusses the basic theoretical background of particles blown by wind.

- Chapter 3 introduces the field and wind tunnel experiments used in this study to validate and calibrate the computational model.

- Chapter 4 describes the theoretical background of the equation of motion for particles driven by the flow field. Different types of forces applied on a particle throughout its trajectory are discussed along with the different Lagrangian procedures employed to track particles within the flow. Different

particle tracking models are implemented in an existing CFD solver, SOFIE, with the proper treatment of boundary and initial conditions. The model is then used to simulate wind blown particles from erodible surfaces over a flat surface and around vertical solid wall perpendicular to the flow direction. Comments on the ability of the model to handle simulations involving particle deposition at obstacles of general shapes are discussed.

- The different two-phase flow models based on the Eulerian approach are discussed in Chapter 5. The theoretical background of the mixture and the homogenous models are introduced. The necessary modifications to the flow field governing equations required to implement the FAVOR technique are discussed. The governing equations are written in a form suitable for the implementation of the FAVOR technique and discretisation based on the finite volume theory. Models for suspended and saltated particles driven by the flow are introduced and added to the particle transport equation source term without the need of empirical expressions to predict the particle mass flow rate. Boundary and initial condition treatments and implementation remarks are discussed and an algorithm of the erosion-deposition process is introduced.

- Chapter 6 presents the assessment of the Eulerian based numerical models and the solution dependency of the controlling parameters. Both physical and numerical related parameters are analysed and discussed paying more attention to their effect on the validity of the model predictions. The advantages and disadvantages of each model are identified and comment on their applicability to problems involving wind blown particles and particle deposition around objects is discussed.

- Chapter 7 presents a validation of the homogenous model coupled with the FAVOR technique against the field and wind tunnel observations discussed in Chapter 2.

- Finally, general discussions, conclusion and recommendations for further extension of the study are presented in Chapter 8.

Chapter 2

Wind blown particles - Basic theory

2.1 Introduction

Wind blowing over a surface covered by loose solid particles can result in movement of the particles as a result of the net force applied to their surfaces. Initially, the particles are eroded from rest then transported a certain distance until they settle back to the ground. Particles driven by wind are generally transported in three different modes according to the physical and dynamical properties of the wind and the particles themselves. A critical wind friction velocity, known as the threshold velocity is used as a control measure for the particle initial movement.

Many authors have proposed empirical expressions for particle mass flow rate, based on the wind friction velocity and the particle threshold velocity. Moreover the relationship between the particle terminal velocity and the wind friction velocity is commonly used as a measure to distinguish between the different particle transportation modes.

The movement of the particles near the surface increases the surface roughness and therefore the wind velocity profile is found to be of a different shape than if the wind passes over a non-erodible surface.

The issues mentioned above are essential to be understood prior to any research relating to wind blown particles. Therefore, this chapter will review the basic theory behind particle erosion, transportation and deposition. The threshold condition, different particle transport modes, empirical expressions developed

for predicting particle mass flow rate and the modified wind profile in the presence of the moving particle are discussed.

2.2 Mechanics of wind blown particles

The erosion, transportation and deposition of wind blown solid particles such as sand, snow or soil involves a number of phenomena. Consider, for example, spherical solid particles spread on a flat surface as seen in figure 2.1.

Wind flowing over the particles creates a pressure difference between the top and bottom surfaces of each particle that generates an aerodynamic force that is resisted by the particle body force.

There are two main aerodynamic forces that are responsible for the initial movement of the particle, drag force in the horizontal direction and lift force in the vertical direction, which acts against gravity.

If the resultant wind force achieves a value that approaches the particle resisting force, then the particle begins to vibrate and roll on the top of other particles. This type of particle movement is known as ***Surface Creep***.

As the wind velocity increases further, the resultant aerodynamic forces will lift the particle off the bed surface but only for a short time. Thus the particle moves in a series of jumps known as the ***Saltation*** mode of particle transportation.

Once a saltating particle is caught by a turbulent eddy, which has a vertical fluctuating velocity component that overcomes the particle settling velocity, then the particle is carried by the wind for a greater time and distance. This mode of transport is known as ***Suspension***.

Commonly, small and light particles are easily caught by turbulent eddies and remain in suspension while the larger and heavier particles remain either in the saltation or surface creep zones. These three particle transport modes are shown in figure 2.2.

In a typical sand storm, the majority of the particle mass transport rate is found to be in the saltation layer while about one fifth to one quarter of that mass transport is as surface creep, [Bagnold (1941), Iversen (1981), Kind (1990), Pay and Tsoar (1990) and others]. Details of these three particle transportation modes will be discussed later in this chapter.

2.2.1 Threshold condition

As has been mentioned, when the wind strength increases the aerodynamic forces applied on the particle surface will approach the particle's body forces but act in the opposite direction. The resultant of these forces is the sum of many forces that may have a significant effect on the movement of the particle.

Examples of these forces are the drag and lift forces, particle weight, spinning and virtual mass forces, pressure gradient, cohesive and coriolis forces, Magnus force, buoyancy force, electrostatic force, particle-particle bonds and the particle-particle collision forces. In a typical wind flow over a flat surface covered by solid particles, most of the above mentioned forces have a negligible effect on the initiation of a particles movement from rest, Bagnold (1941) and others. These forces will be defined and discussed in more detail when discussing the particle equation of motion in Chapter 5.

Bagnold observed in his original wind tunnel experiment that the initiation of particle movement takes place at a certain wind velocity when the wind shear stress applied on the particle exceeds the particle threshold shear stress.

Since the shear stress is related to the shear velocity (friction velocity), Bagnold defined two types of threshold velocity: the impact threshold and the fluid threshold. The impact threshold is the wind velocity that must be exceeded for the movement to be maintained, whereas the fluid threshold is the wind velocity that must be exceeded for the movement to be initiated. Generally the fluid threshold is thought of as being greater than the impact threshold, figure 2.3.

The difference in the fluid and impact threshold velocities is due to the kinetic energy of the particle during movement, Pye & Tsoar (1990). Pomeroy (1988)

found that there was no obvious difference between these two values, so that throughout this thesis they are assumed to be equal and known as the *threshold velocity*, U_t^*.

The force required to overcome the sum of forces resisting particle motion is related to the surface shear stress. Since the shear stress is proportional to the friction velocity, the threshold velocity is in fact a critical friction velocity $\tau_t = \rho\, u_t^2$. The threshold velocity is then defined as the minimum friction velocity required to maintain the movement of the particle.

It has been shown that the threshold velocity is function of the particle size, shape and density [Schmidt (1980) and Kind (1990)].

Bagnold (1941) obtained an expression for the threshold velocity when applied to sand particles in terms of the fluid and the particle physical properties:

$$U_t^* = A\left(\frac{\rho_p\, g\, D_p}{\rho}\right)^{1/2} \qquad (2\text{-}1)$$

Where: A is the dimensionless threshold velocity.

Equation (2.1) is only applied when both cohesive and adhesive forces are negligible thus for wet sand or frozen snow particles the value of the threshold velocity is much higher than for dry sand or newly-fallen snow particles.

Iversen et al. (1979a,b) carried out a large number of wind tunnel experiments on particles of different size and density. Results of these experiments are illustrated in figure 2.4 and show the measured threshold velocity plotted against the threshold parameter $\left(\rho_p\, g\, D_p/\rho\right)^{1/2}$. It is clearly indicated that for large particle sizes, the dimensionless threshold parameter A, which is in fact the slope of the curve, is essentially constant.

It can be seen that there is a minimum value of the parameter A that varies as the particle size is changed. This indicates that A is not identical for all particle sizes otherwise all curves must meet at one minimum value.

Figure 2.5 shows the threshold dimensionless parameter against the particle threshold Reynolds number, Re_p, and is compared to the threshold curves presented by other researchers. It is clearly seen that for $Re_p \geq 3.0$ the results are comparable but for smaller Reynolds numbers they are somewhat disparate. Also for a large Reynolds number, the parameter A has an almost constant value for all particles, which indicates that the parameter A is not a function of the physical properties of the particles for high Reynolds numbers.

2.2.2 Particle transport modes

- Surface creep

A particle will start to roll (or creep) as a result of two external forces acting on its surface. Firstly, the torque caused by the drag and lift forces that generates a rotating force around the point J, figure 2.1. Another major cause of the surface creep is the momentum that is exerted on settled particles from the impact of saltating particles.

- Saltation

If the wind friction velocity reaches a higher value than the particle threshold velocity, the particle is then entrained into the flow field with an initial horizontal and vertical velocity u_1 and v_1 as shown in figure 2.6. The particle then extracts horizontal momentum from the flow and is transported along a trajectory typically similar to the one in figure 2.6.

As the particle is blown by the wind, gravitational force pulls it downward, eventually hitting the ground with horizontal and vertical velocities u_2 and v_2, with an impact angle α varying between 30°-50°, according to White & Schulz (1977) and Willetts & Rice (1986).

The nature of the saltation process has been analysed extensively in field studies, wind tunnel experiments and numerical modelling by many authors [Bagnold (1941), Owen (1964), Iversen (1982), Jensen (1983), Horikawa et al. (1984), Willetts & Rice (1986), Warner & Haff (1988), Anderson & Haff (1988),

McEwen (1990) and Dover (1993)]. The aim being to gain a better understanding of the principals of the erosion, saltation and deposition processes.

The zone in which saltation movement occurs is known as the saltation layer and the thickness of this layer is defined by the maximum height that saltating particles could attain. However, since the saltation layer thickness is dependent on the physical properties of the particles, such as particle size and density and the fluid flow density and velocity, the saltation height is taken as the mean maximum saltation trajectory height. According to Kind (1990) it is usually a few centimetres from the bed.

The aerodynamic lift force is found to have a significant effect on the particle spinning velocity, which therefore affects the saltation height, White & Schulz (1977). Owen (1964), proposed that the drag force has less effect on the maximum height of the particle trajectory and suggested that the trajectory height to be proportional to the particle lift velocity $[v_1^* / 2g]$. He also suggested that v_1 is comparable to the flow friction velocity $[u^{*2} / 2g]$.

Schmidt (1985) agreed that the saltation height is proportional to $[u^{*2} / 2g]$ and that it could be used as an acceptable approximation to the saltation height in the case of snow particles. Whilst Gerety (1984) argued that this approximation is not a good prediction of the saltation trajectory height but it could give a good approximation for the surface roughness height during the saltation, which might by used to predict the modified wind velocity profile in the presence of saltating particles.

In this study the maximum saltation height was taken as:

$$H_{sal.} = C u^{*2} / 2g \qquad (2\text{-}2)$$

Owen (1964) suggested two values of the constant C. To predict the mean maximum saltation height C is assumed to be 1.6. Where the same formula is used to predict the mean maximum axial length it is 20.6. As shown in figure

2.6, the horizontal distance L is about 12.5 times the maximum trajectory height H that the particle can attain. Detailed discussions about this issue can be found in Pay and Tsoar (1990).

- Suspension

If the wind friction velocity becomes higher than the threshold velocity and the vertical fluctuation velocity component of turbulent eddies is at least equal to the particle's settling velocity, then the particle will transport in the suspension manner, Bagnold (1973) and Nickling (1994). Whilst in a state of suspension particles may be carried to heights much greater than the saltation height as a result of turbulent diffusion, figure 2.2. Fine particles, such as dust, may rise up to several hundreds of meters and be in suspension for long periods of time that may extend to a few days Budd et al. (1966).

Whilst coarser particles under moderate wind may travel for a few meters both in length and height Takeuchi (1980).

Whatever the height reached by a particle, it is obvious that since the particle falling velocity is directly related to its physical properties, such as the particle size and density, and to the carrier fluid properties, such as the density and viscosity, smaller particles are more easily carried to greater heights and for longer time.

The settling velocity of a freely falling particle is proportional to the particle diameter and density. It can be calculated according to Stokes Law:

$$v_f = \frac{\rho_p g D^2}{18 \mu} \qquad (2\text{-}3)$$

Tsoar and Pye (1987), suggested that the ratio of the settling velocity to the friction velocity could be used as a measure of the particle susceptibility to be carried in suspension, figure 2.7 (Pye and Tsoar p101). Suspension occurred when $v_f/u^* << 1$. During a typical windstorm, when the value of the wind friction velocity varies between 0.18 - 0.6 m/s, the corresponding maximum size of

particles that can be transported by suspension ranges between 0.04 - 0.06 mm diameter, Pye & Tsoar (1990). For $v_f/u^* << 0.1$, long term suspension occurs corresponding to a maximum particle size of 0.015 - 0.02 mm, Gillette (1981). Finer particles are assumed to be non-settling particles according to Tsoar & Pye (1987) and others.

2.3 Mass transport rate

Many authors from different scientific backgrounds have developed mathematical models to predict mass transport rate for sand, snow and soil particles blown by wind [Bagnold (1941), Kawamura (1951), Owen (1964), Kind (1976), Lettau & Lettau (1978), Owen (1980), Andersen (1983), Ungar & Haff (1987) and Sϕrensen (1991)].

Since large portions of the particles are transported either by suspension or saltation, most of the research efforts have been aimed at models predicting the mass transport rate under these two transportation modes. Outlines of the mass transport rate expressions both in suspension and saltation layers are outlined below.

2.3.1 Mass flow rate in Saltation

Bagnold (1941) developed the leading semi-empirical formulae to predict the mass transport rate in the saltation layer. Bagnold built his analysis based on the fact that the flow rate at which sand particles can be driven by wind is strongly related to the wind shear forces that are applied on the particle surface. Due to the pressure difference between the upper and lower surfaces of a single particle, the particle is injected vertically into the flow with initial horizontal velocity u_1 known as the lift-off velocity. The particle hits the ground after a certain distance L with impact velocity u_2 figure 2.6. Therefore, the momentum extracted by the particle from the wind over the distance L is:

$$m_g \frac{(u_2 - u_1)}{L} \qquad (2\text{-}4)$$

where: m_g is the particle mass.

Since u_1 is small comparing with u_2, the rate of momentum loss per unit width is:

$$M\frac{u_2}{L} \tag{2-5}$$

where M is the total mass in unit width.

Equation (2.5) is equivalent to the surface shear stress resisting the fluid due to saltated particles. The total shear stress exerted by the fluid flow is the sum of the shear stress due to the saltation $\tau_{Saltation}$ and the shear stress required to initiate a particle from rest $\tau_{Threshold}$. Bagnold in his first derivation ignored the threshold shear stress and related the mass flow rate due to saltation to the fluid friction velocity, $u^* = \sqrt{\tau/\rho}$, thus:

$$Q_{Sal.}\frac{u_2}{L} = \rho u^{*2} \tag{2-6}$$

Bagnold then assumed that: $\frac{u_2}{L} = \frac{g}{v_1}$ where v_1 is the particle lift-off velocity. Also he assumed that v_1 directly changes as the friction velocity changes, $v_1 = 0.8u^*$ hence:

$$Q_{Sal.} = 0.8\frac{\rho}{g}u^{*3} \tag{2-7}$$

Later and after some experimental work carried out by Bagnold, he approximated that the surface creep is about 25% of the total mass flow rate then:

$$Q_{Sal.} = 1.1\frac{\rho}{g}u^{*3} \tag{2-8}$$

More than 10 different expressions, found in the literature, are used to predict the mass flow rate, all of which are based on Bagnold's expression, table 2-1. Iversen & Rasmussen (1999) and Pye & Tsoar (1990) discussed the differences

between these formulas, which are all based on wind tunnel observations over flat surfaces accept Ungare & Haff (1987) and Sϕrensen (1991), which are derived from numerical analysis involving the prediction of the saltation trajectories. The rate of mass transport in the saltation layer predicted by different models for uniform particle size shows considerable discrepancies, figure 2.8.

2.3.2 Mass flow rate in Suspension

In the steady state suspension, the differential equation for the vertical particle concentration is a simple balance of gravitational settling and turbulent diffusion of particles, and takes the form:

$$\frac{\partial}{\partial y}\left[\Gamma_p\left(\frac{\partial c}{\partial y}\right)\right]=-v'_f\left(\frac{\partial c}{\partial y}\right) \tag{2-9}$$

where Γ_p is the effective diffusion coefficient for the particle and c is the particle concentration.

By assuming that there is no source or sink of particles (no erosion or deposition), the equation can be integrated over a certain height to give:

$$\Gamma_p\left(\frac{\partial c}{\partial y}\right)=-v_f c \tag{2-10}$$

where v_f is the concentration weighted average settling velocity.

Assuming that the particle is small enough to follow the fluid flow, the particle diffusion coefficient can be assumed to be equal to that of the fluid. The fluid diffusion coefficient varies linearly in the boundary layer and is characterised by the logarithmic velocity profile ($\Gamma_p=\kappa u^* y$), Anderson & Hallet (1986). Thus, integrating equation (2.10) again, the equation of suspended particle concentration distribution becomes:

$$c=c_o\left(\frac{y}{y_o}\right)^{\frac{-v_f}{\kappa u^*}} \tag{2-11}$$

where c_o is the concentration at reference height y_o.

Particle concentration profiles at different heights are shown in figure 2.9 for different surface roughness y_o and constant particle settling velocity and wind friction velocity. It shows that according to equation (2.11), the particle concentration reaches maximum values near the bed surface and decreases with height.

2.4 Wind profile characteristic

Wind velocity increases with height due to decrease in the shear stress. For fully turbulent boundary layers and in the absence of the saltating particle, whether for flow over a non-erodible surface or where the friction velocity is less than the threshold value, the vertical velocity profile will follow the logarithmic profile:

$$\frac{u}{u^*}=\frac{1}{\kappa}\ln\left(\frac{y}{y_o}\right) \qquad (2\text{-}12)$$

Over a surface of stationary particles, the surface roughness (y_0) was found to be approximated by $D_p/30$ and adopted for airflow over sand surface by Bagnold (1936) and Monin & Yaglom (1965).

In the presence of saltating particles, the velocity profile is significantly affected as the surface roughness increases. The wind profiles measured by Bagnold with and without saltation for different wind strength are shown in figure 2.10. It shows that the focal point, the point where wind profiles of different shear velocity meets, moves upward, which means that the surface roughness increases due to saltation.

A modified form of the logarithmic profile has been introduced to take into account the effect of the saltated particles, Bagnold (1941), Owen (1964) and Whit & Schulz (1977). The modified velocity profile can be derived using the information from the focal point:

$$\frac{u}{u^*}=\frac{1}{\kappa}\ln\left(\frac{y}{y'_o}\right)+\frac{u_t^*}{u^*} \qquad (2\text{-}13)$$

where u_t^* is the threshold velocity and y'_o is the saltation surface roughness.

2.5 Closure

The physical and theoretical background of particle blown by wind was reviewed. The threshold conditions of the particle movement and settlement and the different modes of particle transport were defined. It was clearly found that a particle can be considered to be moved in either suspension, saltation or surface creep if the ratio of the falling velocity to the friction velocity is defined. Many empirical expressions of the mass flow rate of particles transported in saltation were found all of which rises the fluid friction velocity to the power three. The vertical distribution of the suspended particles was defined in terms of friction velocity, surface roughness and the freely falling particle velocity.

In addition, the vertical wind profile based on the atmospheric natural logarithmic law and the effect of the saltating particles on the profile were reviewed.

Table 2-1. Empirical expressions of the particle mass transport rate predicted by different authors. From Iversen & Rasmussen (1999).

Bagnold (1941)	$1.5\frac{\rho}{g}u^{*3}$
Kawamura (1951)	$1.5\frac{\rho}{g}\left[1-\left(\frac{u}{u^*}\right)^2\right]\left(1+\frac{u}{u^*}\right)$
Owen (1964)	$1.0\frac{\rho}{g}\left[0.25+\frac{1}{3}\left(\frac{u_f}{u^*}\right)\right]\left[1-\left(\frac{u_t^*}{u^*}\right)^2\right]$
Kind (1976)	$1.5\frac{\rho}{g}\left[1-\left(\frac{u_t^*}{u^*}\right)^2\right]$
Lettau & Lettau (1978)	$1.5\frac{\rho}{g}\left[1-\left(\frac{u_t^*}{u^*}\right)\right]$
Owen (1981)	$1.5\frac{\rho}{g}\left[1-\left(\frac{u_t^*}{u^*}\right)^2\right]\left(1+\frac{C'}{C}\right)$
Ungare & Haff (1987)	$280\frac{\rho}{g}\left[1-\left(\frac{u_t^*}{u^*}\right)^2\right]\sqrt{\frac{\rho}{\rho_p}}\left(\frac{u_t^*}{u^*}\right)$
Sϕresen (1991)	$4\frac{\rho}{g}\left[1-\left(\frac{u_t^*}{u^*}\right)\right]\left(1+17.75\frac{u_t^*}{u^*}\right)$

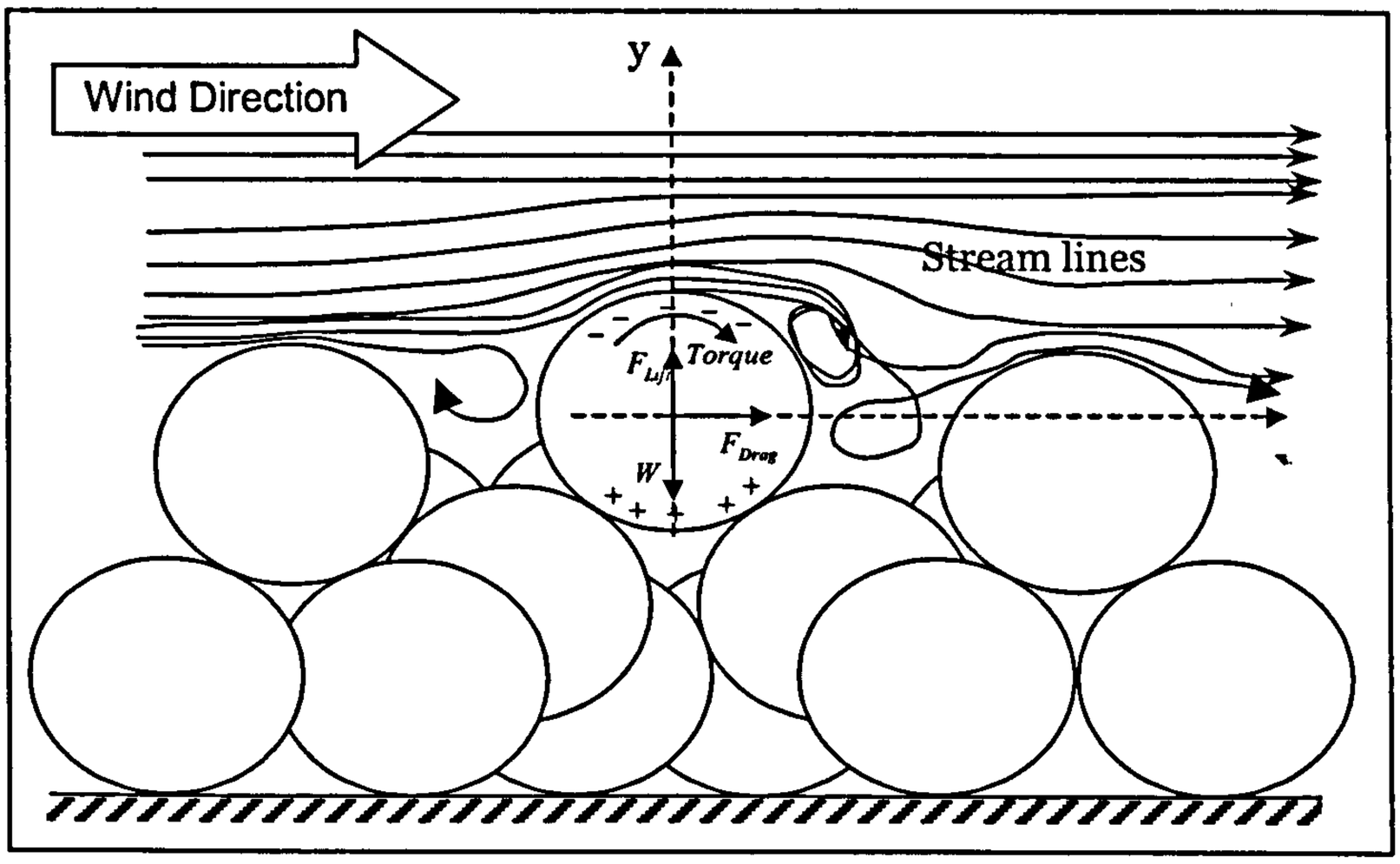

Figure 2.1: Definition diagram for the forces acting on particles spread on a granular bed subject to a steady fluid flow.

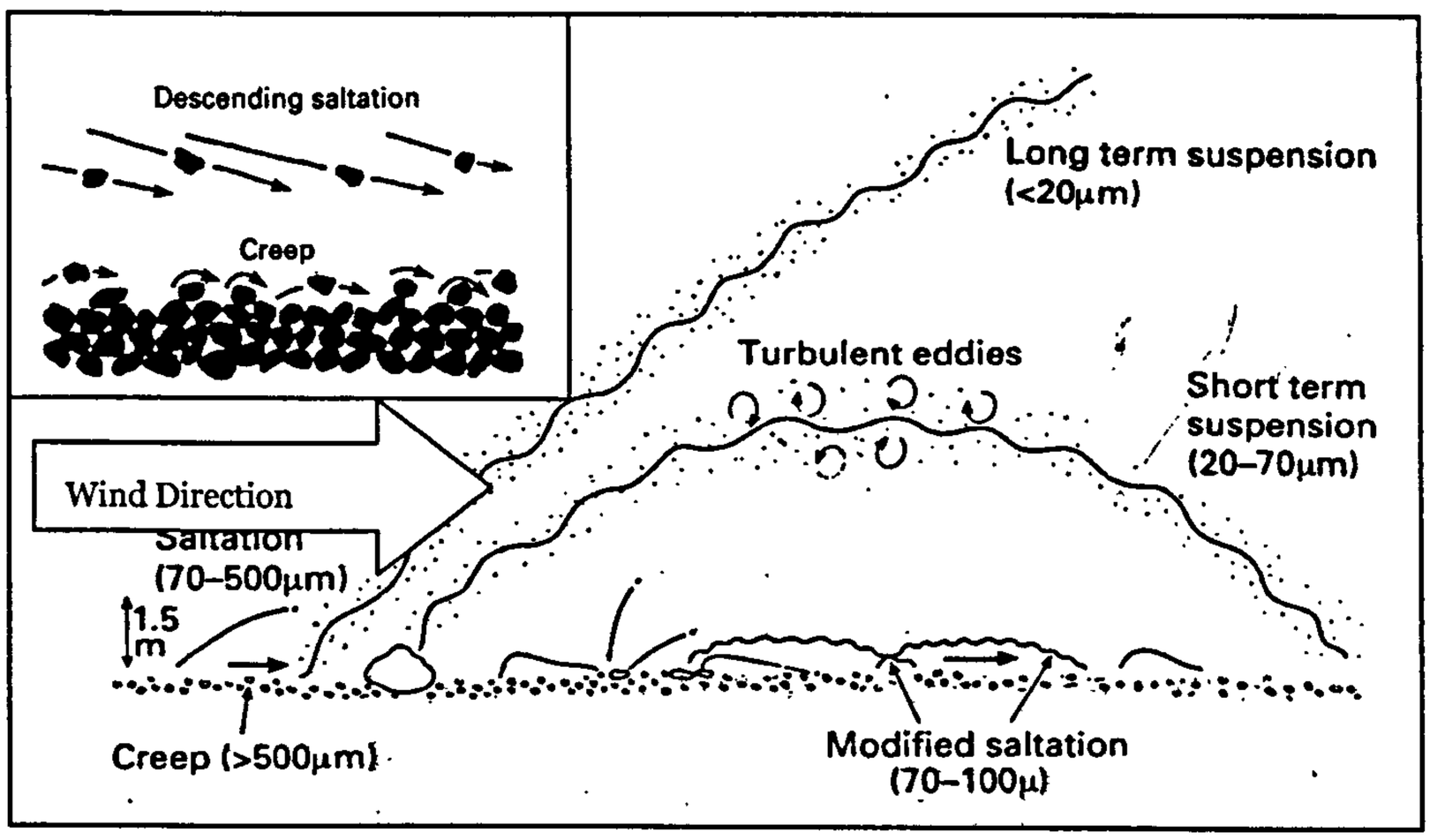

Figure 2.2: Modes of particle transport by wind showing the typical particle size ranges transported during moderate windstorm. From Nickling (1994). In the frame zoom on the surface creep region. From Allen (1994).

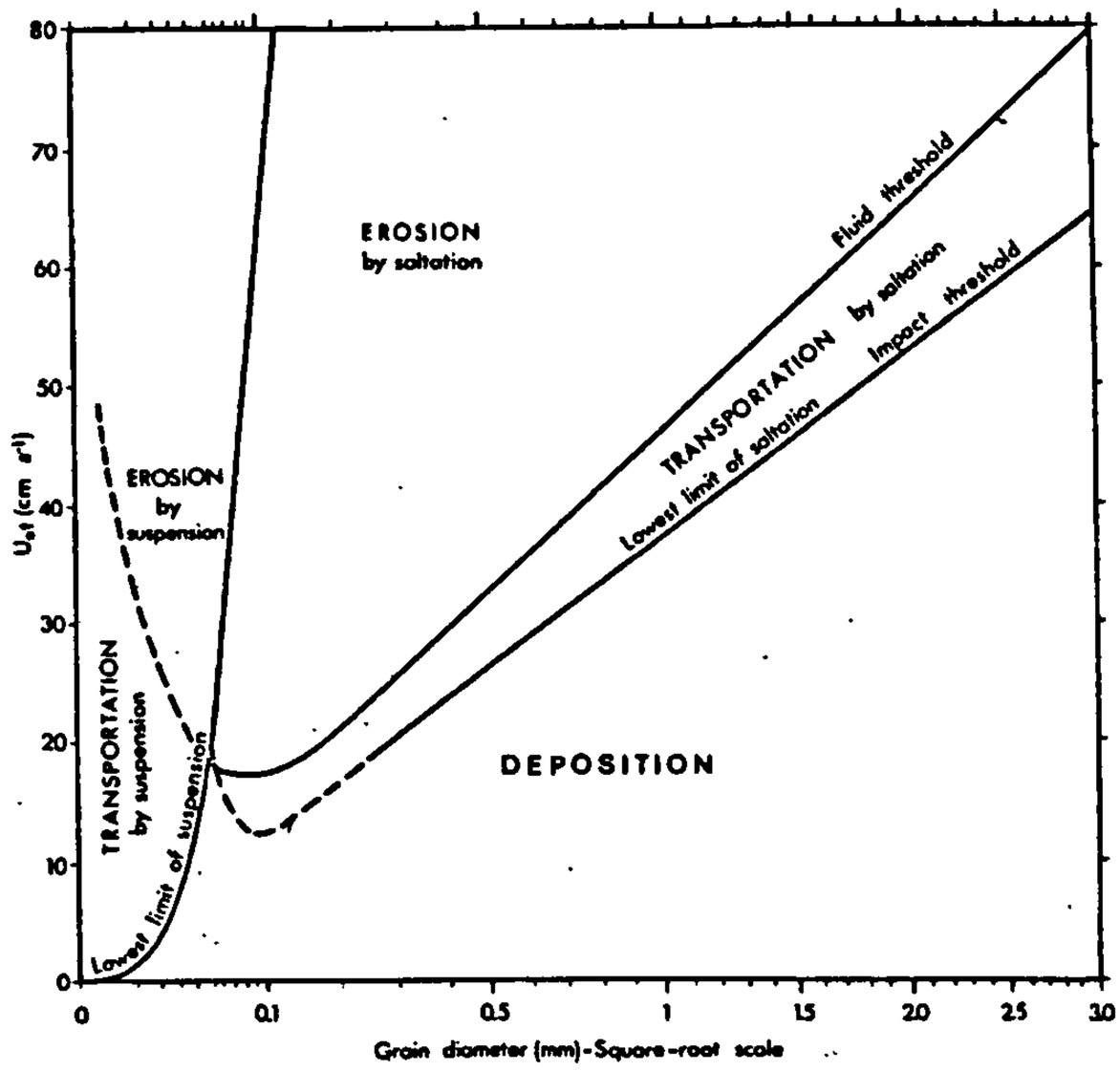

Figure 2.3: Relationship of the threshold velocity to particle size. From Pye and Tsoar (1990).

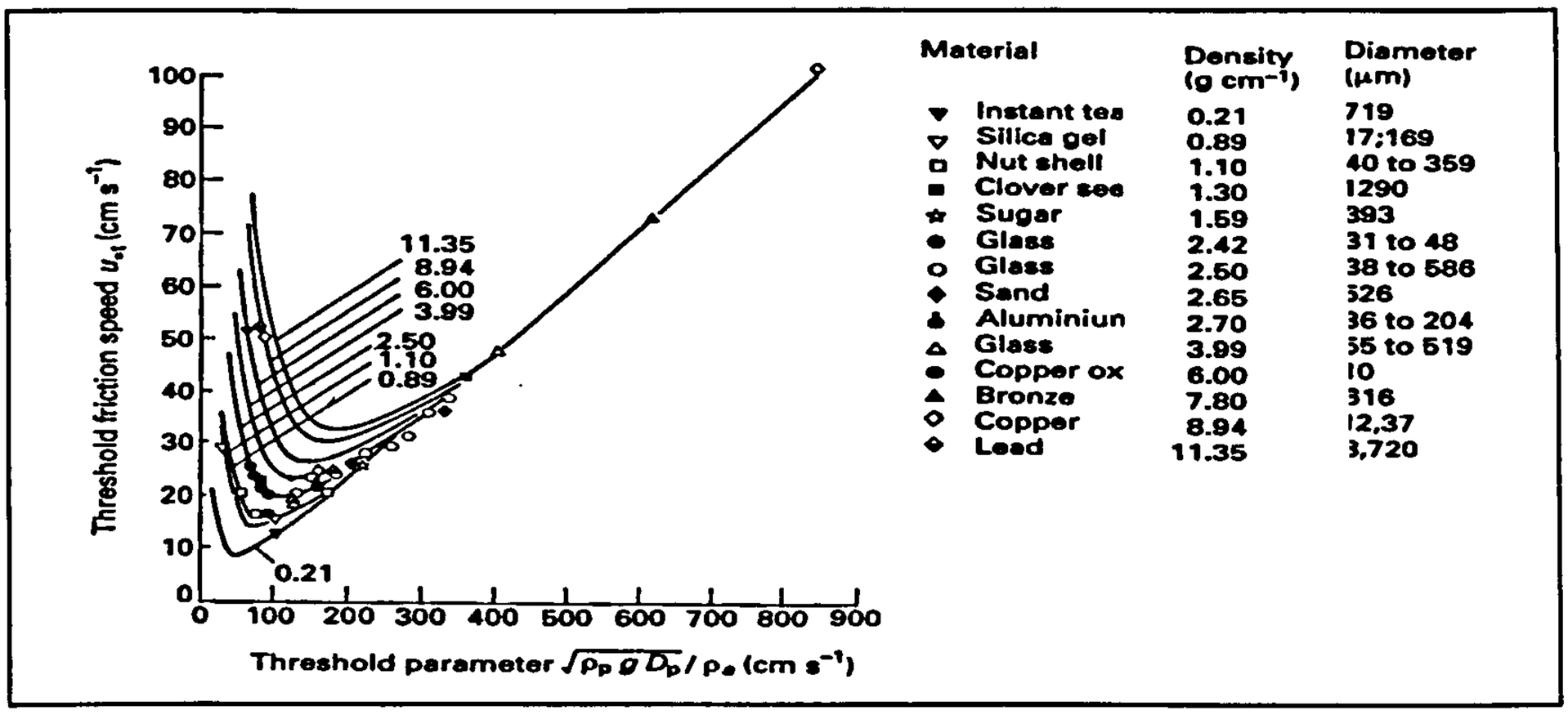

Figure 2.4: Threshold velocity as a function of the threshold parameter of different particle sizes and densities. From Iversen et al. (1976).

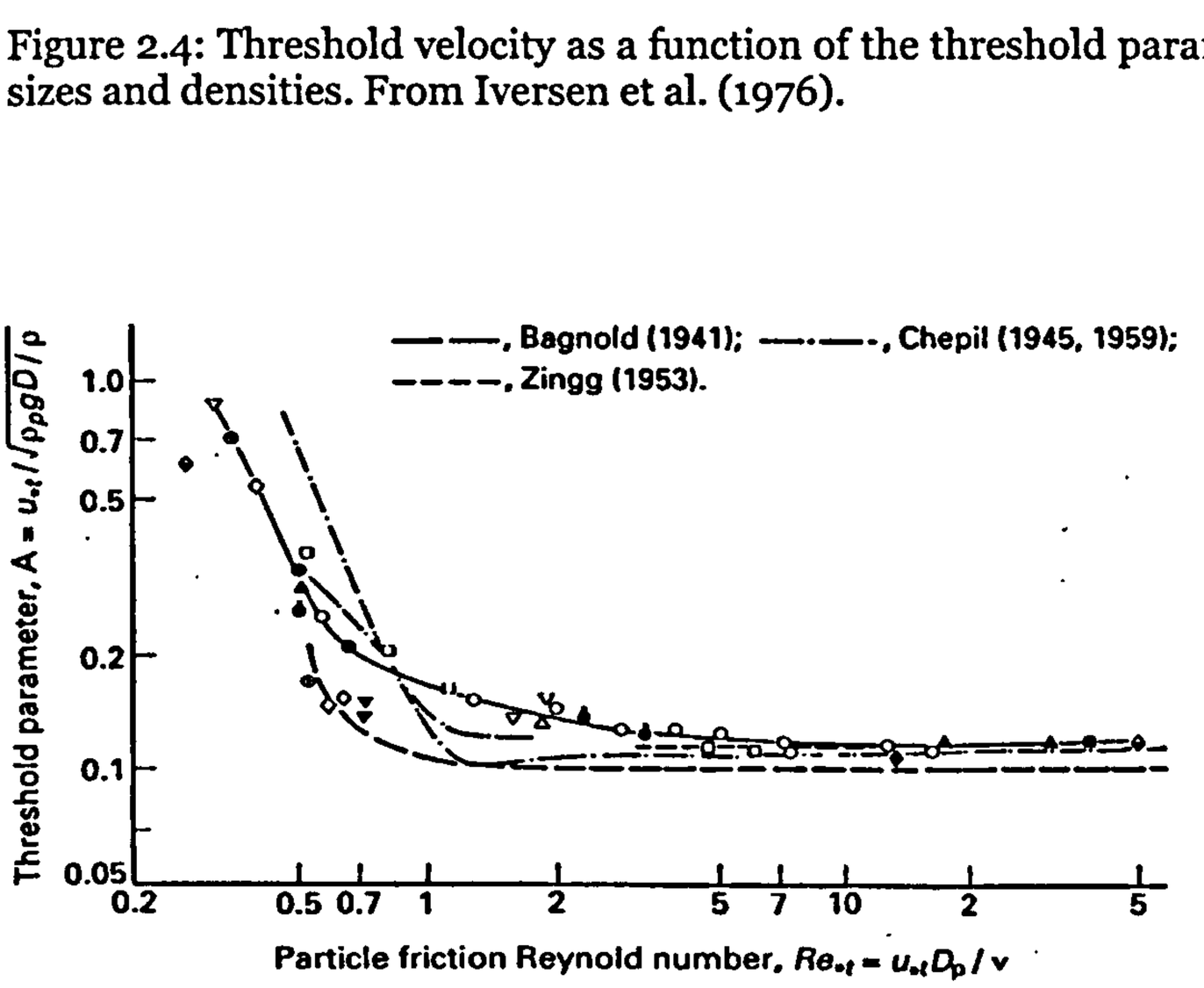

Figure 2.5: Dimensionless threshold velocity parameter versus the particle threshold Reynolds number comparing the data curves of Bagnold (1941), Chepil (1945b, 1959) and Zingg (1953). From Greeley and Iversen (1985).

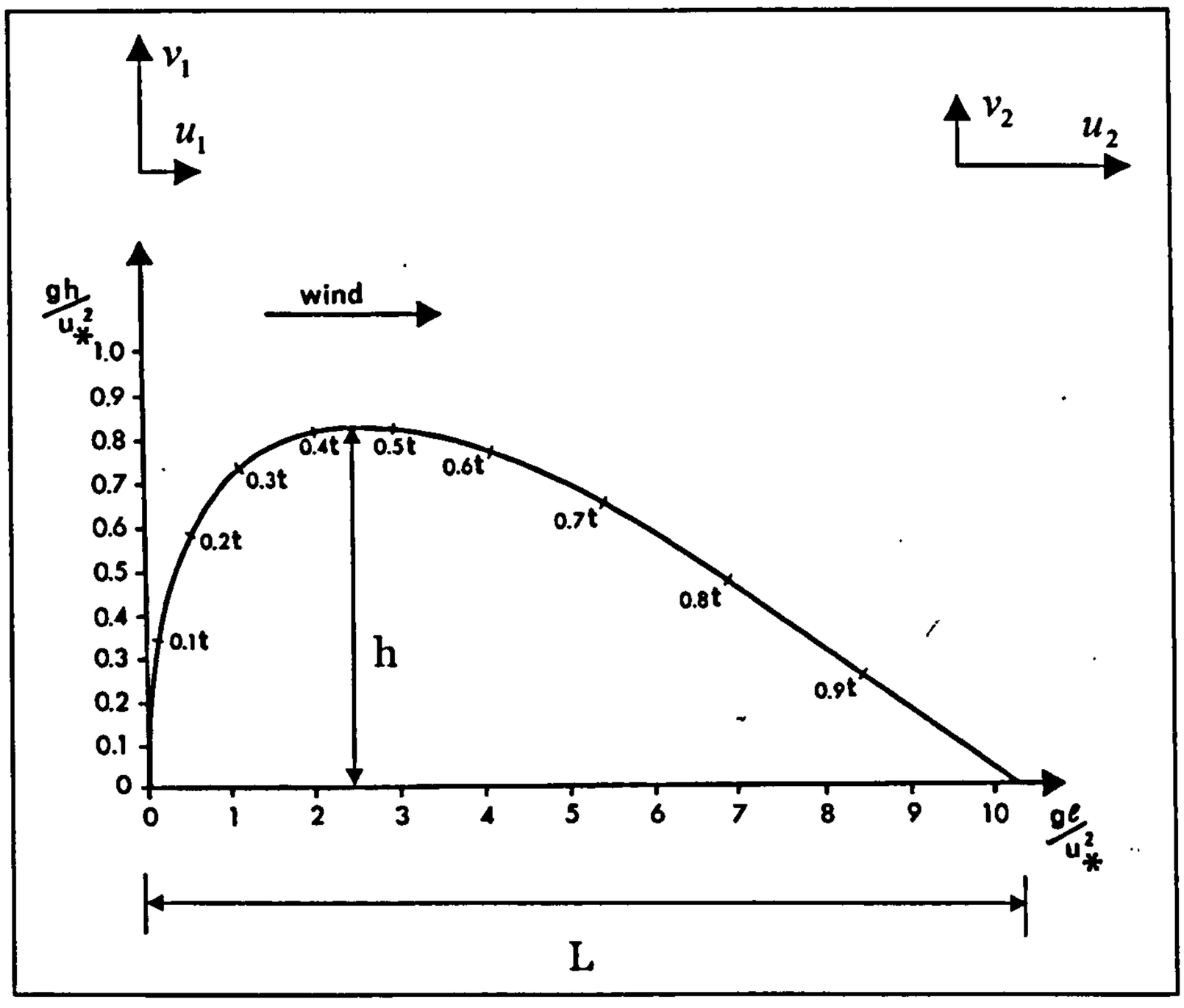

Figure 2.6: Typical saltating particle trajectory. From Pye and Tsoar (1990).

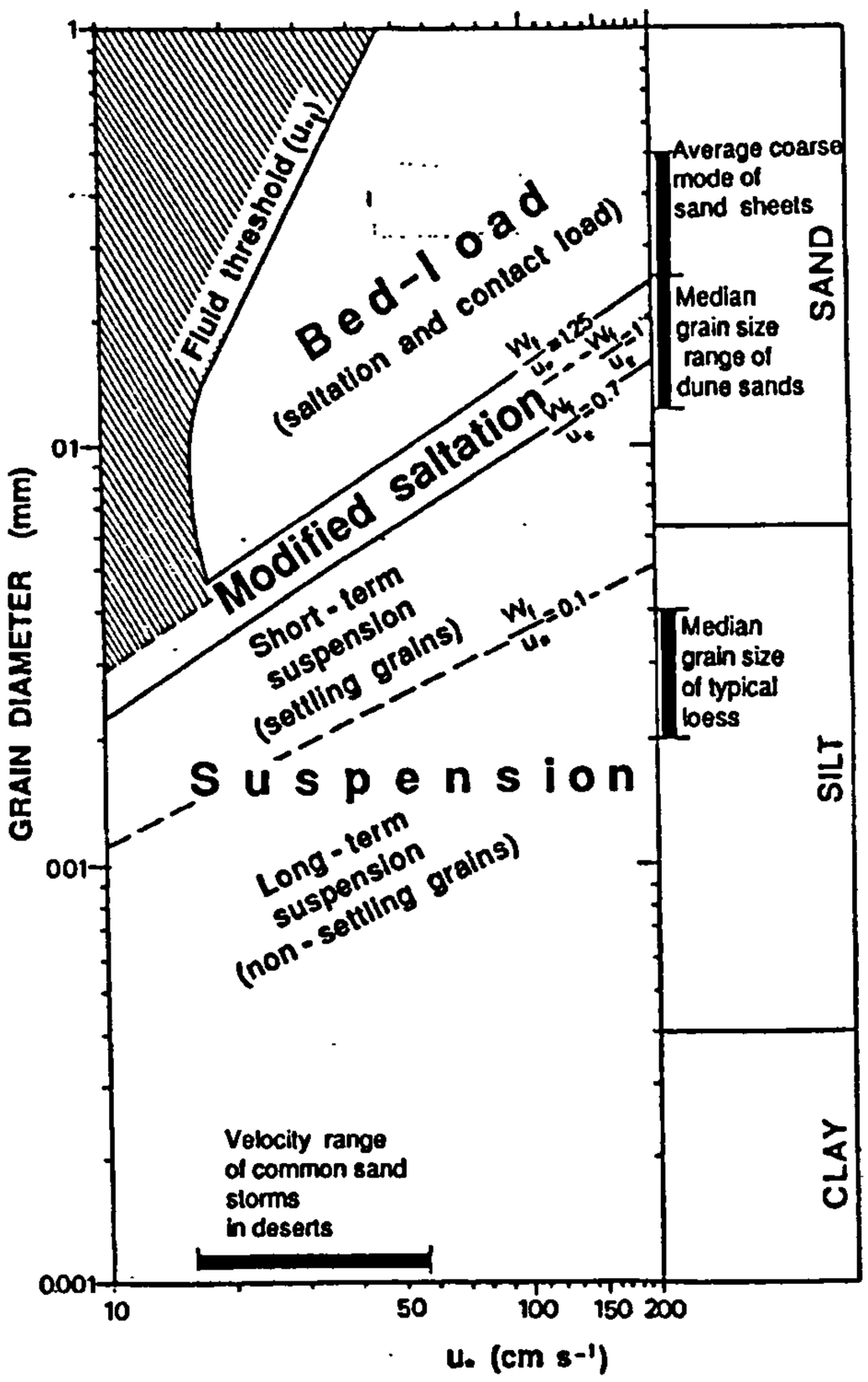

Figure 2.7: Falling to friction velocity ratio as a measure to the transportation mode. From Pye and Tsoar (1990).

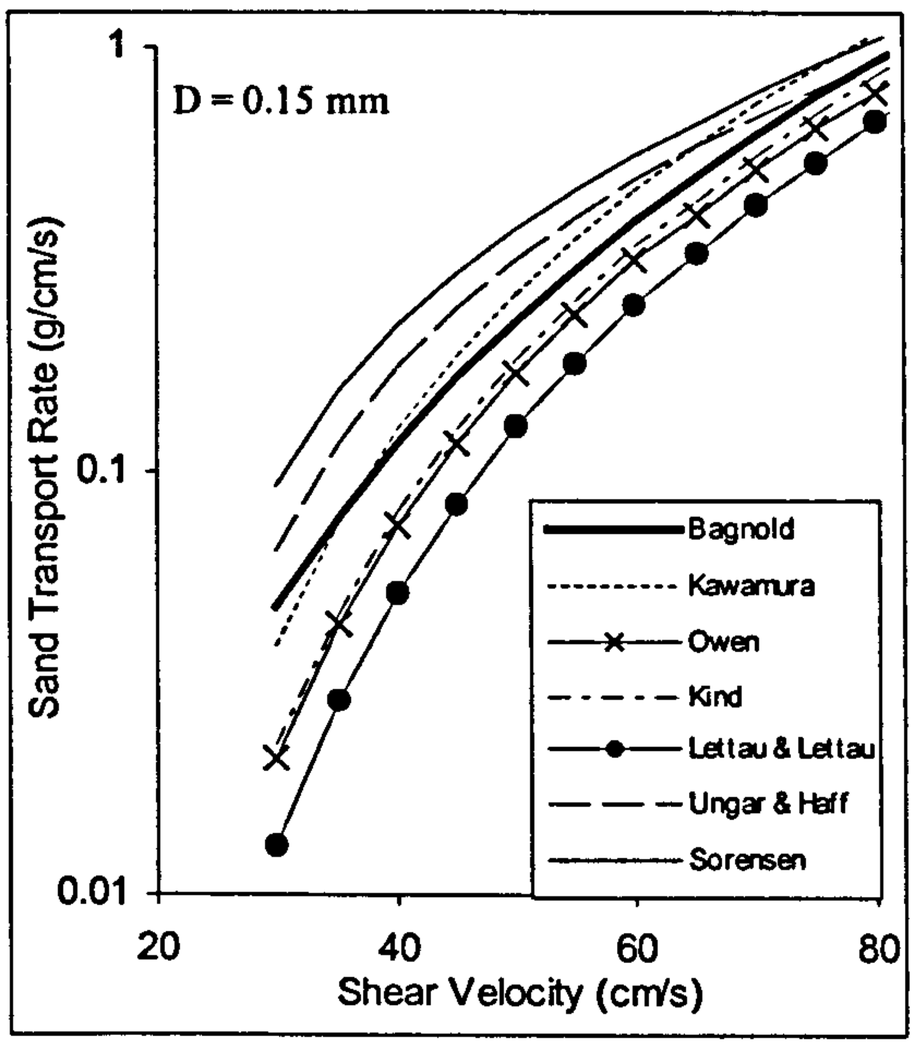

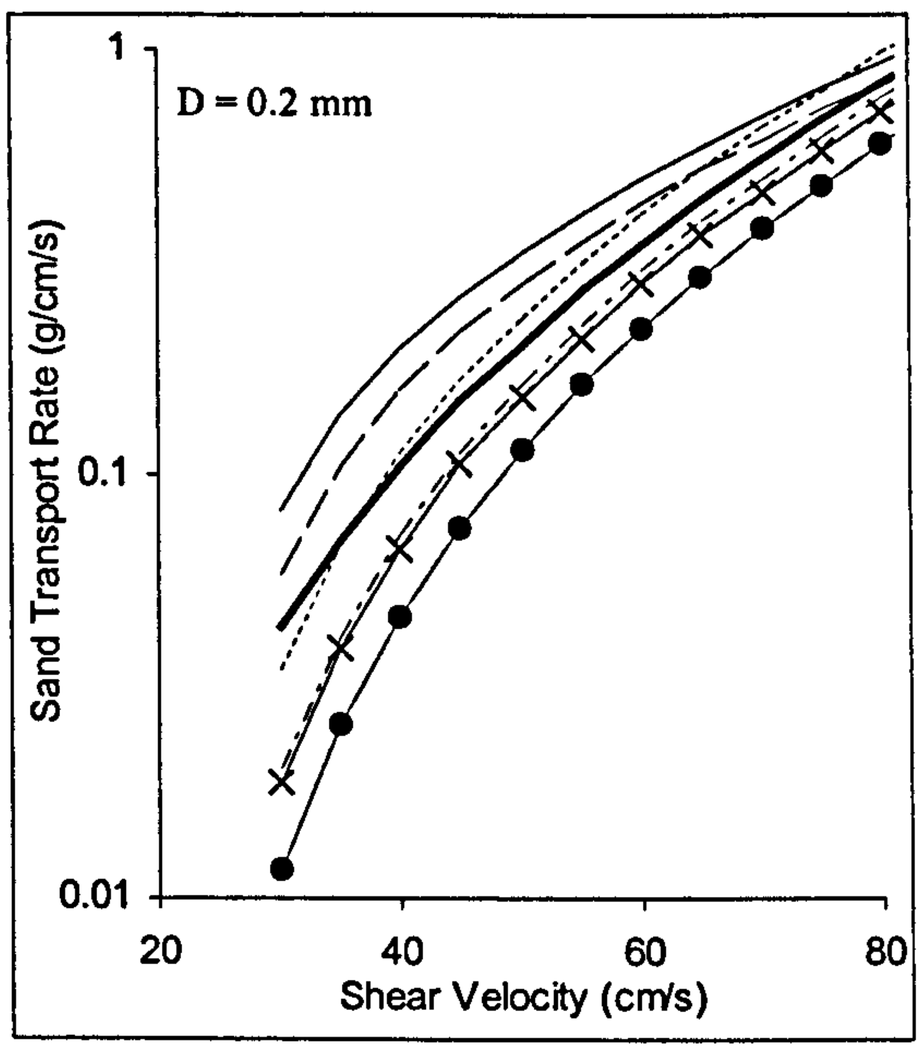

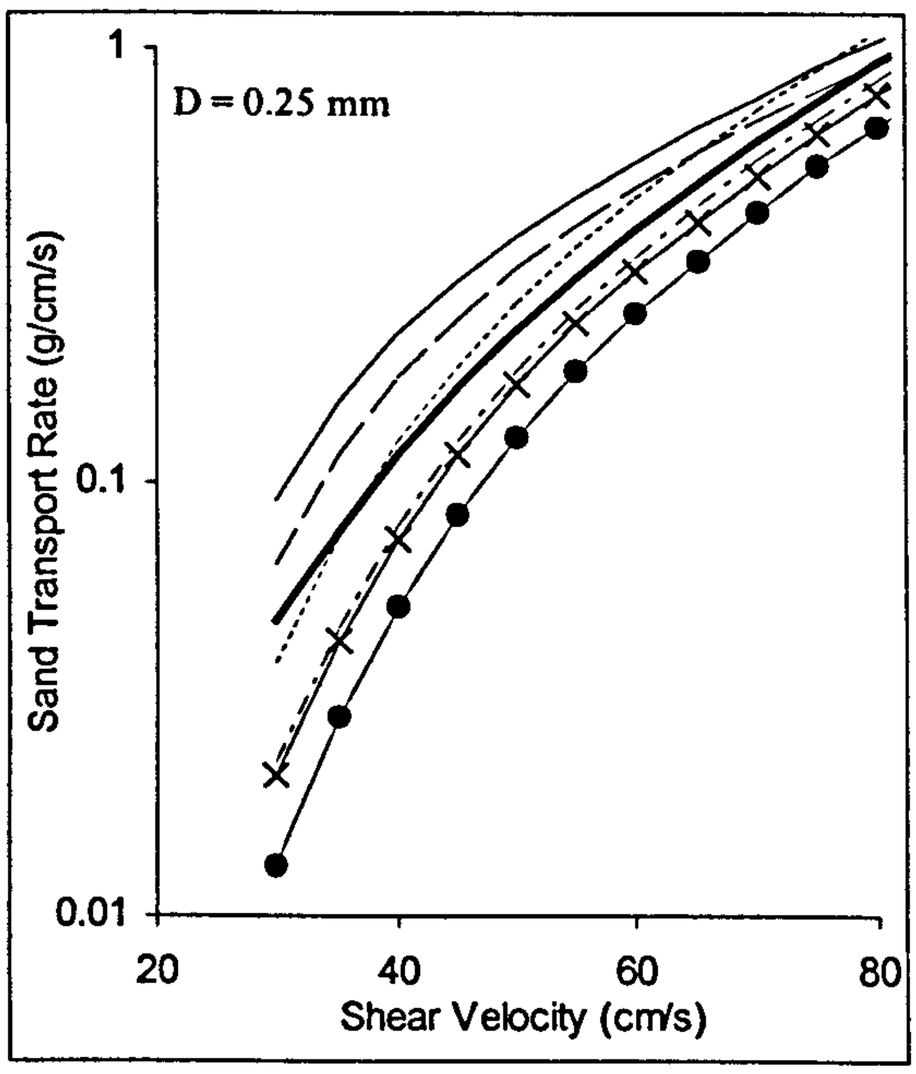

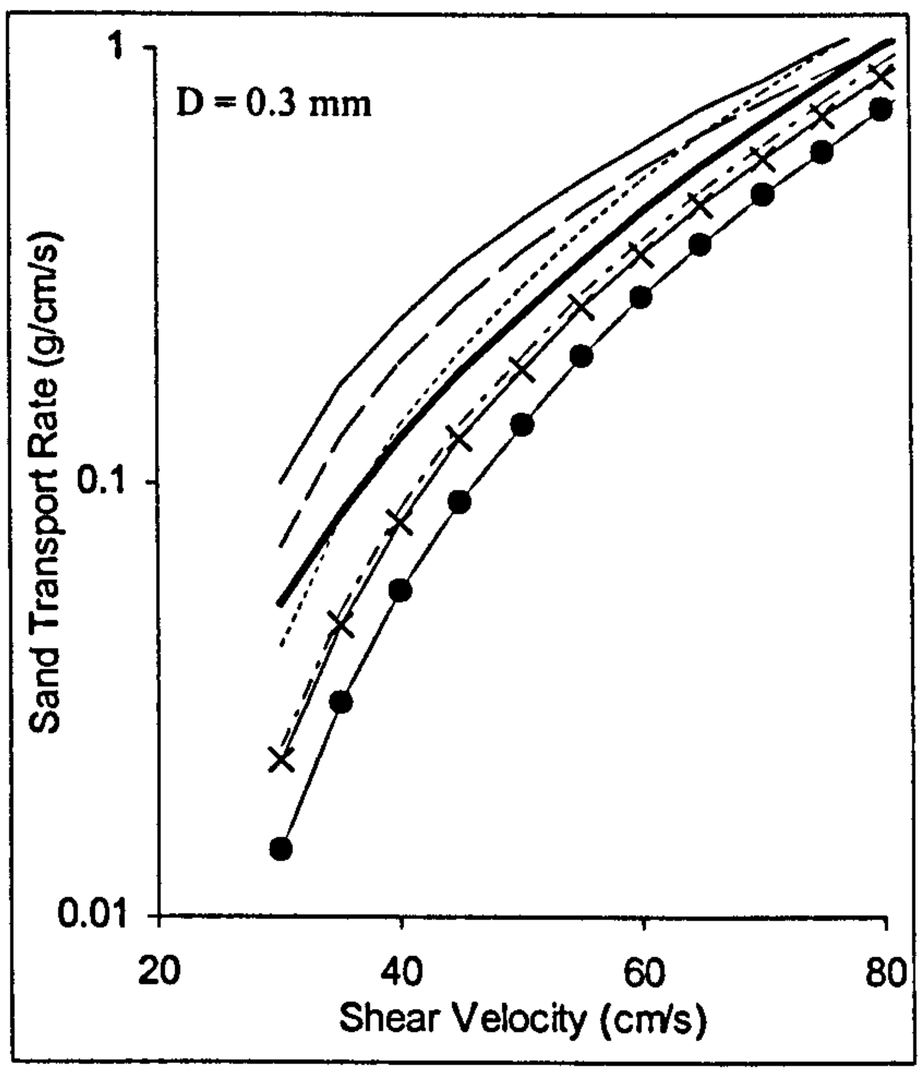

Figure 2.8: Sand flow rate as function of the wind friction velocity that predicted by different transport equations for sand of different sizes.

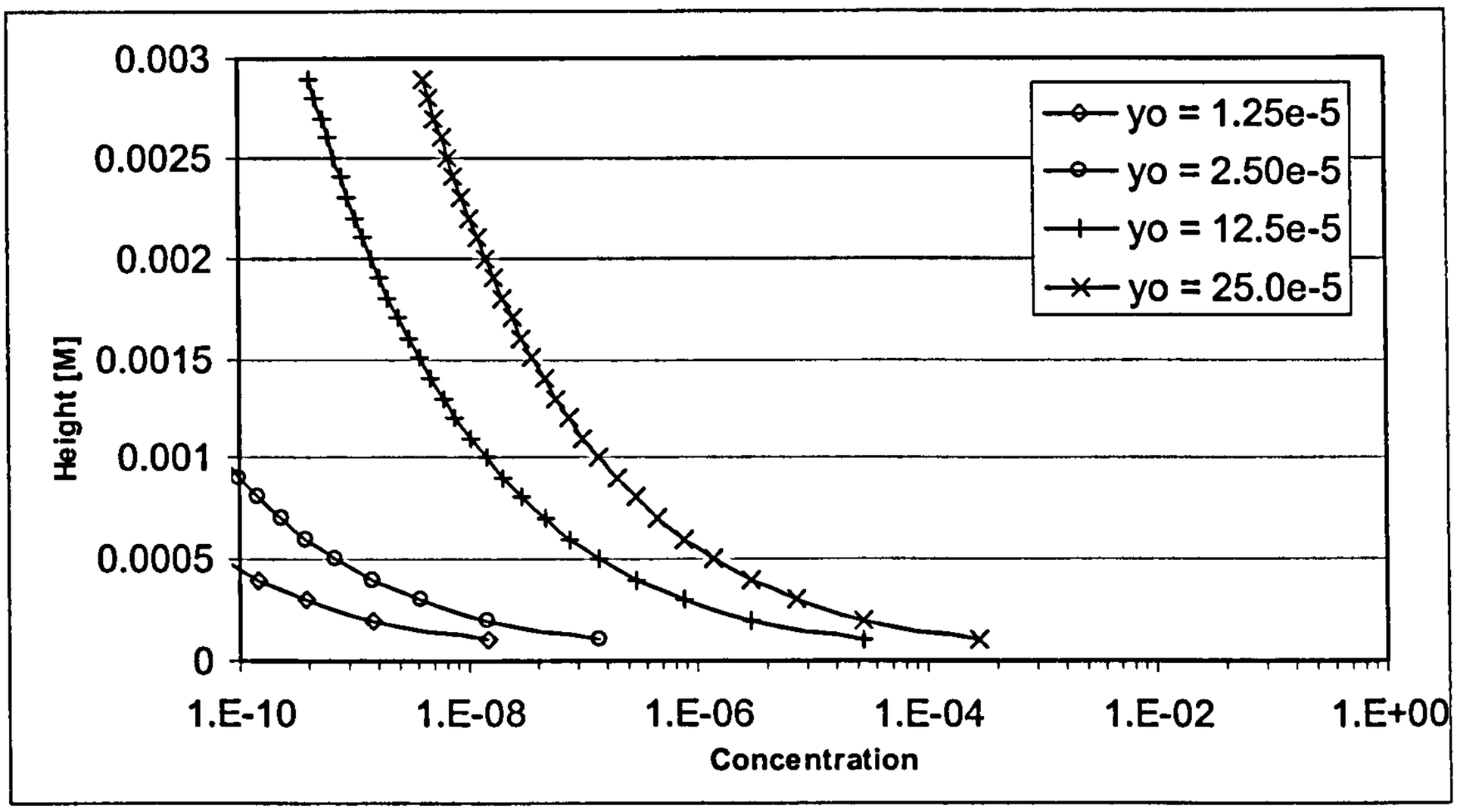

Figure 2.9: Vertical concentration profiles at different surface roughness using equation 2.11. After Andersen (1983).

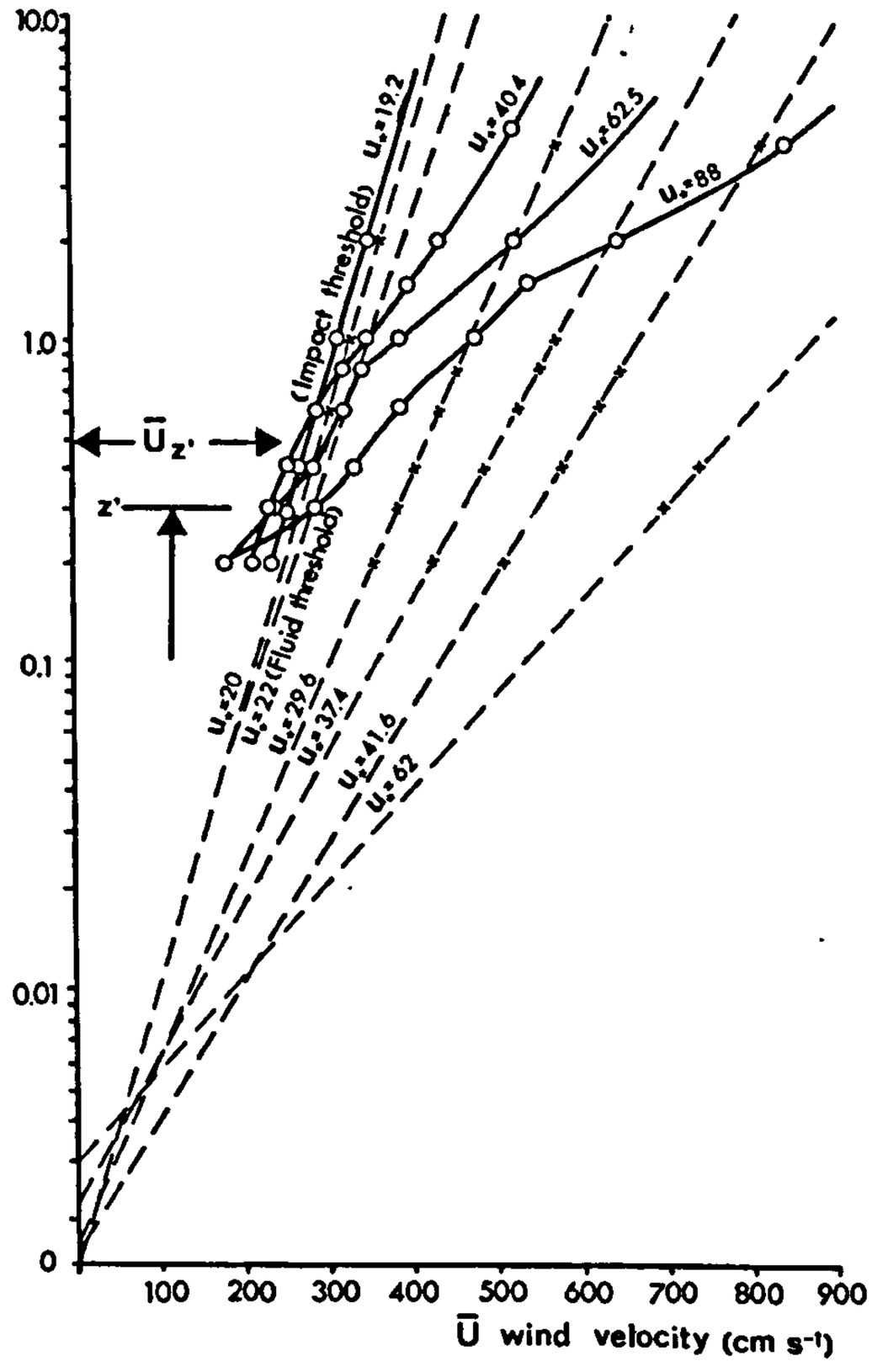

Figure 2.10: Vertical wind profiles at different wind friction velocity measured by Bagnold (1936). Dashed lined are the measurements without sand movement and the solid line is the measurements with the sand movement.

Chapter 3

Field and wind tunnel studies on drifting particles around obstacles

3.1 Introduction

Well-understood field studies and wind tunnel measurements are essential for the development of accurate and practical numerical models. Experiments considering drifting sand and snow at fences of different porosity have been conducted by many authors with the aim of establishing relationships between the many parameters controlling the location and amount of particles that can be captured by such fences. These parameters, such as wind friction velocity, particle mass flow rate, volume, shape and location of the particle deposition profile, fence height and fence porosity, have been discussed by a number of authors including [Iversen (1999), Tabler (1994), Tsoar (1983), Iversen (1981) and Phillips (1980)].

This chapter presents a review of the field and wind tunnel experiments of drifting sand and snow at solid and porous fences, which will be used later in this thesis as benchmark case studies for validation of the numerical models. In addition, field measurements from the Kuwaiti desert were collected from multiple row sand fence systems. The measurements will be used as additional case studies to validate the models against full-scale field data to strengthen their accuracy and improve their capability for more complicated applications.

Finally, a field experiment of drifting sand and sand dune development stages around an open gate facing the prevailing wind was conducted in the Kuwaiti desert as part of this study. The observations will be compared later with the numerical models in a three-dimensional flow domain.

3.2 Drifting particles around solid wall

The early stages of sand particle deposition were observed by Tsoar (1983), in a wind tunnel simulation of an air-sand flow at a vertical solid wall. The formation of the early stages of particle deposition was monitored in front of a vertical solid wall that spanned the full width of the tunnel, figure 3.1. Table 3-1 shows that at the initial stages of the deposition process the reverse flow generated in front of the wall would not allow any particles to settle near the wall for a distance, d, upstream of the wall position. Tsoar showed that as the wall height, H, increases the distance d increases and the average ratio of d/H is about 0.35.

In the experiments of Tsoar, the dune started as a thin flat layer of particles settled in front the wall. As more particles are deposited, the dune gradually grows with the distance from the wall to the crest point varying between 0.5 and 0.6 of the ratio d/H, figure 3.2. As the dune grows, particles from the front slip face of the dune start sliding down filling the gap between the dune and the wall until the dune is attached to the wall. At this point, the dune starts climbing the remaining height of the wall.

In the case of snow drift, the steady state deposition profile at a full scale solid wall was observed by Tabler (1986) in the field. Similar to the observations of Tsoar, Tabler shows that, before the deposition process reaches an equilibrium state, the snow particles are deposited at a certain distance from the wall depending on the strength of the recirculation eddy that is generated adjacent to the wall front side. He shows that when the drifting process reaches a steady state, the deposition profile extends for about 10 to 12 times the wall height both upstream and downstream from the wall, figure 3.3. At this stage there will be no more deposition and the incoming particles will pass the wall.

Table 3-1: Measurements of the distance d as it varies with the wall height H. From Tsoar (1983).

H [cm]	d [cm]	d/H
1.90	0.60	0.32
3.90	1.30	0.33
5.70	1.90	0.33
7.60	2.50	0.33
9.55	3.70	0.39
12.00	4.50	0.38

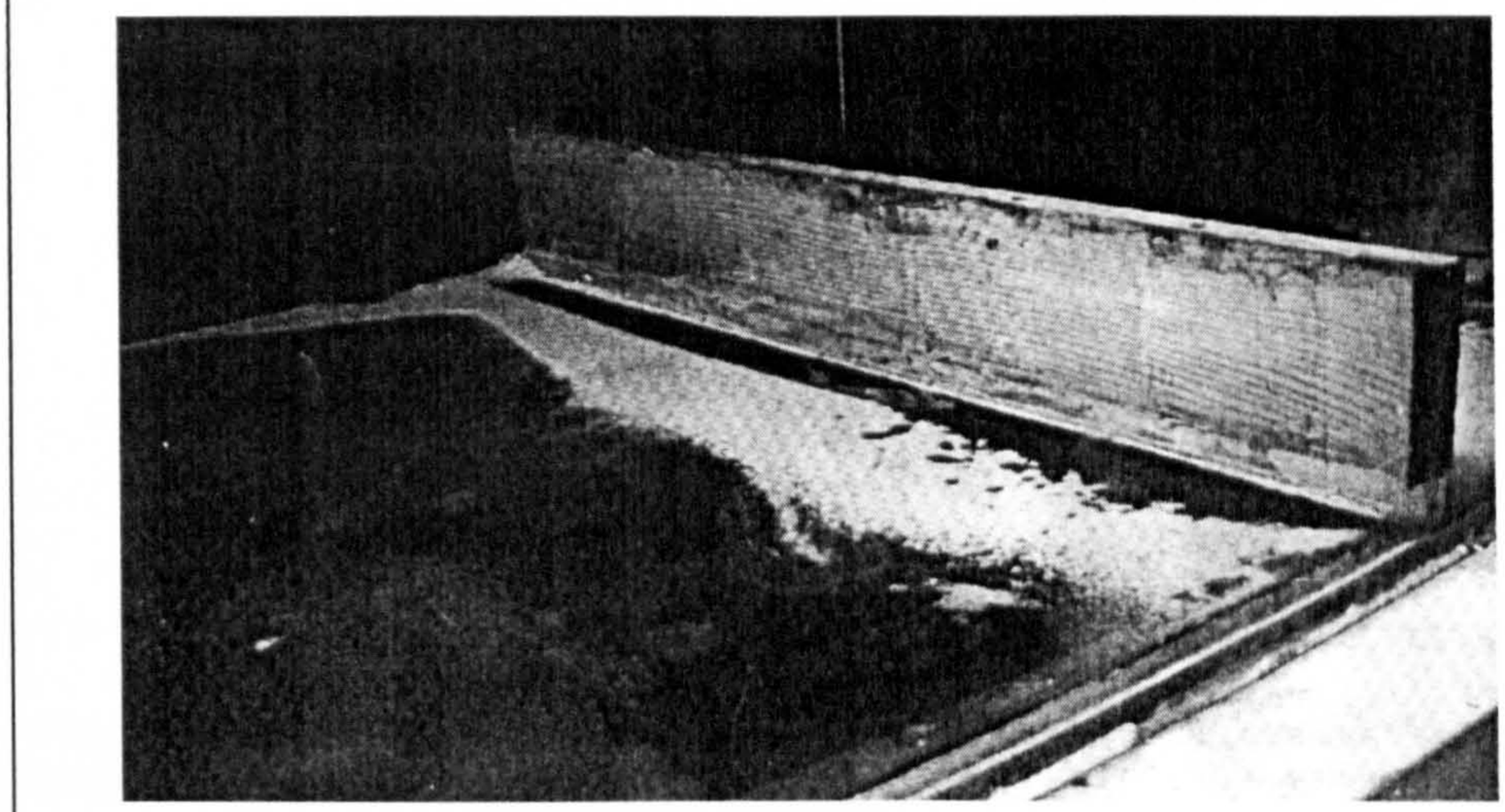

Figure 3.1: Wind tunnel initial particle deposition at a solid wall. From Tsoar (1983).

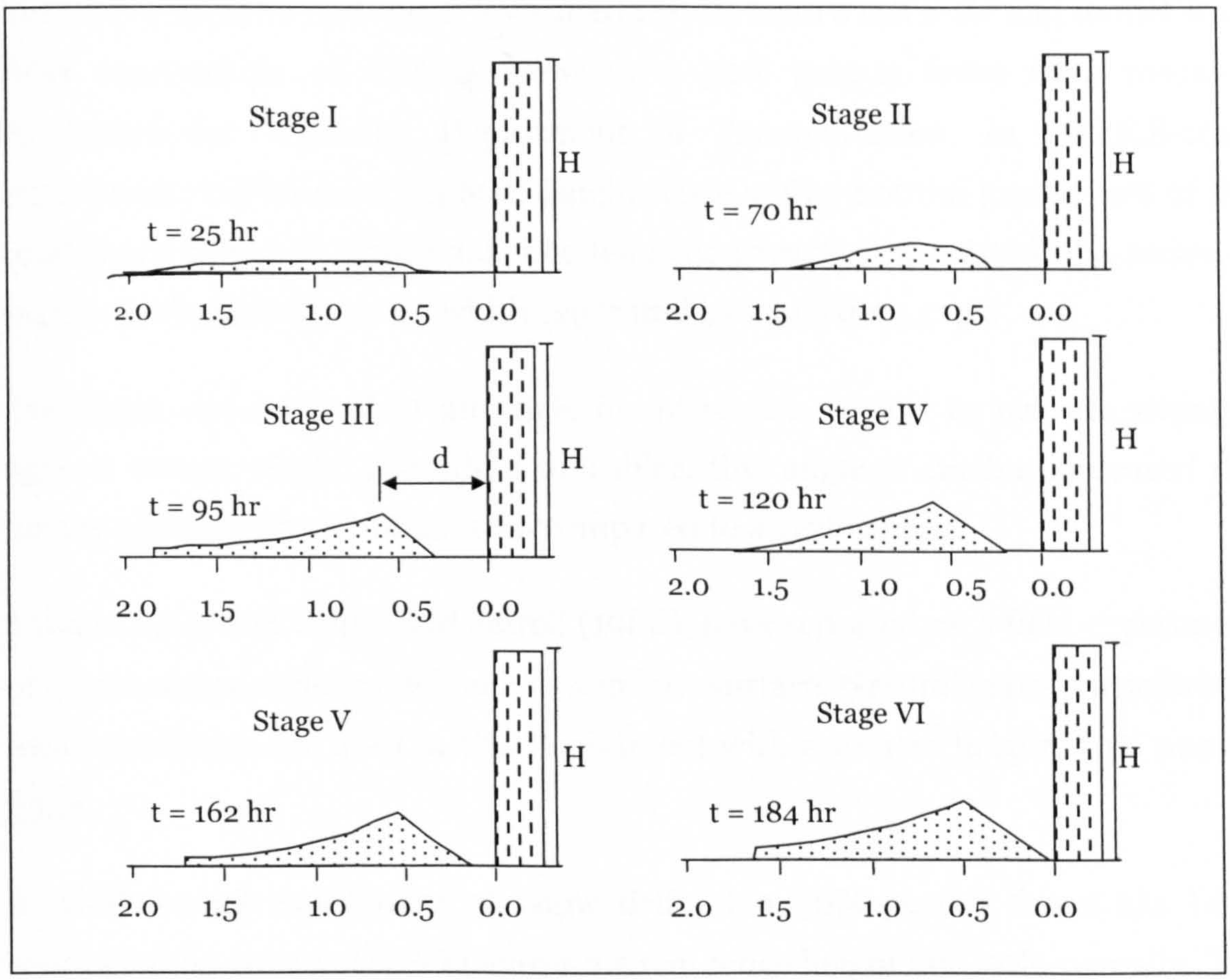

Figure 3.2: Wind tunnel particle deposition cross-sectional profiles at a solid wall representing six stages in the formation and development of the deposition dune. From Tsoar (1983).

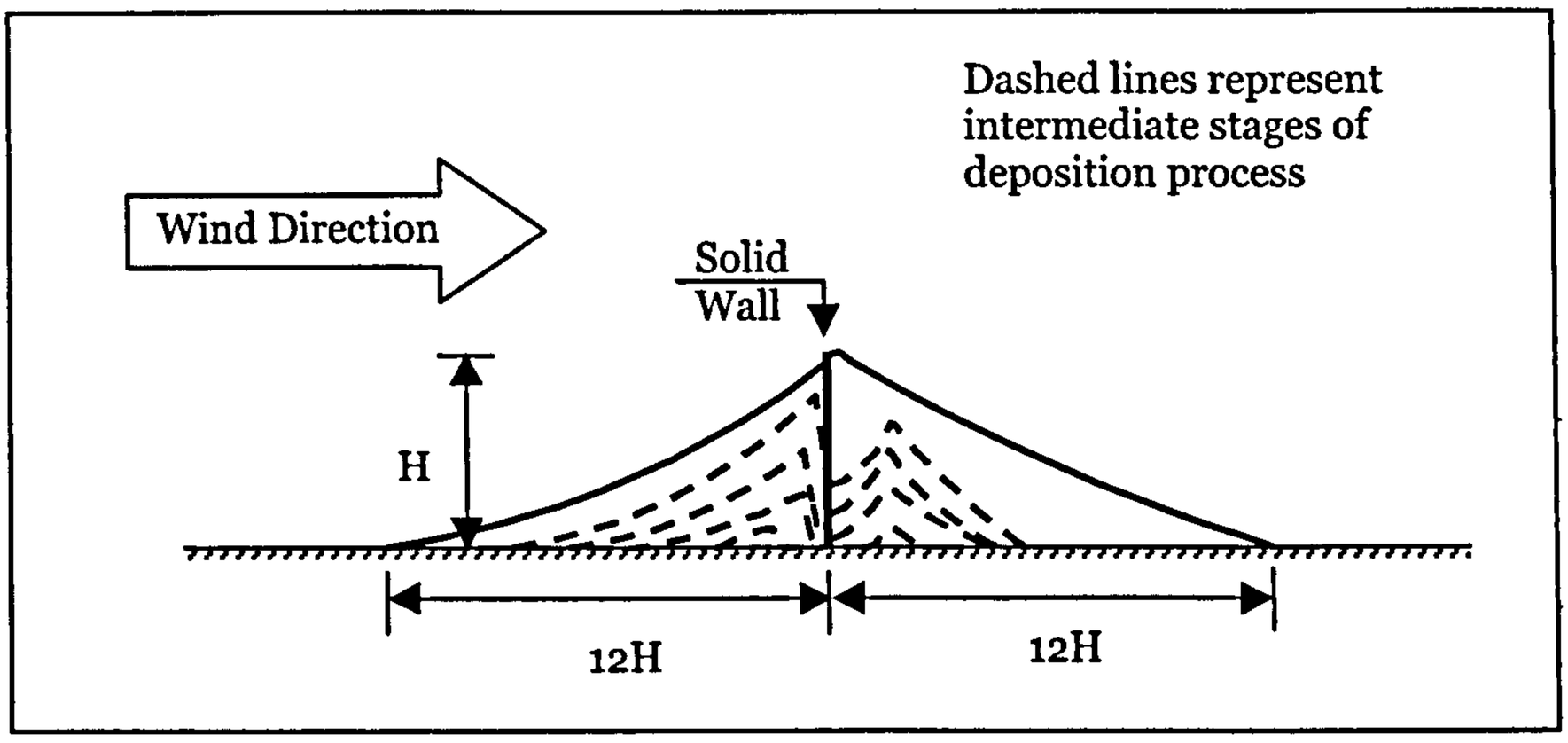

Figure 3.3: Field observation of snow particle deposition stages at a solid wall of height H. From Tabler (1994).

3.3 Snow drift at solid and porous fences

Tabler (1980, 1986 and 1994) presented results from a full scale and model scale field experiments of drifting snow at a 50% porous fence in a research conducted for Wyoming Department of Transportation. In his full-scale experiment, Tabler used a 3.66m height fence with a bottom gap of 10% of the total fence height H, figure 3.4. The fence construction consisted of a series of horizontal boards of 2.5 cm width separated by equivalent gaps.

The fence was inclined at an angle of 15° to the vertical to provide strength against strong winds. According to Tabler, this angle of incline increased the fence's efficiency by less than 10% compared to a vertical one.

Tabler (1981) and Tabler and Jairell (1980), have reported on a field experiment of a snow fence scale-model on a frozen lake surface. Natural snow particles and wind conditions are used in this experiment with a 12.4cm height, 50% porous fence.

A wind tunnel experiment of snow drift at a 50% porous fence has been conducted by Iversen (1981) using a 2.54cm fence height and 50% porosity. The scale ratio of the full-scale to the wind tunnel scale model was 1:144 while it was 1:25.5 in the frozen lake model.

To achieve the model similitude in the wind tunnel, Iversen used glass spheres of 3990 kg/m^3 density and 49 μm diameter to represent the snow particles. The average real snow particle was assumed to be 700 kg/m^3 density and 150μm diameter. The threshold friction velocity in the wind tunnel simulation was found to be 21.5 cm/s, while it is 14.0 cm/s for a typical dry snow particle.

Tabler shows that the early stages of the deposition process begin at some distance downstream of the fence. In the equilibrium state, the bulk of the dune volume is found to be downstream of the fence with a height equal to 120% of the fence height, 20% above the fence, and extends downstream to about 30 times the fence height, figure 3.5.

The measurements of full-scale deposition profiles at fences of different heights as well as the wind tunnel scale measurements are shown in figure 3.6. It shows that the wind tunnel measurements immediately downstream of the fence lie just under the full-scale while it shows no deposition occurring upstream. Iversen related two reasons for this phenomenon; first, the wind friction velocity is probably just above the threshold velocity. The second probable reason is due to that the wind tunnel deposition process not yet having reached Equilibrium State.

Iversen also shows a comparison between the wind tunnel measurements and the data of the frozen lake experiment conducted by Tabler, figure 3.7, for the drift profiles in an intermediate and equilibrium state.

Details of these experiments will be discussed later, with relation to the comparison made against the results produced using the numerical models in chapter 7.

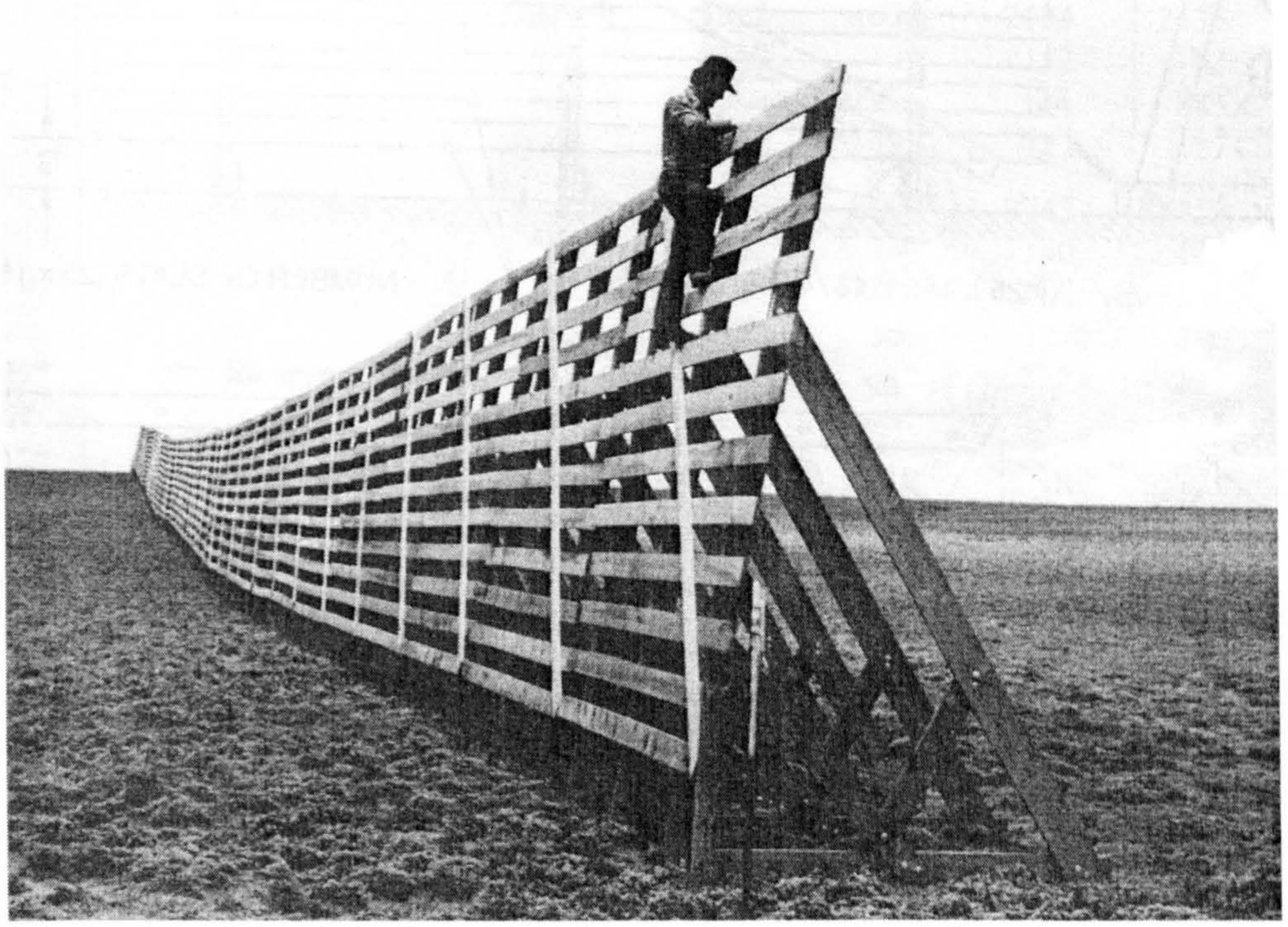

Figure 3.4: Wyoming snow fence with 50% porosity. From Tabler (1994)

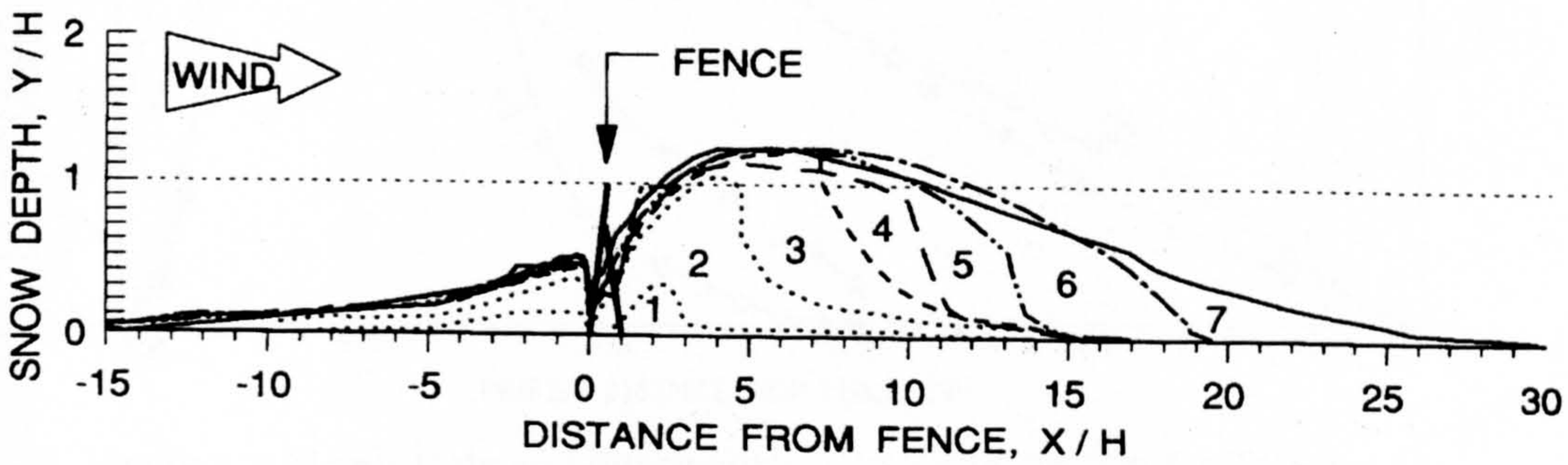

Figure 3.5: Different deposition stages at Wyoming snow drift fence that is 3.66m height and 50% porous. From Tabler (1986).

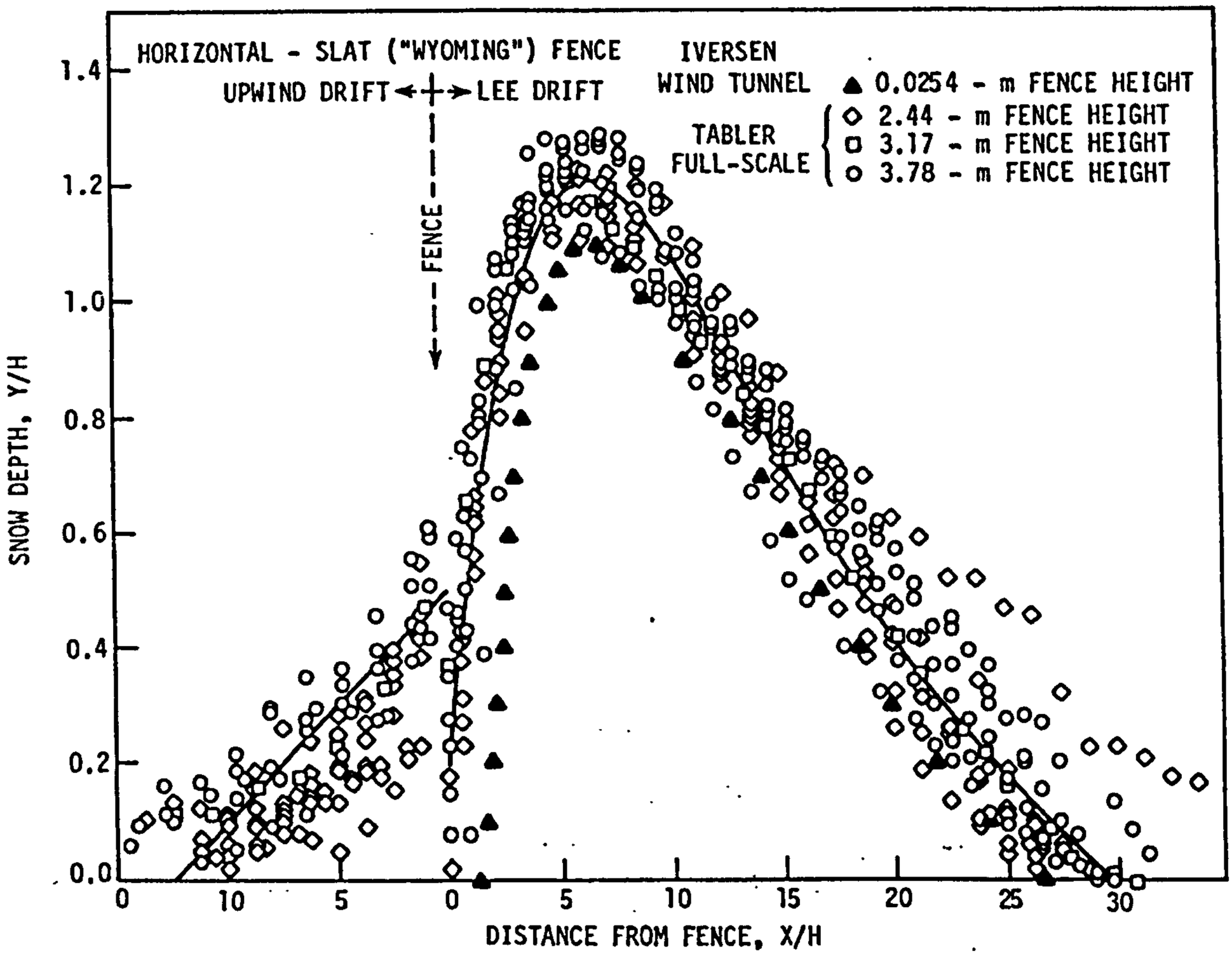

Figure 3.6 Full-scale deposition profiles at Wyoming snow fence compared to wind tunnel measurements. From Iversen (1981).

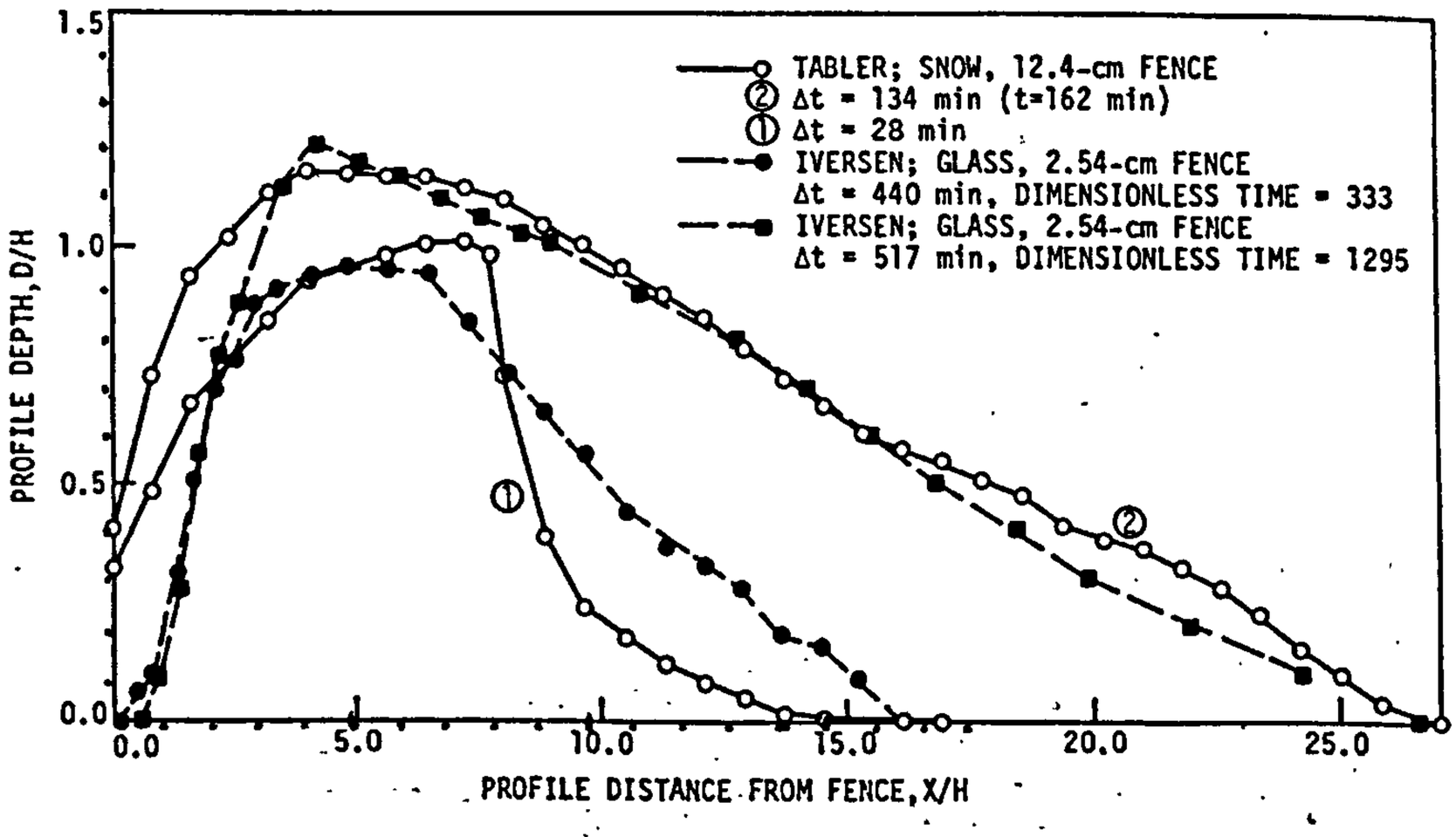

Figure 3.7: Steady state and intermediate deposition profiles for Tabler frozen lake experiments compared to wind tunnel simulation for 50% porous fence. From Iversen (1981).

3.4 Sand drift Field study in the Kuwait desert

The objective of the study conducted in the desert of Kuwait was to provide different case studies for the validation of the numerical model against full-scale field data from real life situations associated with sand drift. The difference between the field and wind tunnel studies covered in the previous sections and the Kuwait field study is that in the field the wind direction, wind speed, particle size, particle mass flow rate and the experiment duration are considered as uncontrollable parameters. While the snow drift field experiments of Tabler and the wind tunnel experiments were conducted under 'supposed' specified conditions.

Kuwait Institute for Scientific Research (KISR) established a series of field studies as a part of research projects sponsored internally by KISR to protect a research site relating to KISR and by Kuwait Oil Company (KOC) to protect oil industry installations in the desert from drifting sand, Al-Ajmi (1994).

Three field sites representing the highest drifting rate in the country -A, B and C- were chosen in this study all of which lie within the global pathway of an active sand sheet as shown from the satellite image, figure 3.8. The average width of this sheet varies between 20-50 km and enters the country from the Northwest and leaves from the Southeast.

The experiments at the sites A and B were installed in 1988 and 1995 respectively whereas the experiment at site C has been designed and conducted by the author as part of the present study.

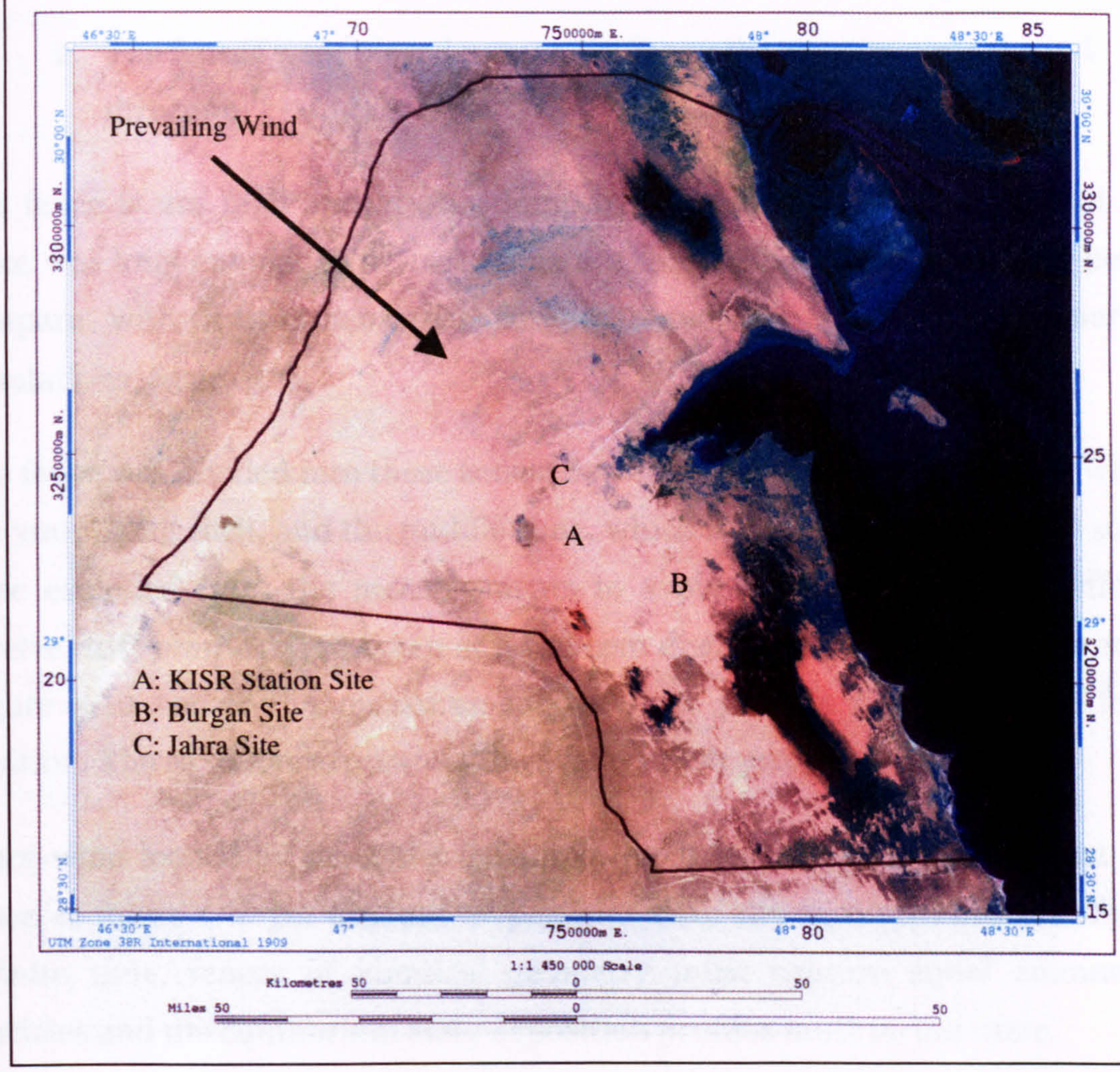

Figure 3.8: Landsat satellite image of the State of Kuwait showing areas under an active mobile sand sheet. After Kwarteng (1997).

3.4.1 Single and multiple raw sand fence system

A. KISR station field experiment:

Site A is a working case study consisting of a series of porous fences placed upstream of an agricultural research centre owned by KISR, to protect from drifting sand. The fences were installed in the summer of 1988. Figure 3.9 shows an aerial photo of the site taken in 1995. It shows that there are three sets of fences placed at different angles with respect to the prevailing wind direction. The upper most fences were chosen for simulation in the present study for two main reasons:

1. They are the first fences facing the incoming wind.

2. The fences were placed perpendicular to the average annual wind direction.

The fence is 2m high and 2000m long, figure 3.10. It was assumed that the fence was long enough to be treated as a 2-dimensional case study and hence compare with a 2-dimensional computational domain in the numerical simulations, figure 3.11.

The fence was divided into three zones; two edge zones at the fence ends, which are 300m long each, and the middle zone, which is 1400m long. The edge zones were excluded from the measurements to avoid the fence end eddy effects. Twelve drift profiles were taken at a uniform distances within the middle zone. Figure 3.12 shows the measurements of drift profiles related to the fence position. The solid line represents the average drift profile.

Since wind loaded by sand hits the upper most fence first, it is clear that this fence captures a larger amount of particles than the second. Theoretically, at infinite time, fences of identical geometry must capture equal amount of particles and the equilibrium state deposition profiles must be the same.

It is clearly shown from figure 3.12 that after about 12-years the system has not achieved its maximum capability of trapping particles. Thus, since the amount of sand deposited at the front fence is higher than that of the second one, either the front fence has consumed its entire efficiency while the second one has not or both of them have not yet reached their maximum capacity. In either case, it should be note that the measurements taken must be considered as an intermediate stage of the deposition process and the steady state deposition profiles have to be the same at both fences.

B. Burgan field experiment:

The experiment at site B is a part of two year research project sponsored by KOC and conducted by KISR in 1995-1997 to study different techniques of protecting oil field installations, such as oil wells and terminals, from the drifting sand. The

study aimed to assess the effects of the number of fence lines and the space between each two lines on the location and the amount of sand particles that can be captured. Figure 3.13 shows the experiment geometry, which is divided into three zones according to the overlap between fence lines.

1. Two fence system with 50m in between.

2. Three fence system with 50m between each line.

3. Two fence system with 100m in between.

Five measurements were taken from each zone for the deposition profile, figure 3.14. The experiment was installed at the beginning of the summer 1996 and these measurements were taken in December 1999. Comparing the average deposition profile with the profile taken from site A, it is clear that all fences are well behind their maximum capacity and still can capture more drifting particles.

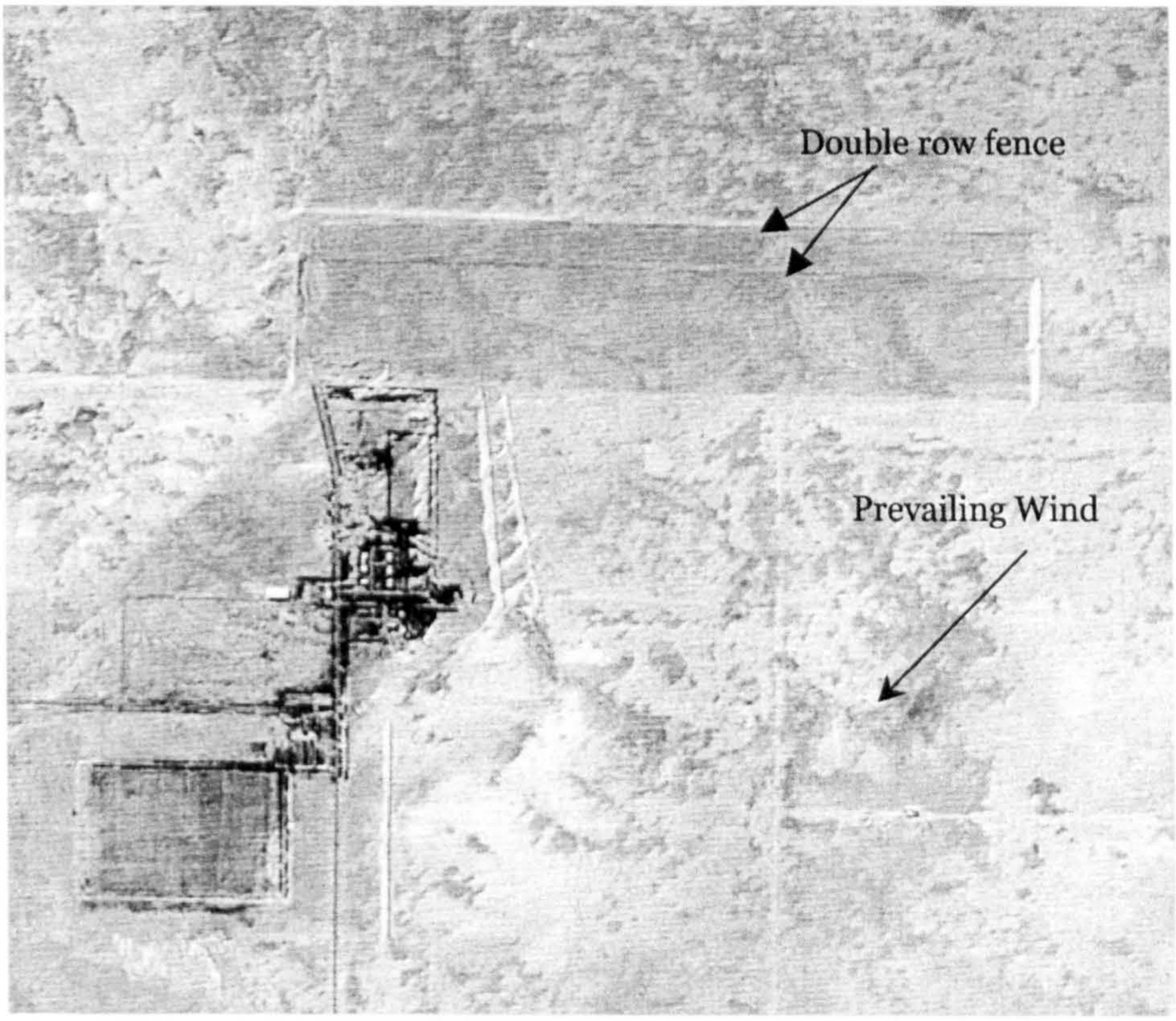

Figure 3.9: Aerial photo of KISR station showing lines of fences used to protect the station from drifting sand.

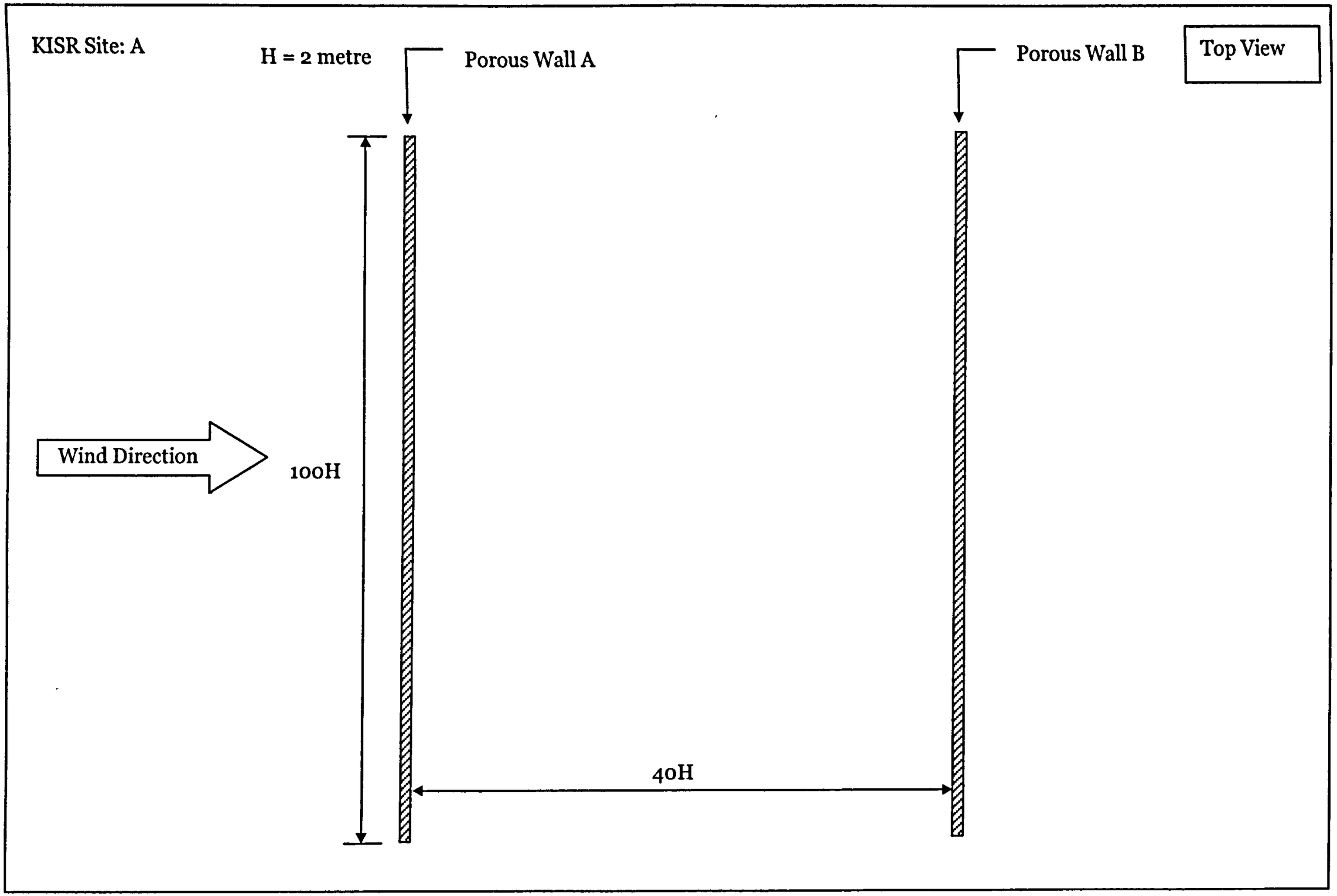

Figure 3.10: Geometry of two parallel fence lines used at KISR station site.

Figure 3.11: Drift formed at the 1st fence line, 2m height, facing the wind direction at KISR site. Photograph by author, December 1999. Wind from right to left.

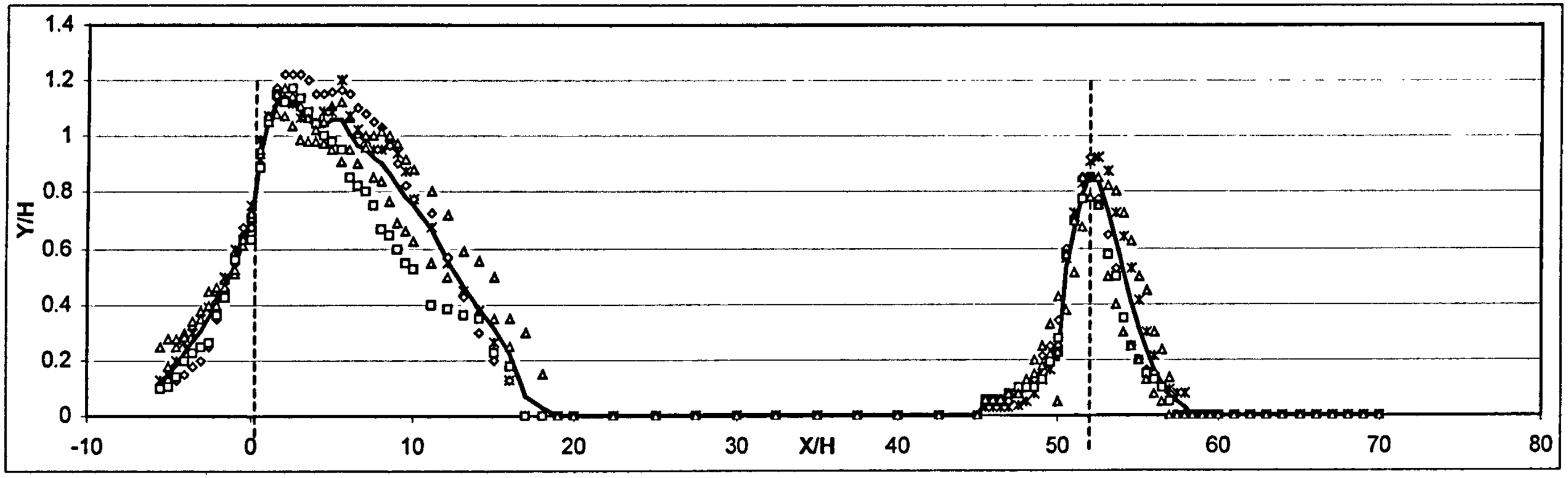

Figure 3.12: Field measurements of drift profile at KISR station double row fence system. Solid line represents the averages of twelve measured profiles at the intermediate section.

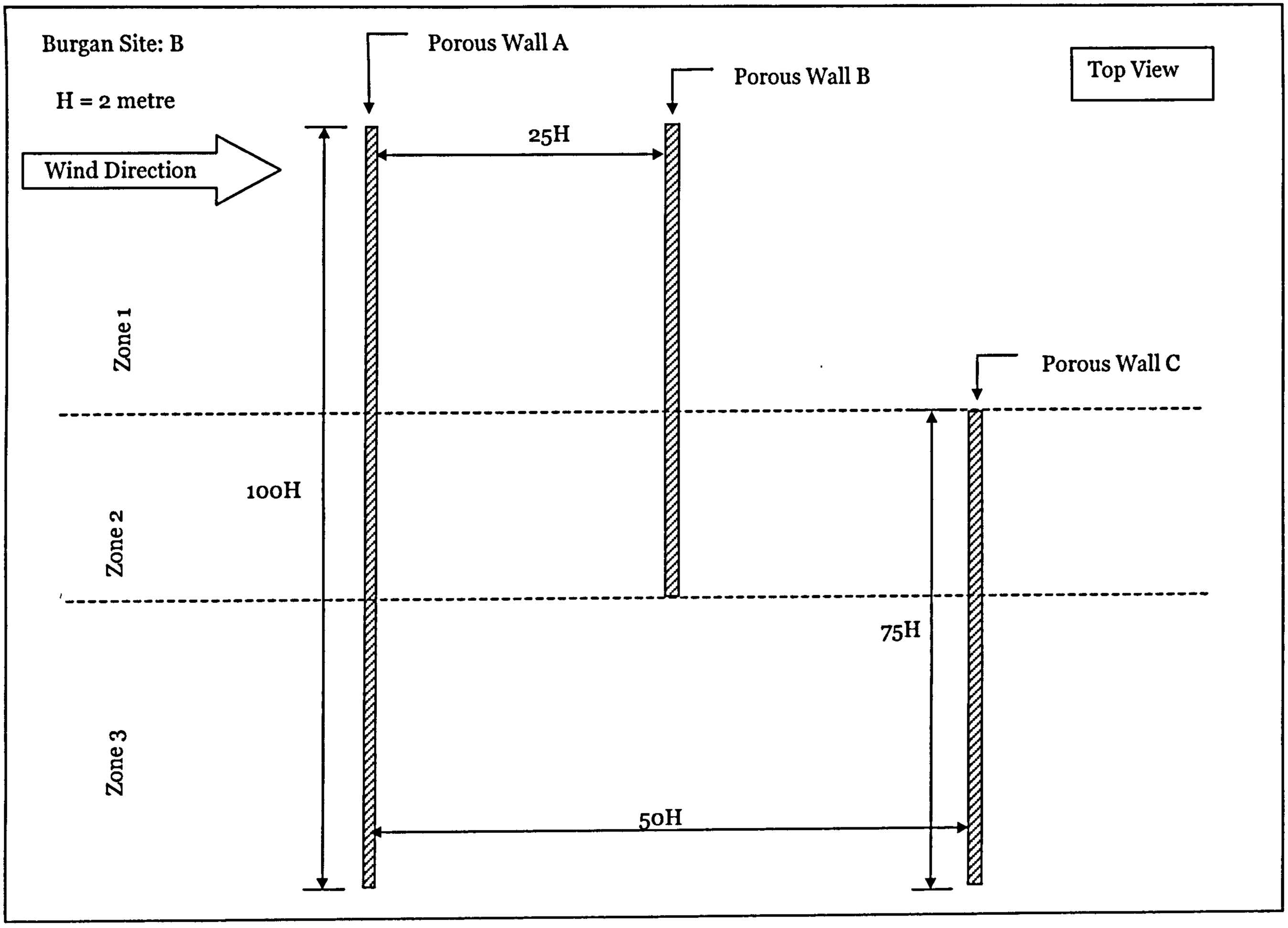

Figure 3.13: Geometry of three parallel fence lines used at Burgan field study.

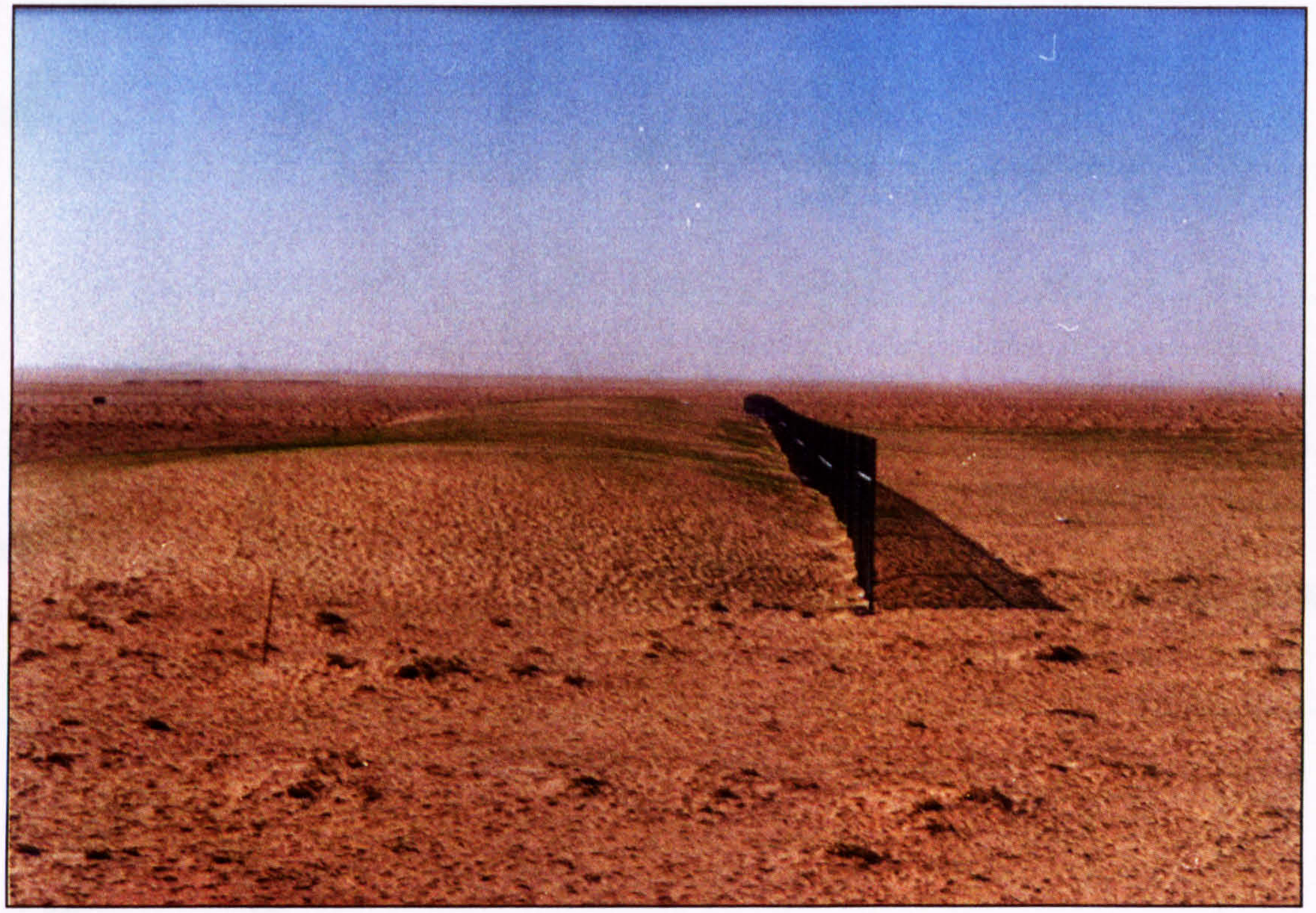

Figure 3.144a: Drift formed at the 1st fence line of zone A, 2m height, facing the wind direction at Burgan site. Photograph by author, December 1999. Wind from right to left.

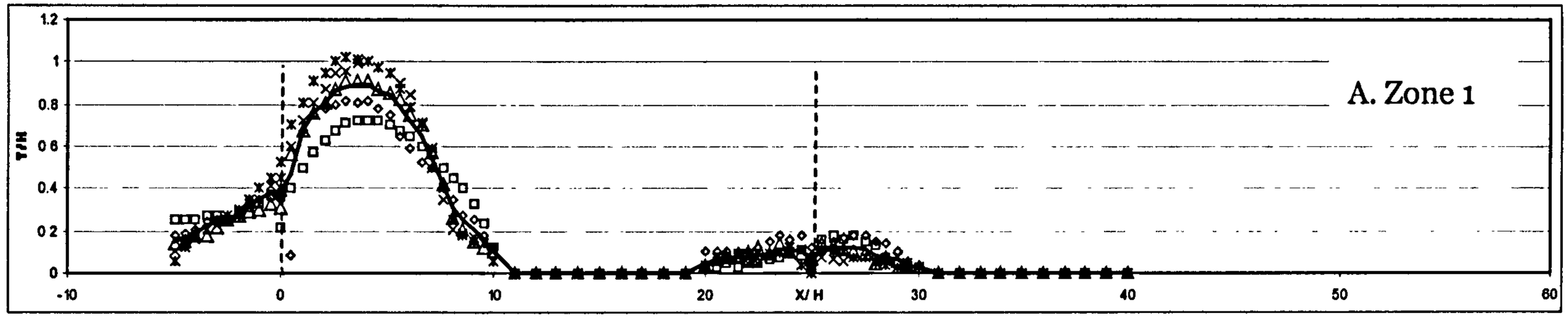

Figure 3.15b: Accumulation profiles around double and triple fence system at Burgan site. Solid line represents the averages of five measurements of the profile taken at different location along the fence.

3.4.2 Drifting sand at solid wall with an open gate

Entrances and gates of farms, military bases, oil terminals and electricity transformation stations are examples of where sand drift can cause daily blocking problems. The aim of this experiment was to provide another real case study set specifically, during the work of the present research, to validate the numerical models developed against a three-dimensional full-scale simulation of sand drift around an open gate facing the prevailing wind direction.

The experiment considered the sand dune development around a gate by placing a solid wall of 1.5m height and 39m length on a surface of high sand movement rate, site C in figure 3.8. The wall has been split into two sections of 20m and 15m length. A 4m gap has been left between the two sections to represent the gate as shown in figure 3.15.

Since the focus was on the different stages of the sand dune accumulation process and the steady state deposition profile, the natural flow rate of sand particles is assumed not to be important. Theoretically, under constant wind velocity and direction, the steady state deposition profile can be achieved much faster under high mass flow rate than that of lower flow rate, in both cases, the final deposition profiles have to be identical. Therefore, a sand bed of 0.3m depth was spread over 60x30 square metre upstream the wall, figure 3.15. Consequently, the speed of the dune development is increased and the time required for the experiment is reduced.

A cross-sectional deposition profile was measured by placing 30 vertical beams of 2m height along a 20m distance at the wall centreline and those were used as a reference point for the measurements. The deposition height is measured by subtracting the height of the beam that appeared above the ground from the original beam height.

Figure 3.16, shows the deposition profiles at different times during the experiment. Similar to the previous field and wind tunnel observations, the

deposition process started at certain distance from the wall with a crest point at about 50% of the wall height.

When the wind hits the wall, the wind stream is divided into two parts. The upper part passing over the top of the wall causing an increase in the wind velocity. The lower part is forced to bend downward generating a reverse flow zone in front of the wall. The strength of this recirculation eddy is responsible for the initial deposition location. A weak eddy results in the deposition process starting closer to the wall and as the eddy gets stronger the initial deposition takes place at an even larger distance from the wall while the dune crest moves upstream.

As the dune grows the crest point height increases and moves toward the wall until the dune becomes attached to and starts climbing the wall. Figure 3.17 shows a series of photographs taken from the upstream view of the experiment at different times clarifying that the stages of the deposition process and the change in the dune crest shape as it depends on the strength of the reverse flow. It is also clear that the deposition starts at the stagnation point, that is the point at which the reverse flow meets the oncoming flow and where the wind velocity drops to a value under the particle threshold velocity, at which particles begin to settle on the ground.

Near the gate and around the outer edges of the wall, the eddy strength is weaker since part of the wind streams move around the wall sides causing a reduction in the reverse flow strength. This results in the dune crest moving closer to the wall near its edges producing the crescent like deposition shape, figure 3.17a. Moreover, the wind accelerates as it passes through the gate causing an increase in the wind velocity and therefore erosion of the particles at this area is to be expected. As shown in figure 3.18, particles are completely eroded from the region where the wind friction velocity is raised to a value higher than the threshold velocity. However, in the middle of the pass-way, some particles do settle when the wind friction velocity is less than the particle threshold velocity.

Downstream of the gate, figure 3.19, the wind streamlines diffuse in all directions causing a reduction in the wind momentum and therefore the capability of the wind to carry particles for further distances. This results in a circular shaped particle deposition area. The direction of the sand waves on the dune surface could be used to establish the wind direction in that area, demonstrating that the diffusion of the wind occurs in all directions.

Also it could be concluded that the wind will form symmetrical circular waves if the incoming wind is perpendicular to the gate and asymmetrical shapes otherwise.

3.5 Conclusion

Several field and experimental studies were presented, some from the available data found in the literature and the rest were taken either from field trips to previously conducted experiments with no recent measurements or from field experiments developed for the purposes of the present study.

The data discussed in this chapter described the different case studies that will be used as benchmark studies to compare with the two-phase flow numerical models developed in the remaining part of this thesis.

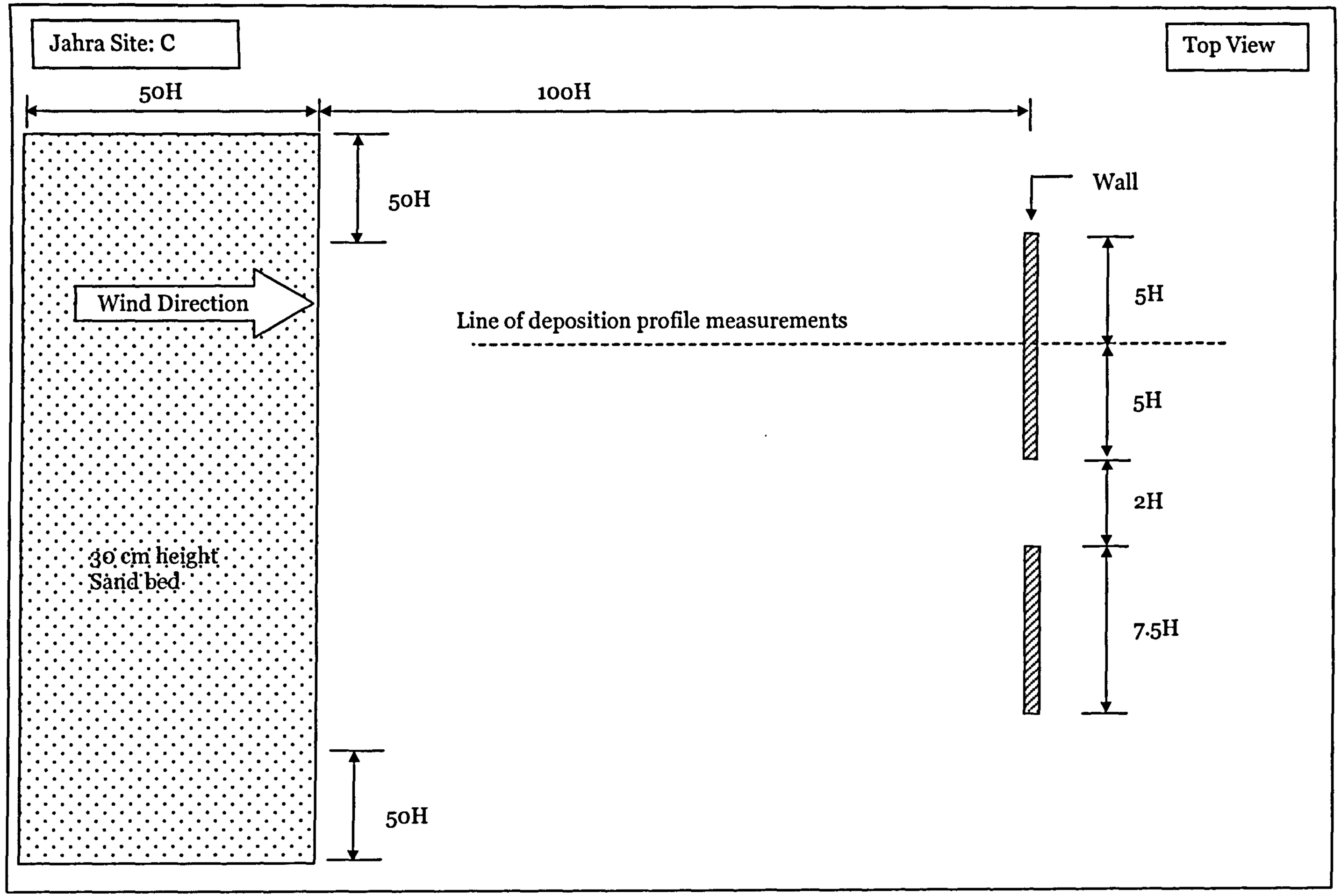

Figure 3.16: Geometry of the gate simulation experiment at Jahra site.

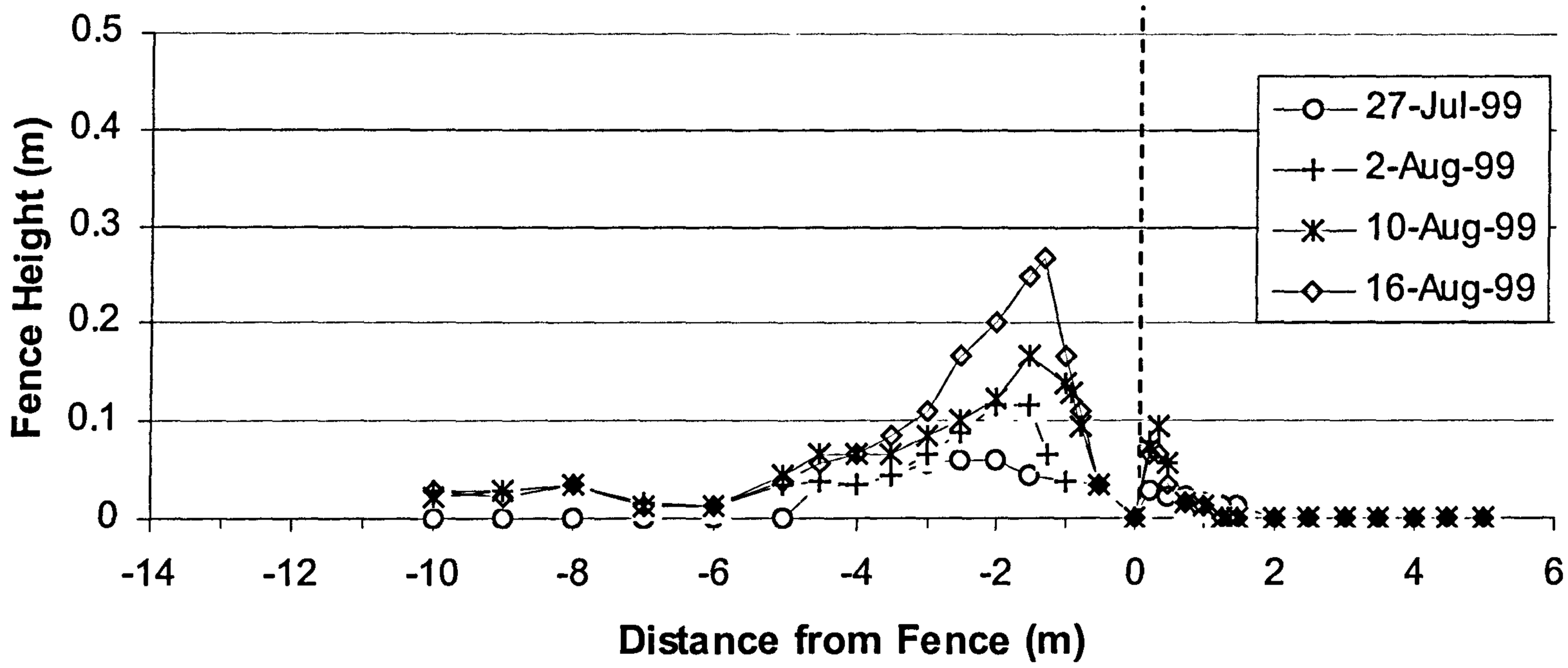

Figure 3.17: Four stages of the deposition profile at the middle of the 20m wall in the gate simulation experiment at Jahra site.

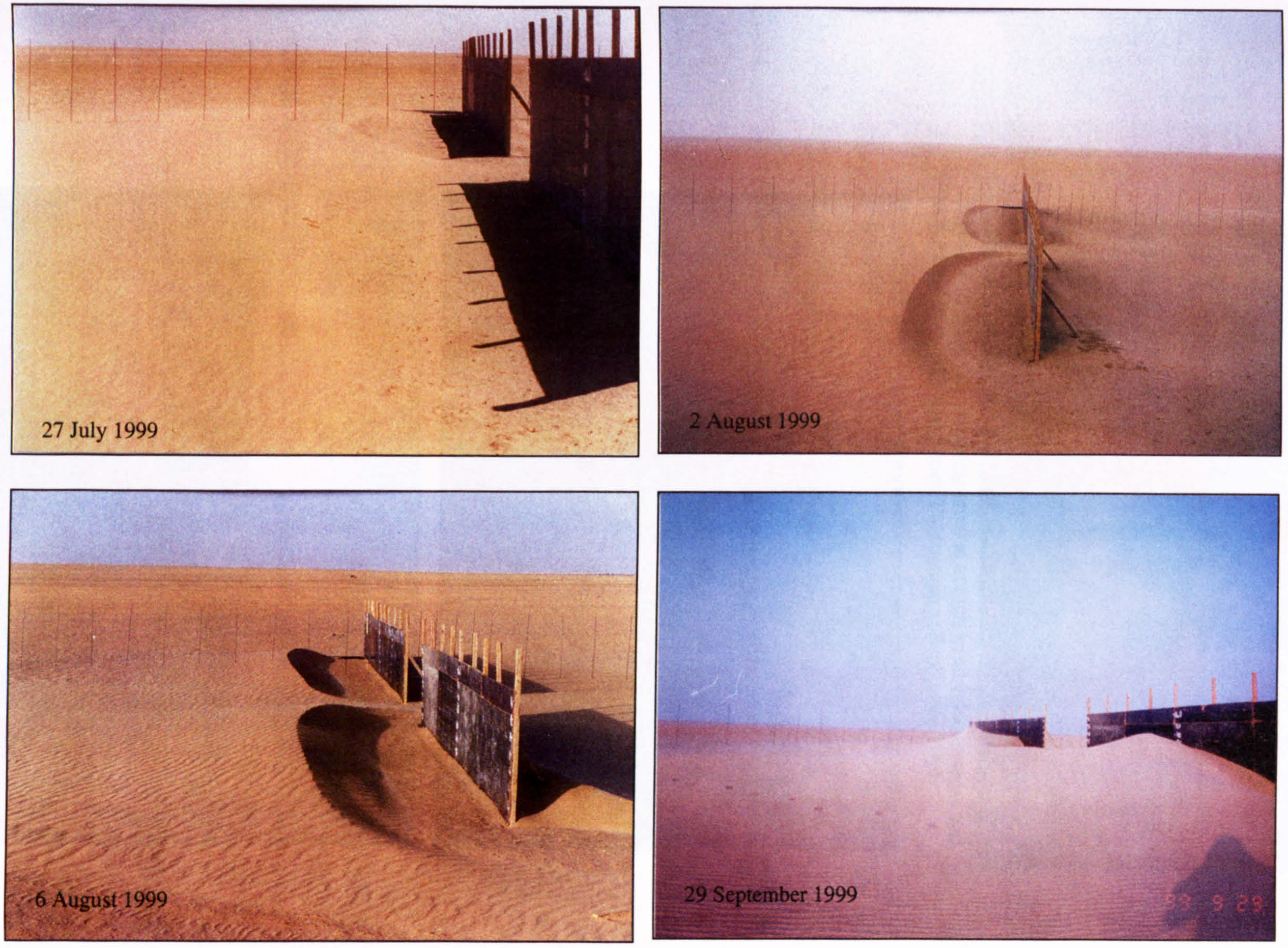

Figure 3.18: Four stages of the deposition process around simulated gate at Jahra site.

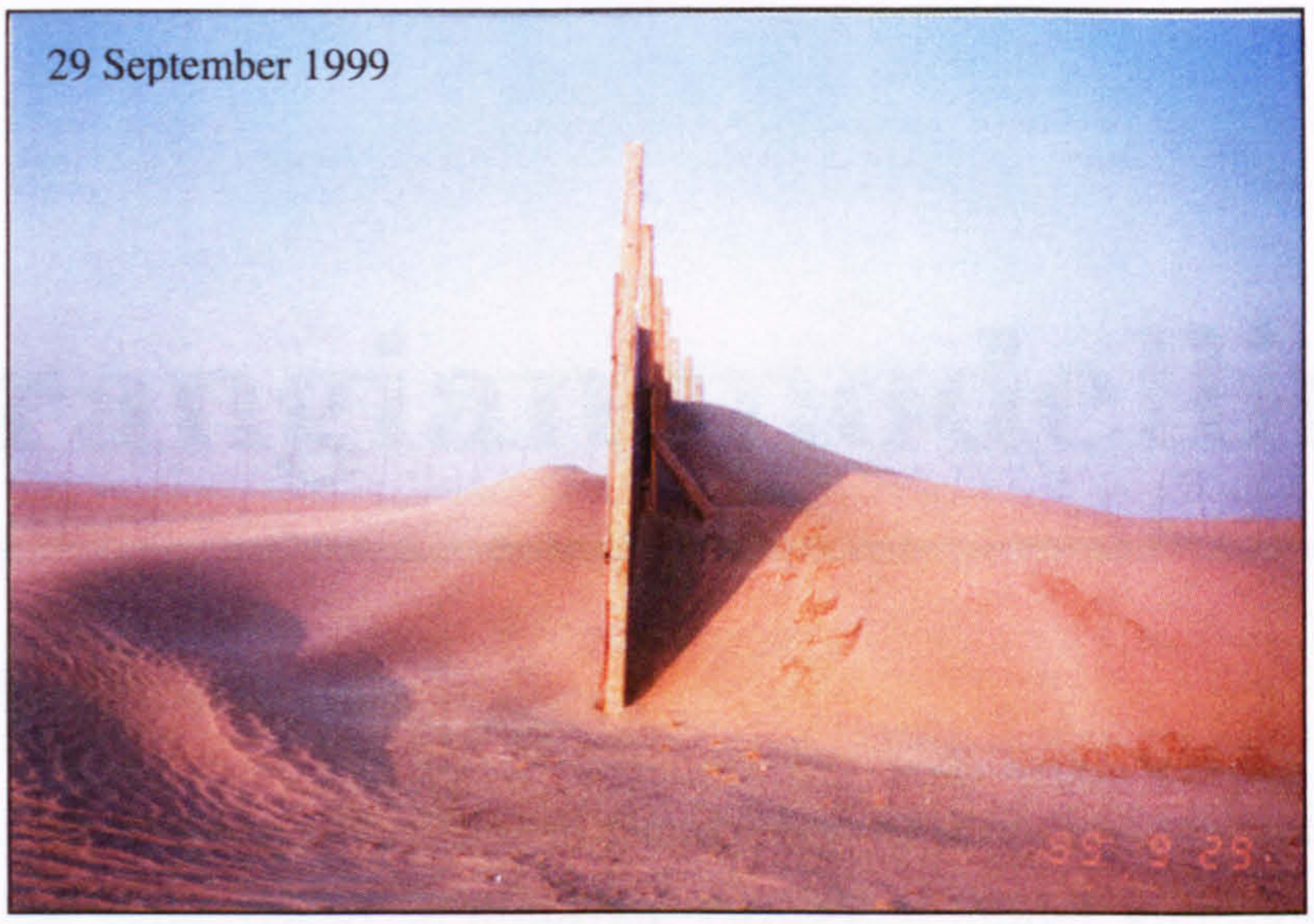

Figure 3.18: Side view showing erosion at high wind velocity areas and deposition at reverse flow zones. Photograph at September 1999.

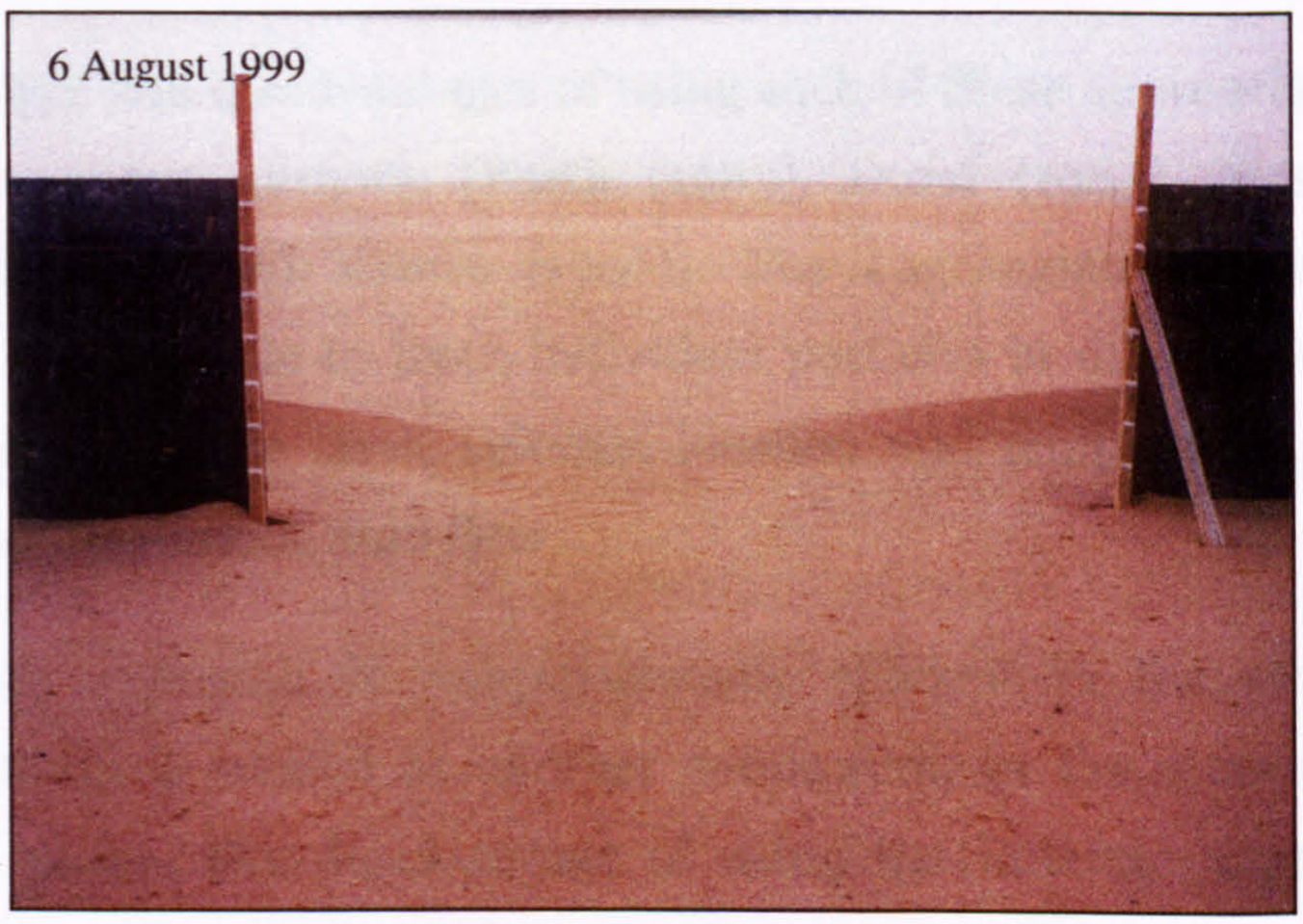

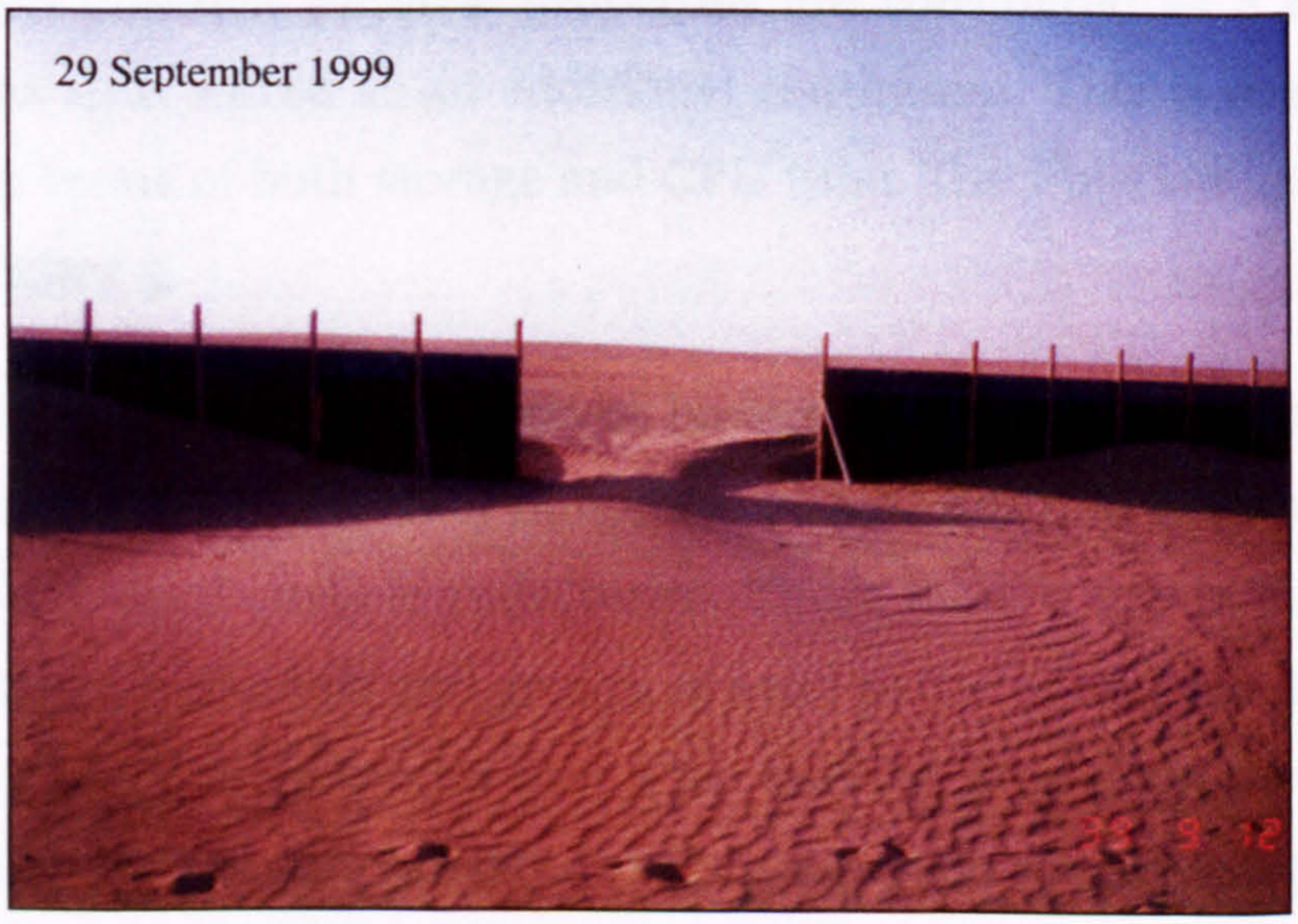

Figure 3.19: Front view showing the deposition at the diffusion zone immediately downstream the gate.

Chapter 4

Lagrangian modelling

4.1 Introduction

There are two fundamentally different theoretical approaches utilised to predict two-phase flows, those based on Eulerian, Two-Fluid model, and those based on a Lagrangian, Particle Tracking model, reference frames.

The advantages and disadvantages of using each of these approaches have been identified by many authors, [Faeth (1983), Durst (1984), Mostafa (1987), Shirolkar et al. (1996), Crowe (1996)]. The Lagrangian approach has the advantage of being able to track individual particles in diluted flows, starting from an initial particle sizes, velocity, location and temperature, as they are driven by the continuous fluid flow.

The Eulerian approach is computationally efficient in the sense that the dispersed phase is treated as another continuum, in the same sense as the continuous phase. The disadvantage of using the Eulerian approach is that particles with different physical properties are considered as a separate flow phase and as such solved as an additional continuum. This is computationally expensive in terms of both storage and CPU time. The Eulerian approach is the scope of Chapter 5.

This chapter discusses the theoretical background of the particle equation of motion followed by the different numerical procedures that are commonly used to predict individual particle trajectories. These models are implemented and analysed against individual and groups of sand particles that are moved both in suspension and saltation modes over a flat surface. Moreover, the behaviour of these particles has been investigated as they approach a solid wall perpendicular to the flow direction.

4.2 Particle Equation of motion

The Lagrangian approach considers individual particles, which are tracked as they are driven by the flow of the continuous phase. The particle trajectory can be determined by solving its equation of motion, which can be deduced from Newton's Second Law. The particle equation of motion was first derived by Basset, Boussinesq and Oseen, and is commonly known as the B-B-O equation, Shirolkar et al. (1996).

$$\frac{d\vec{U}_p}{dt} = \sum F \tag{4-1}$$

Where the RHS consist of the summation of all forces exerted on the particle along its trajectory. These summed forces are conventionally separated into the effects of drag, body forces, lift, Basset force, virtual mass force and other forces (e.g. particle-particle collision, Saffman force and wall interactions):

$$\frac{d\vec{U}_p}{dt} = F_D + F_g + F_L + F_{pressure} + F_B + F_V + F_{ohters} \tag{4-2}$$

Separation of the total sum of forces given by the above equation is not always valid, as there can be non-linear interactions between the various forces. Such interactions are not well understood but are typically small enough to be neglected for many flow applications [Feath (1983), Durst (1984), Soo (1990), Shirolkar et al. (1996), Crowe (1996) and Loth (2000)].

Assuming that the particle is of a spherical shape these forces can be summarised as follow:

4.2.1 Drag Force

This is considered to be the major force affecting the motion of a particle. The interaction between the particle and fluid induced forces at the particle-fluid interface is shown in figure 2.1. In the case of a spherical particle this results in a normal and shear stress. The normal stress is a result of the pressure applied on the surface; the pressure drag force. The shear stress is a result of the fluid

viscosity; the viscous drag force. The general equation describing the aerodynamic drag is:

$$F_D = \frac{1}{2}\rho C_D \frac{1}{\tau_p} \left|\vec{U}_{rel}\right| \vec{U}_{rel} \tag{4-3}$$

Where C_D is the drag force coefficient.

$\vec{U}_{rel}$ particle-fluid relative velocity.

τ_p is the particle relaxation time.

Particle relaxation time τ_p:

The particle relaxation time is defined as the rate of response of particle acceleration to the relative velocity between the particle and the carrier fluid, Shirolkar et al. (1996).

$$\tau_p = \frac{24\,\rho_p\, D_p^2}{18\,\mu C_D \,\mathrm{Re}_p} \tag{4-4}$$

Where the particle relative Reynolds number is:

$$\mathrm{Re}_p = \frac{\rho \left|U_{rel}\right| D_p}{\mu} \tag{4-5}$$

The relative velocity can be defined simply by the absolute value of the difference between the gas and particle velocities:

$$U_{rel} = \sqrt{\sum (\vec{U} - \vec{U}_p)^2} \tag{4-6}$$

Figure 4.1 shows the relationship between particle relaxation time and particle size for different particle densities.

The Particle relaxation time is an important parameter when particles are tracked in turbulent flows. Particles smaller than the eddy size will remain inside an eddy for a certain time before jumping to another. The maximum time that a particle can remain under the influence of a particular eddy is known as

the eddy lifetime. A common approximation in the particle/turbulent interaction models is the assumption that the eddy properties remain constant for the entire eddy lifetime and therefore, particles trapped by an eddy can experience constant turbulent properties. In this study, the turbulence properties were predicted via the two-equation k-ε turbulence model. Details of the interaction between the particle relaxation time and the eddy lifetime will be discussed in section 4.3.3 where Stochastic Separated Flow model is presented.

Drag Coefficient C_D:

The drag force on a solid sphere has been described by a number of different approximations for the drag coefficient. It is primarily dependent on the particle's relative Reynolds number. Different correlations of the drag coefficient for various particle relative Reynolds numbers are found in the literature, see Crowe (1996).

A. Stokes Drag Coefficient: $C_D = \frac{24}{\mathrm{Re}_p}$ $\mathrm{Re}_p \ll 1$

B. Oseens drag coefficient: $C_D = \frac{24}{\mathrm{Re}_p}(1 + 0.15\,\mathrm{Re}_p^{0.687})$ $0 < \mathrm{Re}_p < 1\times10^3$

C. Newton's Drag coefficient: $C_D = 0.44$ $700 < \mathrm{Re}_p < 2\times10^4$

D. Morris and Alexander developed empirical expressions for drag coefficient as a function of Reynolds number. They divided the relationship between the particle Reynolds number and the drag coefficient into seven regions.

$$C_D = a_1 + \frac{a_2}{\mathrm{Re}_p} + \frac{a_3}{\mathrm{Re}_p^2}$$

Where a_i: constants that apply over different values of Re given in table 4.1.

Table 4.1: Drag Coefficient as a function of Re are after Morris and Alexander.

Re_p range	C_D
$Re_p < 0.1$	$24.0/ Re_p$
$0.1 < Re_p < 1.0$	$22.73/ Re_p + 0.0903/ Re_p^2 + 3.69$
$1.0 < Re_p < 10.0$	$29.1667/ Re_p - 3.8889/ Re_p^2 + 1.222$
$10.0 < Re_p < 100$	$46.5/ Re_p - 116.7/ Re_p^2 + 0.6167$
$100 < Re_p < 1000$	$98.33/ Re_p - 2778/ Re_p^2 + 0.3644$
$1000 < Re_p < 5000$	$148.62/ Re_p - 4.75/ Re_p^2 + 0.357$
$5000 < Re_p < 10,000$	$-490.546/ Re_p + 57.87E04/ Re_p^2 + 0.46$
$10,000 < Re_p < 50,000$	$-1662.5/ Re_p + 5.4167E06/ Re_p^2 + 0.5191$

Oseens and Newton's drag coefficients are applied in the present study to determine the particle drag coefficient.

4.2.2 Gravity force

Gravity force is applied in the negative vertical direction. This force is directly proportional to the mass of the particle and defined simply based on the density difference between the particle and surrounding fluid:

$$F_g = g(\rho_p - \rho)$$

4.2.3 Lift force

Lift force acts perpendicular to the drag force and depends on many factors, such as, irregularity of the particle shape, size and density. For low Reynolds number, two lift forces have been identified, first, the shear induced (Saffman lift force) and, second, the forces due to particle spin (Magnus lift force).

The Saffman force is the lift force that a small spherical particle may experience as a result of the local gradients of viscous fluid flow. However, the Saffman force was identified for a uniform shear flow, which is of practical use only for limited applications.

The Magnus or spin force is a result of the particle rotation around its own centre due to differences in the surface shear stress applied by the surrounding fluid flow in the particle surface. This rotation is a direct result of the increase in the fluid velocity on one side and decrease in the other side.

4.2.4 Forces due to Pressure Gradient

Forces associated with pressure gradient may influence the particle threshold condition. This force has a significant effect if the ratio of the particle density to the fluid density is close to unity (e.g. particle in water), otherwise it is of negligible effect Soo (1990):

$$F_{pressure} = -\frac{\pi D^3}{6}\frac{\partial p}{\partial X}$$

4.2.5 Basset Force

The flow pattern around the particle is not steady and changes during acceleration of the particle. This results in an instantaneous flow resistance on the particle. The force generated by this resistance is known as the Basset force, and represents the influence of the history of the particle motion on its movement. The Basset force is estimated by the following formula:

$$F_{Basset} = \frac{3}{2}D^2\sqrt{\pi\rho\mu}\int_{t_0}^{t}\frac{d(U-U_p)}{\sqrt{t-\tau}}d\tau$$

4.2.6 Virtual mass Force

The relative velocity between the fluid and particle affects the fluid momentum boundary layer around the particle. Thus, if the particle is faster than the fluid then the particle can accelerate the surrounded fluid, i.e. more mass is accelerated than the mass of the particle itself. Therefore, the work done to accelerate the particle is in fact greater than the work required to accelerate the particle alone.

Hence the kinetic energy required to accelerate the particle is divided between the particle itself and the surrounding fluid attached to the particle surfaces. This is known as the Virtual or Apparent Mass Force.

The extra amount of mass accelerated can be expressed as a fraction of the displaced fluid. The added mass is given as a constant and is equal to one half of the displaced fluid mass. The force associated with this increase is defined by:

$$F_{vmi} = \frac{1}{2}\frac{4}{3}\pi D^3 \rho \frac{d}{dt}(U - U_p)$$

The Virtual Mass Force effect needs only to be considered if the fluid-particle density ratio is close to unity.

Consideration of the above forces applied to a particle suspended in a flow field gives the general form of the equation of motion given by BBO, Faeth (1983):

$$\underbrace{\frac{d\vec{U}}{dt}}_{Particle\ Acceleration} = \underbrace{F_D(\vec{U} - \vec{U}_p)}_{Drag\ Term} - \underbrace{\frac{1}{\rho_p}\frac{\partial P}{\partial r}}_{Pressure\ Gradiant\ Term} + \underbrace{\frac{1}{2}\frac{d}{dt}(\vec{U} - \vec{U}_p)}_{Apparent\ Mass\ Term} + \underbrace{\frac{3}{2m_p}D^2\sqrt{\pi\rho\mu}\int_{t_0}^{t}\frac{\frac{d(\vec{U}-\vec{U}_p)}{d\tau}}{\sqrt{t-\tau}}d\tau}_{Basset\ Term} + \underbrace{\vec{g}}_{Gravity\ Term} \quad (4\text{-}7)$$

As mentioned above, when the ratio of the fluid density to the particle density is very small, as in the case of air-sand flows and most of the diluted flows of engineering interest, the effect of the pressure gradient, apparent mass and Basset terms are negligible Faeth (1983). Thus the equation of motion can be simplified to include only drag and gravity terms as follows:

$$\frac{d\vec{U}_p}{dt}=\frac{\vec{U}-\vec{U}_p}{\tau_p}+\vec{g} \tag{4-8}$$

The above particle equation of motion is a first order, non-homogenous non-linear differential equation. It is analytically possible to solve this over a small time step where the instantaneous fluid velocity and the particle relaxation time are assumed to be constant..By knowing the initial particle velocity, the new particle velocity can be calculated using the following formula:

$$U_p^{t+\Delta t}=U+(U_p^t-U)e^{\frac{-\Delta t}{\tau_p}}+g\tau_p\left[1-e^{\frac{-\Delta t}{\tau_p}}\right] \tag{4-9}$$

It is worthwhile to mention here that equation (4-9) is valid only for low particle Reynolds number, which is within the range of the particles driven by wind.

Also by integrating the particle equation of motion twice the new particle position can be calculated as follows:

$$\frac{dX_p}{dt}=\vec{U}_p \tag{4-10}$$

This can be solved under the same assumptions as previously mentioned to give:

$$X_p^{t+\Delta t}=X_p^t+\frac{\Delta t}{2}(U_p^{t+\Delta t}+U_p^t) \tag{4-11}$$

note that these equations should be solved for each component direction.

Alternatively, the instantaneous velocity of the particle and its new position after each time step can be determined by iteratively integrating the non-linear ordinary differential equations using a numerical technique such as Rung-Kutta method to an acceptable accuracy. This approach is applied to solve equations (4-8) and (4-10) in the present work.

4.3 Lagrangian numerical models

Equations (4-4), (4-8) and (4-10), are most commonly used in Lagrangian models to track individual particle trajectories. The solution of equation (4-8) accounting for the effect of the fluid velocity fluctuation due to turbulent eddies requires the full-time history of turbulent flow. Such information requires solution of the instantaneous flow governing equations, the Navier-Stokes equations, on an Eulerian reference frame (see Chapter 5).

Thus different techniques that involve random sampling of the fluctuating velocity components have been developed, [Hutchinson et al. (1971), Gosman and Ioannides (1983), Feath (1983), Durst (1984) and Soo (1990), Shirolkar et al. (1996)]. Conventional particle tracking models are summerized below.

4.3.1 Direct particle-tracking model

This model generates particle trajectories directly using a stochastic model known as the *random walk model* for Lagrangian velocities. This method is efficient since it does not require the solution of the continuous flow field and the particle trajectory is simulated directly as if it is a fluid particle.

The application of this model is limited to passive particles in high Reynolds number flows, where the effects of the molecular diffusion on the fluid particle trajectory are negligible. This is a valid assumption if the particle is small enough that it behaves as a fluid particle, such as the flow of a pollutant particle in the atmosphere. This model will not be covered in the current work; more details and discussion of this model can be found in Shirolkar et al. (1996)

4.3.2 Deterministic Dispersion model (DDM)

The basic idea of particle tracking models was first proposed by Hutchinson et al. (1971), and was employed by Gosman and Ioannides (1983), in conjunction with the k-ε turbulence model. Shuen et al. (1985) identified the importance of the initial condition to the accuracy of the Lagrangian calculation. Since

Gosman and Ioannides work, many authors have reported success with these stochastic models in predicting dilute fluid-particles flows.

DDM is the simplest way of solving the particle equation of motion since the effect of the fluctuating velocity components of the fluid velocity is not included. Particle suspension relies on velocity fluctuations, therefore this model is only useful when studying saltating particles. Once the mean average continuous fluid velocity field is calculated, the particle equation of motion can be directly computed. Since only the particle convective velocity, u_p^c, is included, particles of the same initial conditions and physical properties will follow identical trajectories.

The turbulent dispersion effect could be included by estimating the dispersive component of the particle velocity which can be obtained from the gradient diffusion approximation Shirolkar et al. (1996) such that:

$$u_p = u_p^c + u_p^d \tag{4-12}$$

where

$$u_p^d = -\Gamma_p \frac{1}{\overline{n}_p} \frac{\partial \overline{n}_p}{\partial x} \tag{4-13}$$

is the dispersive component of the particle velocity, $\overline{n}_p$ is the particle density number, $\Gamma_p = \frac{\mu_p^t}{\sigma_p^t}$ is the particle diffusivity and μ_p^t and σ_p^t are the turbulent particle viscosity and turbulent particle Schmidt number respectively. The turbulent particle viscosity is related to the fluid turbulent viscosity by the following expression:

$$\mu_p^t = \frac{\mu_t}{1 + \frac{\tau_p}{\tau_{fL}}} \tag{4-14}$$

where τ_p is the particle relaxation time, and τ_{fL} is the Lagrangian fluid time scale, which will be discussed in the following section. This model is easy to implement and does not require a large number of particles to be tracked in order to statistically satisfy realistic trajectories, i.e. *the statistically significant* number of particles need to be tracked is small.

4.3.3 Stochastic Separated Flow Model (SSF)

This model involved the instantaneous fluid velocity instead of the mean average velocity used in DDM. The key problem in this model is to determine:

1. *The fluctuating component of the fluid velocity along the particle trajectory.*
2. *The integration time step over which the fluid properties can be assumed locally constant.*

The particle is assumed to interact with a series of turbulent eddies as it moves along the flow field. Thus turbulent information is required to evaluate the velocity fluctuation components, eddy lifetime and eddy length scale. Eddy lifetime and length scale can be estimated from the local turbulent kinetic energy k and the rate of kinetic energy dissipation ε along the particle trajectory.

Different assumptions are made in order to simplify the nature of the turbulent particle dispersion. Some frequently used assumptions are:

1. Assuming that the statistical properties of the turbulent quantities are independent of space, the turbulent flow can be referred as homogenous.

2. The turbulence is called isotropic if its statistical features show no preference for any direction.

Therefore, based on these assumptions the turbulent kinetic energy contained in an eddy is given by:

$$k=\frac{1}{2}\left(u'^2+v'^2+w'^2\right)=\frac{3}{2}u'^2 \qquad (4\text{-}15)$$

Since the fluid velocity fluctuation component is assumed to be the same in all directions, the standard deviation is given by:

$$\sigma = \sqrt{\frac{2k}{3}} \tag{4-16}$$

Assuming that the local turbulent properties are constant over each time step, each turbulence eddy is characterised by a constant velocity fluctuation, time scale (eddy lifetime) and length scale (eddy size).

The velocity fluctuation used in each eddy is determined by random sampling over a Gaussian PDF, which has a mean of zero and unity variance, and is given by:

$$u' = \xi \sqrt{\frac{2k}{3}} \tag{4-17}$$

where ξ is the Gaussian random variable.

Thus, for each time step u' is randomly sampled and its corresponding PDF assumed to be a Gaussian form. For an isotropic assumption, the variance of the fluctuating velocity can be estimated from the local turbulent kinetic energy; therefore, the mathematical expression for the PDF of the fluctuating velocity in isotropic flows is given by:

$$P(u') = \frac{1}{\sqrt{2\pi}\sqrt{\frac{2k}{3}}} e^{\left[-\frac{3u'^2}{4k}\right]} \tag{4-18}$$

note that under the non-isotropic flow assumption, for each coordinate direction independent fluctuating velocities are randomly sampled using the above PDF expression at every time step.

The local turbulence properties determine whether or not a given particle remains in an eddy. The particle may stay in an eddy for the whole eddy lifetime and then it follows the turbulence properties of another eddy or it may have enough momentum to cross the eddy boundaries to become involved with another eddy.

This is commonly known as the *Crossing Trajectory Effect*. In order to account for the crossing trajectory effect, the time interaction between the particle and an eddy should be determined properly. Thus it should be the minimum of either the eddy lifetime or the time required for the particle to cross the eddy, which is known as the residence time.

Both eddy and residence time scales are dependent on the eddy length scale. Thus many authors have used different expressions to determine the eddy time and length scales whilst using the same expression for the residence time scale. Table 4.2 summarises these expressions, Shirolkar et al. (1996).

The expression generally applied to the residence time scale, also known as the eddy transit time, is:

$$\tau_r = -\tau_p \ln\left(1 - \frac{l_e}{\tau_p \left|\vec{U} - \vec{U}_p\right|}\right) \tag{4-19}$$

where:

$l_e = \dfrac{C_\mu^{3/4} k^{3/2}}{\varepsilon}$ or as in Table 4.2

Therefore, the particle is assumed to interact with an eddy as long as both the integration time step and the relative distance of interaction satisfies the following criteria:

$$\Delta t = Min[\tau_{JL}, \tau_r] \tag{4-20}$$

and

$$\left|\Delta \vec{X}\right| \leq l_e \tag{4-21}$$

where the fluid-particle relative velocity during the eddy-particle interaction time is approximated by its value at the beginning of the interaction. It is important to note that the expression of the residence time scale has no solution

when $l_e > \tau_p \left| \vec{U} - \vec{U}_p \right|$, and in this case the particle assumed to be trapped by the eddy and the interaction time will be the eddy lifetime.

Knowledge of the particle-eddy interaction time and the randomly sampled fluctuating velocity allow equations (4-8) and (4-10) to be solved for the particle's new position and velocity. At each new position, a new fluctuating velocity is sampled from a new PDF generated based on the new local turbulent properties. Thus the movement of the particle can be tracked throughout the flow domain until the full particle trajectory is finished.

This is the basis of the SSF model, which is based on the eddy lifetime concept. Unlike DDM, particles with the same physical properties and initial conditions will not have identical trajectories rather these will change as a result of the local fluctuating velocity component.

Table 4.2. Time and length scale coefficient after Shirolkar et al. (1996).

Author	Time scale $\tau_{fl} = A\frac{k}{\varepsilon}$ A	Length scale $l_e = B\frac{k^{\frac{3}{2}}}{\varepsilon}$ B
Gosman and Ioannides, (1981)	0.37	0.3
Shuen et al. (1983)	0.2	0.167
Faeth, (1983)	0.2	0.164
Chen and Crowe, (1984)	0.56	0.457
Kallio and Stock, (1986)	0.2	0.164
Mostafa and Mongia, (1987)	0.2	0.164
Adeniji-Fashola and chen, (1990)	0.2	0.164
Milojevic, (1990)	0.3	0.245

4.3.4 Time-Correlated Dispersion Models

Previous models accounted for the time correlation between the fluctuating fluid velocity through an isotropic assumption where an independent fluctuating velocity that is assumed to be constant for each eddy size and time step was randomly sampled.

Yuan (1989) illustrated a simple way to account for anisotropy by randomly and independently sampling two fluctuating velocities (u'_1 *and* u'_2 in two-dimensional problems) by using a correlation coefficient ξ:

$$\xi = \frac{\overline{u'v'}}{\sqrt{u'^2}\ \sqrt{v'^2}} \tag{4-22}$$

therefore:

$$u' = u'_1 \qquad and \qquad v' = \xi\, u'_1 + u'_2 \sqrt{1 - \xi^2\, u'_2} \tag{4-23}$$

This correlation coefficient is a special case of a more generalised correlation proposed by Ormancey and Martinon (1984), that is based on following a fluid particle trajectory simultaneously with the trajectory of a discrete particle. The focus of this approach, to determine the fluctuating fluid velocity, is to account for both time and cross-correlation. This model is not considered in the present study, however, details can be found in Berlemont et al. (1990) , Burry and Bergeles (1993) and Chen and Pereira (1995).

4.3.5 PDF Propagation Models

The main weakness of the stochastic dispersion models is the need to track a relatively large number of particle trajectories to achieve a statistically significant solution. This deficiency is overcome by basing the model on a probabilistic distribution of the fluctuating components. This approach has been introduced in a wide range of studies. These models are governed by a prescribed PDF, and are called PDF propagation models.

The principle of these models is to track a single PDF distribution for particle position, which then represents a group of particles of the same physical properties and initial conditions. These models are promising in terms of reduced the computational time but the particle properties required to account for complex flows are more difficult to estimate than the fluid particle properties required in the eddy lifetime models. Review of the PDF propagation models are given by Shirolkar et al. (1996).

4.4 Numerical Solution

The governing equations for the continuous phase and turbulence closure model have been solved in this work using the finite volume based CFD code SOFIE, Rubini (1997). The numerical procedure for the Lagrangian approach has been coupled with SOFIE as a post-processing to the solution of the continuous phase and k-ε turbulence flow field.

The governing equations of the continuous phase flow field are solved first providing the necessary flow field velocity and the turbulence properties at every grid point in the computational space. Then, particle trajectories are computed for a number of representative particles such that a statistically significant solution is obtained for the overall particle flow field.

The solution procedure for the Lagrangian approach of tracking particles will be outlined in this section. The treatment of the initial and boundary conditions and the particle-wall interaction are also presented. Moreover, an efficient and optimised searching algorithm is presented in order to locate the new particle position in the computational grid after every time step.

4.4.1 Initial Conditions

The starting point of the particle tracking calculation is the definition of the initial conditions. The initial conditions of the problem defines the initial positions from where the particles are injected into computational domain, the initial velocity and any other information or properties that are required to define and solve the problem, such as particle size and density. These initial conditions are summarised below.

Initial position: Specifies the co-ordinates of the position where the particle is introduced into the computational domain x_{pi}, y_{pi}, z_{pi}. For example the initial particle position can be defined at the computational domain boundaries or at any location within the domain.

For a single particle source, figure 4.2a a stream of particles are injected into the computational domain from the same initial point.

Another way of defining the injections of particles is by defining an initial spatial distribution of the particle streams, which can be defined as uniform, figure 4.2b, or non-uniform, figure 4.2c. Moreover, particles can be injected as a spray of a number of particles into different random directions from the same initial position as in figure 4.2d.

The final method of introducing particle into the flow field is to inject particles from a patch specified on the ground surface of the computational domain figure 4.2e. In this case particles are injected whenever the threshold conditions discussed in Chapter 2 are satisfied. In the case of wind blown sand or snow particles this is the default particle initial condition requiring only the length of the patch surface in a two-dimensional domain or the length and depth of the patch surface in the three-dimensional space.

The initial velocity u_{pi}, v_{pi}, w_{pi}. These velocities are either defined as an input values or, as in the case of wind blown particle, will be calculated based of theory discussed in Chapter 2.

The particle initial size (Diameter) D_{pi} is usually an input parameter. The code allows particles of different sizes to be tracked simultaneously.

4.4.2 Boundary Conditions

The particle injected into the computational domain is tracked until it reaches the boundaries of the computational domain or settles somewhere within the computational domain such as a wall, inlet or an outlet boundary.

The particle behaviour at these boundaries is dependent on the type of the boundary where the particle reached. The particle reactions at these boundaries are summarised below:

1. Reflection: Where the particle hits a solid surface with an angle θ_1 and velocity $\overline{U}_1$ then rebounds with an angle θ_2 and velocity $\overline{U}_2$ figure 4.3.

2. Trap: This terminates the trajectory calculation and records that the particle has trapped. An example of this boundary treatment is when the particle residential time scale is less than the eddy length scale.

3. Escape: This terminates the trajectory calculation when it passes through the outlet or inlet boundaries.

4. Mirror: When the particle hits a mirror boundary, that means the particle leaves the domain while another particle is injected to the domain from the same position where the particle left the domain but with opposite direction.

4.4.3 Coefficient of restitution

The coefficient of restitution is defined by the amount of momentum in the direction normal to the wall that is retained by the particle after collision with the boundary. It takes the value of 1.0 when the particle retains all of its normal momentum after the rebound, which expresses an elastic collision, and it is equal to 0.0 if the particle retains none of its normal momentum.

The same treatment of the restitution coefficient could be applied for the tangential particle momentum where the value of the coefficient can vary with the angle at which the particle impinges on the wall and is defined as:

$$e_n = \frac{U_{2,n}}{U_{1,n}} \tag{4-24}$$

$$e_t = \frac{U_{2,t}}{U_{1,t}} \tag{4-25}$$

4.4.4 Optimum Particle Searching Algorithm

It is a time-consuming procedure in Lagrangian trajectory computations to determine the location of a particle inside a Eulerian computational grid. The simplest but most computationally expensive way of locating a particle in the computational domain is to check all the Eulerian control volumes. Note that

this procedure has to be repeated along all the trajectories at each time step. Two questions need to be answered quickly and efficiently for each particle at each time step in order to reduce the time required to define the particles new co-ordinates:

1. *Is the particle still inside the control volume or not?*

2. *If not. In which control volume can the particle be found?*

The answer to these questions is usually simple when viewed on a piece of paper, but it may lead to expensive computations unless an efficient searching algorithm is employed. An efficient and relatively simple searching algorithm has been introduced so that the searching procedure is optimised to the minimum possible way in an orthogonal grid domain. Details of this algorithm are presented in appendix A.

4.4.5 Numerical Procedure

The subroutine LAGRANGIAN has been divided into three main loops. The outer loop goes through each different initial and physical condition (Position, Size, Density and Velocity). Inside that, a loop is set to cover the number of particle trajectories necessary to satisfy the statistically significant solution. The inner loop is set for the number of time steps required for a particle to complete its trajectory until it either leaves the computational domain or settles somewhere inside the computational domain.

Therefore, the majority of the particle-tracking model calculations exist in the inner most loop, steps 2 to 8, as follows:

1. Calculation of particle volume, mass and mass flow rate.

2. Based on the local flow field information, calculate the fluid-particle relative velocity, Reynolds numbers, drag coefficient and particle time relaxation.

3. Calculation of the integration time step from the minimum of the eddy lifetime and the particle residential time.

4. Solution of equations (4-8) and (4-10) in order to calculate the new particle velocity position.

5. Search for the control volume where the particle is located after one time step.

6. Establish whether the particle has hit one of the computational domain boundaries such as wall, outlet, inlet or mirror boundary, then to let the particle respond to it.

7. From the new location repeat the above steps for the next time step.

8. Repeat steps 2 to 7 until one complete particle track finished.

9. Repeat steps 1 to 8 for the number of particle trajectories required to achieve statistically significant solution.

10. Repeat steps 1 to 9 for particles with different initial and physical conditions.

4.5 Results and discussions

Lagrangian models, DDM and SSF, were implemented to simulate drifting sand particles over a flat sand surface and around a solid wall perpendicular to the flow direction.

The aim of these two case studies was to examine the Lagrangian models against flow fields comprising of a mixture of air and sand particles. First, different modes of particle movement such as suspension and saltation were considered when the flow passes over a flat bed covered by loose spherical solid particles.

Then, a solid wall was placed perpendicular to the flow direction to emphasise the effect of the re-circulation eddies generated around the wall on the particle trajectories.

4.5.1 Flow over flat surface

The flow field domain was specified as a flat surface of 100m length with a 5m height. The computational domain consisted of 100x50 grid points in the axial and vertical directions respectively. The grid distribution in the axial direction were set to be uniform with resolution of 0.1m and non-uniform in the vertical direction with higher resolution close to the surface. This arrangement ensures sufficient resolution in the flow boundary layer near the surface.

The inlet velocity was set according to the atmospheric log-law profile, equation (2.12) with friction velocity 0.374 m/s and surface roughness 1.0e-4 m. The surface was divided into erodible and non-erodible patches. Particles were patched over a 5m long erodible section starting 5m downstream from the domain inlet boundary. A maximum of ten thousand particles was enabled to entrain from the patch surface into the flow field whenever the threshold conditions are satisfied.

The first case considered was that of a single particle set to inject at a given time. Figure 4.4 shows the trajectories of a 0.25mm diameter particle injected vertically at a lift-off velocity 1.0, 1.5 and 2.0 m/s respectively with zero coefficient of restitution. It shows that the span of the trajectory increases with the lift-off velocity while they all follow a similar path shape.

For constant lift-off velocity, 0.5 m/s, the trajectories of particles of different diameters are shown in figure 4.5. It shows that smaller particles have a longer trajectory span than larger particles. Ten identical particles were injected using the same initial conditions and different numerical models DDM and SSF as shown in figure 4.6. As mentioned above, DDM leads to identical particle trajectories for particles of the same physical and initial conditions, as shown in figure 4.6a all 10 particles followed the same path and they appeared as a single trajectory. In SSF, figure 4.6b, shows that when the effect of the flow field

fluctuating velocity is involved, the particle trajectories were not identical even for the same physical and initial conditions.

Due to the turbulent eddies the particles may or may not follow the mean flow field. If the particle response time is higher than the eddy lifetime then the particle will move with no turbulent effects on it as shown in figure 4.6b for SSF model using 0.1-mm particle diameter.

Figure 4.7 shows particle trajectories of different particle sizes. Using the DDM model, small particles are suspended in the flow and move for a long distance before striking the surface while heavier particles saltated (bounced) on the surface with a definite saltation trajectory span. When the turbulent effect is involved in the trajectory calculation using the SSF model, the saltated particle followed the turbulent eddy whenever the eddy lifetime exceeds the particle responds time and it responds to the gravity force if the eddy lifetime becomes lower than its response time.

Figure 4.8 shows a comparison between the saltation trajectories using the SSF model when turbulent eddies have influenced the particle trajectory. The figure shows the randomness of the trajectories of a sample of 100 particles injected from identical initial conditions using two different particle sizes. It shows that from figure 4.8a the smaller particle trajectories are affected by the turbulent eddies and move in non-smoothly saltation trajectories. Whilst for the heavier particle, figure 4.8b, the saltation trajectories are clearly defined, showing no effect of turbulence on the trajectory.

Ten thousand particles were patched on the erodible surface defined in the flat surface, figure 4.9. When the particle threshold condition is satisfied, the flow will start to drift particles from the surface. It shows that particles start with some lift-off velocity and then move with the flow field according to the forces applied on an individual particle. A high particle concentration is found near the surface, which illustrates how the majority of particles move close to the surface in saltation mode and only few of them are suspended in the flow for some longer time and distance.

4.5.2 Particle trajectories Around Solid Wall

A solid wall of 2-metre height and 0.2-metre width was placed in the computational domain perpendicular to the flow direction. It is presumed that this will result in two recirculation regions as shown in figure 4.10. Particles entering into either of these regions are expected to settle and accumulate as a result of the reduction in the flow momentum.

The behaviour of individual particles entering these recirculation zones has been examined using the SSF model. Initially, particles were patched over a 5m length and were distributed uniformly upstream from the wall in a similar manner to those in the flat surface example.

For SSF simulation, 10 representative parcels of particles were injected from each location where the threshold conditions are satisfied.

This number of parcels is much lower than the statistically significant number of particles required from a single location. Since a qualitative idea of where most of the particles could be captured is all that is required and realising that a high computational time is required to inject statistically significant number of particles, this low number of representatives are chosen.

Figure 4.11 shows the drifting particles for different time steps. It can be seen that when particles reach the front recirculation zone, most particles are captured when the reverse flow meets the incoming flow where the friction velocity drops to values below the particle threshold velocity.

4.6 Closure

Different Lagrangian, particle trajectory, numerical models were implemented and analysed in this chapter. The advantages and disadvantages of these models were clarified through several test cases. These models were employed to simulate the an individual and group of particle trajectories as they are driven by the flow field under the influence of both drag and gravitational forces.

The different particle transport modes such as suspension and saltation were investigated using different Lagrangian models and different particle physical and initial conditions.

Moreover, an optimistic search algorithm was introduced to locate the particle coordinates after each time step within the computational grid starting from the recent particle location.

The model shows good qualitative results for the particle behaviour on flat surface and as the particle approaches flow eddies that were generated around obstacles that may exist in the flow field.

The major drawback of the Lagrangian models tested in this chapter was the requirement of tracking relatively high number of particles that were necessary to satisfy the statistically significant solution.

In general, The Lagrangian approach shows a potential ability to provide detailed information of individual particle behaviour in more complicated flow fields as long as the flow regime can be considered as a diluted flow. In dense flow systems, the theory behind these models is considered impractical and more complicated as more forces, such as particle-particle collision and Magnus forces must be involved, which were ignored for diluted flows.

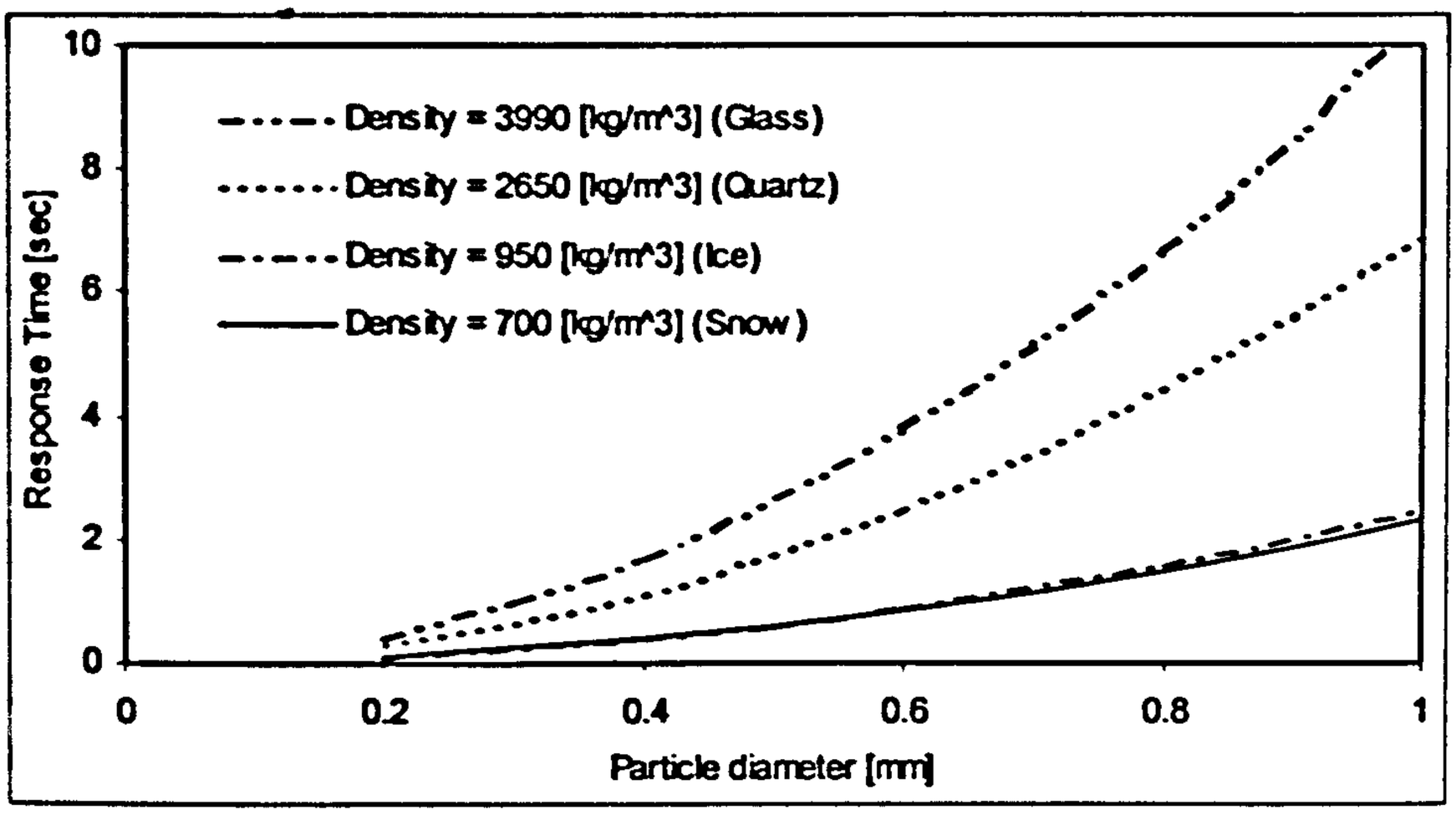

Figure 4.1: Particle response time for different particle densities as a function of its diameter.

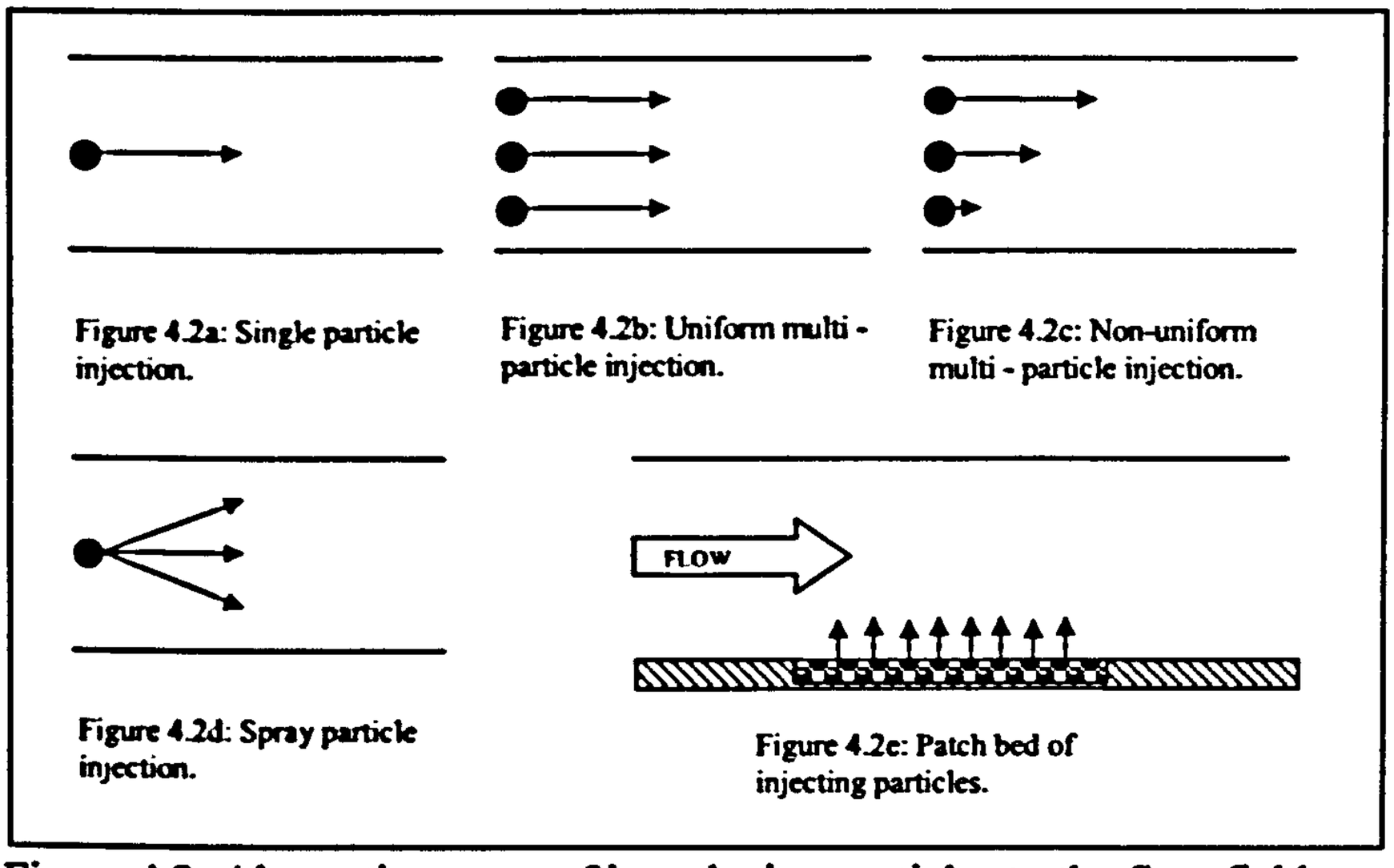

Figure 4.2a: Single particle injection.

Figure 4.2b: Uniform multi - particle injection.

Figure 4.2c: Non-uniform multi - particle injection.

Figure 4.2d: Spray particle injection.

Figure 4.2e: Patch bed of injecting particles.

Figure 4.2: Alternative ways of introducing particles to the flow field.

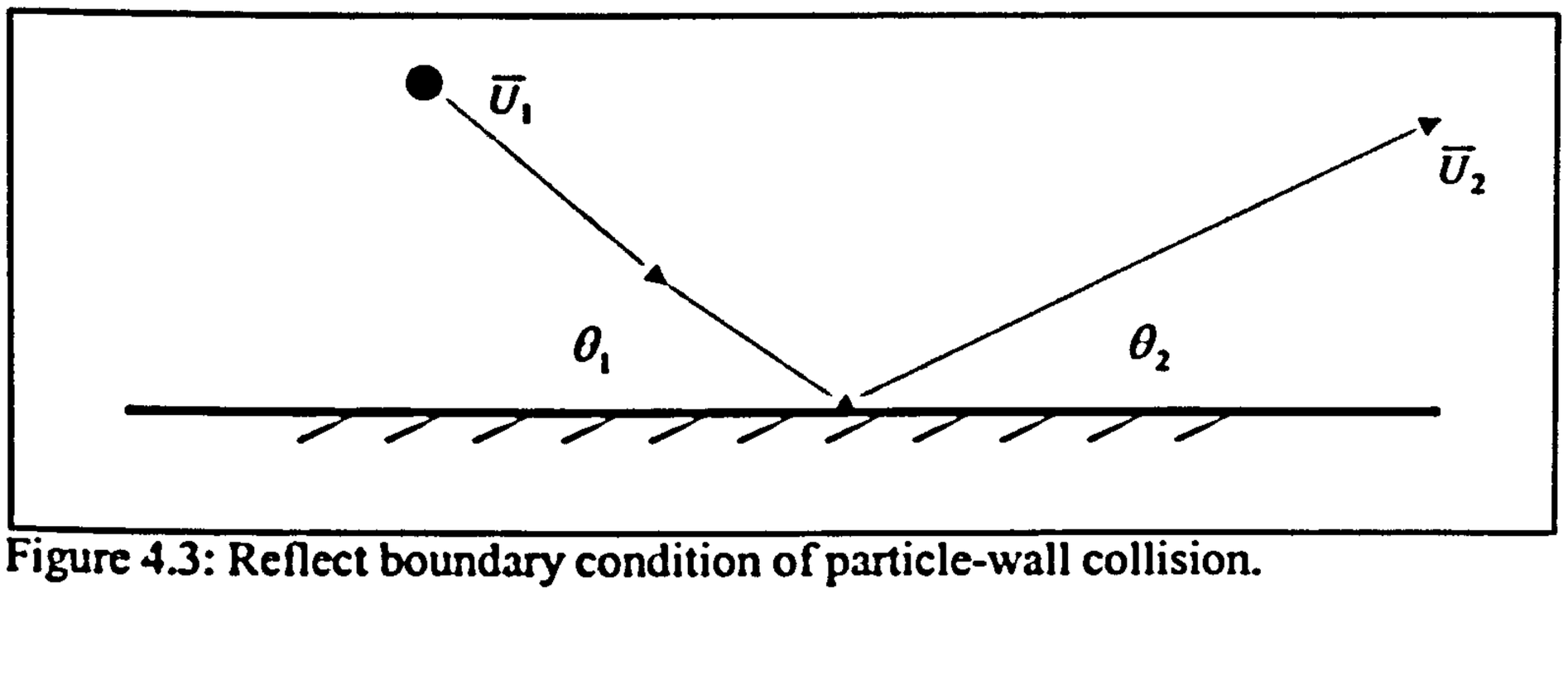

Figure 4.3: Reflect boundary condition of particle-wall collision.

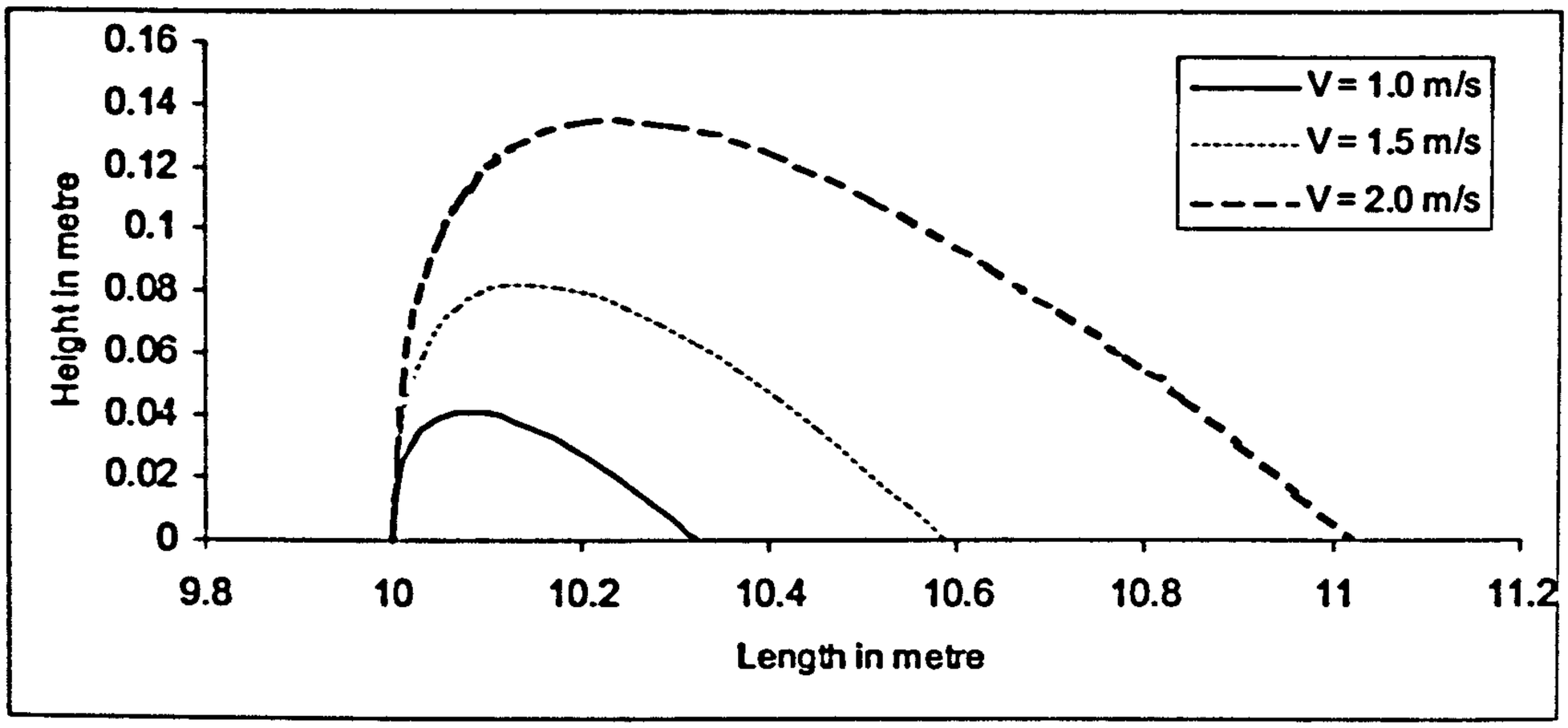

Figure 4.4: Single particle injected vertically into the flow field with different initial vertical velocity.

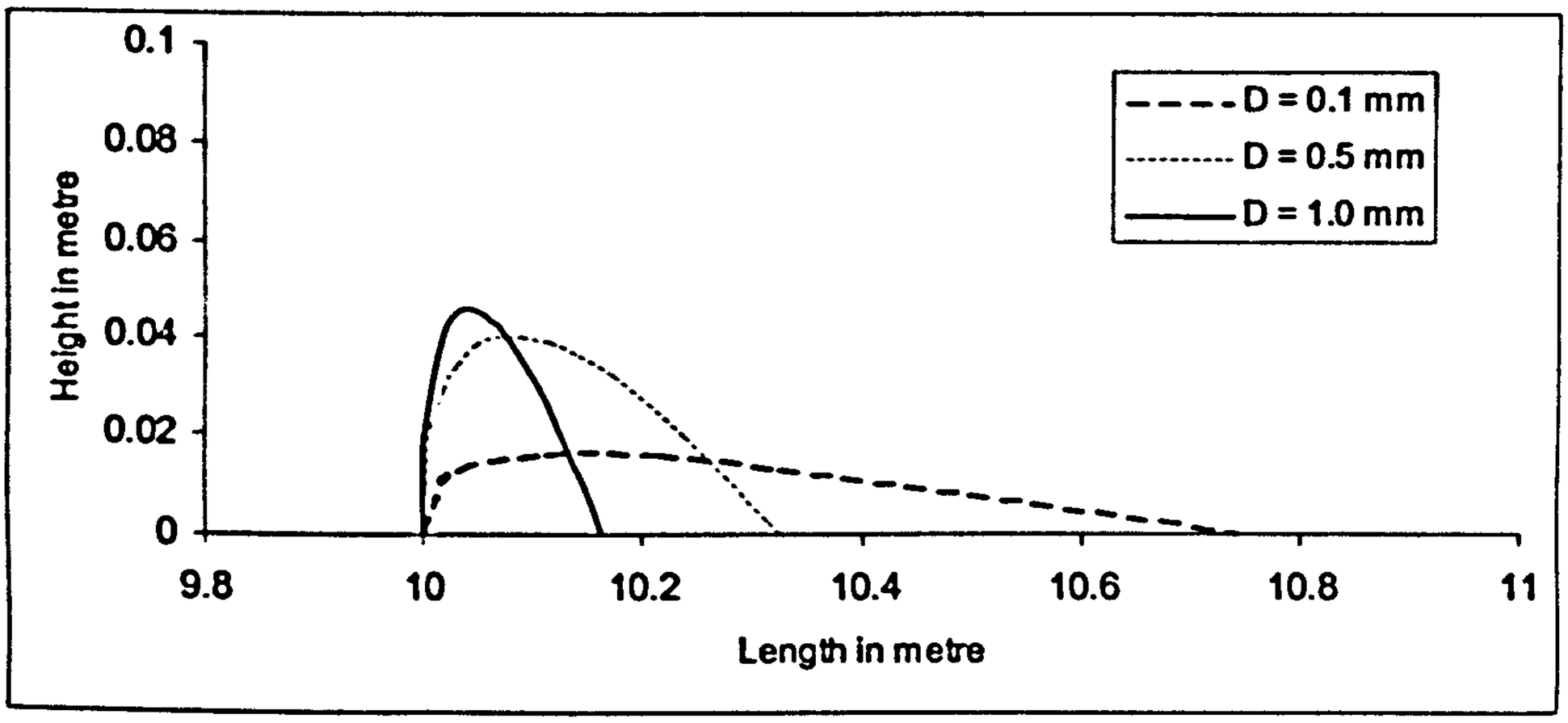

Figure 4.5: Single particle injected vertically into the flow field with different initial diameter.

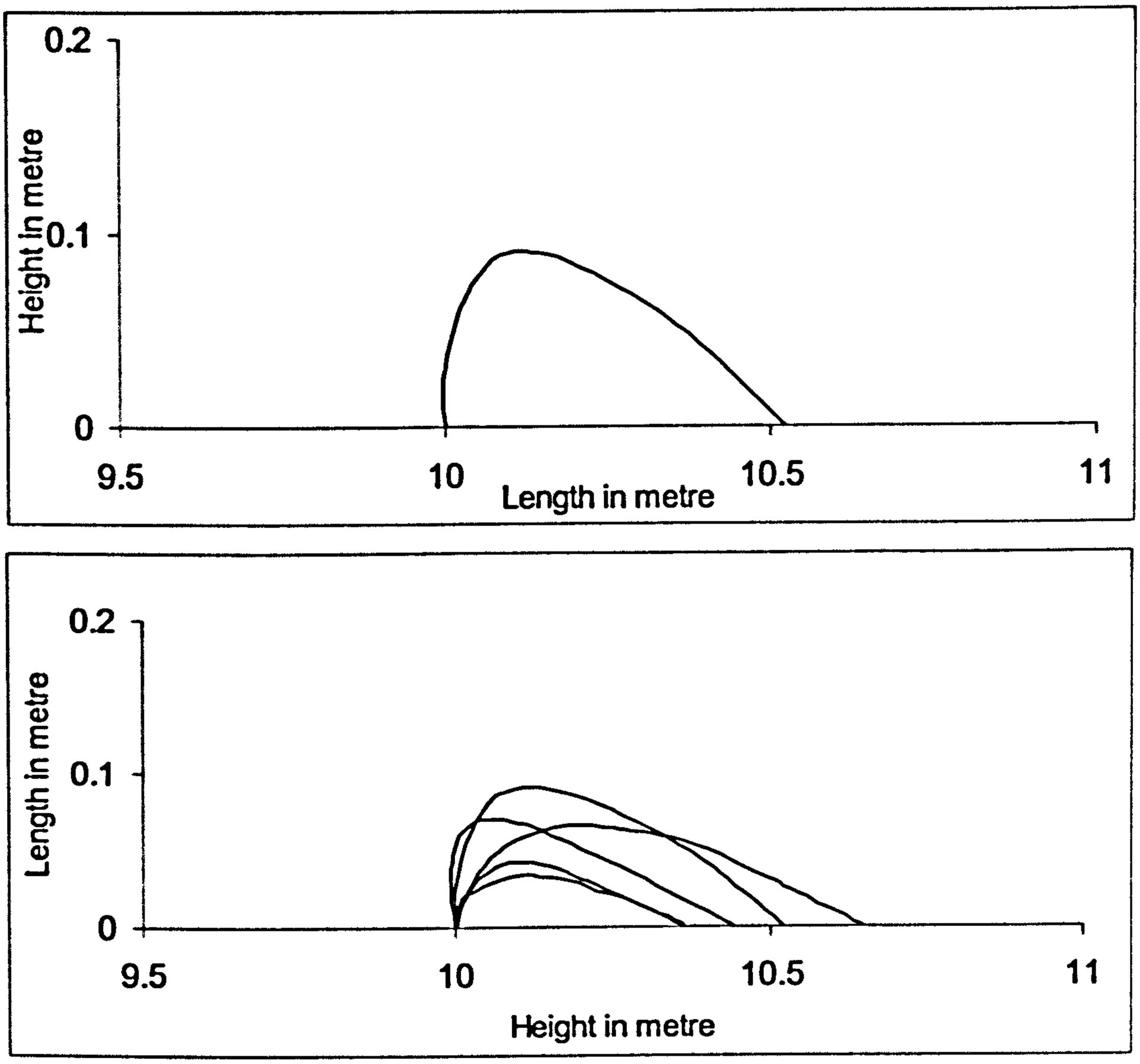

Figure 4.6: Group of particles injected vertically into the flow field with identical initial conditions. a. DDM model and b.SSF model.

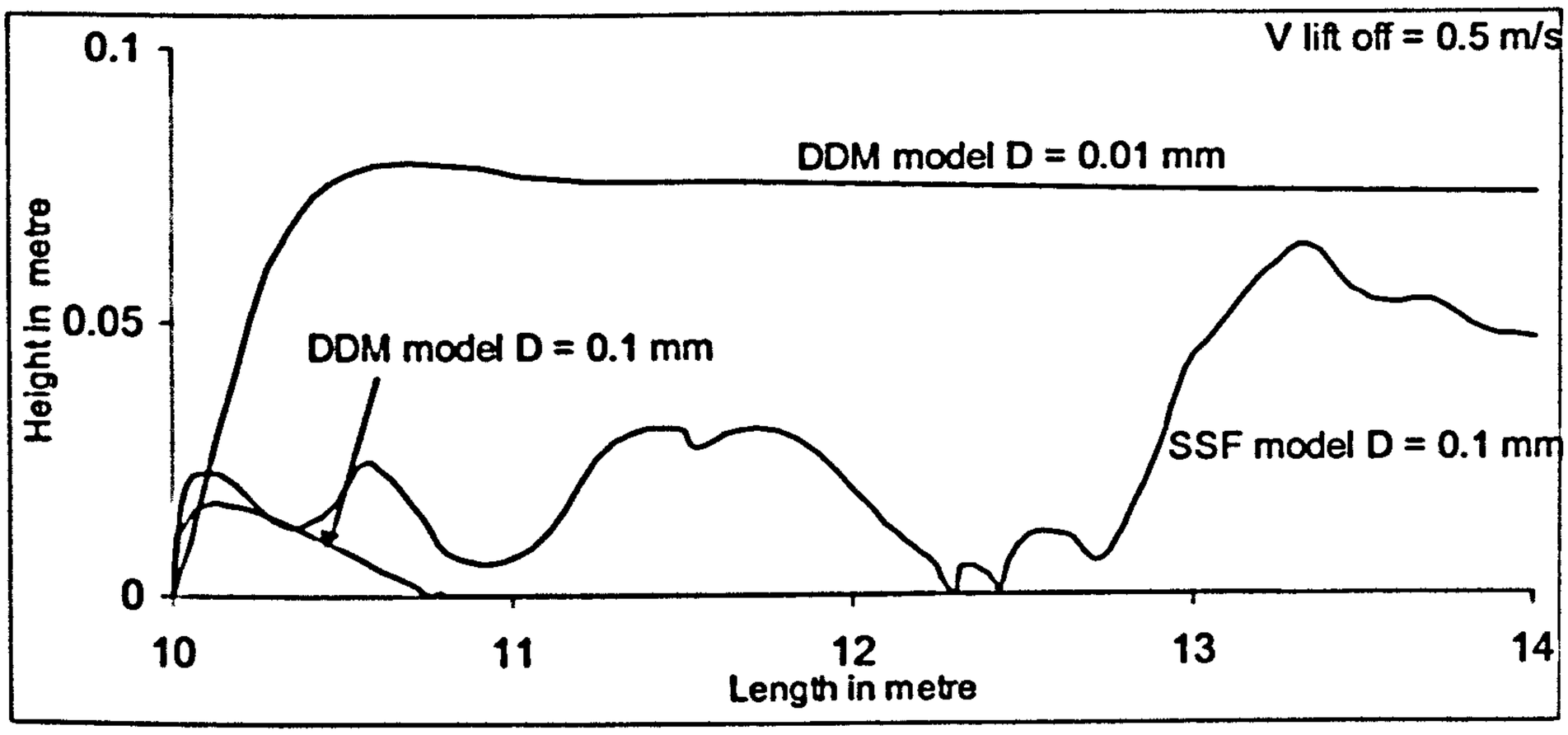

Figure 4.7: Saltation and suspension trajectories of a single particle injected vertically into the flow field with different particle sizes using the DDM and SSF models.

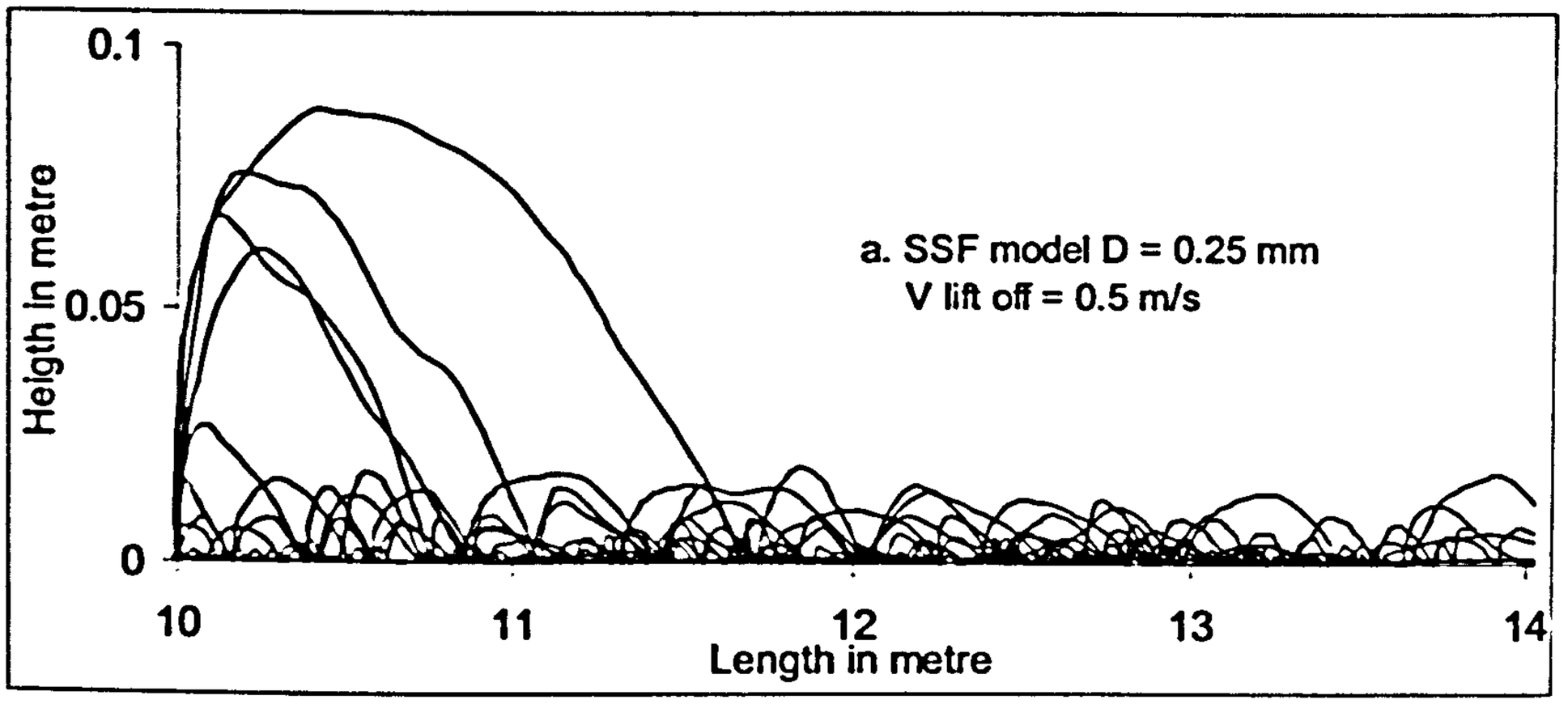

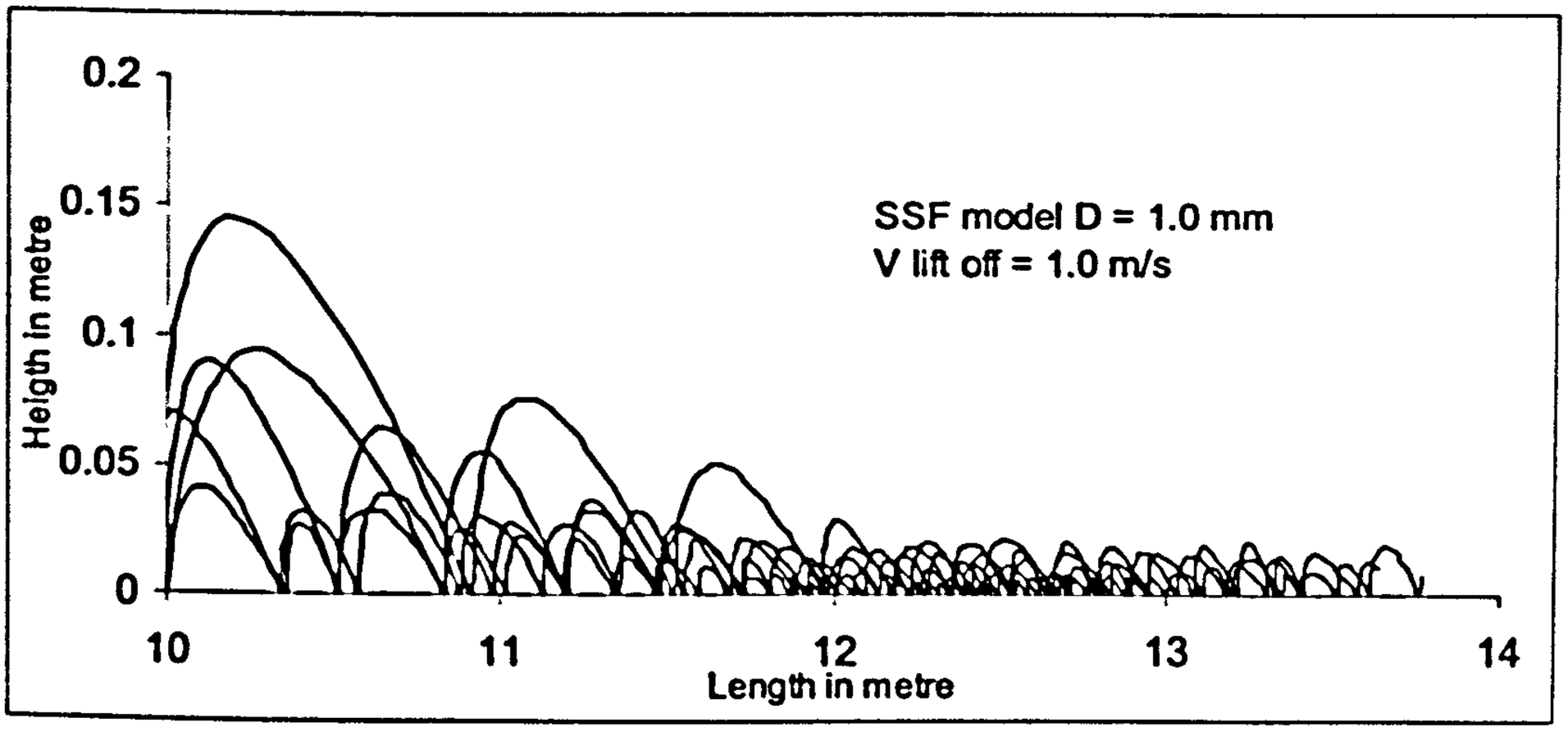

Figure 4.8: Group of particles injected vertically into the flow field with identical initial conditions using SSF model.

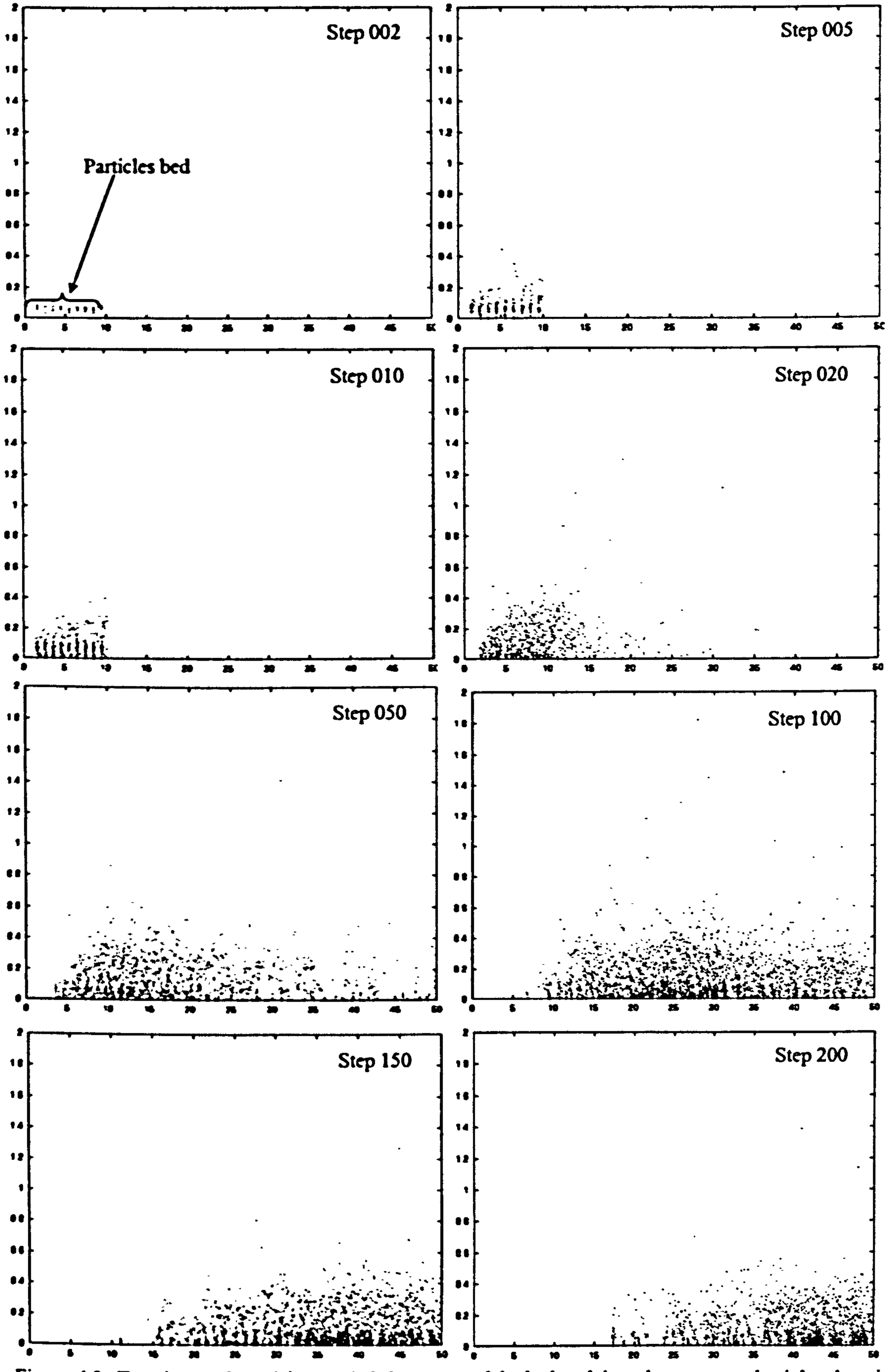

Figure 4.9: Ten thousand particles eroded from a sand bed placed just downstream the inlet domain. Figures show different steps of the Lagrangian calculations using SSF model.

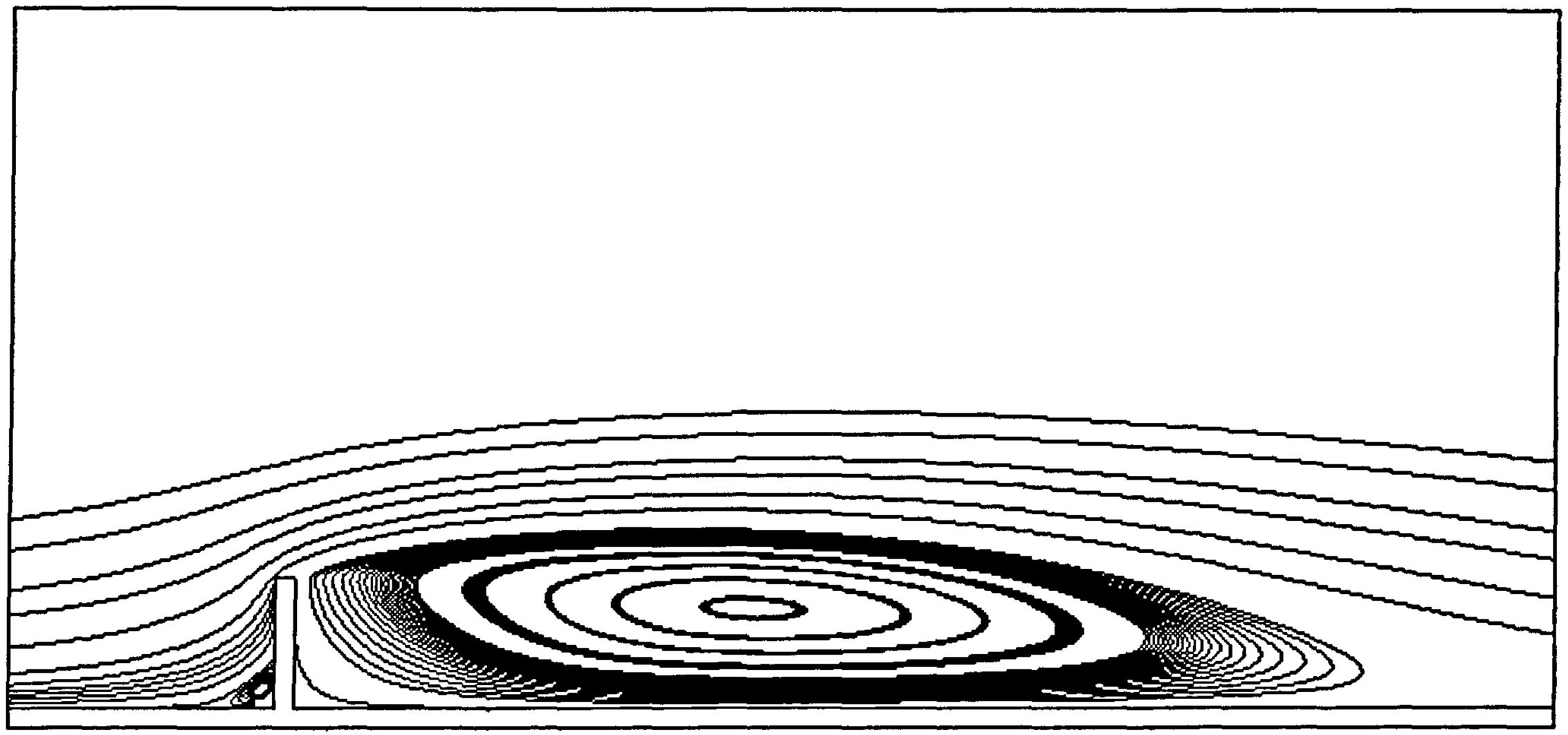

Figure 4.10: Stream lines of the flow field around a solid wall showing reverse flows generated in front of and behind the wall.

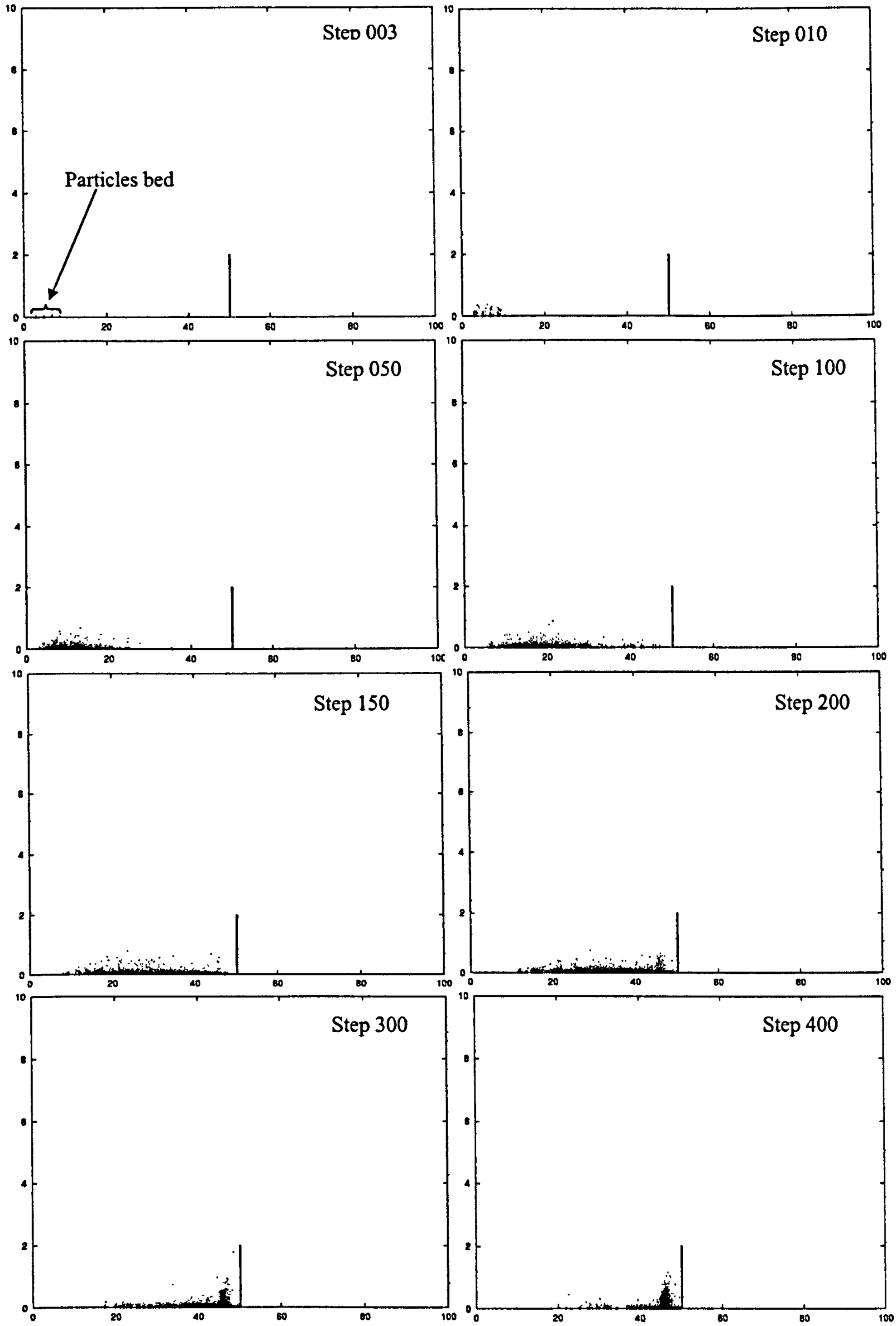

Figure 4.11: Ten thousand particles injected upstream of a solid wall placed perpendicular to the flow direction. Figures show different steps of the Lagrangian calculations using SSF model.

Chapter 5

Eulerian Two-Phase modelling

5.1 Introduction

This chapter presents a numerical model for two-phase flow in which the particle phase is considered as another continuum that can be solved based on a Eulerian reference frame. Different Eulerian multiphase flow numerical models will be discussed together with the necessary constitutive equations required to close the model's set of equations. Moreover, numerical modelling of the different modes of particles blown by wind such as suspension and saltation is developed to incorporate their effect in to the particle transport equation.

The following section summarises previous numerical studies, which have been employed to simulate the transport and deposition of particles around obstacles based on two-phase flow theory.

Many two-phase flow models have been developed for industrial and environmental applications in order to predict gas-particle flow based on a Eulerian approach. The two-fluid model is considered to be the most general form of the partial differential equations describing the flow of a mixture containing two or more fluids of different physical properties.

Two-fluid models and simplified models, derived basically from the two-fluid model (e.g. the mixture and homogenous models), are presented in section 5.3.

In section 5.4 the derivation of the different forms of the approximated fluid-particle relative velocity are presented.

The novel Fractional Area/Volume Obstacle Representation (FAVOR) model, introduced by Hirt (1993), is covered in section 5.5. The flow governing equations are rewritten in a form, which easily enables the implementation of the FAVOR model. The FAVOR technique was originally developed as a means of defining obstacles of general shapes within a fixed computational grid. However, it has been employed in the present work to introduce a solid interface boundary representing the particle deposition profile as a moving interface boundary.

The two-phase flow models coupled with the FAVOR technique provide a powerful tool, which is relatively simple to implement, to simulate the development of the particle deposition profile around obstacles.

A contribution was made in modelling the effect of particles transported by either suspension or saltation modes into the particle transport equations as a source (sink) terms. These, together with an erosion-deposition algorithm are presented in section 5.6. Finally, the solution procedure and some implementation remarks are presented in section 5.7.

5.2 Previous numerical studies

Numerical models based on solving the flow field governing equations, the Navier-Stokes equations, have been employed by many authors to simulate wind blown solid particles.

Drifting snow around buildings and sand dune emigration over flat surface are examples where numerical results have been successfully reported, [Uematsu et al. (1991), Sundsbo (1997), Wipperman and Gross (1986) and Kawamura et al. (1999)].

Wipperman and Gross attempted to numerically simulate the emigration of an isolated sand dune over a flat surface using the following procedure:

1. Solve the flow field governing equations in order to obtain an approximation for the flow friction velocity throughout the computational domain.

2. Based on the predicted friction velocity, the sand transport rate was calculated at each point in the computational domain using an empirical expression due to Lettau and Lettau (1977).

3. The erosion and deposition rates were predicted by computing the divergence of the transported sand.

4. The change in the surface height due to both erosion and deposition processes was added to the initial surface height to obtain a new surface.

5. This procedure then was repeated until an Equilibrium State solution was achieved.

Uematsu et al. and Sundsbϕ both followed a procedure similar to that of Wipperman and Gross to simulate the snow drift around obstacles such as snow fences, hills and houses.

Uematsu suggested that suspension, which was ignored in Wipperman and Gross study, must be taken into account when calculating snow drift. Therefore, Uematsu accounted for suspension through the solution of an extra transport equation for the snow density.

Sundsbϕ's model was similar to the model presented by Uematsu. However, the computational domain was divided into four zones dependent on the particle local concentration. The saltation effect was accounted for in the particle transport equation. The four regions introduced by Sundsbϕ were as follows:

1. Suspension zone, which represents the flow far from the ground where no saltating particles are expected.

2. Saltation-erosion zone, which is the zone, near the ground that is dominated by the erosion process.

3. Saltation-deposition zone, which is the zone, near the ground that is dominated by the deposition process.

4. Solidified zone where computational cells are fully blocked by deposited particles.

Although Sundsbo's model is independent of empirical expressions, which were used in the other models to predict the particle mass flow rate. This method is computationally complicated in the sense of using different forms of the particle transport equation within the same computational grid.

Recently, Kawamura et al. (1999) applied the procedure introduced by Wipperman and Gross to simulate sand deposition around a circular cylinder. Moreover, Van Dijk et al. (1999) introduced a CFD model based on solving the flow field governing equations in the atmospheric boundary layer. The model was employed to simulate the change in the surface of a dune with an initial sinusoidal shape. The erosion deposition rate was estimated using the empirical expression of Kawamura (1964) to predict the particle mass flow rate.

The last decade has seen interest in the application of CFD to drifting particles such as sand, snow or soil, increase considerably. However, as described above, these models are either dependent on empirical expressions for approximating the particle mass flow rate or are based on a complicated multi-zone domain approach where different forms of the particle transport equation is applied.

In the following sections, a multi-phase flow based CFD model will be discussed and implemented considering the particle phase as another continuum. The model will be able to simulate drifting particles independent of the explicit use of an empirical expression to predict the particle mass flow rate. In addition, the model will consider the domain as a whole without for sub-division the computational domain based on the particle transport modes.

5.3 Eulerian (continuum Two-Phase Flow) Modelling

Fluid flow consisting of one, two or more fluids of different physical properties is considered as single, two or multiphase flow systems respectively and can be classified according to the degree of the combination between the different phases along with the nature of the flow system, Ishii (1975).

In the modelling of flows that contain two or more fluids of different physical properties, the two-fluid model is the leading Eulerian numerical model, which can handle a system of multi-phase flows. This is classified as the most accurate but most complicated model to implement.

Simplification of the two-fluid model has led to less complicated models that can give an acceptable degree of accuracy at least from the engineering point of view. Examples of these simplified models are the mixture and the homogeneous models.

This section will present the basic conservation equations of these simplified Eulerian models as they are derived from the general two-fluid model.

5.3.1 Governing equations

The general form of the governing transport equations for continuity, momentum and general scalars such as turbulent kinetic energy k, kinetic energy dissipation rate ε and particle volume fraction α_p can be written in the framework of non-orthogonal curvilinear coordinates system as, [Peric (1985), Melaaen (1990)]:

$$\underbrace{\frac{\partial \rho \phi}{\partial t}}_{\text{Rate of change in } \phi} + \underbrace{\frac{1}{J}\frac{\partial}{\partial X^j}\left[(\rho U_m \phi)\beta^{mj}\right]}_{\text{Convection term}} = \underbrace{\frac{1}{J}\frac{\partial}{\partial X^j}\left[\left(\frac{\Gamma_\phi}{\sigma_\phi}\frac{\partial \phi}{\partial X^m}\right)\beta^{mj}\right]}_{\text{Diffusion term}} + \underbrace{S_\phi}_{\text{Source term}} \qquad (5\text{-}1)$$

Where ϕ represents the variables that are need to be expressed such as ρ, u, v, w, k, ε and α_p. Thus following the different expression of ϕ it is possible to form continuity, momentum and general scalar equations by substituting the

variable ϕ, the diffusion coefficient Γ_ϕ and the source term S_ϕ by the proper values as shown in table B-1, (Appendix B).

β^{mj} represent the co-factor of the coordinate transformation and J, the Jacobian determinant. Equation (5-1) can be expanded in terms of orthogonal or non-orthogonal coordinates system. The expanded form of the governing equations together with the turbulent closure model is given in Appendix B.

Details of the derivation, discretisation and numerical implementation of these equations are given by Peric (1985) and Melaaen (1990).

5.3.2 Two-Fluid Models

The two-fluid model treats the particle phase as a pseudo-continuum phase mixed with the primary phase, which is in this case the carrier phase, air. The conservation equations for each phase can thus be formulated in the Eulerian manner and have the form of equation (5-1). Derivations and discussions on the two and multi-phase flow numerical models have been widely covered during the last few decades, [Ishii (1975), Ahmadi and Ma (1990), Gidaspow (1994)].

Ishii's notation has been adapted in which each phase is described by the subscript k. The governing equations for the particle continuum phase may then be written as:

Mass conservation:

$$\frac{\partial}{\partial t}(\alpha_k \rho_k) + \nabla\cdot(\alpha_k \rho_k u_k) = Q_k \qquad (5\text{-}2)$$

Momentum conservation:

$$\frac{\partial}{\partial t}(\alpha_k \rho_k u_k) + \nabla.(\alpha_k \rho_k u_k u_k) = -\alpha_k \nabla.P_k + \nabla.(\tau_k + \tau_{kT}) + \alpha_k \rho_k g + M_k \qquad (5\text{-}3)$$

However, constitutive equations for the stress terms and interaction forces between phases have to be modelled separately. The literature contains a

number of different models for these constitutive equations dependent on the nature of the multiphase flow system.

Since all phases may or may not coexist at each point in the computational domain, each phase is assumed to occupy a fraction of an infinitesimal volume in the space. However, the conservation equations for each phase need to be solved simultaneously at every particular point in the computational domain. As a result of this, the shape and location of the interface boundary between the flow phases is required to be determined, which adds another dimension of complexity to the problem.

Due to this complexity there is no single multiphase flow model that can be employed for all types of flow regimes. In addition, the significant computational effort required to solve a set of conservation equations for each single phase in the two-fluid model along with relatively limited computational resources, makes the two-fluid model not the first choice to simulate multiphase flows. Therefore simplified models, which can be derived from the two-fluid model are more appropriate and will be discussed in the following two sections.

5.3.3 Mixture Model

The mixture model considers the mixture as a whole rather than two separate phases as in the two-fluid model.

Considering that the relative velocity between the two phases is assumed to be small, the mixture model can be expressed in terms of five field equations. One continuity and three momentum equations for the mixture as whole, one for every flow direction in three-dimensional domain and one transport equation for dispersed phase volume fraction equation.

Under this estimation, the set of the transport equations required to be solved in the mixture model are less than those required by the two-fluid model by two in two-dimensional space and three in three-dimensional space problems.

The major simplification in the mixture model is the replacement of the dispersed phase momentum equation by an algebraic formulation of the relative velocity.

The mixture model equations describing the dynamics of a mixture of two fluid phases have been cast in many forms for different purposes [Ishii (1975), Gidaspow (1994) and Ungarish (1993)]

The mixture model is also called the diffusion model, the drift-flux model or the slip-velocity model depending on how the diffusion velocity is approximated. The phase volume fraction and the mixture physical properties are defined as follows:

Volume fraction:

$$\alpha_p = V_p / V_{Total} \tag{5-4}$$

$$\alpha + \alpha_p = 1 \tag{5-5}$$

Mixture density:

$$\rho_m = \alpha \rho + \alpha_p \rho_p \tag{5-6}$$

Mixture viscosity:

$$\mu_m = \alpha \mu + \alpha_p \mu_p \tag{5-7}$$

Mixture velocity:

$$\rho_m u_m = \alpha \rho u + \alpha_p \rho_p u_p \tag{5-8}$$

$$\text{Or} \quad u_m = \sum_{k=1}^{n} \frac{\alpha_k \rho_k u_k}{\rho_m} = \sum_{k=1}^{n} c_k u_k$$

Ishii (1975) derived the general mixture equations by summing over all the phase continuity and momentum equations as follows:

$$\frac{\partial}{\partial t}\sum_{k=1}^{n}(\alpha_k \rho_k) + \nabla\cdot\sum_{k=1}^{n}(\alpha_k \rho_k u_k) = \sum_{k=1}^{n} Q_k \qquad (5\text{-}9)$$

$$\frac{\partial}{\partial t}\sum_{k=1}^{n}(\alpha_k \rho_k u_k) + \nabla\sum_{k=1}^{n}.(\alpha_k \rho_k u_k u_k) = -\sum_{k=1}^{n}\alpha_k \nabla.P_k + \nabla\sum_{k=1}^{n}\alpha_k.(\tau_k + \tau_{kT}) + \sum_{k=1}^{n}\alpha_k \rho_k g + \sum_{k=1}^{n} M_k \qquad (5\text{-}10)$$

where n is the total number of phases included in the mixture.

Mixture Continuity Equation

Since only two phases are present in the mixture, the two-fluid model continuity equation (5-2) can be rewritten for each phase as:

$$\frac{\partial}{\partial t}(\alpha\ \rho) + \nabla\cdot(\alpha\ \rho\ u) = Q \qquad (5\text{-}11)$$

$$\frac{\partial}{\partial t}(\alpha_p \rho_p) + \nabla\cdot(\alpha_p \rho_p u_p) = Q_p \qquad (5\text{-}12)$$

Assuming that the net mass exchanged between phases is conserved then,

$$Q + Q_p = 0$$

Summing up equations (5-11) and (5-12) as in (5-9) gives:

$$\frac{\partial}{\partial t}(\alpha\ \rho + \alpha_p \rho_p) + \nabla\cdot(\alpha\ \rho\ u + \alpha_p \rho_p u_p) = 0$$

or $$\frac{\partial}{\partial t}(\rho_m) + \nabla\cdot(\rho_m u_m) = 0 \qquad (5\text{-}13)$$

In this form, the mixture velocity represents the velocity at the centre of mass of the mixture. Equation (5-13) has the same form as the continuity equation of single-phase flow. For incompressible mixture flow where the densities of all phases are constant, the mixture continuity equation can be written in terms of the velocity at the centre of mixture volume as:

$$\nabla\cdot J_m = 0 \qquad (5\text{-}14)$$

Where J_m is the volumetric mixture flux.

Mixture momentum equation

Similarly, the mixture momentum equation can be derived from the general two-fluid model momentum equations by summing up the momentum equations of each individual phase:

$$\frac{\partial}{\partial t}(\alpha\ \rho\ u\ ) + \nabla.(\alpha\ \rho\ u\ u\ ) = -\alpha\ \nabla.P + \nabla.\alpha\ (\tau\ + \tau_T) + \alpha\ \rho\ g + M \tag{5-15}$$

$$\frac{\partial}{\partial t}(\alpha_p \rho_p u_p) + \nabla.(\alpha_p \rho_p u_p u_p) = -\alpha_p \nabla.P_p + \nabla.\alpha_p(\tau_p + \tau_{pT}) + \alpha_p \rho_p g + M_p \tag{5-16}$$

To avoid the presence of the individual phase velocity, the second term in the left-hand side is defined in terms of the mixture and diffusion velocities.

$$\nabla.\sum_{k=c,p}(\alpha_k \rho_k u_k u_k) = \nabla.(\rho_m u_m u_m) + \nabla.\sum_{k=c,p}(\alpha_k \rho_k u_{Dk} u_{Dk}) \tag{5-17}$$

The second term in right-hand side of (5-17) is known as the mixture diffusion stress term where u_{Dk} is defined as the diffusion velocity, which is the velocity of k^{th} phase relative to the velocity of the centre of the mixture mass.

$$u_{Dk} = u_k - u_m \tag{5-18}$$

Substituting (5-17) in to the summation of (5-15) and (5-16), the mixture momentum equation can be written as:

$$\frac{\partial}{\partial t}(\rho_m u_m) + \nabla.(\rho_m u_m u_m) = -\nabla.P_m + \nabla.(\tau_m + \tau_{mT}) + \nabla.\tau_{Dm} + \rho_m g + M_m \tag{5-19}$$

Where, the mixture pressure gradient is defined as:

$$\nabla.P_m = \sum_{k=1}^{n} \alpha_k \nabla.P_k \tag{5-20}$$

The mixture viscous stress:

$$\tau_m = \sum_{k=1}^{n} \alpha_k \tau_k \tag{5-21}$$

The mixture turbulent stress as:

$$\tau_{mT} = \sum_{k=1}^{n} \alpha_k \overline{\rho_k u_{kk}^{'} u_{kk}^{'}} \tag{5-22}$$

The diffusion stress as:

$$\tau_{Dm} = -\sum_{k=1}^{n} \alpha_k \rho_k u_{Dk} u_{Dk} \tag{5-23}$$

and M_m is any external force applied on the mixture.

The mixture viscosity requires careful treatment particularly when solid particles are included in the calculations where the viscosity is a quantity, which has no physical meaning.

The simplest method of determining the mixture viscosity for multiphase flow system is by applying formula (5-7) suggested by Ishii (1975). This formula cannot be taken as a general definition of the mixture viscosity since it has no relevance if the dispersed phase consists of solid particles.

In the case of a diluted flow, where the particles are always suspended and do not accumulate to form highly concentrated regions, the viscous shear stress due to the dispersed phase can be ignored compared to that of the continuous phase [Drew (1983), Joseph et al. (1990)]. Therefore, the mixture shear stress is reduced to the continuous phase shear stress by taking the mixture viscosity to be the viscosity of the continuous phase. This assumption is valid only for diluted flows. Ishii and Mishima (1984) present a general model for the mixture viscosity, which is valid for solid particles as well as for bubbles and droplets.

$$\mu_m = \mu\left(1-\frac{\alpha_p}{\alpha_{pm}}\right)^{-2.5\alpha_{pm}\mu^*} \tag{5-24}$$

α_{pm} is the maximum volume fraction of the dispersed phase assuming that space is completely packed by the particles. According to Ishii and Mishima (1984) $\alpha_{pm} \approx 0.62$. In equation (5-24):

$$\mu^* = \begin{cases} 1.0 & \textit{Solid Particles} \\ \dfrac{\mu_p + 0.4\mu}{\mu_p + \mu} & \textit{Bubbles and Droplets} \end{cases} \tag{5-25}$$

Note that as the mixture viscosity approaches the continuous phase viscosity the particle volume fraction approaches zero.

Dispersed phase continuity equation

The continuity equation of the dispersed phase can be written as:

$$\frac{\partial \alpha_p \rho_p}{\partial t} + \nabla.(\alpha_p \rho_p u_p) = 0 \tag{5- 26}$$

The equation can be rewritten in terms of mixture and diffusion velocities using (5-18) to avoid the appearance of phase velocity, which is referred to as *the dispersed phase diffusion equation* Ungarish (1993):

$$\frac{\partial \alpha_p \rho_p}{\partial t} + \nabla.(\alpha_p \rho_p u_m) = -\nabla.(\alpha_p \rho_p u_{Dp}) \tag{5-27}$$

If the phase densities are constant then the diffusion equation can be written in terms of the volumetric flux

$$\frac{\partial \alpha_p}{\partial t} + \nabla.(\alpha_p u_m) = -\nabla.(\alpha_p u_{Dp}) \tag{5-28}$$

The diffusion velocity can be defined in terms of the relative velocity (velocity of the dispersed phase relative to the velocity of the continuous phase):

$$u_{rel} = u_p - u \tag{5-29}$$

Using equations (5-8) and (5-18) and substituting into (5-29), the diffusion velocity can be written in terms of the relative velocity and particle mass fraction as follows:

$$u_{Dp} = (1 - c_p) u_{rel} \tag{5-30}$$

In the case of constant densities, the diffusion velocity in equation (5-27) is usually called the drift velocity. The model consisting of the dispersed phase continuity equation (5-27) is called the drift-flux model, Ishii (1975). The drift velocity can also be formulated in terms of the relative velocity and particle volume fraction as:

$$u_{Dp} = (1 - \alpha_p) u_{rel} \tag{5-31}$$

Ishii (1975) and Simonin (1990), included the fluctuating effect of the relative velocity into the diffusion equation as follows:

$$u_{rel} = u_{rel_0} + \Gamma_{Dp} \nabla . \alpha_p \tag{5-32}$$

Where u_{rel_0} is the averaged part of the relative velocity and Γ_{Dp} the dispersed phase eddy diffusion coefficient.

A correlation for the eddy diffusion coefficient is required if the turbulent effect is included. Picart et al. (1986), suggested a simplified theoretical model for turbulent flow in pipes based on the $k - \varepsilon$ model as:

$$\Gamma_{Dp} = \nu_T \left(1 + 0.85 \frac{u_{rel}^2}{2k/3} \right)^{-1/2} \tag{5-33}$$

where ν_T is the turbulent kinematic viscosity of the continuous phase and k is the turbulent kinetic energy. This formula demonstrates that as the relative velocity decreases the particle eddy diffusion coefficient tends to be equal to the turbulent kinematic viscosity of the continuous phase. It has been reported that

this formula is commonly used in diluted particle flow where the particle size is small enough to follow the continuous phase flow, Simonin (1990).

If the diffusion coefficient term is also included into equation (5-27), a general convection-diffusion equation for the dispersed phase can be written as:

$$\frac{\partial \alpha_p \rho_p}{\partial t} + \nabla.(\alpha_p \rho_p u_m) = \nabla.(\Gamma_{Dp} \nabla \alpha_p) - \nabla.(\alpha_p \rho_p u_{Dp}) \tag{5-34}$$

The mixture model, which is derived from the two-fluid model, does not include any further assumptions other than those assumed in the two-fluid model. Therefore, the main assumption in the mixture model is the replacement of the dispersed phase momentum equation by an algebraic approximation of the diffusion velocity, which will be discussed in more details in the next section.

5.3.4 Homogenous Model

The simplest Eulerian representation of the dispersed phase is to assume that a particle has the same local instantaneous velocity as that of the primary fluid. Hence, they are locally assumed to be in mechanical equilibrium over an infinitesimal volume in the computational space.

Based on this assumption the two-fluid model can be further reduced to a single-phase flow problem requiring only a transport equation for the particle property. Thus, the homogenous model is a special case of the mixture model, which itself is a simplification of the two-fluid model.

The homogenous model is derived by assuming that the mixture properties in equations (5-13) and (5-17) are those of the continuous phase only and the momentum exchange between the phases is negligible.

Thus the flow field of the continuous phase is required as a pre-processing step to the flow of the dispersed phase and therefore the dispersed phase does not affect the flow of the continuous phase even in highly concentrated regions.

The dispersed phase is then considered as a suspended particle in the flow by solving the transport equation for the particle volume fraction.

$$\frac{\partial \alpha_p \rho_p}{\partial t} + \nabla.(\alpha_p \rho_p u) = \nabla.(\Gamma_{Dp} \nabla.\alpha_p) + S_p \qquad (5\text{-}35)$$

Where:

S_p is the source term representing the particle source (sink) terms.

Γ_p is the particle eddy diffusion coefficient, which in the homogeneous model is assumed to be equal to that of the continuous phase.

If the terminal particle settling velocity is included as a source term in equation (5-35), this equation becomes the general suspension transport equation for the dispersed phase volume fraction, which is constant for a specific particle size and density. Moreover, a variable source term can be introduced if the relative velocity is related to the particle settling velocity and volume fraction.

Approximation of the particle-fluid relative velocity is covered in the following section, which will be used in the present work for both mixture and homogenous models.

5.4 Approximation of the relative velocity

The main approximation in the mixture model is the replacement of the phase momentum equations with an algebraic approximation of the relative velocity. There are two different possible ways of approximating the relative velocity, both are derived from the general two-fluid model momentum equations:

1. Subtracting the continuous phase momentum equation from the dispersed phase momentum equation.

2. Using the mixture momentum equation rather than the continuous phase momentum equation to be subtracted from the dispersed phase momentum equation.

Since they both give an approximation for the relative velocity, no advantages or disadvantages of using either way have been investigated thus the current work adopts the second approach due to the simplicity of its derivation.

Consider the mixture momentum equation (5-19) multiplied by the dispersed phase volume fraction and subtracted from the dispersed phase momentum equation (5-35):

$$\begin{aligned}&\frac{\partial}{\partial t}\alpha_p(\rho_p u_p-\rho_m u_m)+\nabla.(\alpha_p\rho_p u_p u_p)-\nabla.(\alpha_p\rho_m u_m u_m)=\\&\quad-\alpha_p(\nabla P_p-\nabla P_m)+\nabla\alpha_p(\tau_p+\tau_{pT})-\nabla\alpha_p(\tau_m+\tau_{mT}+\tau_{Dm})+\alpha_p(\rho_p-\rho_m)g+M_p-M_m\end{aligned}\qquad(5\text{-}36)$$

The definition of the diffusion velocity, (5-30) and (5-31) is used to avoid the appearance of the dispersed phase velocity. Neglecting the surface forces due to the mixture M_m, and omitting the pressure terms, the above equation can be rearranged to be:

$$\begin{aligned}M_p=&\alpha_p\left[\frac{\partial}{\partial t}(\rho_p u_{Dp})+\frac{\partial}{\partial t}(\rho_p-\rho_m)u_m\right]\\&+\alpha_p\left[\nabla.(\rho_p u_p u_p)-\nabla.(\rho_m u_m u_m)\right]\\&-\nabla\alpha_p(\tau_p+\tau_{pT})+\nabla\alpha_p(\tau_m+\tau_{mT}+\tau_{Dm})-\alpha_p(\rho_p-\rho_m)g\end{aligned}\qquad(5\text{-}37)$$

Further assumptions are applied to the above equation in order to obtain a mathematically feasible form of the relative velocity. First, using the local equilibrium assumption, the rate of change of the diffusion velocity with time is assumed small compared to the rate of change of the mixture velocity. Thus, the second term in the LHS of (5-37) can be assumed comparable to the mixture term: $\nabla.(\rho_p u_p u_p)\approx\nabla.(\rho_m u_m u_m)$

Ishii et al. (1984), neglected the viscous and diffusion terms as small compared to the leading terms in the equation while the turbulent stress term is retained if the turbulent diffusion of the dispersed phase needs to be considered. Thus

$$-\nabla.\alpha_p(\tau_{pT})+\nabla.\alpha_p(\tau_{mT})=\alpha_p\nabla.(\alpha\tau_T)-\alpha\nabla.(\alpha_p\tau_{pT})$$

Applying these assumptions to equation (4-34) gives:

$$M_p=\alpha_p(\rho_p-\rho_m)\left[g-u_m\nabla.(u_m)-\frac{\partial u_m}{\partial t}\right]-\alpha_p\nabla.(\alpha\tau_T)-\alpha\nabla.(\alpha_p\tau_{pT}) \qquad (5\text{-}38)$$

This equation is equivalent to the force balance applied on a single particle driven by fluid flow. Neglecting all viscous forces that can be applied on a single spherical particle except the drag force, gravity and shear stress, equation (5-38) can be written as:

$$\frac{3}{4}\frac{C_D\rho}{d_p}|u_{rel}|u_{rel}=\alpha_p(\rho_p-\rho_m)\left[g-u_m\nabla.(u_m)-\frac{\partial u_m}{\partial t}\right]-\alpha_p\nabla.(\alpha\tau_T)-\alpha\nabla.(\alpha_p\tau_{pT}) \qquad (5\text{-}39)$$

The simplest way to apply the relative velocity equation is by considering the Stokesian flow around a spherical particle in a diluted suspension under gravitational force only. The relative velocity in this case becomes constant and equal to the free falling velocity:

$$u_{rel}=\frac{d_p^2\,\rho_p}{18\mu}g \qquad (5\text{-}40)$$

The mixture model used with this simple form of the relative velocity is commonly called the *Drift Flux Model* [Hirt (1990)] and appeared as the *Algebraic Slip Velocity model* in FLUENT5.0 (March 1999). If all forces from equation (5-39) except drag and gravity are omitted, the relative velocity can be approximated in terms of particle volume fraction:

$$|u_{rel}|u_{rel}=\frac{4}{3}\frac{d_p}{C_D}\frac{\alpha_p\,(\rho_p-\rho_m)}{\rho}g \qquad (5\text{-}41)$$

The approximated relative velocity can also be derived in terms of the pressure gradient instead of the inertial force terms. If the inertial terms are eliminated in equation (5-37) rather than the pressure term, the relative velocity in terms of the pressure gradient can be written as:

$$|u_{rel}|u_{rel} = \frac{4}{3}\frac{d_p}{C_d}\frac{\alpha_p(\rho_p - \rho_m)}{\rho}\nabla P \qquad (5\text{-}42)$$

The application of the homogenous model results in the mixture density in equations (5-40), (5-41) and (5-42) being replaced by the continuous phase density.

5.5 Fractional Area-Volume Obstacles Representation (FAVOR)

In this section a powerful and relatively simple modelling technique is presented which was originally developed as a means of defining obstacles of general shape within a fluid computational domain defined in terms of a fixed grid.

This technique was originally developed by Hirt (1993) as an alternative to the Volume-of-fluid (VOF) model of Hirt and Sicilian (1985), to represent interface boundaries using volume fractional method. FAVOR is an efficient computational tool since it requires much less computer memory and less computational time than other methods for modelling geometry within a flow field, yet it is not widely used.

In the present work, the flow field governing equations discussed above are rewritten in a form suitable for implementation of FAVOR. The combination between two-phase flow models and the FAVOR technique provide a powerful solution strategy for representing the interface boundary separating the flow field from the growing profile of accumulated particles.

This technique introduces four new parameters to the flow governing equations, one cell volume fraction and three cell area fractions (one for each flow direction). The values of these fractions are related to the secondary phase volume fraction, which has a value varying between zero and one.

The governing equations are derived in a form suitable for finite volume discretisation with the appearance of the area-volume fractions.

Details of the derivation and discretisation of a single phase flow governing equations following finite volume approach in general curvilinear coordinates are given by Peric (1985) and Melaaen (1990). Following Peric and Melaaen work, the governing equations are derived introducing the new parameters necessary for FAVOR to implement.

FAVOR equations in the compacted form can be written as follow:

Continuity: $$\frac{\partial \rho}{\partial t}+\frac{1}{JV_f}\frac{\partial}{\partial X^j}\left(\rho u_m \beta^{mj} A_{f,j}\right)=Q_m \qquad (5\text{-}43)$$

Momentum: $$\frac{\partial \rho u_i}{\partial t}+\frac{1}{JV_f}\frac{\partial}{\partial X^j}\left[\left(\rho u_m u_i - T_{m,i}\right)\beta^{mj} A_{f,j}\right]= S_i^u \qquad (5\text{-}44)$$

General scalar: $$\frac{\partial \rho \phi_i}{\partial t}+\frac{1}{JV_f}\frac{\partial}{\partial X^j}\left[\left(\rho u_m \phi_i - q_{m,i}\right)\beta^{mj} A_{f,j}\right]= S_{\phi_i} \qquad (5\text{-}45)$$

Where, area fractions in vector form are expressed as:

$$A_{f1} = \lfloor A_{f11} \quad A_{f12} \quad A_{f13} \rfloor$$

$$A_{f2} = \lfloor A_{f21} \quad A_{f22} \quad A_{f23} \rfloor \qquad (5\text{-}46)$$

$$A_{f3} = \lfloor A_{f31} \quad A_{f32} \quad A_{f33} \rfloor$$

V_f = *Is the volume fraction of a given cell*

In the above equations $A_{f,i}$ are the open area fractions associated with the local volume fraction V_f in a specific cell. $T_{m,i}$, $q_{m,i}$ *and* β^{mj} are defined in Appendix C.

The FAVOR technique is based on the evaluation of the value of the volume fraction in each cell of the computational grid, figure 5.1a. The volume fraction enables a description of the cell contents, which are one of the following:

1. Fully occupied by the primary phase, air.

2. Fully occupied by the secondary phase, particles.

3. Both phases exist simultaneously in the same cell.

In cells where the particle volume fraction is 1, the area fractions of the cell faces (4 in 2-D domain and 6 in 3-D) are set to be one to prevent any flow from passing across the cell's boundaries. This will be automatically considered according to equations (5-43), (5-44) and (5-45).

If volume fraction of only 0 or 1 is considered in the calculations, the computational domain will be in the form shown in figure 5.1b when FAVOR is applied.

If the contribution of cells partially filled by both phases are involved, the fluxes through the cell sides will be multiplied by the side area fraction as if the side is partially open to the flow, figure 5.2.

A special numerical treatment to these faces is necessary to avoid numerical instability and to assure the mass balance across the cell boundaries, which is beyond the scope of the present work thus, no more details are provided.

Equations (5-43), (5-44) and (5-45) were expanded in the general curvilinear co-ordinates system, although all the case studies utilise in this work are in orthogonal grid. The expanded forms of these equations are given in appendix C.

5.6 Suspension-Saltation Model and Erosion-Deposition algorithm

The particle phase volume fraction is represented by a general scalar transport equation, which incorporates the physical phenomena of convection and diffusion. The particle volume fraction equation can be represented in general transport equation form as:

$$\underbrace{\frac{\partial(\rho\alpha_p)}{\partial t}}_{\text{Rate of change in } \phi} + \underbrace{\frac{\partial}{\partial x_j}(\rho u_j \alpha_p)}_{\text{Convection term}} = \underbrace{\frac{\partial}{\partial x_j}\left[\Gamma_p \frac{\partial \alpha_p}{\partial x_j}\right]}_{\text{Diffusion term}} + \underbrace{S_p}_{\text{Source term}} \qquad (5\text{-}47)$$

Under the homogenous flow assumption, particles are assumed to be small and light enough such that they follow the airflow particles and therefore the eddy diffusion coefficient Γ_p is assumed to be equal to that of the carrier phase.

Mass added to or removed from a single computational grid is dependent on the flow friction velocity parallel to the particle bed and the net mass balance across the cell boundaries. These mass changes are implemented as a source term to the above equation as follows.

5.6.1 Suspension-Saltation source term modelling

Particles transported by wind usually take three forms, surface creep, saltation or suspension. As mentioned in chapter 2, these processes are dependent on the particle physical properties such as size and density and on the strength of the wind velocity component parallel to the particle bed. The contribution from both suspension and saltation are incorporated into the transport equation as source terms. These source terms works as a source or sink of particle volume fraction to or from the flow field according to the value of individual source terms while the net source added to the transport equation is:

$$S_p = S_{Sus.} + S_{Sal.} \qquad (5\text{-}48)$$

Suspension Source term $S_{Sus.}$

Considering the convection term in the dispersed phase continuity equation:

$$\frac{\partial}{\partial x_j}(\rho \alpha_p u_p) = 0 \qquad (5\text{-}49)$$

Substituting (5-29) into (5-49) results in:

$$\frac{\partial}{\partial x_j}(\rho \alpha_p u_j) + \frac{\partial}{\partial x_j}(\rho \alpha_p u_{rel}) = 0 \qquad (5\text{-}50)$$

where the second term in the left hand side can be incorporated as a source term to influence the effect of particles in suspension as a function of the relative velocity and particle volume fraction. Where the relative velocity is approximated by equation (5-40), (5-41) or (5-42). Therefore, using the approximate relative velocity, the suspension source term can be rewritten as:

$$S_{sus.} = -\beta_{sus} \frac{\partial}{\partial X_j}[\rho \alpha_p u_{rel,j}] \qquad (5\text{-}51)$$

If the relative velocity above is estimated by equation (5-40), the suspension relative velocity has a constant value equal to the particle free falling velocity, which has only one component in the direction of gravity.

The relative velocity can also replaced by the diffusion velocity defined in (5-31) to be:

$$S_{sus.} = -\beta_{sus} \frac{\partial}{\partial X_j}[\rho \alpha_p (1-\alpha_p) u_{rel,j}] \qquad (5\text{-}52)$$

This form of the suspension source term assures that the source term will have a zero value when the continuous phase volume fraction is one and also zero when the particle volume fraction is one. The purpose of having zero source term

when the particle volume fraction is one is to ensure the volume fraction does not exceed one as a result of extra sources, which is unrealistic.

β_{Sus} is a constant that is found based on numerical experiments to be valid between 0.05 and 0.1, which will be shown in the following chapter.

Saltation Source term $S_{Sal.}$

A saltated particle zone usually has a layer thickness of a few centimetres from the ground. In this layer the suspension source term is modified to take into account the saltated particles. As mentioned in chapter 2, many authors have proposed empirical formulae to estimate the particle mass flow rate in the saltation zone based on field and wind tunnel studies, all of which relate the particle threshold velocity to the fluid surface friction velocity ratio as shown in Table 2-1.

A dimensionless friction-threshold velocity ratio is added to equation (5-52) to represent the effect of the saltation process. Thus the source term due to saltation becomes:

$$S_{sal.} = \beta_{Sal} \frac{\partial}{\partial X_j} \left[\rho \, \alpha_p \left(1 - \alpha_p\right) u_{rel,j} \, U_R^* \right] \tag{5-53}$$

where β_{Sal} is a constant varying between 0.15 and 0.6, as will be shown also in the following chapter.

The normalised friction velocity ratio term U_R^* is defined so that a relationship between the fluid friction velocity and the particle threshold velocity is formed. This term is introduced to the present model to avoid the need of an empirical expression to predict the particle mass flow rate and therefore the rate of the saltating particles involved in the calculation.

Since most of the empirical expressions of the particle mass flow rate, presented in Chapter 2, are based on raising the friction velocity to the power 3, six

different formulations of the normalised friction velocity U_R^* were investigated as shown in table 5-1.

Table 5-1: Normalised threshold friction velocity formulation.

Expression 1	$U_R^* = \frac{u_t^* - u^*}{u_t^*}$
Expression 2	$U_R^* = \frac{u_t^{*2} - u^{*2}}{u_t^{*2}}$
Expression 3	$U_R^* = \frac{u_t^{*3} - u^{*3}}{u_t^{*3}}$
Expression 4	$U_R^* = \frac{(u_t^* - u^*)^3}{u_t^{*3}}$
Expression 5	$U_R^* = \frac{(u_t^{*2} - u^{*2})(u_t^* + u^*)}{u_t^{*3}}$
Expression 6	$U_R^* = \frac{(u_t^{*2} + u^{*2})(u_t^* - u^*)}{u_t^{*3}}$

Considering a quartz particle of 0.25 [mm], diameter, and 2650 [kg/m^3], density, the relationship between U_R^* and the fluid friction velocity can have different trends based on the way U_R^* is calculated, figure 5.3.

All different forms of U_R^* have a zero value when the friction velocity equals the threshold value while it has a maximum value at zero friction velocity. Only model number 6 has a maximum value at a friction velocity of about 40% of the threshold value where the maximum ratio reach values higher than one.

These formulations have a simple physical interpretation. Referring to figure 5.3 and equation (5-53), the saltation source term is equal to zero when both friction and threshold velocities are equal which identifies the critical situation separating the deposition stages from erosion.

If the friction velocity becomes lower than the threshold value then a deposition process occurs. The maximum deposition rate happens at the lowest friction velocity, which is zero as shown in the figure 5.3. While a friction velocity higher than the particle threshold value represents erosion of particles from the ground.

Therefore, the effect of the saltation source term in a specific control volume is one of the following:

1. If the friction velocity is greater than threshold value then the source term will have a negative sign and therefore an erosion process will occur.

2. If the friction velocity is equal to threshold value then the source term will be equal to zero thus, neither erosion nor deposition can exist.

3. If the friction velocity is less than threshold value then the source term will have a positive sign and therefore a deposition process will occur.

Note that, since the particle transport equation represents only particles of the same physical properties, flow involving multiple particle sizes or densities needs individual transport equations to be solved, one for each different particle. Therefore, particles of different size or density will have different threshold velocities so that the source terms will have different values even for the same fluid friction velocity.

5.6.2 Erosion-deposition Algorithm

The particle volume fraction increases and decreases in a single control volume as a result of the net balance of the mass flow rate between the transport equation terms. A control volume is assumed to be full of particles and hence treated as a solid surface in the FAVOR algorithm if the following conditions are satisfied simultaneously:

1. If the particle phase occupies the entire control volume, ($\alpha_p = 1$).

2. Friction velocity drops below the particle threshold velocity, ($U^* < U_t^*$).

Since the highest particle volume fraction is impossible to achieve even in the real live case, a maximum bulk volume fraction is introduced. If the particle volume fraction exceeds the bulk value then the control volume is assumed to be full of particles.

In the present work the maximum bulk volume fraction was assumed to be 75% of the total volume of the cell, figure 5.4. If the above conditions are satisfied simultaneously in a single cell then that cell will be treated as a solid wall in the following calculations and the cell faces attached to the flow are represented by FAVOR as a solid interface boundary.

If the surface friction velocity on the interface boundary exceeds the particle threshold value, the adjacent blocked cells will reopen to the flow calculations in the following calculations.

5.7 Inlet Boundary conditions and wall roughness treatment

Boundary conditions for the dependent variables are required prior to the solution whilst the change in the solid interface boundary due to erosion-deposition process is treated after every change in that boundary.

Five types of boundary condition are required in this study namely: inflow, outflow, mirror boundary, solid wall and deposited particles surface. The solid wall is either a fixed solid wall, which can not be eroded, or a moving solid wall, which can be change according to the erosion-deposition process.

Inlet velocities, turbulent properties and the second phase inlet volume fraction must all specified at the computational domain inlet boundary.

There are two ways of specifying the inlet boundary condition. Firstly the values of the required variable are set uniformly throughout the entire inlet boundary.

In this case each variable takes a specific value, which will be the same at every inlet grid point.

Secondly, non-uniform inlet boundary conditions, where the independent variables have different values at every grid point. In the present study, the second case is implemented to specify the inlet boundary of both the continuous phase inlet velocity profile and the inlet particle concentration profile.

Since the flow of interest in the present work is wind blown particles in the atmospheric boundary layer, it is general practice to describe the wind velocity profile in the logarithmic form presented in equation (2-12).

$$u(y)=\frac{u^{\bullet}}{\kappa}\ln(\frac{y}{y_o})$$

This equation is employed to specify the inlet boundary condition for the velocity profile where the wind velocity tends to zero near the ground and 10 m/s at 10 metre above the ground. The modified wind profile, equation (2-13), can be employed instead if the effect of the saltated particles needs to be incorporated from the domain inlet boundary.

5.7.1 Dispersed phase inlet concentration profile:

In contrast to the wind profile, particle concentration decreases with the height above the ground. The formula suggested by Anderson and Hallet (1986), equation (2-13), is employed in the present study to calculate the particle concentration profile:

$$c=c_0\left(\frac{y}{y_0}\right)^{-\left(\frac{u_s}{\kappa u^{\bullet}}\right)}$$

It is clear that both velocity and particle concentration profiles at the inlet boundary are dependent on the friction velocity, surface roughness and height from the ground. The latter are not affected by the calculations.

The flow over a flat surface retains the inlet profile throughout the computational domain. This is achieved through the treatment of surface roughness and wall shear stress to predict a friction velocity, which gives the required profiles for fully developed flow.

5.7.2 Particle surface roughness

Wind and concentration profiles are significantly affected by the surface roughness. Modelling the boundary layer including the effects of surface roughness can be achieved through modification on the wall shear stress. Cebeci and Bradshaw (1977) modified the law of the wall to included the effect of surface roughness as follow:

$$\frac{u\,u^*}{\tau_w/\rho}=\frac{1}{\kappa}\ln\left(E\frac{\rho u^* y_o}{\mu}\right)-\Delta B \qquad (5\text{-}54)$$

where ΔB is a roughness function that quantifies the shift of the intercept due to roughness effects. In general it depends on the roughness. For a surface covered by uniform sand particles ΔB is correlated to the non-dimensional roughness height:

$$K_S^+=\frac{\rho K_S u^*}{\mu} \qquad (5\text{-}55)$$

where K_S is the physical surface roughness height. In this study it has been taken to be equal to the particle diameter as suggested by Bagnold (1941) and confirmed by other recent experimental studies, [Iversen (1981), Kind (1990), Pay and Tsoar (1990)] .

It has been observed that there are three different ranges of K_S^+ where ΔB is defined analytically by Cebeci and Bradshaw.

1. If $K_S^+ < 2.25$ then the flow is hydrodynamically smooth and

$$\Delta B=0 \qquad (5\text{-}56)$$

2. If $2.25<K_S^+<90$ then the flow is in a transitional stage some times described as semi-rough flow. In this range:

$$\Delta B=\frac{1}{\kappa}\ln\left[\frac{K_S^+-2.25}{87.75}+C_{K_S}\,K_S^+\right]\times\sin\left\{0.4258\left[\ln\left(K_S^+-0.811\right)\right]\right\} \qquad (5\text{-}57)$$

3. If $K_S^+>90$ then the flow is assumed to be fully rough. In this case:

$$\Delta B=\frac{1}{\kappa}\ln\left[1.0+C_{K_S}\,K_S^+\right] \qquad (5\text{-}58)$$

where C_{K_S} is a roughness constant with a value 0.5 for uniform sand surface, increases to1.0 for non-uniform sand surfaces.

In the present study, the effect of the saltating particles is incorporated as an extra surface roughness involved into the shear stress according to the above modification to the logarithmic wall law.

5.7.3 Friction velocity

The friction velocity has a dominant role in the initiation of the particle movement and deposition and on the shape of the vertical wind profile. It represents the shear stresses acting on the surface due to wind forces. Therefore, for each individual particle there is a critical friction velocity which will govern whether movement is initiated or halted. This critical wind friction velocity is commonly known as the particle threshold velocity.

Wind friction velocity is defined in terms of the wall shear stress as:

$$u^*=\sqrt{\frac{\tau_w}{\rho}}$$

Where the wall shear stress is defined in for both laminar and turbulent boundary layer. (see Appendix B).

5.8 Solution algorithm and implementation remarks

Models discussed above have been implemented into an existing CFD solver, SOFIE (Simulation Of Fire In Enclosures), which is developed originally by Dr. P. Rubini at Cranfield University for fire prediction in compartment, Rubini (1997). SOFIE is based on a finite volume differencing approach for incompressible viscous flow in a general curvilinear co-ordinate system.

The isothermal version of SOFIE solves the flow continuity and momentum equations with the $k-\varepsilon$ two-equation turbulent model. This has been modified to incorporate the two-phase flow models, mixture and homogenous models, coupled with the FAVOR technique.

The general form of the governing equations is identical for both mixture and homogenous models. These equations are solved for the mixture flow properties when the mixture model is used. For the homogenous model, the transport equations are solved for the continuous flow phase variables.

The code is implemented such that the homogenous model appears as a special case of the mixture model.

The numerical method employed in this study consists of the following steps:

1. Guess initial values for all variables.

2. Solve the continuous phase flow field, velocities and pressure field.

   For the mixture model calculation, the solution will be for the mixture flow field using the mixture properties such as mixture density and mixture viscosity. If the homogenous model is chosen, the same set of equations can be solved but for the continuous phase flow field only.

3. Solve other scalar transport equations such as turbulent kinetic energy k, turbulent dissipation ε and second flow phase volume fraction α_p.

4. With the latest solved variables, other derived variables such as surface shear stress, viscosity, friction velocity and particle diffusion velocity are calculated.

The sequence of steps 1 to 4 is repeated until the convergence criterion is achieved. When the FAVOR model is activated, a transient solution must be used and between consecutive time-steps the FAVOR model subroutine is called. Due to the particle erosion-deposition process, the solid interface boundary separating the flow field from the deposited particles may change. The solution achieves the steady state when the interface boundary does not change with further iterations.

A converged solution following the above sequence has to be satisfied for every time step. Then calculations are carried out until the required number of time steps is reached or the erosion-deposition process has reached a steady state.

5.9 Closure

Numerical models for Eulerian two-phase flow were presented in this chapter with the necessary constitutive equations required to close the system of partial differential equations. The models were discretised and implemented into the CFD code, SOFIE, based on a finite volume approach and applied to a novel application involving drifting particles such as sand or snow, around obstacles in two and three dimensional computational space.

A new form of the governing equations were derived, both for the homogenous and mixture models, by introducing the area and volume fraction components in a simple and efficient way so that the FAVOR technique can be coupled with the solution to track the interface boundary. FAVOR was implemented and used as a mean of representing solid geometries within a fixed computational grid. The coupling between the two-phase flow models and FAVOR provided an efficient and relatively simple solution algorithm to represent a general shaped solid interface boundary separating the flow field from regions occupied by the deposited particles.

Moreover, an algorithm for the erosion-deposition process was introduced, which enabled the interface boundary to contract or grow as a response to the changing flow field. The different modes of particle transport, such as suspension and saltation, were modelled and added to the particle transport equation as a contribution to the source term.

By considering a small relative velocity between the fluid and particle velocities, three different equations were presented and used to approximate the relative velocity. The equations were derived from the general multi-phase flow governing equations. The necessary initial and boundary conditions were discussed with the proper implementation and the solution procedure was outlined.

In the following chapter, these models will be analysed to assess their performance in the applications of interest and their dependency on the different physical and numerical controlling parameters. Thus, the limitations and capabilities of each model can be identified and the most suitable model configuration can be achieved prior to validation against the field and wind tunnel measurements, which is the core of Chapter 7.

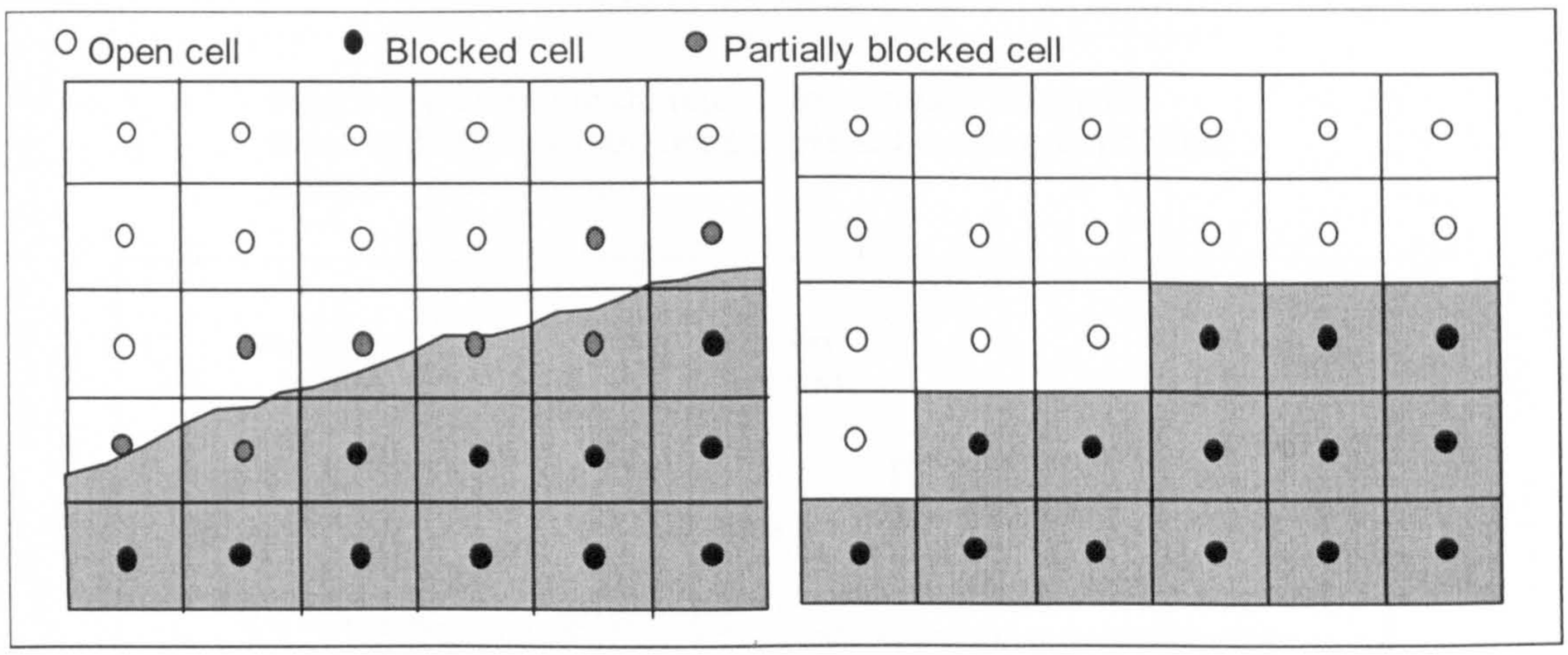

Figure 5.1: FAVOR treatment of control volumes containing deposited particles. Grey cells are of high particle volume fraction and white cells are of high air volume fraction. Cells partially filled contain both phases where the summation of the phase's volume fraction must be one.

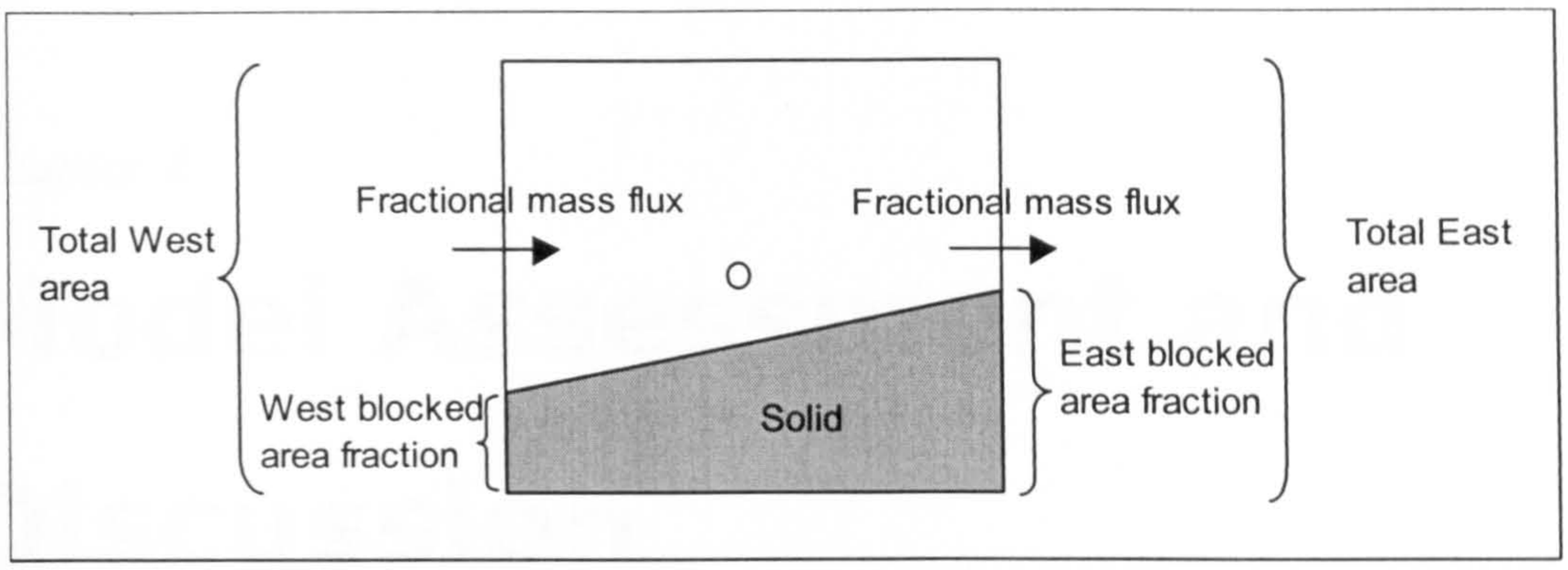

Figure 5.2: FAVOR treatment of control volume partially filled by solid phase.

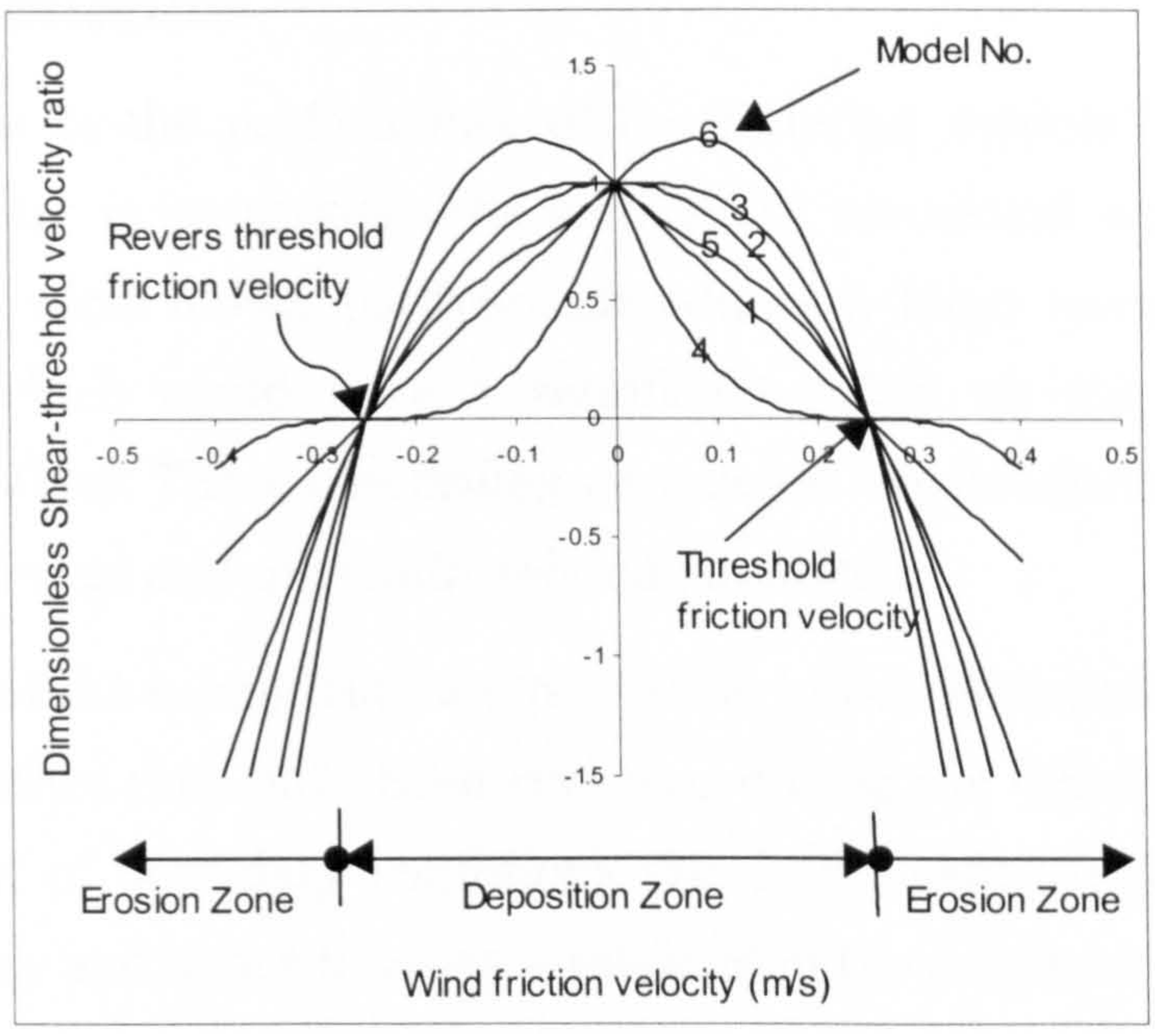

Figure 5.3: Different dimensionless models for shear threshold velocity ratio used to predict erosion/deposition saltation source term.

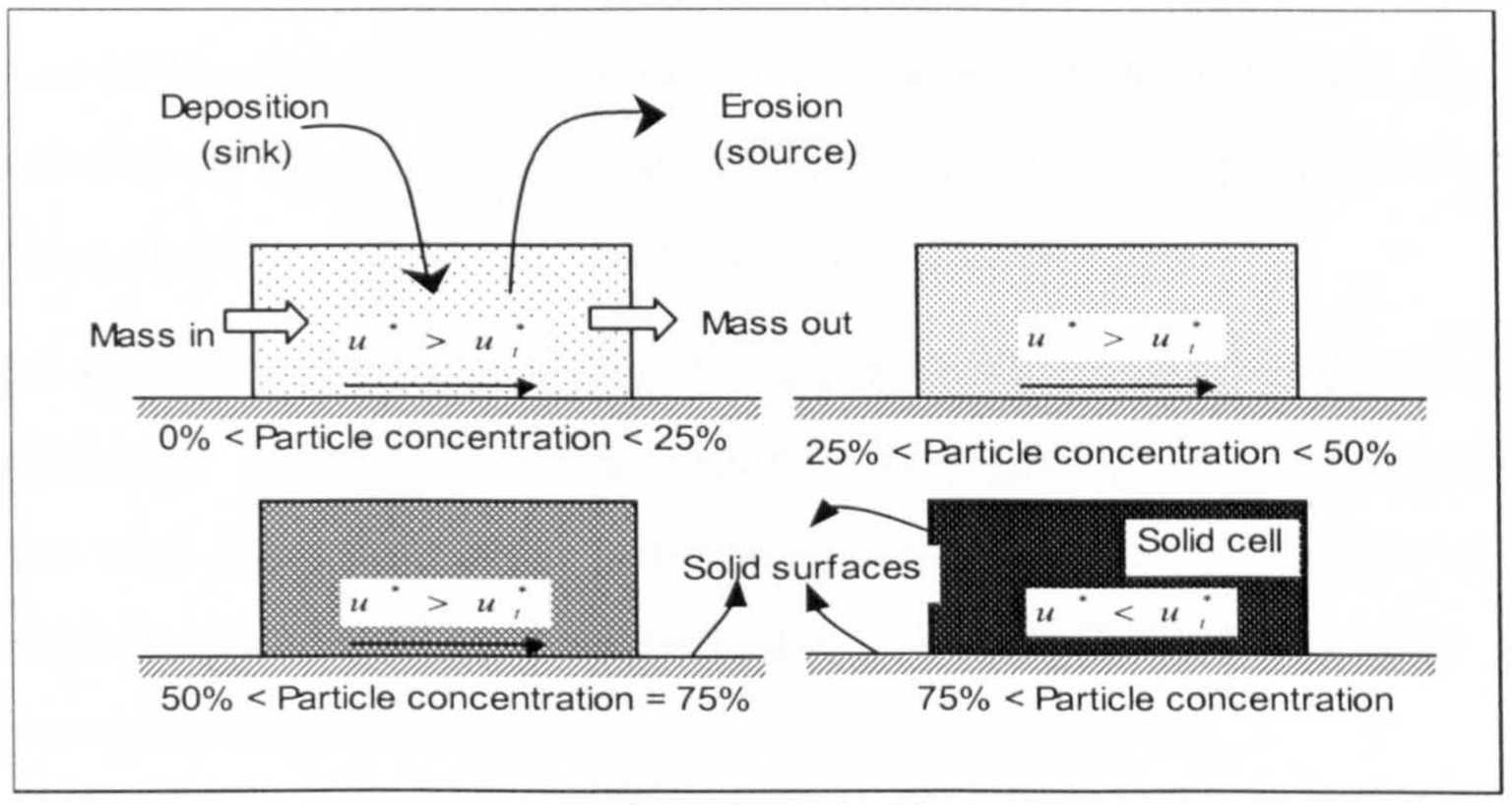

Figure 5.4: Stages of a cell blocked by particles.

Chapter 6

Model Assessment and Discussion

6.1 Introduction

An assessment of the performance of the Eulerian models introduced in the previous chapter is presented. The complexity associated with the numerical simulation of wind blown particles introduces a large number of modelling parameters, which could have a significant effect on the accuracy of the predicted variables. These controlling parameters are categorised into two main sections; numerical and physically related parameters.

The majority of the numerical parameters have been eliminated from the scope of this study since they have been reviewed during the development of SOFIE. The treatment of boundary conditions and grid quality remain novel to this particular study and hence have been retained in the assessment.

The assessment of the physical controlling parameters involves numerical modelling of the different modes of particle transport such as suspension and saltation. Surface roughness, the erosion-deposition process, the physical properties of the transported particles, threshold conditions and the inlet and initial conditions are all considered in the assessment of the model's controlling parameters and hence they are investigated in this chapter.

Table 6-1 shows a sensitivity study of the parameters considered in this chapter. The individual testing of each separate parameter is computationally an expensive and laborious task. Therefore, only the most influential of these parameters is considered in this assessment. The work in this chapter is divided in to several sections as follows:

- Section 6.2 presents the wind and particle concentration profiles for different inlet conditions and surface roughness used to maintain fully developed flow over a flat surface.
- Section 6.3 covers the steady state flow field at a solid wall placed on the flat surface perpendicular to the flow direction.
- Section 6.4 compares both homogenous and mixture models for flow around a solid wall in order to identify the relative limitations and capabilities of each model.
- Section 6.5 contains the introduction of the FAVOR model as a means of representing the deposition profile at a solid interface boundary.
- Section 6.6 presents the dependence of the model on the grid resolution.
- Sections 6.7 and 6.8 assess the modelling of the suspension and saltation modes of particle movement in the flow.
- Sections 6.9 and 6.10 examine the effect of different inlet friction velocities and turbulent intensities on the solution.
- Section 6.11 presents an assessment of the models for different wall geometries.
- Section 6.12 presents a demonstration of the models for simulation of a 3-D scenario.
- Section 6.13 includes a general discussion and comments on the performance, limitations and capabilities of the model.

6.2 Wind profile over a flat surface

The main emphasis of the current work is the simulation of the movement of sand particles in the desert. In order to replicate the physical conditions for this, the inlet boundary condition for velocity and particle concentration must be defined as a profile reflecting the conditions of the atmospheric boundary layer. This profile can be easily established at the inlet boundary for a given friction velocity and surface roughness using the equations defined in Chapter 2.

The shape of this profile must be retained within the computational domain if the flow is to be considered as fully developed. It has been found however that these profiles are dependent on the calculation of the wall shear stress. The shear stress was shown to be dependent on two physical parameters; wall effect and surface roughness (Chapter 5).

The numerical prediction of the flow field from different inlet wind profiles is compared with the logarithmic wind profiles over a flat surface. The two main parameters responsible for the shape and strength of the wind profile are surface roughness and the friction velocity at which the mean wind velocity is defined. These are constant at the inlet boundary whilst the surface roughness is the only constant parameter within the computational domain. The friction velocity within the computational domain is calculated based on the numerical prediction of the wall shear stress and thus the wind profile can change according to both wall effect and surface roughness.

Table 6-2 shows 15 different combinations of the inlet friction velocity and the wall surface roughness, 5 friction velocities and three different surface roughness values. The dimensions of the computational domain were set as 10 metres length and 2 metres height. The domain was divided into 100x50 grid cells in the axial and vertical direction respectively.

The grid was uniformly distributed in the axial direction giving a resolution of 0.1 metres. The distribution in the vertical direction was biased towards the ground surface to assure better resolution of the predicted variables inside the flow boundary layer.

Figure 6.1, shows a comparison between the numerical and the logarithmic wind profiles at a vertical cross section 5 metres downstream from the inlet boundary. For a constant surface roughness, the increase in the inlet friction velocity results in an increase in the strength of the wind profile. This effect is replicated with a decrease in surface roughness i.e. where the flow has less resistance from the surface. The discrepancy observed between the predicted and the logarithmic profiles near the surface is a result of the turbulent flow and the development of the boundary layer, which is ignored in the logarithmic profile equation.

Numerical prediction of the particle concentration in terms of the particle volume fraction is shown in figure 6.2. It shows that as the surface roughness increases, the particle concentration near the surface also increases. Physically this can be interpreted to mean that wind erosivity increases (the ability of the wind to erode particles from the ground) as surface roughness increases.

The numerical prediction of the particle concentration values far from the ground is in a good agreement with the profiles calculated using equation (2.11). The particle concentration shows an over prediction near the surface as compared with equation (2.11), which is a direct influence of the deviations in the velocity profile predicted within the boundary layer.

Figure 6.3, shows the particle concentration throughout the computational domain to clarify the drifting process behaviour predicted by numerical model. This can be considered as a preliminary assessment of the source terms added to the particle transport equation. Suspension and saltation source terms are set roughly in this case.

Since the particles are eroded from the surface at a constant rate, the source term added to the equation for cells adjacent to the surface bed is constant. Particles are then transported with the flow direction to the downstream cell, which results in an increase in the concentration near the surface progressively further downstream. This occurs because of the extra particles entering the downstream cells through their upstream faces as shown in figure 6.4.

Assuming that the flow is fully developed, the wind profile and particle concentration should be uniform across the flow domain. If the surface friction velocity is higher than the threshold value then the source term will have negative values representing an erosion process. On the other hand, the particle concentration near the surface will increase when the surface friction velocity drops to values lower than the threshold value where the source term is positive.

Table 6-1: Sensitivity study sample sheet

Case Study ==> Solid Fence										
Boundary Condition			*Run Index*	1a	1b	1c	1d	1e	1f
	Ustar			0.2	0.22	0.25	0.3	0.4	0.5
	Turbulent Int.			1	1	1	1	1	1
	Char. Length			0.0254	0.0254	0.0254	0.0254	0.0254	0.0254
	U at 10			4.4928	4.9421	5.6161	6.7393	8.9857	11.2321
	tke			0.0030	0.0037	0.0047	0.0068	0.0121	0.0189
	ted			0.0154	0.0205	0.0301	0.0520	0.1232	0.2406
Grid									
x sections									
		section 1	length (m)	1	1	1	1	1	1
			cells	40	40	40	40	40	40
			ratio	0 - 1.05	0 - 1.05	0 - 1.05	0 - 1.05	0 - 1.05	0 - 1.05
		section 2	length (m)	0.002	0.002	0.002	0.002	0.002	0.002
			cells	3	3	3	3	3	3
			ratio	0 - 0	0 - 0	0 - 0	0 - 0	0 - 0	0 - 0
		section 3	length (m)	2.54	2.54	2.54	2.54	2.54	2.54
			cells	80	80	80	80	80	80
			ratio	1.0 - 1.03	1.0 - 1.03	1.0 - 1.03	1.0 - 1.03	1.0 - 1.03	1.0 - 1.03
		Total	length (m)	3.542	3.542	3.542	3.542	3.542	3.542
			Total Cells	123	123	123	123	123	123
y sections									
		section 1	length (m)	*0.0254*	*0.0254*	*0.0254*	*0.0254*	*0.0254*	*0.0254*
			cells	30	30	30	30	30	30
			ratio	0 - 0	0 - 0	0 - 0	0 - 0	0 - 0	0 - 0
		Section 2	length (m)	*1.0746*	*1.0746*	*1.0746*	*1.0746*	*1.0746*	*1.0746*
			cells	30	30	30	30	30	30
			ratio	1.0 - 1.02	1.0 - 1.02	1.0 - 1.02	1.0 - 1.02	1.0 - 1.02	1.0 - 1.02
		Fence Height ==>		0.0254	0.0254	0.0254	0.0254	0.0254	0.0254
		Total	length (m)	1.1	1.1	1.1	1.1	1.1	1.1
			Total Cells	60	60	60	60	60	60
z sections									
		Section 1	length (m)	1	1	1	1	1	1
			cells	1	1	1	1	1	1
			ratio	0 - 0	0 - 0	0 - 0	0 - 0	0 - 0	0 - 0
		Total	length (m)	1	1	1	1	1	1
			Total Cells	1	1	1	1	1	1
Particle									
	Diameter			4.90E-05	4.90E-05	4.90E-05	4.90E-05	4.90E-05	4.90E-05
	Density			3990	3990	3990	3990	3990	3990
	Threshold velocity			0.215	0.215	0.215	0.215	0.215	0.215
	Suspension constant			0.08	0.08	0.08	0.08	0.08	0.08
	Sultation constant			*0.25*	*0.25*	*0.25*	*0.25*	*0.25*	*0.25*
Surface roughness									
	hieght			0.0001	0.0001	0.0001	0.0001	0.0001	0.0001
	constant			1	1	1	1	1	1
Models									
	Drift velocity			2	2	2	2	2	2
	Saltation			3	3	3	3	3	3
	Deposition			1	1	1	1	1	1
	Erosion			1	1	1	1	1	1

Table 6-2: Runs for different inlet friction velocity and surface roughness.

U* [m/s]	Roughness Height A in [m]	Roughness Height B in [m]	Roughness Height C in [m]
0.2	1.0e-3	1.0e-4	1.0e-5
0.296	1.0e-3	1.0e-4	1.0e-5
0.374	1.0e-3	1.0e-4	1.0e-5
0.416	1.0e-3	1.0e-4	1.0e-5
0.62	1.0e-3	1.0e-4	1.0e-5

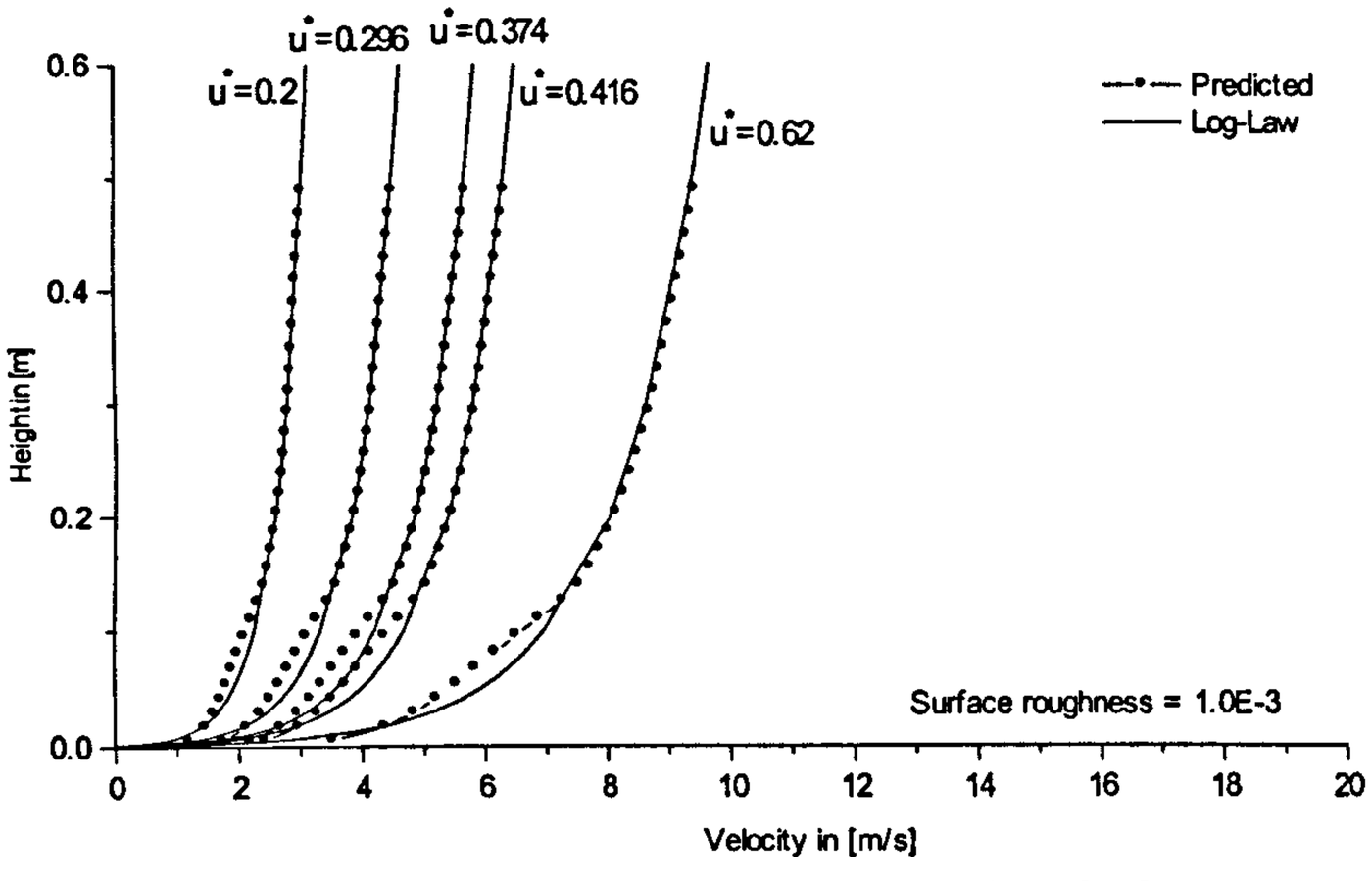

Figure 6.1a: Numerical wind profiles compared to the logarithmic profiles at different inlet friction velocities and a surface roughness of 1e-3 [m].

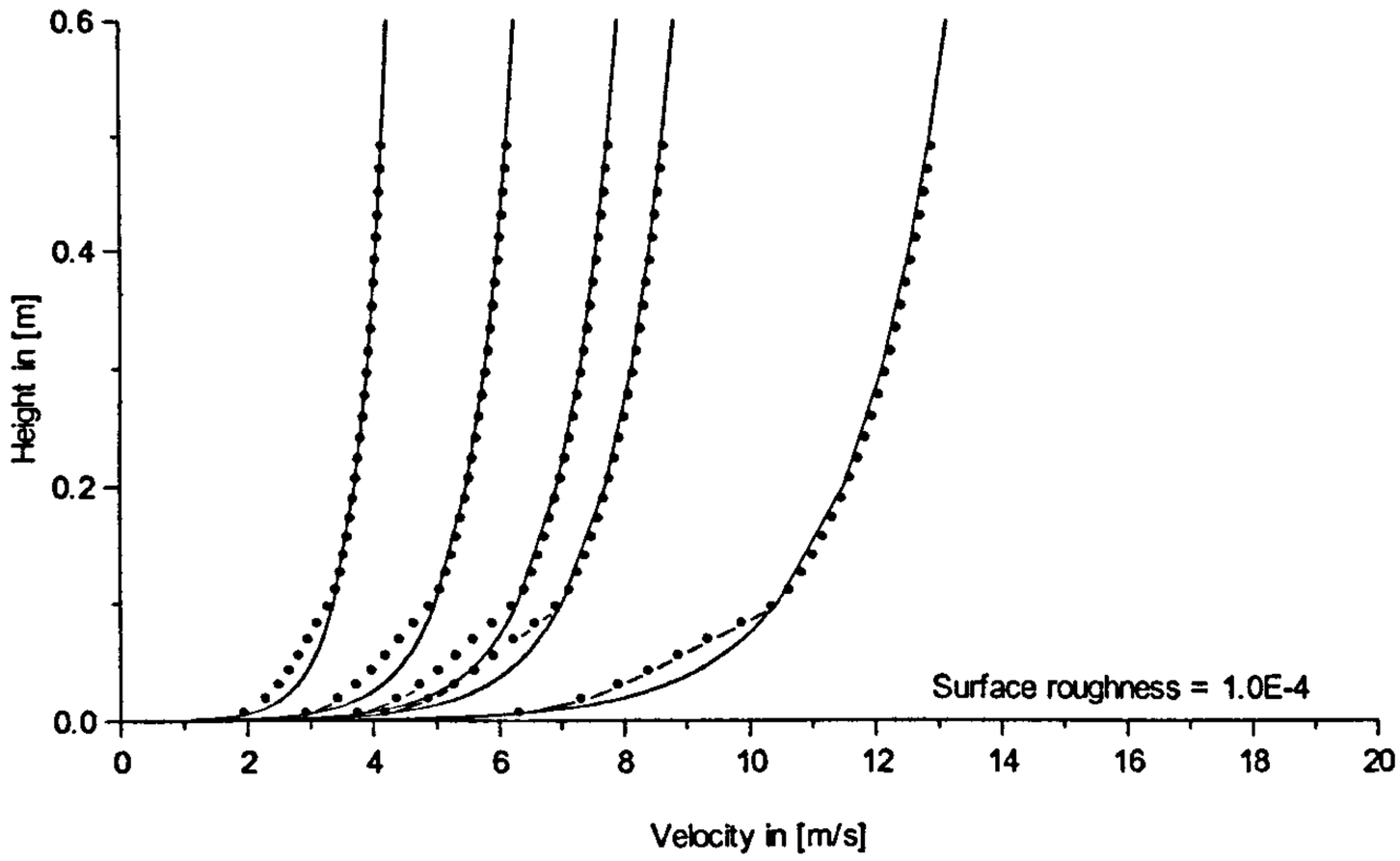

Figure 6.1b: Numerical wind profiles compared to the logarithmic profiles at different inlet friction velocities and a surface roughness of 1e-4 [m].

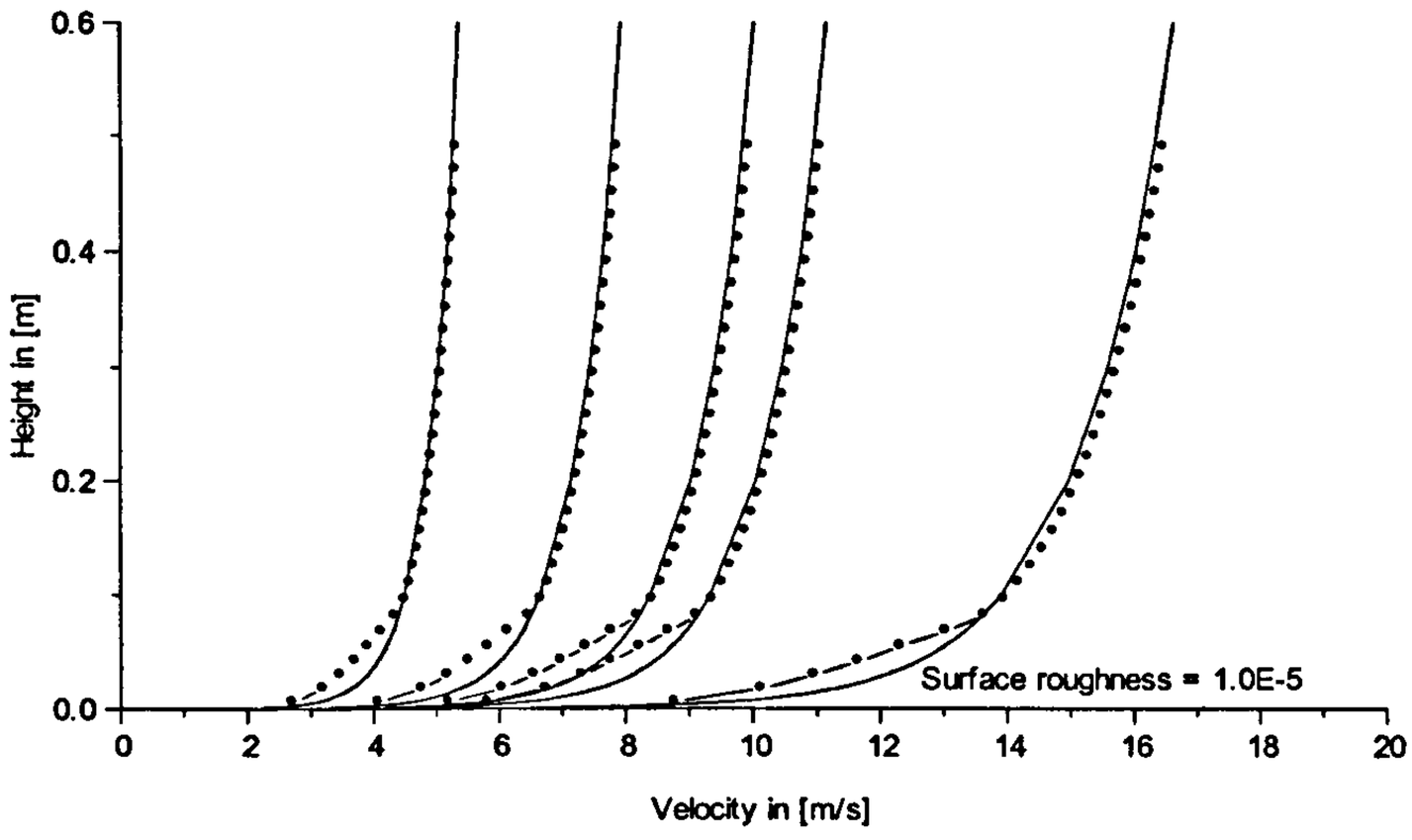

Figure 6.1c: Numerical wind profiles as it compared to the logarithmic profile at different inlet friction velocities and a surface roughness of 1e-5 [m].

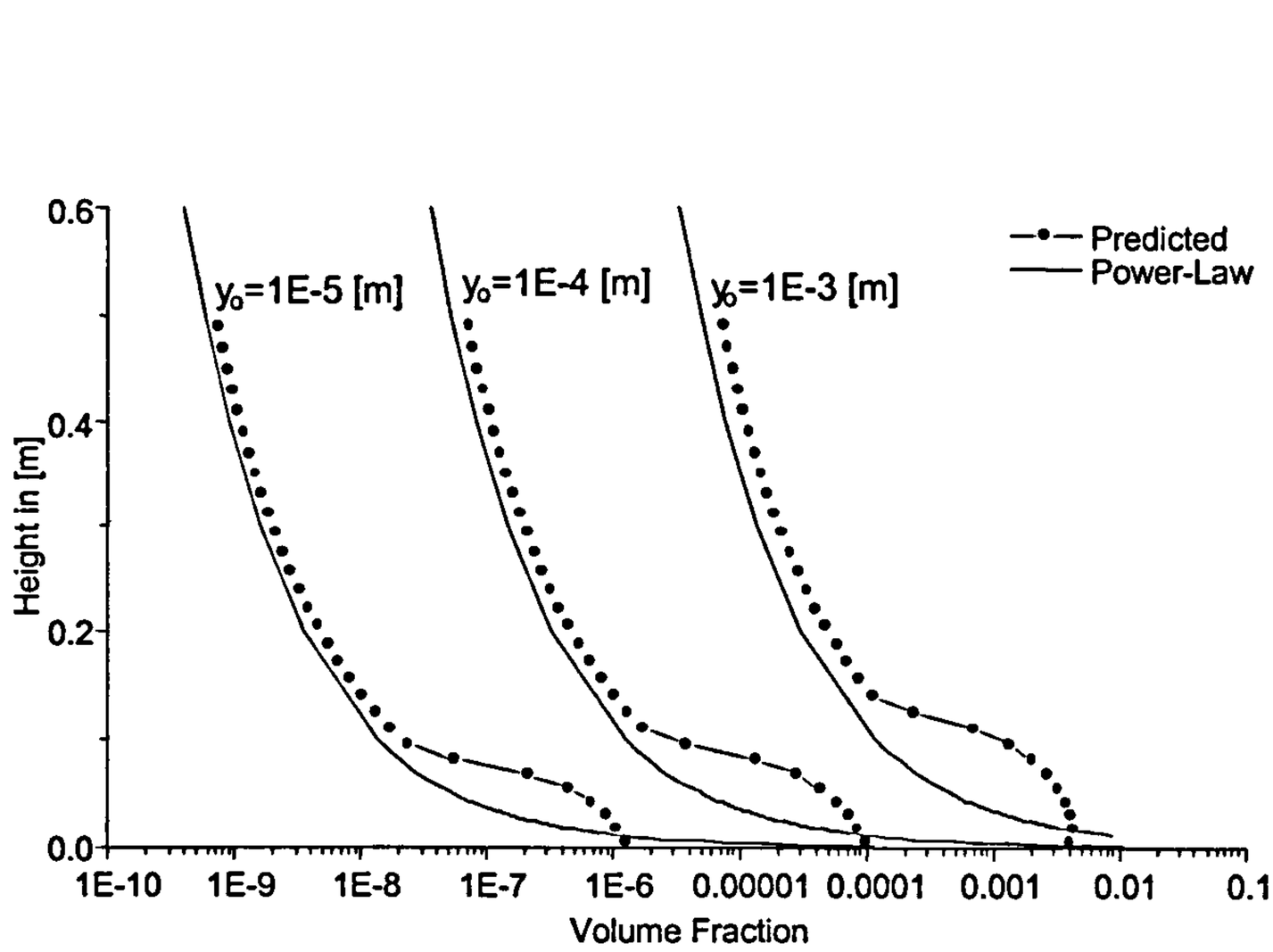

Figure 6.2: Numerical particle concentration profiles compared to the empirical expression for different surface roughness.

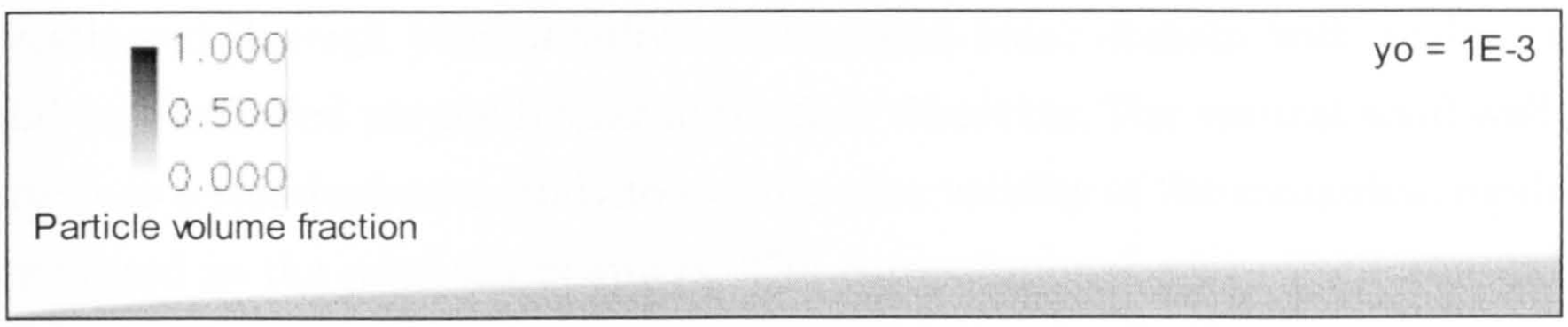

Figure 6.3: Numerical prediction of the particle concentration along a flat surface for different surface roughness.

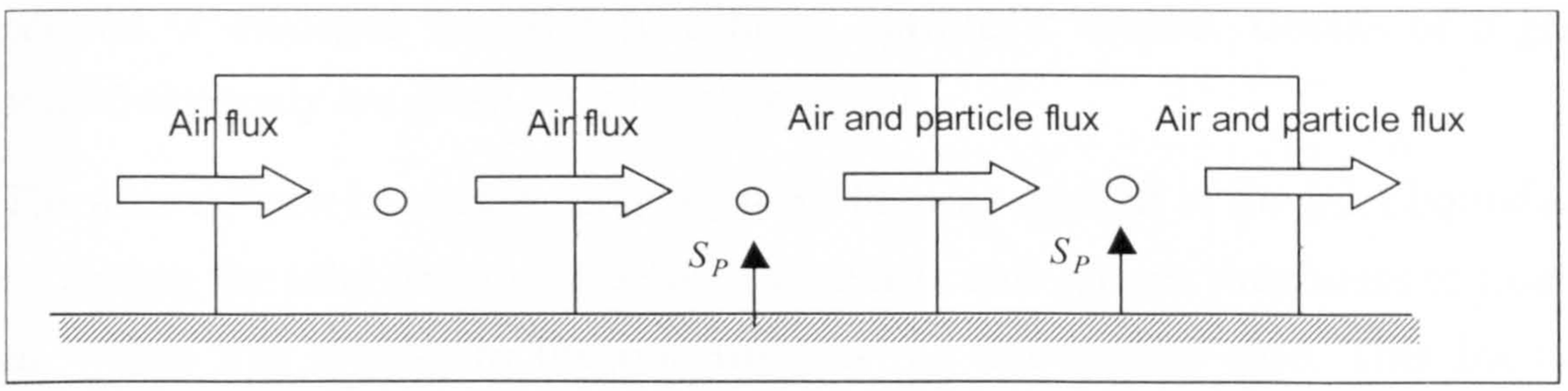

Figure 6.4: Sketch showing effect of the eroded particles on the mixture flux across the cell boundaries.

6.3 Steady state flow field at a solid wall

The previous section demonstrated the capability of the model in simulating a fully developed flow over a flat surface with a desired wind and particle concentration profile. In this section the performance of the model is further investigated through consideration of the same basic domain with an interior solid wall included perpendicular to the flow direction. The vertical solid wall is chosen as a standard case study to examine the validity of the numerical models introduced in the previous chapters. The computational space is chosen to be identical to the wind tunnel working section used by Iversen (1983). The dimensions of the computational space in terms of wall height H is shown in figure 6.5.

The starting point was consideration of the effects and limitations of the controlling parameters of the model; the initial set of the physical and numerical controlling parameter values are shown in table 6-1, set B. At this stage there are no specific guidelines under which this initial set-up was chosen. The number of numerical experiments required to understand the behaviour of the model and then calibrate these controlling parameters for more practical applications, is only a matter of experience.

The domain was divided into a relatively fine mesh to assure a degree of accuracy for the predicted variables. The minimum control volume size was defined to be 0.01m long and 0.001m high. This grid size might need to be refined or enlarged in order to achieve optimistic results. Details of a grid sensitivity study are given later in this chapter.

The atmospheric boundary layer wind profile was applied at the inlet boundary by setting the inlet friction velocity to 0.22 m/s and surface roughness to 1.0e-4 m, which was similar to the one used in the flat surface case. This friction velocity was set to be equivalent to the threshold value of a spherical glass particle of density 3990 kg/m^3 and diameter 4.9e5 m.

The turbulent properties at the inlet boundary were set in terms of the turbulent intensity and length scale. The turbulent intensity in the atmospheric boundary layer wind tunnels can vary between 0.5 % and 10%. A starting condition of 1%

turbulent intensity was chosen. A detailed analysis of the effect of inlet turbulent intensity on the solution accuracy will be discussed later in this chapter. The solid wall height was chosen as the inlet turbulent length scale.

Deposition of particles around an obstacle is highly dependent on the flow structure around that obstacle and the particle volume fraction. The homogenous model was used in this case, where the flow field is predicted by solving the continuous phase governing equations while the particle volume fraction is predicted by solving the particle transport equation with the particle suspension source term only.

Figures 6.6a and b show the wind velocity vector and the streamlines around the wall. Two main recirculation eddies are generated around the wall, A and B, an upstream small eddy with a separation point close to the wall 'A' and larger downstream eddy with a reattachment point far downstream 'B'.

At the separation and reattachment points, the flow velocity drops to values such that the friction velocity becomes lower than the particle threshold value. Therefore, these points are expected regions of high particle concentration and can give an important indication of the starting area of the deposition process.

The dotted line in figure 6.6b represents the stagnation points, which are the points where the flow changes its direction. Further down wind, at the point when the dashed line reaches the ground, the flow will be completely reattached to the ground and no more separation or reverse flow occurs unless there is another topographical change such as another wall.

A series of investigations were undertaken to establish the dependence of these points on the wall height and inlet friction velocity. Initially the wall height was fixed and the inlet friction velocity varied, then the wall height was varied with a single inlet friction velocity.

The vertical wind profiles at different distances from the wall, see figure 6.6b, are shown in figure 6.7 but for different inlet friction velocities. It is clear from the figure that all the profiles meet at the reverse flow points, it is thus assumed that the size of the eddies around the wall is independent of the inlet wind strength at least within the range of the friction velocities examined.

The same effect is not observed with variation of wall height, as shown in figure 6.8a. Both the separation and reattachment points move outward and inward respectively according to the eddy size. A high wall generates a larger eddy with stagnation points distant from the wall while a shorter wall generates smaller eddies with a stagnation point closer to the wall. Figure 6.8b shows the surface velocity profiles just above the ground in the axial direction. It shows a negative velocity on both sides of the wall resulting from the eddy flow; this negative velocity is small in front of the wall and large behind it. Moreover, it is clearly shown that there is a large disturbance to the flow from the high wall, which is reduced as the wall height decreases. As a result, the reattachment points, shown as solid circles in the figure move further downstream as the wall height increases.

Figures 6.9 and 6.10 show a significant change in the turbulent kinetic energy as a result of the presence of the wall. The change in the kinetic energy is proportional to the change in both inlet friction velocity and wall height. Maximum energy production occurs at a distance above the ground in the flow zone separating the flow affected by the wall from the undisturbed flow. The location of the maximum kinetic energy moves upward as the wall height increases while the maximum value increases with the increase in both inlet wind profile and wall height.

Turning attention to the particle concentration as expected a high concentration of particles is found in the weak regions around the wall as shown in figures 6.11 and 6.12. Consideration of the suspension source term alone in the particle transport equation demonstrates that the volume fraction increases as the inlet friction velocity decreases. This provides an explanation for the particle settlement due to gravity forces only, which are included into the suspension source term. For high axial wind velocity, the drag forces applied on the particle surface will reach values much higher than the particle resistance forces. Therefore, particles will not settle on the surface but drift due to the high drag with the flow. Slower flow has lower drag forces and at the weak regions around the wall the settling force exceeds the drag and results in an increase in the particle concentration.

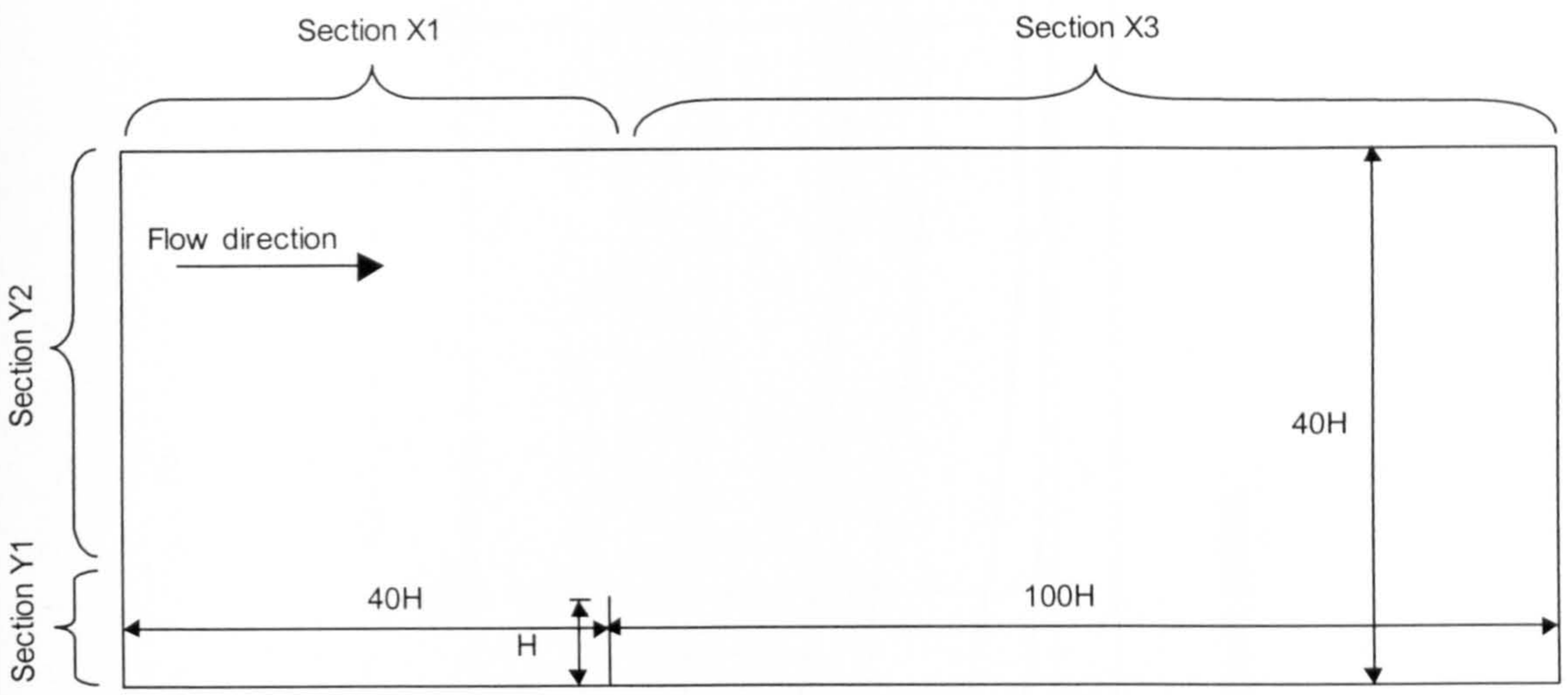

Figure 6.5: The computational domain in terms of the wall height H divided in to different grid distribution sections. (Sketch not to scale).

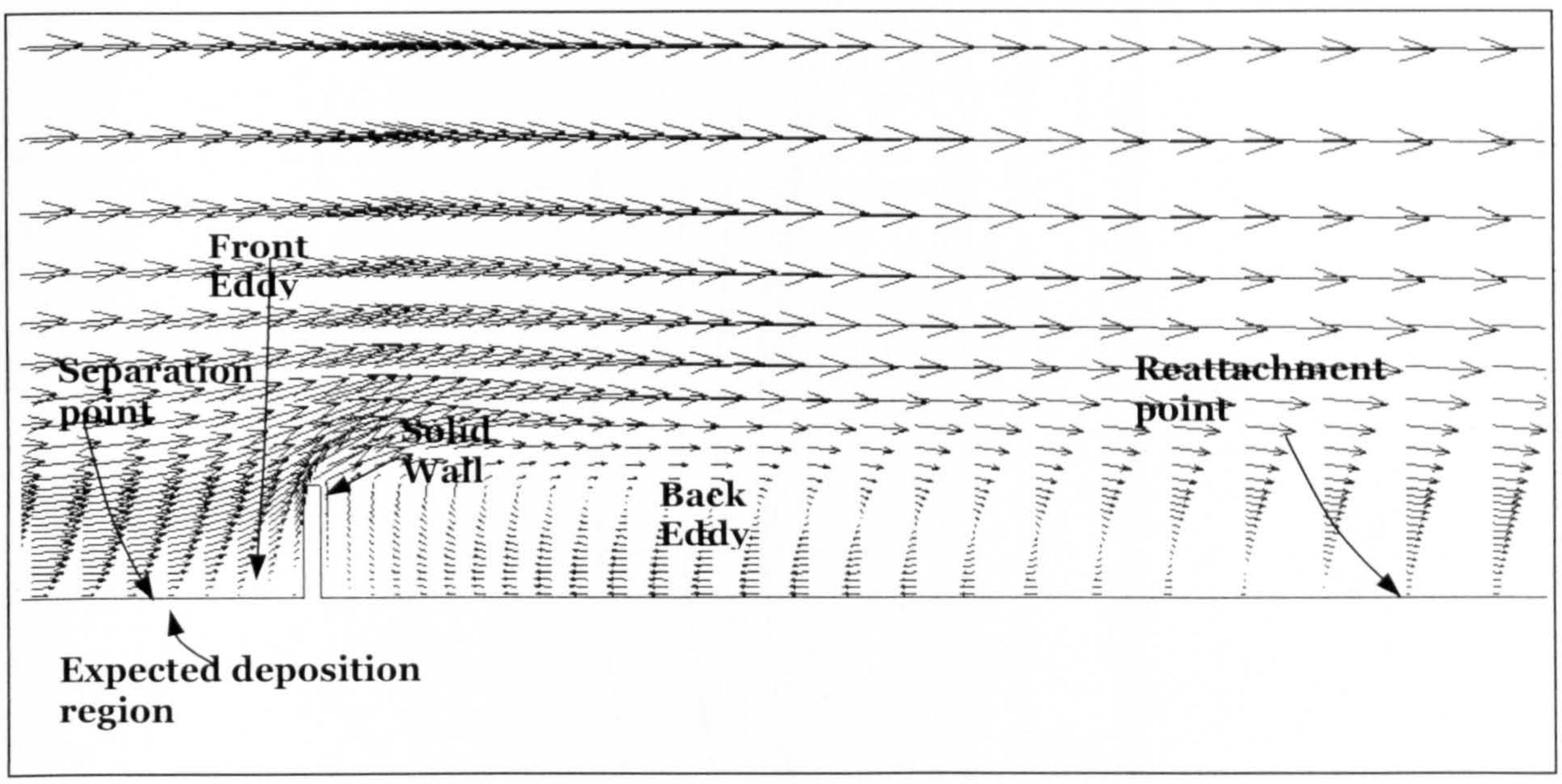

Figure 6.6a: Velocity vectors around solid wall showing the separation and reattachment points.

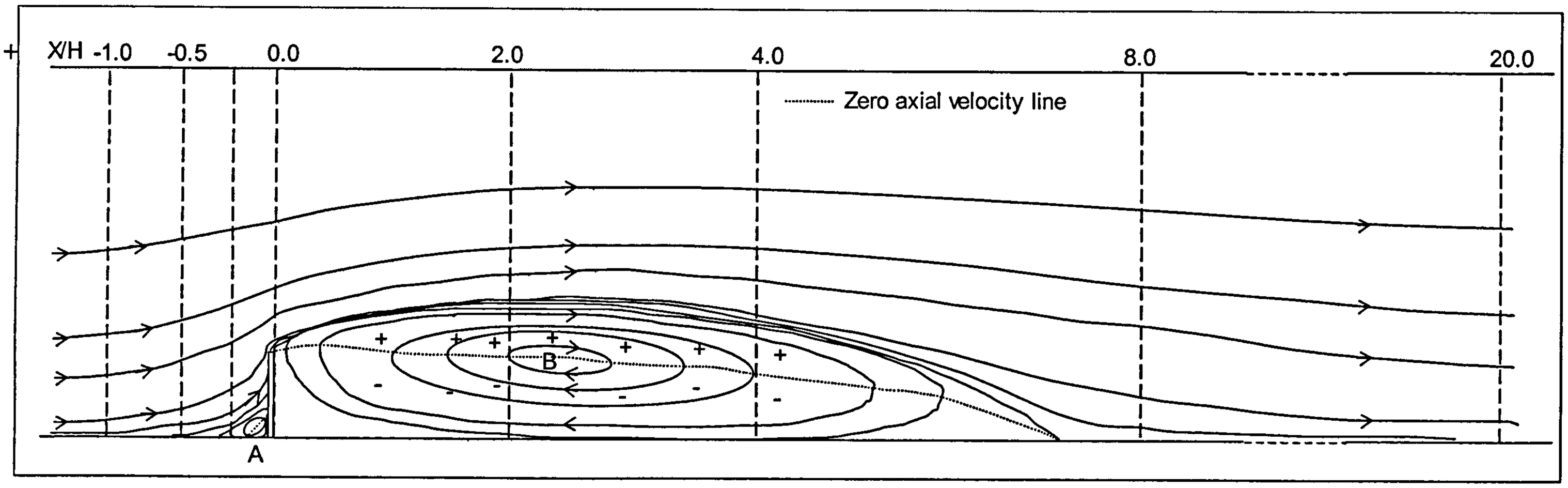

Figure 6.6b: Streamlines around solid wall showing the separation and reattachment points.

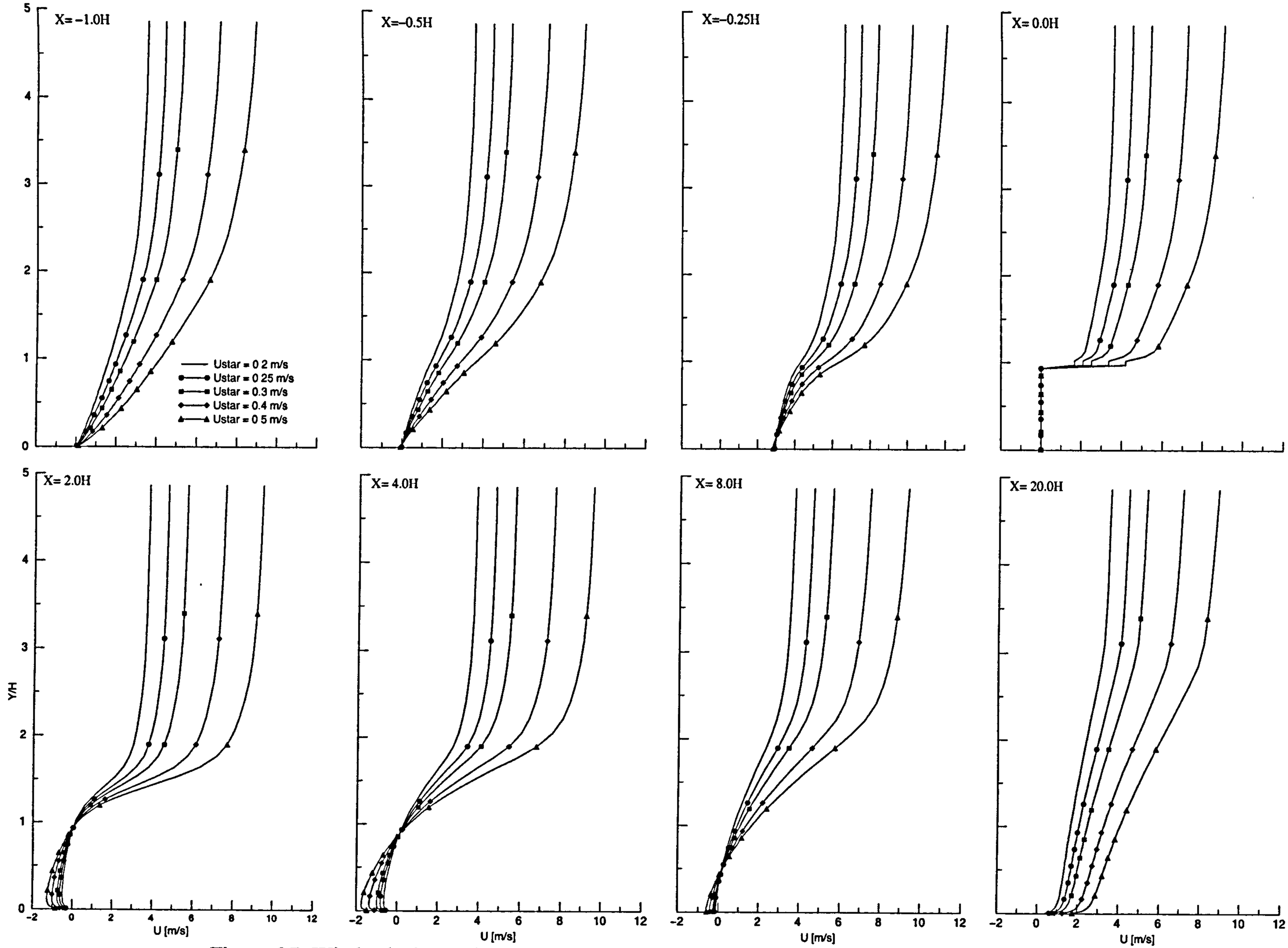

Figure 6.7: Wind velocity profile at different distances from the solid wall with variable inlet friction velocity.

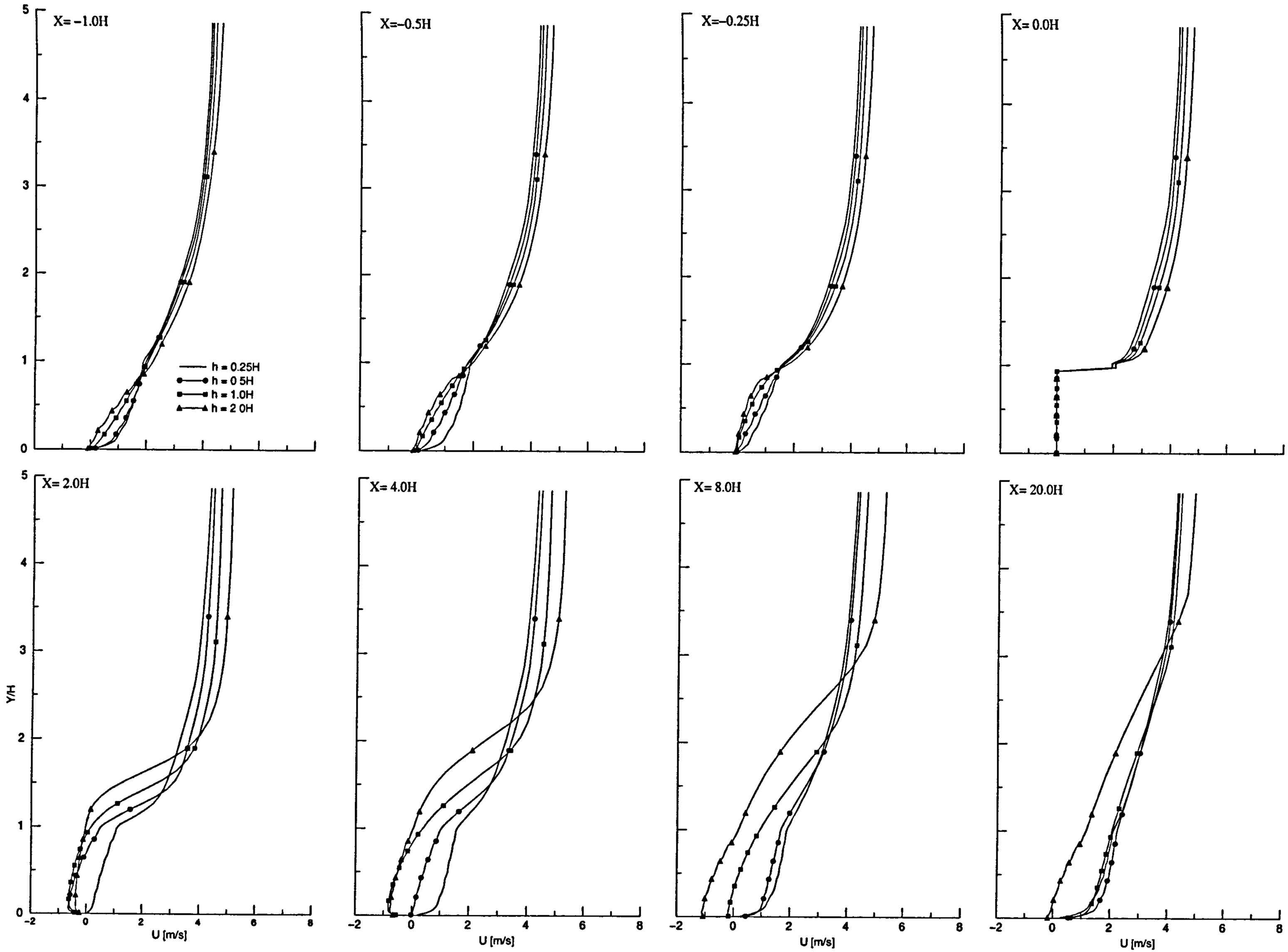

Figure 6.8a: Wind velocity profile at different distances from the solid wall with variable wall height h.

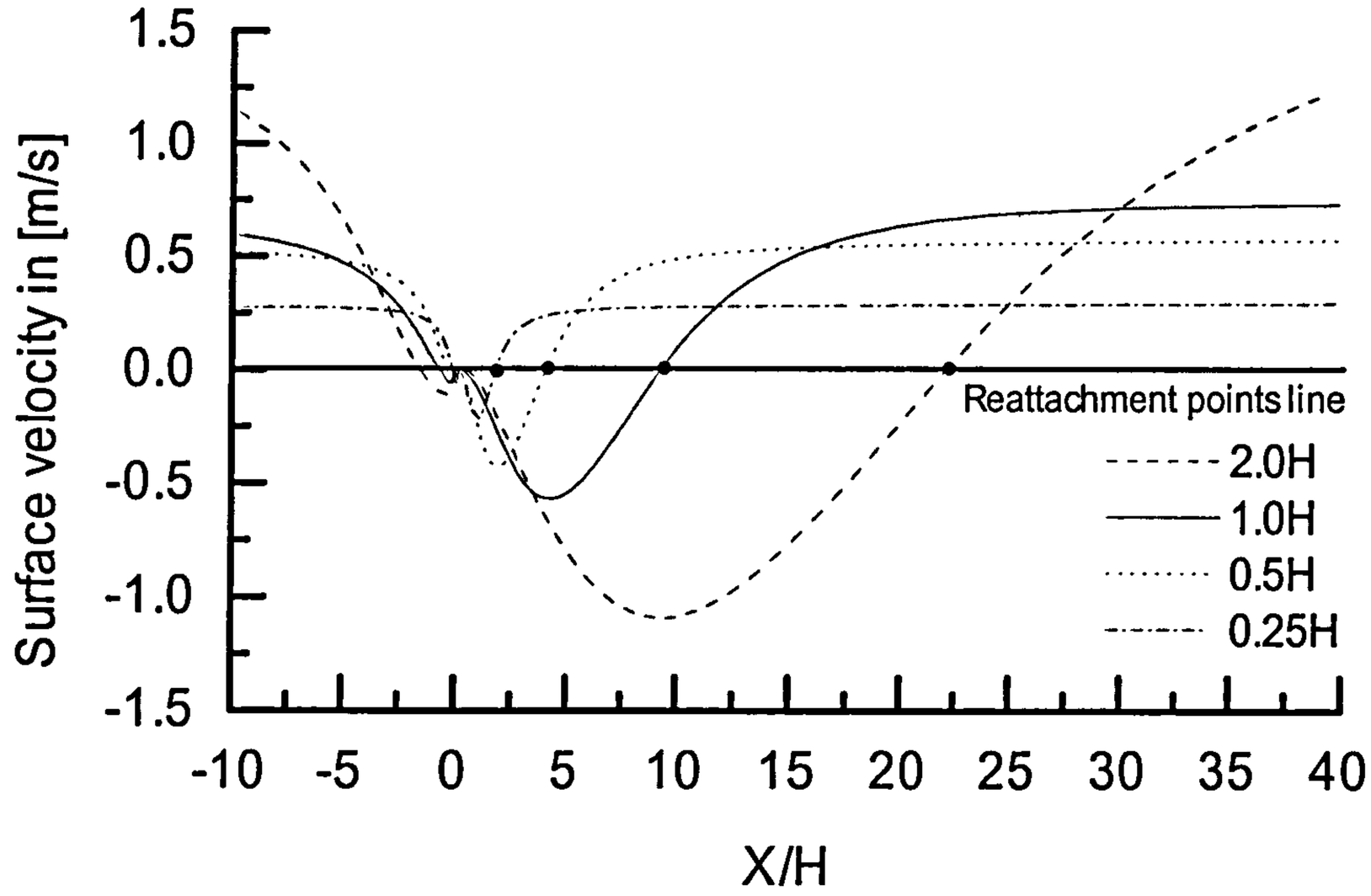

Figure 6.8b: Wind surface axial velocity profiles showing the changes in the reattachment points as the wall height change.

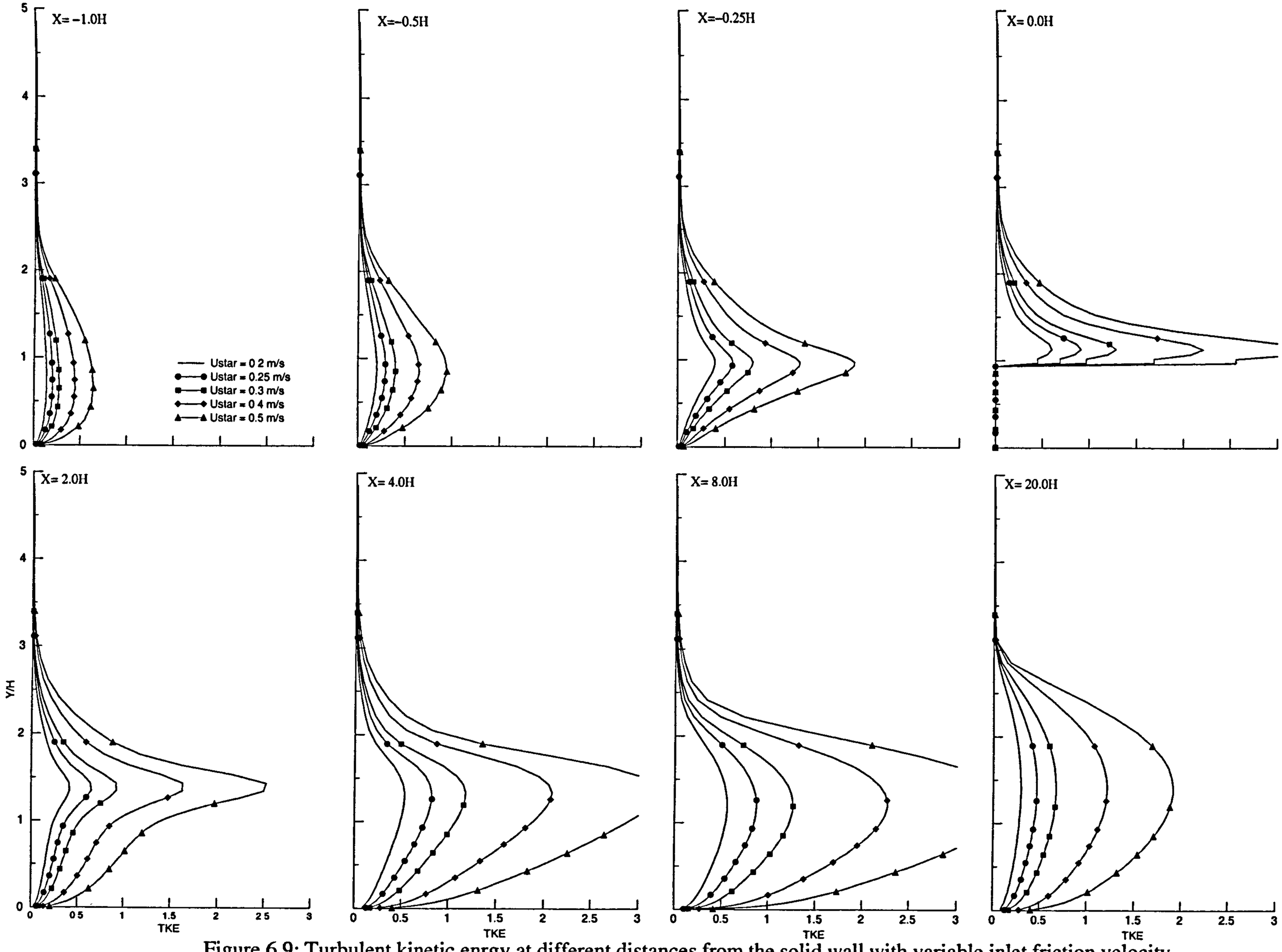

Figure 6.9: Turbulent kinetic enrgy at different distances from the solid wall with variable inlet friction velocity.

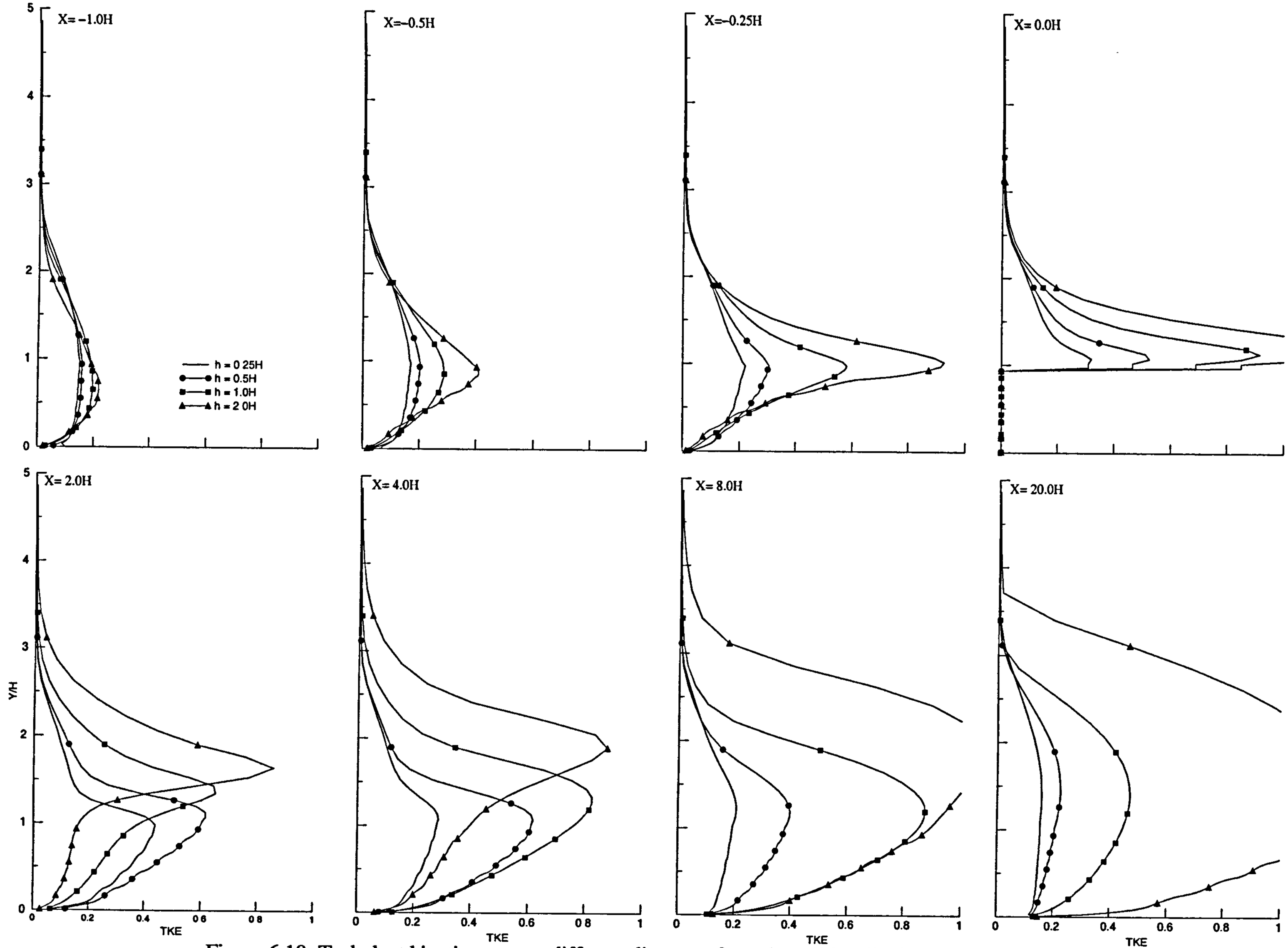

Figure 6.10: Turbulent kinetic enrgy at different distances from the solid wall with variable wall height.

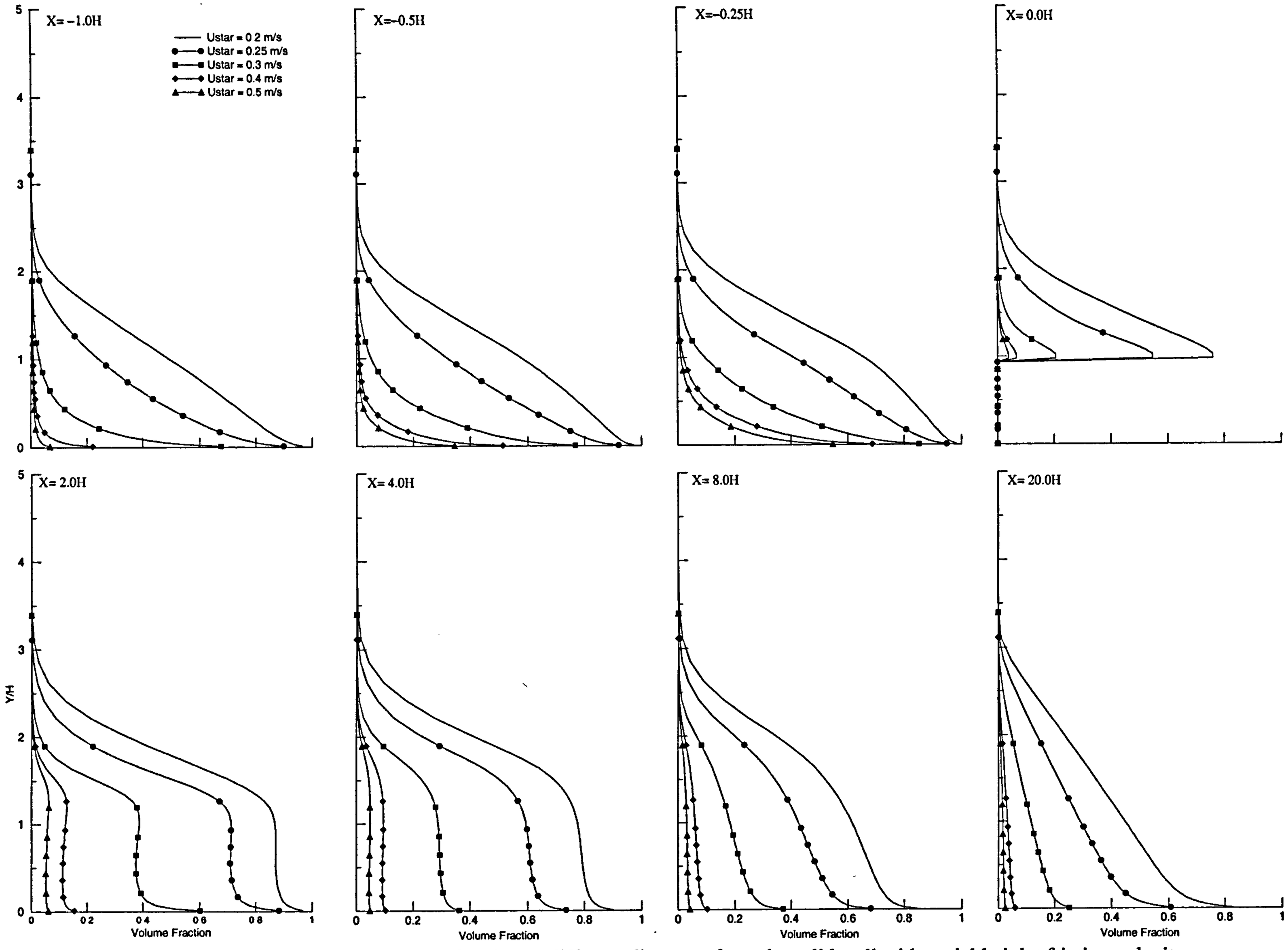

Figure 6.11: Particle volume fraction at different distances from the solid wall with variable inlet friction velocity.

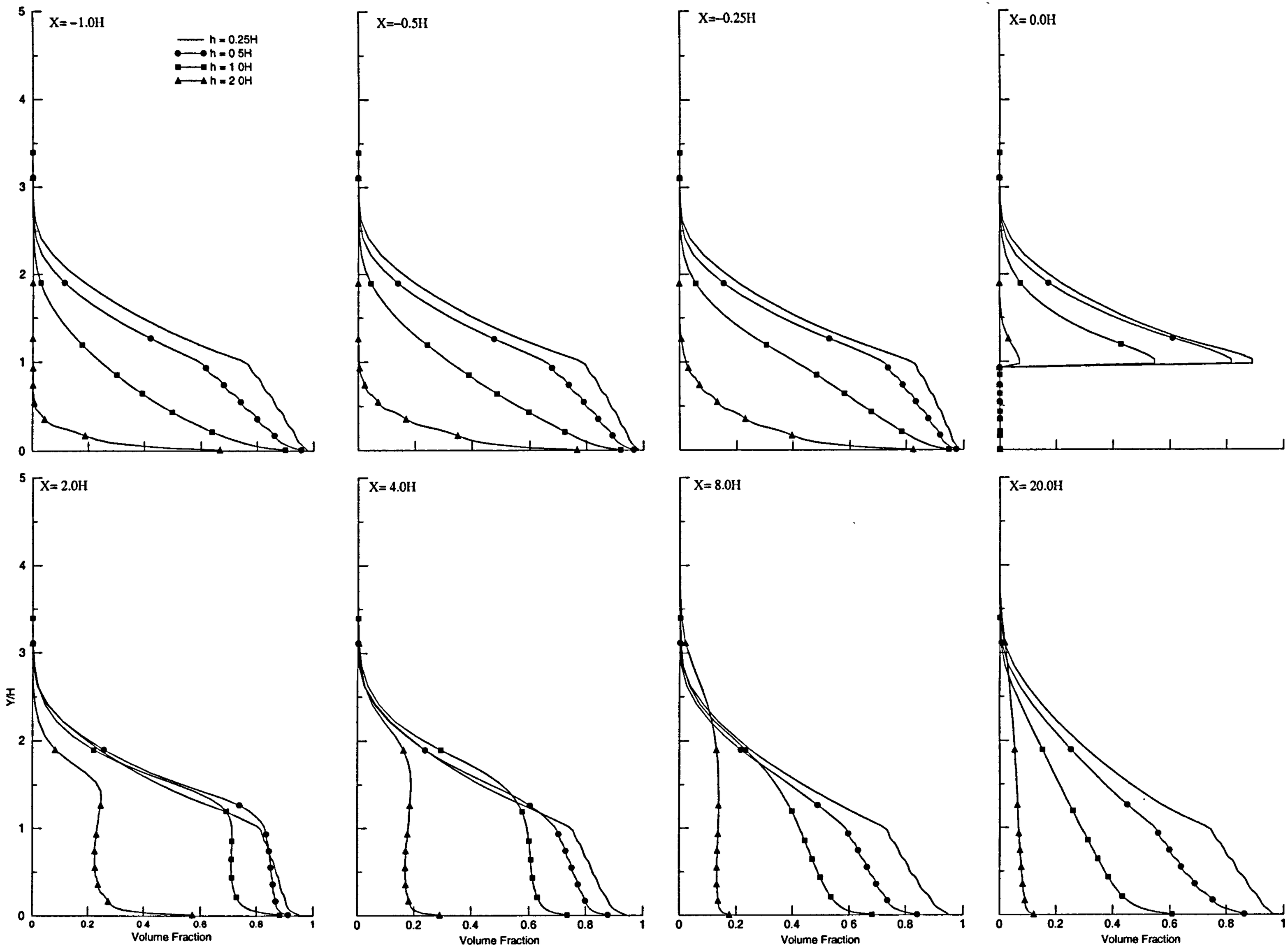

Figure 6.12: Particle volume fraction at different distances from the solid wall with variable wall height.

6.4 Mixture verses Homogenous model

A number of computations were undertaken to assess the limitations and capabilities of both the homogenous and mixture models when employed in the prediction of the flow of an air-particle mixture and particle deposition at a solid wall.

Regions of high particle volume fraction are considered as regions of expected accumulation. The mixture model is a two-way coupled model thus regions of high particle concentration affect the flow field of the whole mixture and therefore the flow field of the continuous phase. Hence, high particle volume fraction must be avoided to maintain the model's basic assumptions.

Ungarish (1993) reported that in a diluted vertical flow of suspended particles, volume fractions greater than 0.16 showed strong computational instability. In the current work, the flow changed from diluted to a mixture of diluted and dense flow regimes when particles start to accumulate. Dense flow areas have high particle volume fraction while diluted areas have high continuous phase volume fraction.

Sundsbo (1994) employed the drift-flux mixture model for snow drift around porous wall by assuming that regions of expected deposition are considered to exist where the particle volume fraction become 1E-4.

Due to this limitation, the particle inlet concentration profile is chosen to be of small value and the suspension source term coefficient, β_{sus}, is also reduced so that high volume fraction values are prevented in regions of expected deposition near the wall.

Figure 6.13a shows the particle volume fraction profiles at different axial sections across the flow domain using both homogeneous and mixture models where β_{sus} = 0.02. As expected, the mixture model with a small suspension source term behaves like the homogenous model and the values of the particle volume fraction are almost the same. Figure 6.13b shows no clear differences in the wind velocity profiles across the computational domain.

The discrepancies between homogenous and mixture models increases when β_{sus} rises to 0.08, figure 6.14a. The significant jump in the volume fraction has a physical description that is; when the value of the particle volume fraction increases, the continuous phase volume fraction decreases ($\alpha+\alpha_p=1$). Therefore, a reduction in the mixture velocity, figure 6.14b, occurs due to the increase in the diffusion stress term, which appears in the mixture momentum equation (5.19).

Since the mixture model is based on the assumption of small relative velocity between fluid and particle, the model is limited to certain values of the particle volume fraction where this assumption is applicable. The maximum volume fraction value at which the model can be employed varies according to the application itself and on the fluid-particle density ratio. In the present study, the density ratio, ρ_p/ρ, is of the order 2000, e.g. $\rho_p=2650$, $\rho=1.17887$, which is relatively high and therefore the mixture model shows computational instability when the β_{sus} exceeds a value of 0.08.

Since the particle concentration in the homogenous model has no feedback effect on the flow field, the particle volume fraction in this model can reach higher values as shown previously in figures 6.11 and 6.12.

In general both models demonstrated identical regions of the expected depositions in the weak recirculation zone, figures 6.15 and 6.16, which confirms the results produced using the Lagrangian model in chapter 4, figure 4.11.

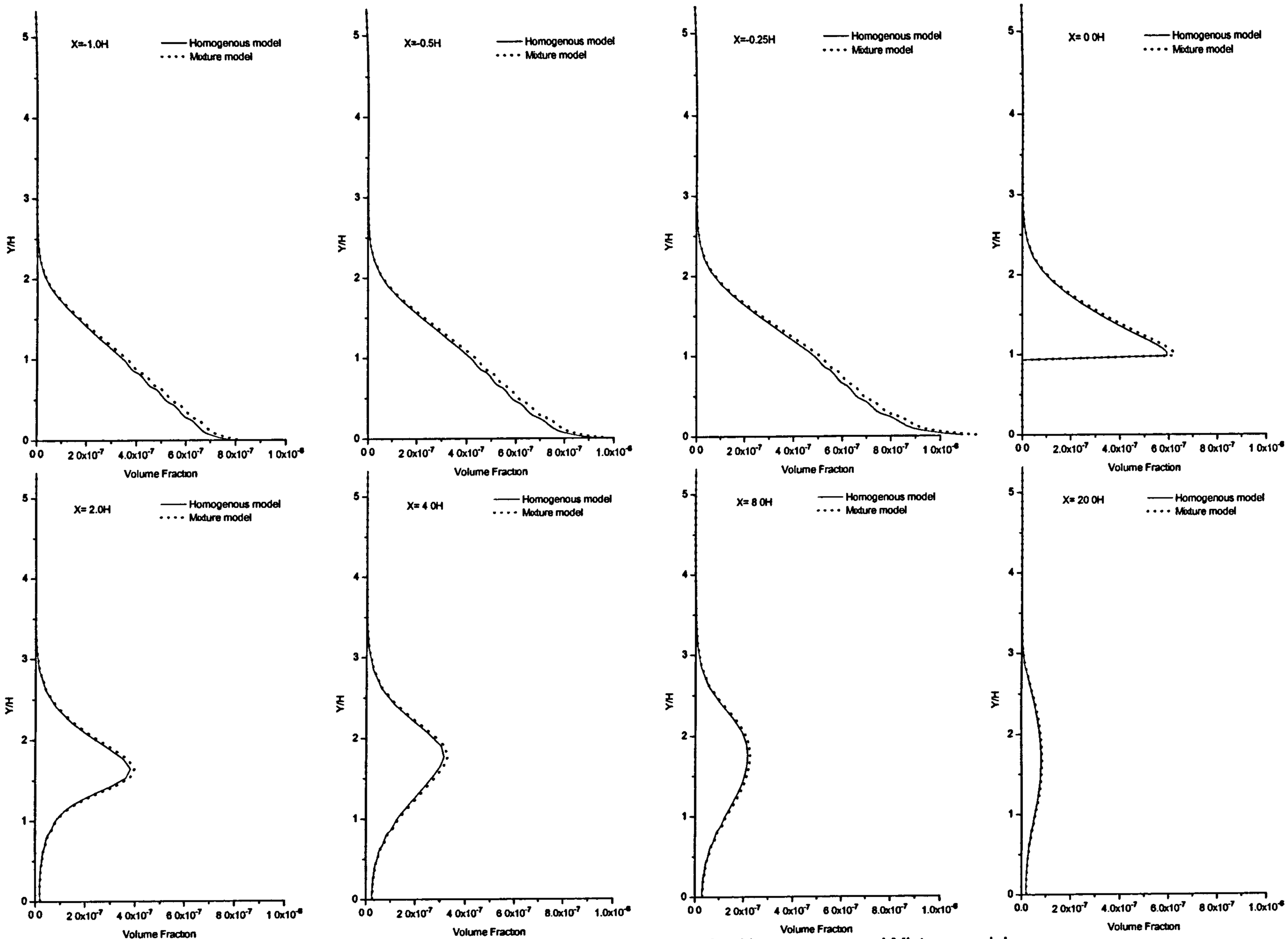

Figure 6.13a: Particle volume fraction at different distances from solid wall using Homogenous and Mixture models.
(Suspension source term constant = 0.02)

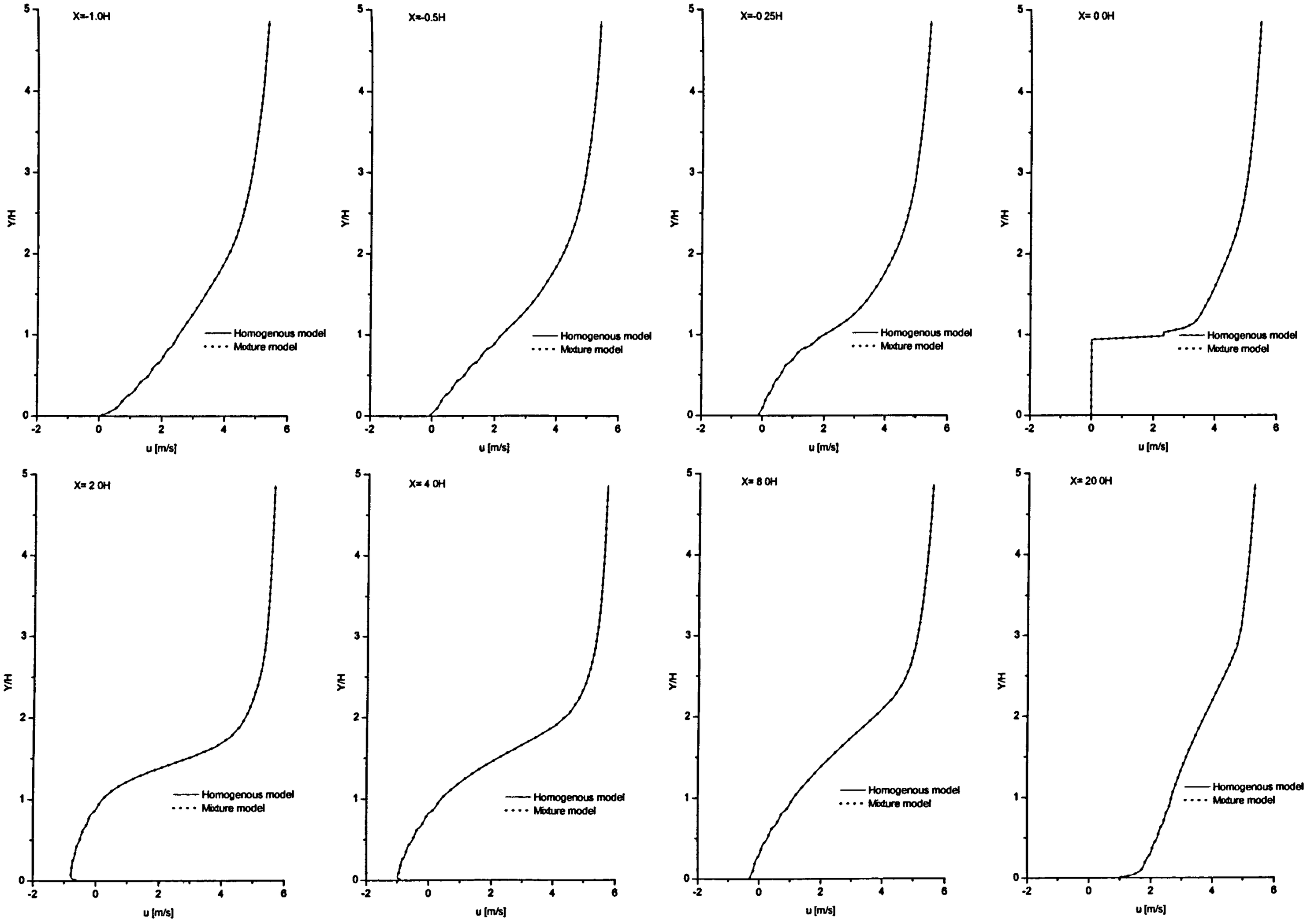

Figure 6.13b: Wind velocity profile at different distances from solid wall using Homogenous and Mixture models.
(Suspension source term constant = 0.02)

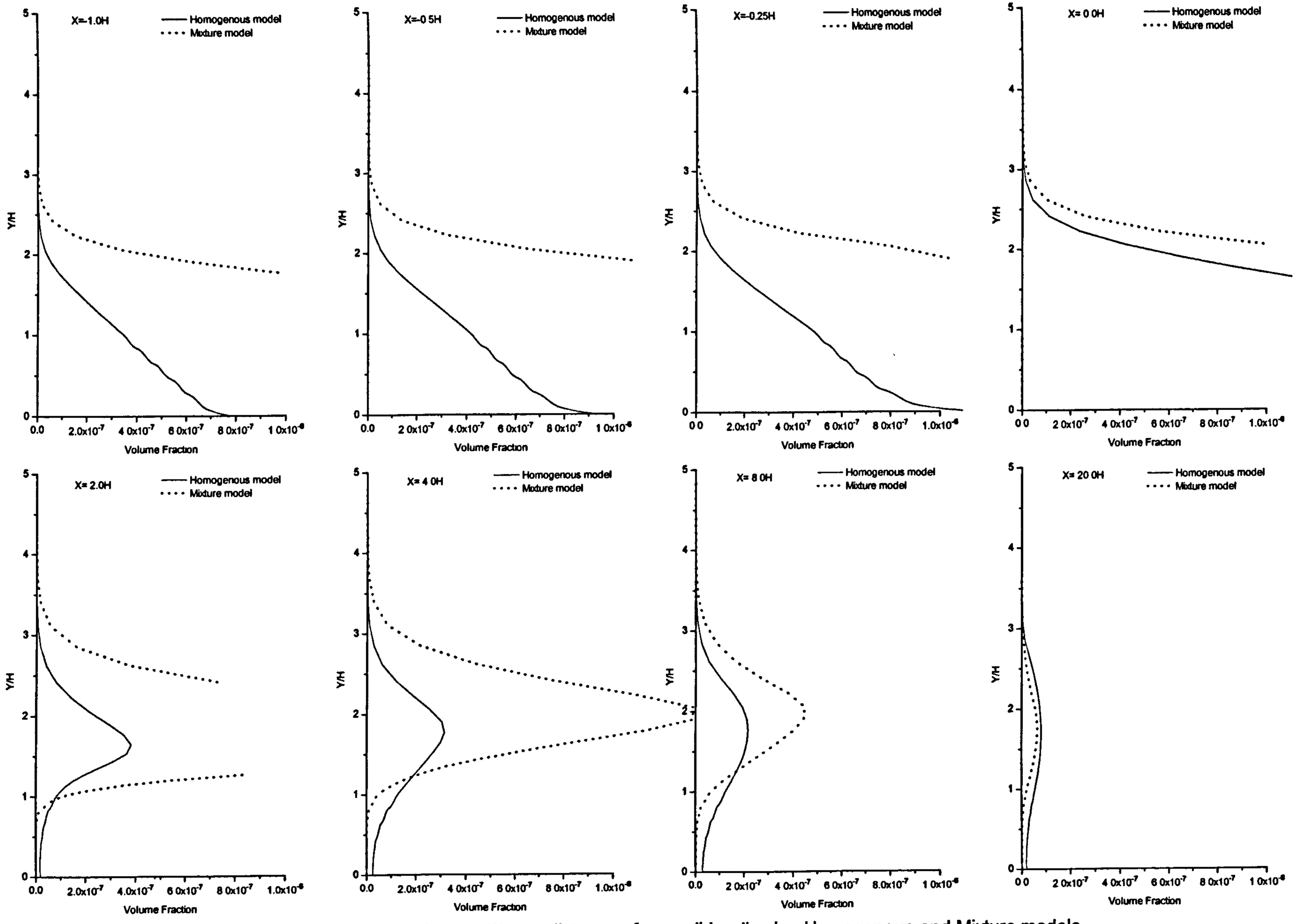

Figure 6.14a: Particle volume fraction at different distances from solid wall using Homogenous and Mixture models.
(Suspension source term constant = 0.08)

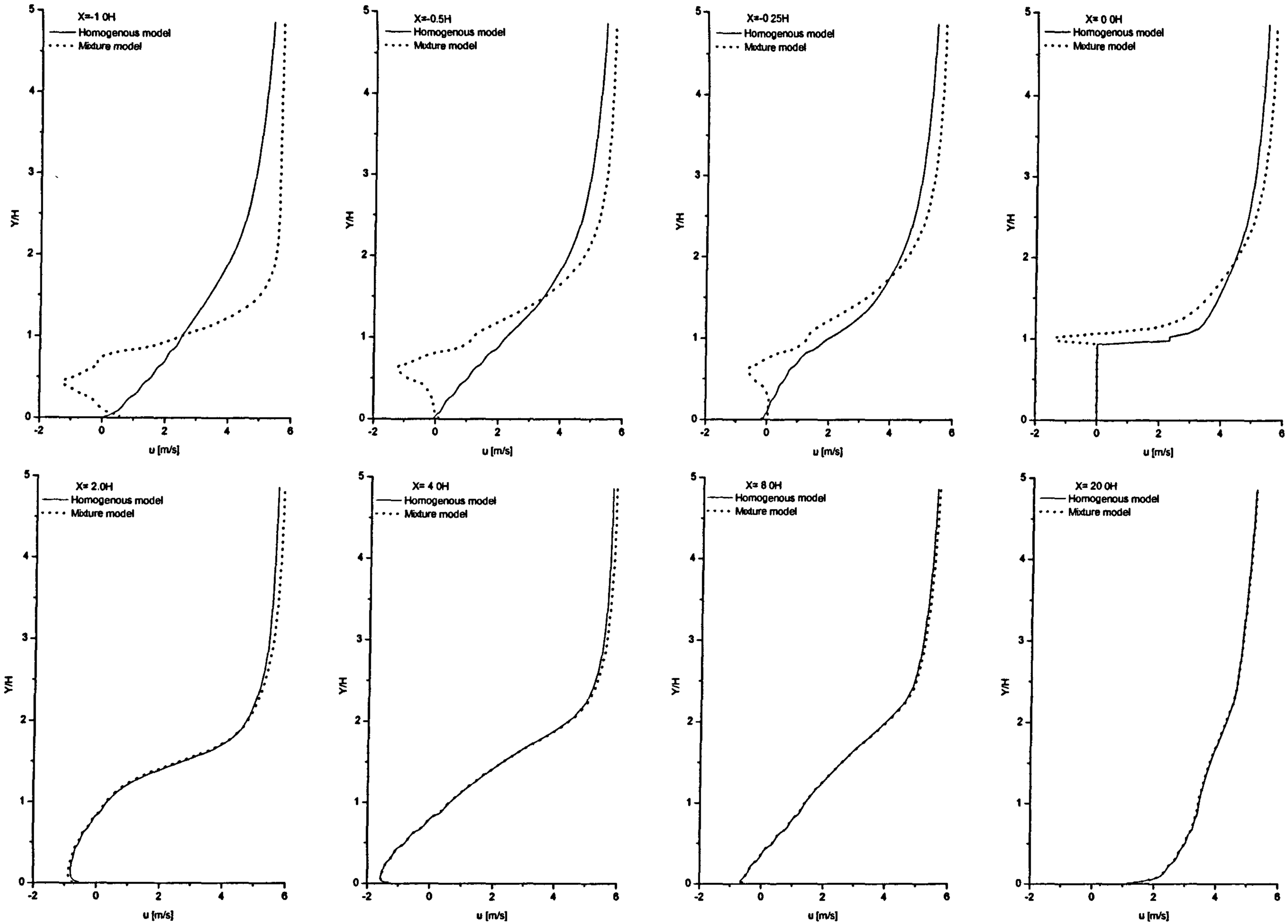

Figure 6.14b: Wind velocity profile at different distances from solid wall using Homogenous and Mixture models.
(Suspension sourec term constant = 0.08)

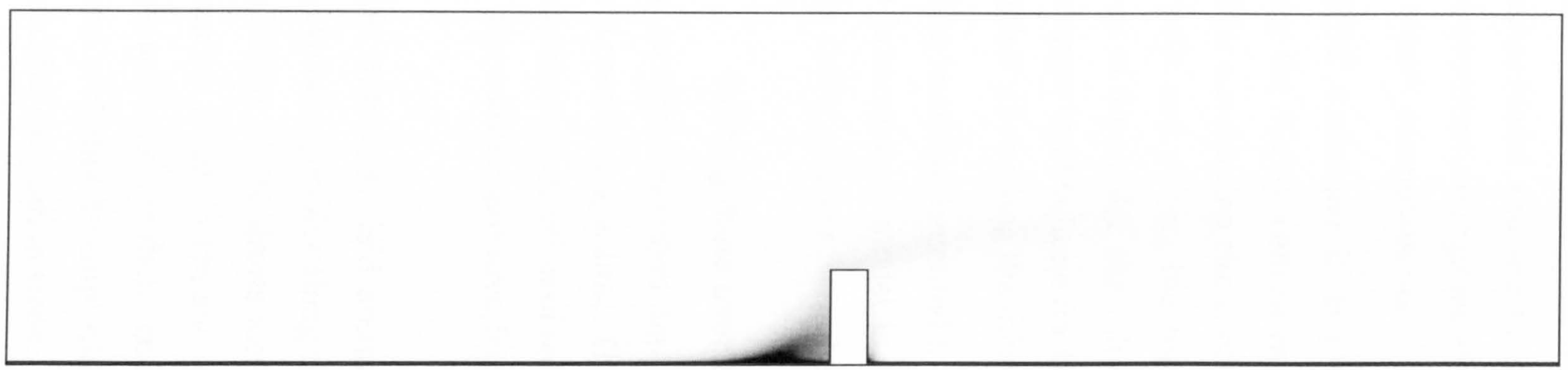

Figure 6.15: Homogenous model steady state solution of particle concentration around solid wall.

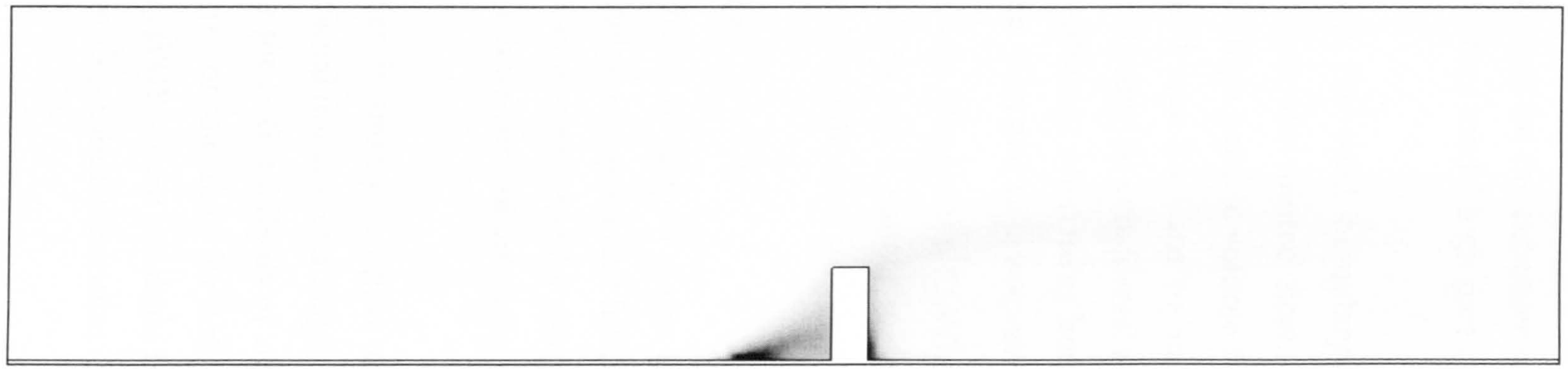

Figure 6.16: Mixture model steady state solution of particle concentration around solid wall.

6.5 Homogenous model coupled with FAVOR boundary interface

Both homogenous and mixture models have certain limitations. In the homogenous model, the flow field does not account for the existence of the high particle concentration regions, while in the mixture model high particle volume fraction causes computational instability.

The FAVOR technique is employed to track the solid boundary interface separating the highly concentrated regions from the diluted flow. This was achieved by considering the control volume of high particle volume fraction as blocked cells and setting the cell's volume and area fractions to one. Due to limitations of the model, the value at which cells may be considered as blocked cells, the upper limit volume fraction value, is different when using homogenous model to that when using the mixture model e.g. 0.75 and 1E-4 respectively.

FAVOR has been implemented in both models. In this section FAVOR coupled with the homogenous model is discussed, which has a simple mathematical derivation and is efficient from the computational point view.

6.5.1 Drifting dune over a flat surface

First, the erosion-deposition algorithm introduced in chapter 5 was tested for flow over a conical shape dune. The dune geometry was generated initially using the conventional description of solid control volumes and then by using FAVOR in which the volume and area fractions of the dune control volumes are set to unity.

The steady state flow field around both dunes is shown in figure 6.17a and shows the velocity profiles along the computational domain at a height equal to the dune height 'H'. It shows identical results for both methods of setting the dune geometry. Figure 6.17b shows the pressure contour lines for both cases. A multi stage solution was then achieved using FAVOR where the dune boundary was allowed to change by employing the erosion-deposition algorithm after each two consecutive calculation steps.

The erosion-deposition process was tested on the dune surface. Due to the high surface friction velocity on the dune upstream side, the dune surface is expected to erode whenever the particle threshold velocity is exceeded. Therefore, particles start to drift from that control volume opened to the flow, from the dune upstream side, to the downstream flow domain where they either settle or may drift to the domain outlet.

In the weak region behind the dune, the friction velocity dropped to values below the threshold value and the particle volume fraction increases to some value above the upper blocked limit thus a deposition process occurs.

Figure 6.18, shows the different stages of the dune movement, from the initial movement of the dune until the whole dune has left the computational domain through the outlet boundary. Since there were no other sources of particles in this example, the flow field becomes a clean airflow when the dune completely leaves the computational domain.

It can be assumed that FAVOR is working well in this example since the dune shape does change its shape according to the change in both flow velocity field and particle volume fraction.

It should be noticed that the FAVOR model is implemented in a way, which allows for the generation of obstacles of different geometry within the computational domain even if a single-phase flow problem is solved.

6.5.2 Dune growth at solid wall

The FAVOR model was then applied to the solid wall problem introduced in section 6.3. The transient homogenous-FAVOR model was employed to introduce the solid interface boundary separating the deposition areas from the flow field wherever the deposition conditions mentioned above are satisfied.

In this case, the upper limit volume fraction was chosen to be 0.75. Therefore control volumes were considered as a solid wall if 75% or above of its volume was occupied by the settled particles.

Figure 6.19a shows the different stages of the dune growth around the wall. In the early stages, the deposition process starts at a distance upstream as a result

of the reverse flow generated in front of the wall. After each deposition stage, the last introduced interface boundary will reform the flow field around the wall, figure 6.19b.

This will create new layers, normally on the top of the first interface boundary, where the deposition conditions are satisfied and therefore another layer of the solid boundary is generated and so on. When the solution has reached a steady state situation, neither deposition nor erosion occurs with further computations.

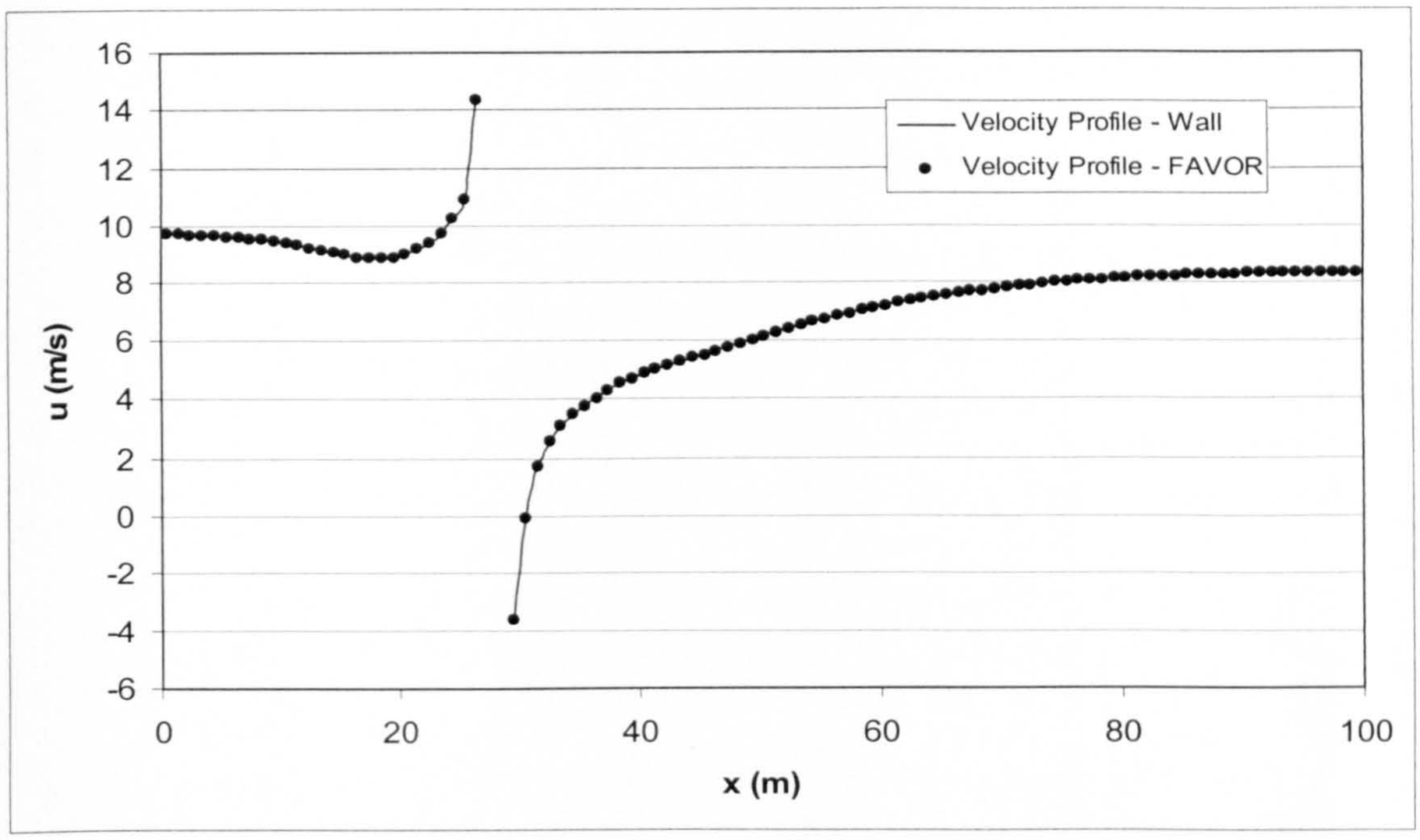

Figure 6.17a: Velocity profile comparison between conventional and FAVOR representation of stationary dune in the axial direction at y = Dune Height "H".

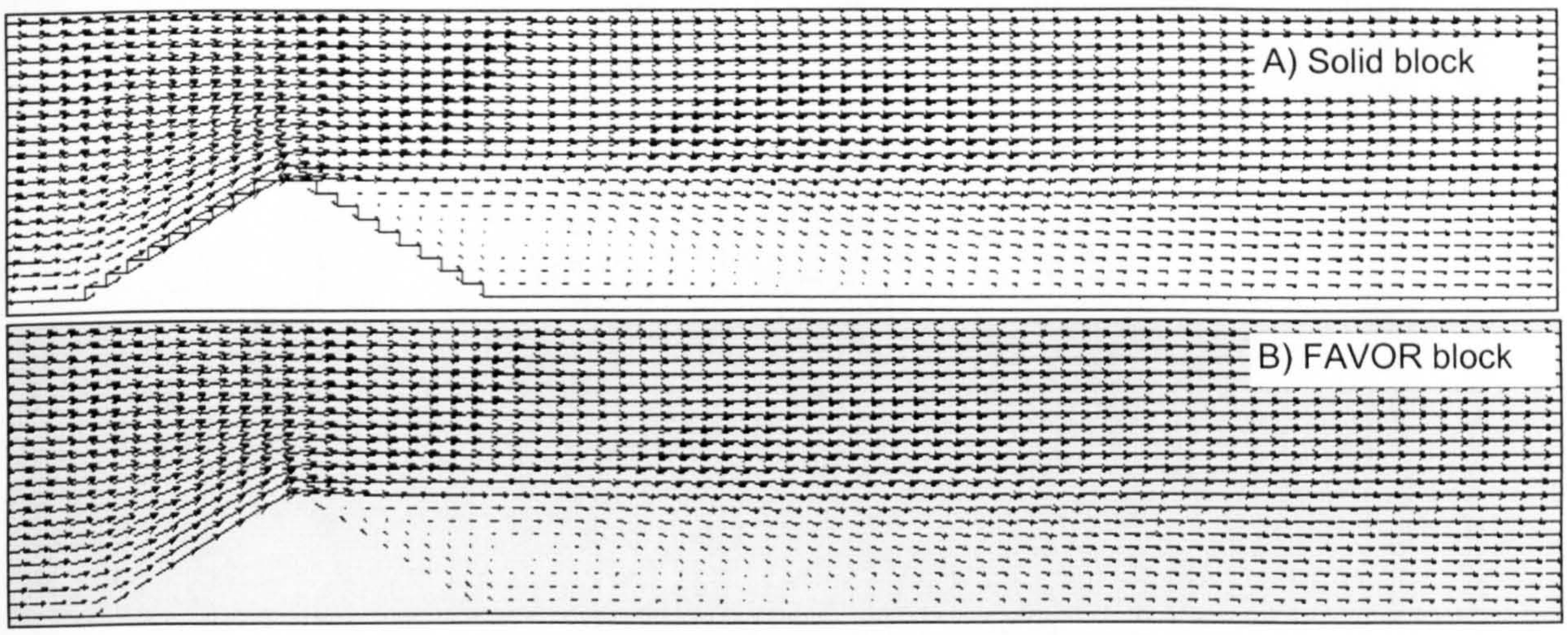

Figure 6.17b: Flow velocity contour plot for steady state solution of homogenous model around fixed dune. A) Using conventional way of setting dune as solid block. B) Using FAVOR model.

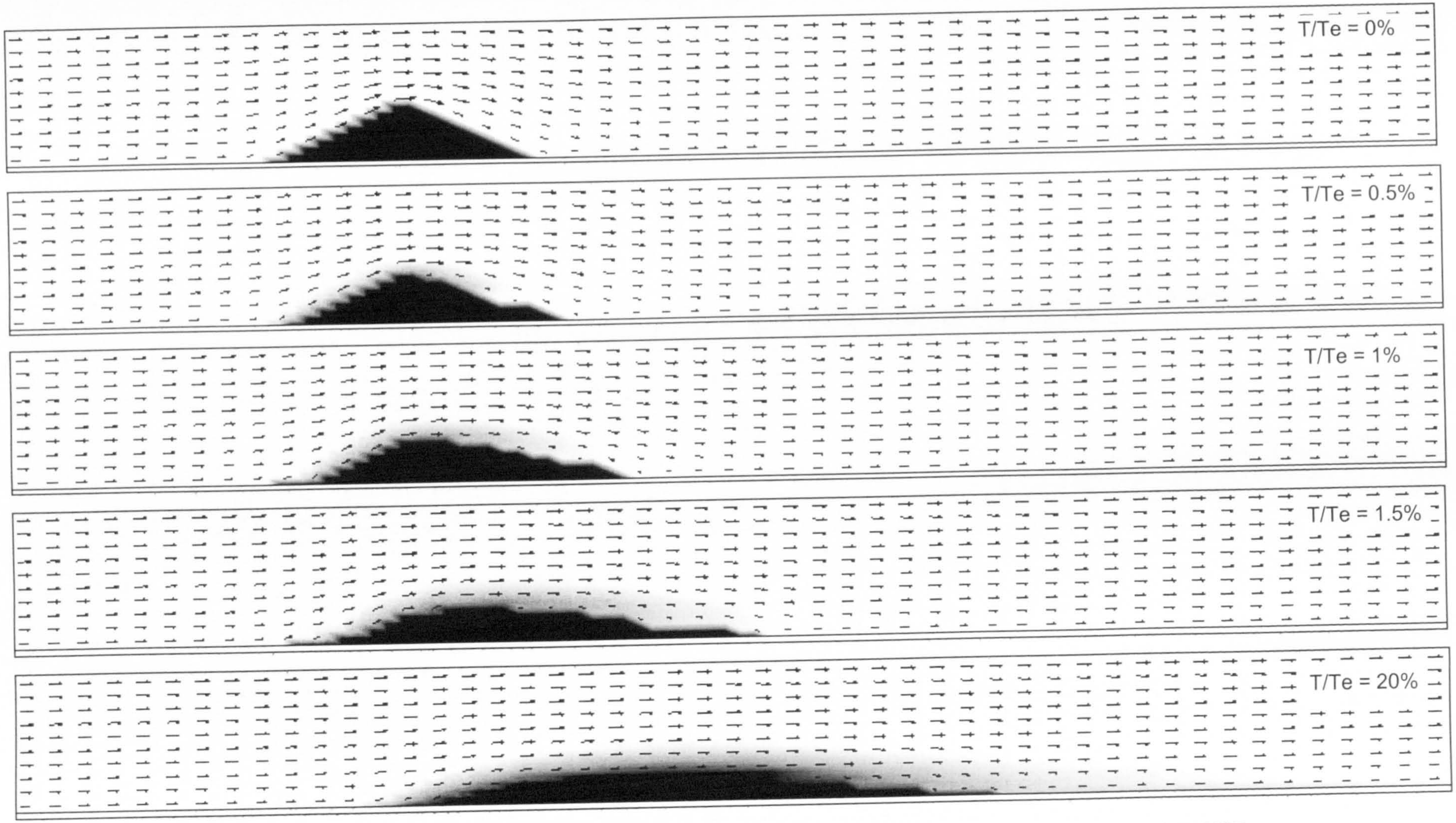

Figure 6.18: Different stages of sand dune emigration using over a flat surface using homogenous model coupled with FAVOR.

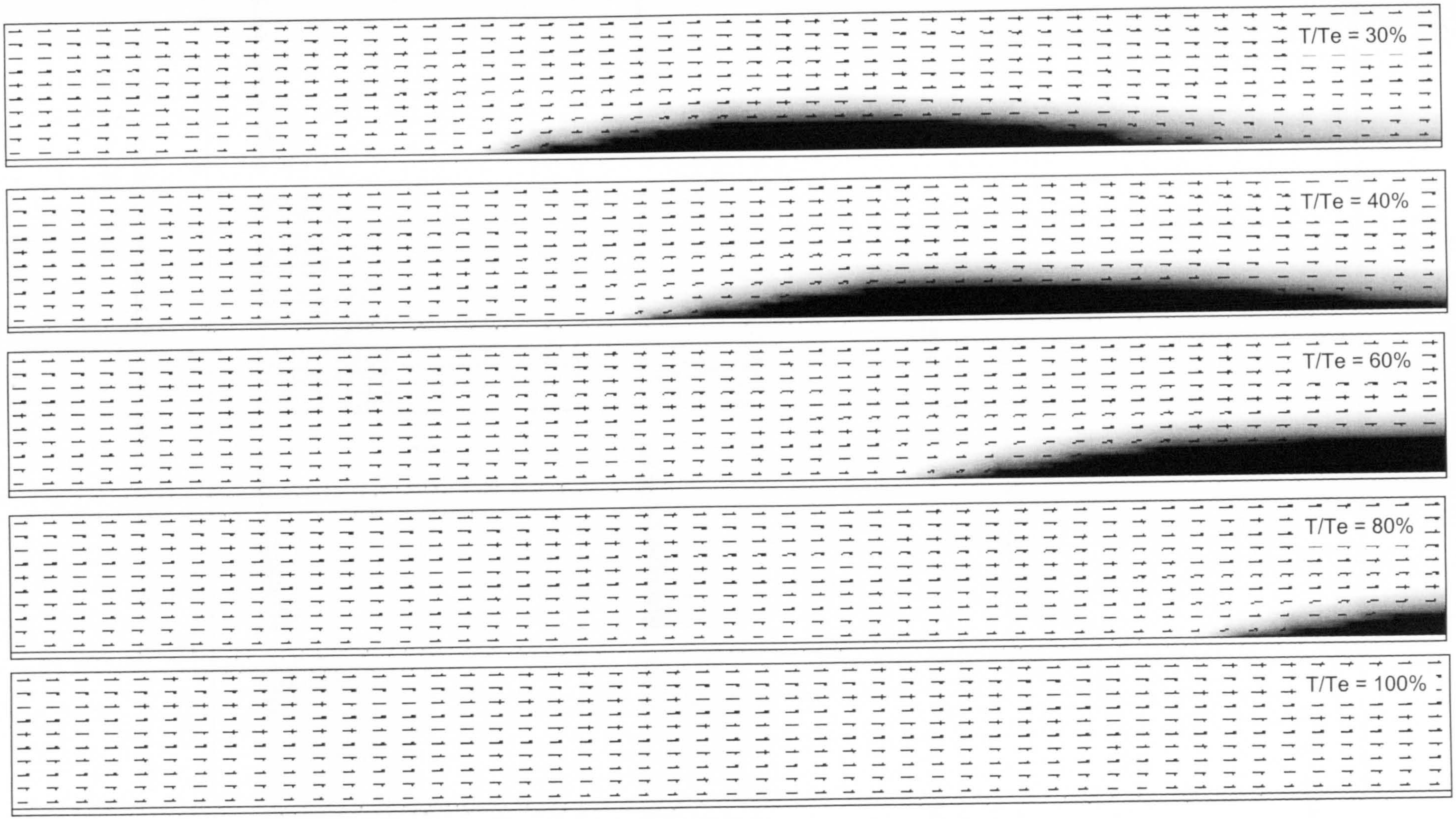

Cont . Figure 6.18: Different stages of sand dune emigration using over a flat surface using homogenous model coupled with FAVOR.

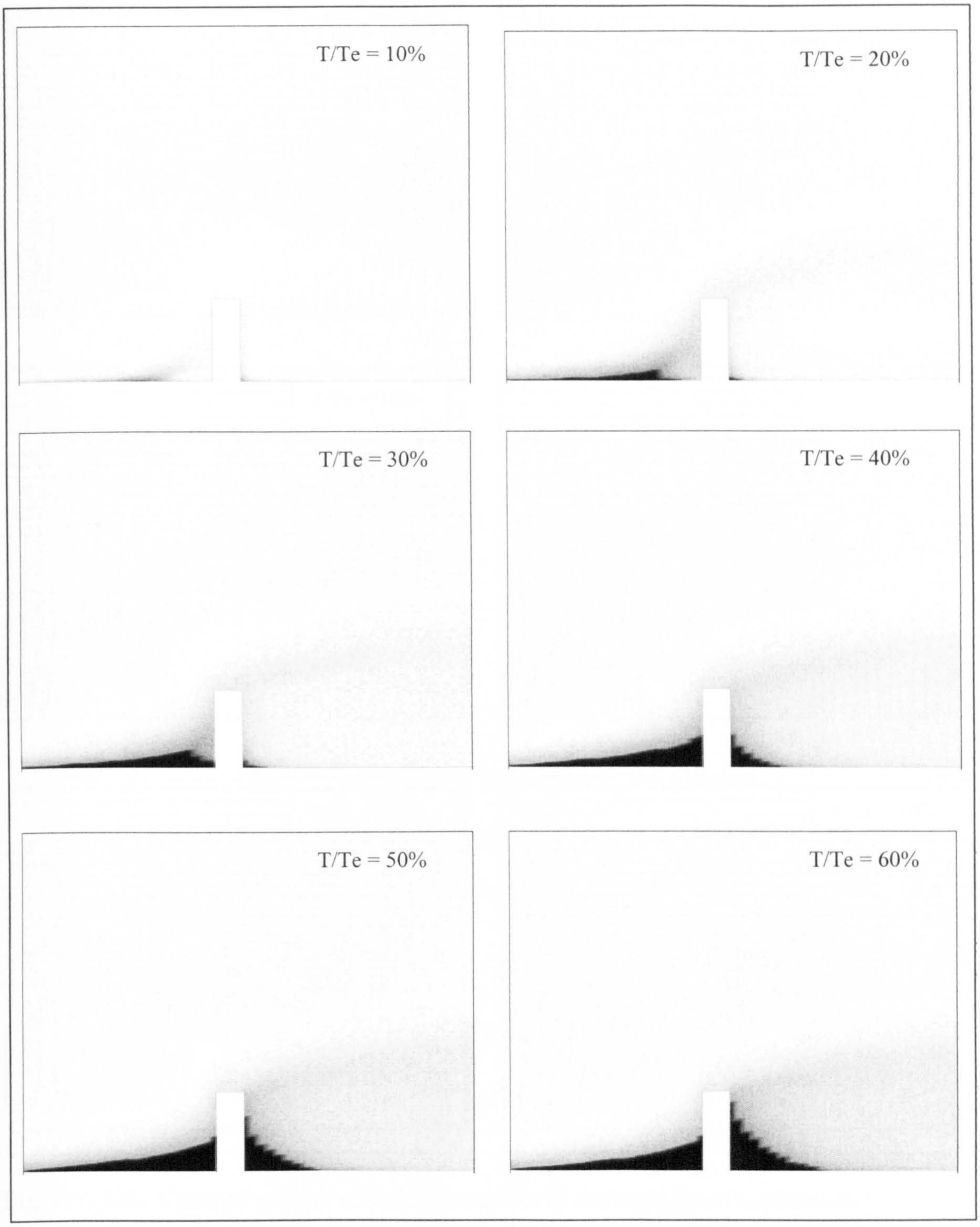

Figure 6.19a: Stages of particle deposition profile using homogenous model coupled with FAVOR.

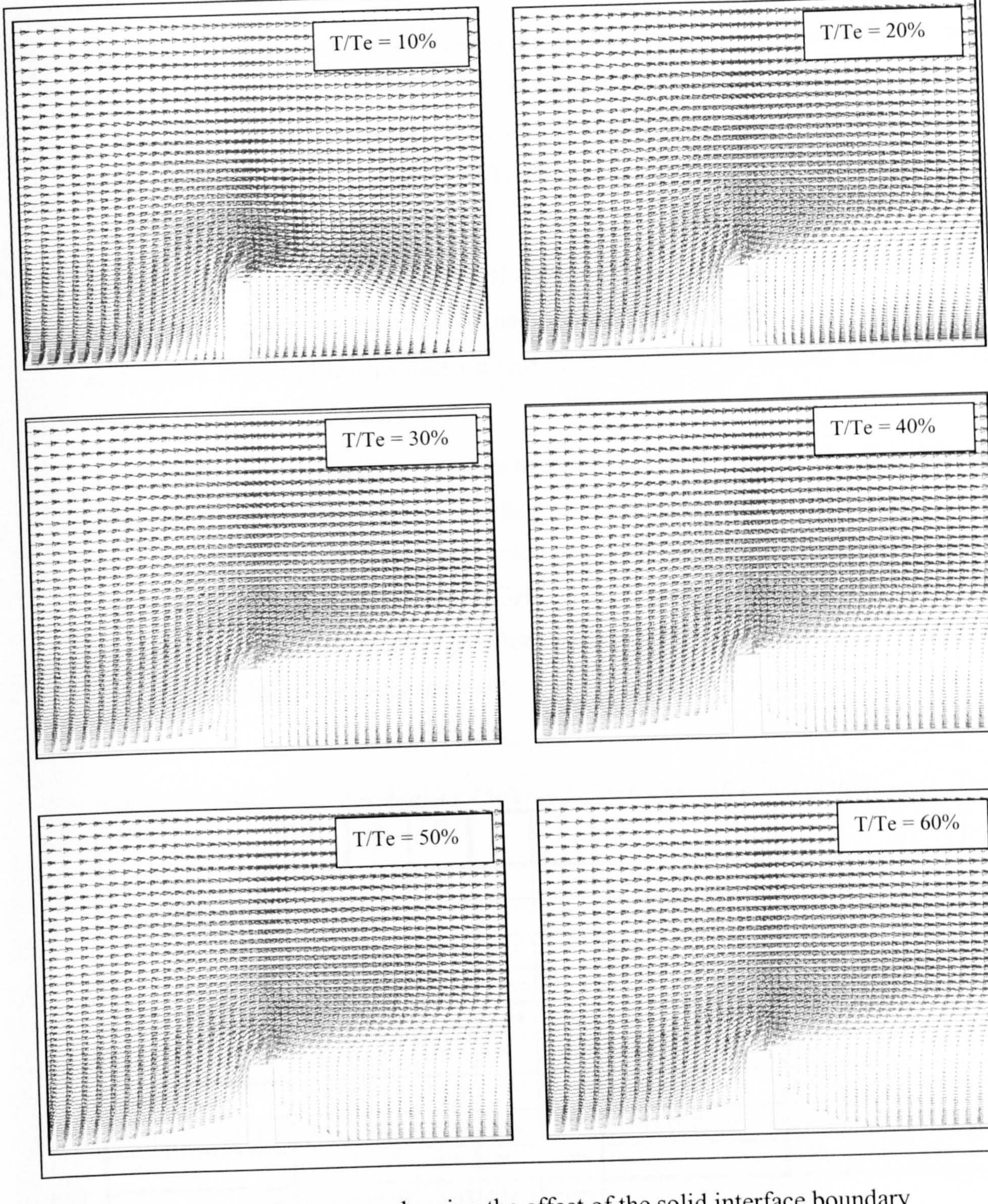

Figure 6.19b: Velocity vectors showing the effect of the solid interface boundary introduced using FAVOR on the flow field at different stages of particle deposition process.

6.6 Grid sensitivity

A grid sensitivity study was undertaken to ensure that the comparisons made between CFD results and field or wind tunnel measurements were independent of the grid density. The study, reported in this section, consisted of simulating the flow round a solid wall with grids of varying distributions, as shown in table 6-3 with reference to figure 6.5.

The controlling parameters for all the simulations were set to the same values used in the previous section. Thus, any differences that may exist in the simulation reported in this section can be assumed to be mainly a result of the differences in the grid resolution.

The steady state deposition profiles around the solid wall for the five different grid distributions are shown in figure 6.20. The coarse grid shows poor deposition profiles while the finer grids predict a deposition profile that spreads outward from the wall position. Grid C is chosen for use in the remaining assessments, since the grids of greater resolution show no significant variance in the solution downstream of the wall.

Table 6-3: Different grid distributions. *(Refer to figure 6.5 for definitions of the domain sections)*

RUN == >	A	B	C	D	E
X-Direction					
Section X1 in [m]	1	1	1	1	1
Cells	50	50	100	150	200
Ratio	0-1.05	0-1.05	0-1.05	0-1.05	0-1.05
Section X2 in [m]	0.02	0.02	0.02	0.02	0.02
Cells	3	3	3	3	3
Ratio	0 - 0	0 - 0	0 - 0	0 - 0	0 – 0
Section X3 in [m]	2.54	2.54	2.54	2.54	2.54
Cells	100	100	200	250	300
Ratio	1-1.03	1-1.03	1-1.03	1-1.03	1-1.03
Total Length in [m]	3.54	3.54	3.54	3.54	3.54
Total Cells	153	153	303	403	503

	A	B	C	D	E
Y-Direction					
Section Y1 in [m]	0.0254	0.0254	0.0254	0.0254	0.0254
Cells	30	40	40	40	40
Ratio	0 - 0	0 - 0	0 - 0	0 - 0	0 - 0
Section Y2 in [m]	0.5	0.5	0.5	0.5	0.5
Cells	30	40	40	40	40
Ratio	1-1.02	1-1.02	1-1.02	1-1.02	1-1.02
Total Length in [m]	0.5254	0.5254	0.5254	0.5254	0.5254
Total Cells	60	80	80	80	80

6.7 Suspension Model

The suspension source term β_{sus} in the particle transport equation is responsible for the deposition rate that results from suspended particle transport mode, as discussed in section 5.6. Field and wind tunnel observations (Bagnold 1941, Iversen 1982, Pye and Tsoar 1990), established that only a few percent of the total number of deposited particles are transported by suspension, while the majority of the movement occurs within the saltation layer.

For steady wind speed with uniform particle size distribution, the distinction between suspended and saltated particles are more recognizable than that in the case of unsteady wind acting on a non-uniform particle size.

In this section, the effect of the value of β_{sus} on the deposition rate is examined with constant values for the saltation source term coefficient β_{Salt}. The deposition rate increases with the increase in β_{sus} as shown in figure 6.21. Under this setting, no deposition occurred for $\beta_{sus} \leq 0.02$ and unrealistically large deposition occurred for $\beta_{sus} \geq 0.15$. Between these two limits, the deposition rate was found to be in a direct proportion to the increase in the values of the suspension coefficient.

6.8 Saltation Model

Two different features of the saltation source term have been examined, the normalised friction to the threshold velocity ratio, U^*_{Norm} and the saltation source term coefficient, β_{Salt}.

The saltation process is known to occur within a thin layer existing a few centimetres above the surface, as such, the saltation source term is implemented as a boundary source term. Positive values of the source term imply that an erosion process has occurred while negative values imply that a deposition of particles has occurred.

As mentioned in section 2.3.1, the different expressions of friction to threshold velocity ratios, U^*_{Norm}, were considered in the saltation source term to avoid the requirement of the empirical expressions to predict the particle mass flow rate in the saltation layer.

The six suggested expressions of U^*_{Norm}, table 5-1, were examined first to analyse the effect of each expression on the final deposition profile at the solid wall. For uniform glass spheres of 49-μm diameter and density 3990 $\frac{kg}{m^3}$, the particle threshold value was estimated using equation (2-1) to be 0.215 m/s.

Referring back to figure 5.3, it can be seen that when the friction velocity is equal to the threshold value, U^*_{Norm} becomes zero and hence the saltation source term also becomes zero. This means that there will be neither deposition nor erosion due to saltating particles when the friction velocity and the threshold value are equal.

Higher friction velocities will result in negative U^*_{Norm} and erosion will occur, whereas for lower friction velocities U^*_{Norm} has a positive value and hence deposition will occur due to particles being transported in the saltation layer.

The different expressions of U^*_{Norm} were tested using identical initial and boundary conditions. The steady state deposition profiles at the solid wall are shown in figure 6.22. Expression 4 in table 5-1 shows no deposition throughout the computational domain while small deposition profiles have appeared on both sides of the wall using expressions 1 and 5. The remaining expressions, 2, 3 and 6, show almost the same deposition profiles on the downstream side of the wall while only expressions 3 and 6 show significant deposition profiles at the upstream side of the wall. Therefore, expressions 3 and 6 were chosen for further investigations. They were both tested for different values of β_{Salt}.

Figures 6.23 and 6.24 show the deposition profiles for both expressions using different values for β_{Salt}. The deposition profile was found to be directly

proportional to β_{Salt}. A small value of the coefficient eliminates the effect of the source term while higher values result in a larger deposition profile.

It is noticeable that for the same β_{Salt} value, the deposition profile generated using expression 6 is higher than that when using expression 3. Consideration of figure 5.3, reveals the reason for this to be that when U^*_{Norm} has a greater value than one, as in the case of expression 6 at a friction velocity equal to about $U_t^*/2$, the saltation source term will be higher than that when using expression 3 at the same friction velocity.

6.9 Inlet friction velocity

In the simulation of the flow over a flat surface, section 6.2, it was shown that the inlet friction velocity changes the wind velocity profile. In this section, the effect of the inlet friction velocity on the particle deposition profiles around the solid wall is analysed.

Five different inlet wind profiles were examined. The lowest velocity was calculated from an inlet friction velocity 7.0% below the particle threshold value while the highest was from a friction velocity 16.3% above the threshold value as shown in table 6-4.

Table 6-4: Inlet friction velocities as it related to the particle threshold velocity

Ustar [m/s]	% from Threshold velocity
0.2	-7.0%
0.215	0.0%
0.22	2.3%
0.23	7.0%
0.25	16.3%

Figure 6.25 shows the deposition profiles for the different inlet wind velocity profiles. It shows that under a strong wind the ability of the particles to settle is less and thus the minimum deposition rate occurs. The largest deposition profile was found with the inlet friction velocity just below the threshold value. Inlet friction velocities much lower than the threshold value result in no particle movement thus in no depositions.

It has been established in the field and laboratory observations that a slower wind carries fewer fine particles whereas a strong wind carries large amounts of both heavy and light particles.

Theoretically, if the wind friction velocity drops to values below the particle threshold velocity, then the flow becomes clean air and therefore no particles would be transported neither by saltation or by suspension. The largest amount of particle deposition will occur when the steady wind friction velocity is maintained near the particle threshold velocity. Then as the wind strength becomes stronger, the deposition area near the wall is reduced in volume and moves closer to the wall location.

Moreover, the trap efficiency of the wall will decreases as the deposition profile reaches the steady state. The equilibrium state would take the longer time to achieve in the case of a slow wind; when the flow is just strong enough to move the particles. The time required to achieve the equilibrium state decreases with an increase in the wind strength while the maximum trap efficiency decreases.

6.10 Inlet Turbulent parameters

As mentioned in section 6.2, the transport of particles depends on many parameters. Vertical velocity fluctuations associated with the wind turbulence intensity effects the particle settlement. When the fluctuating velocity components of the flow are included into the instantaneous velocity, the friction velocity applied on a particle may exceed the particle threshold velocity, then the particle remains in suspension for a greater distance and time.

Moreover, when the aerodynamic forces are slightly greater than the particle body forces then the particle will move in saltation and if it is below the particle velocity has a direct impact on the particle motion and settlement process.

In this section, the inlet turbulent parameters will be examined. Turbulent kinetic energy and its dissipation can be related by a reference wind speed such as free stream velocity, to the length scale and turbulent intensity. The free stream velocity is taken to be the wind velocity well above the ground where the

velocity gradient in the vertical direction has become negligible while the wall height was taken as a length scale.

The turbulent intensity was changed at the inlet boundary to vary between 1.0% and 10% while the inlet wind profile was held constant.

Figure 6.26 shows the variation in the deposition profile near the wall as the inlet turbulent intensity changes. High turbulent intensity leads to higher friction velocity near the wall and therefore a lesser deposition rate. Reduction of the turbulent intensity results in a decrease of the friction velocity and as a consequence the deposition rate increases.

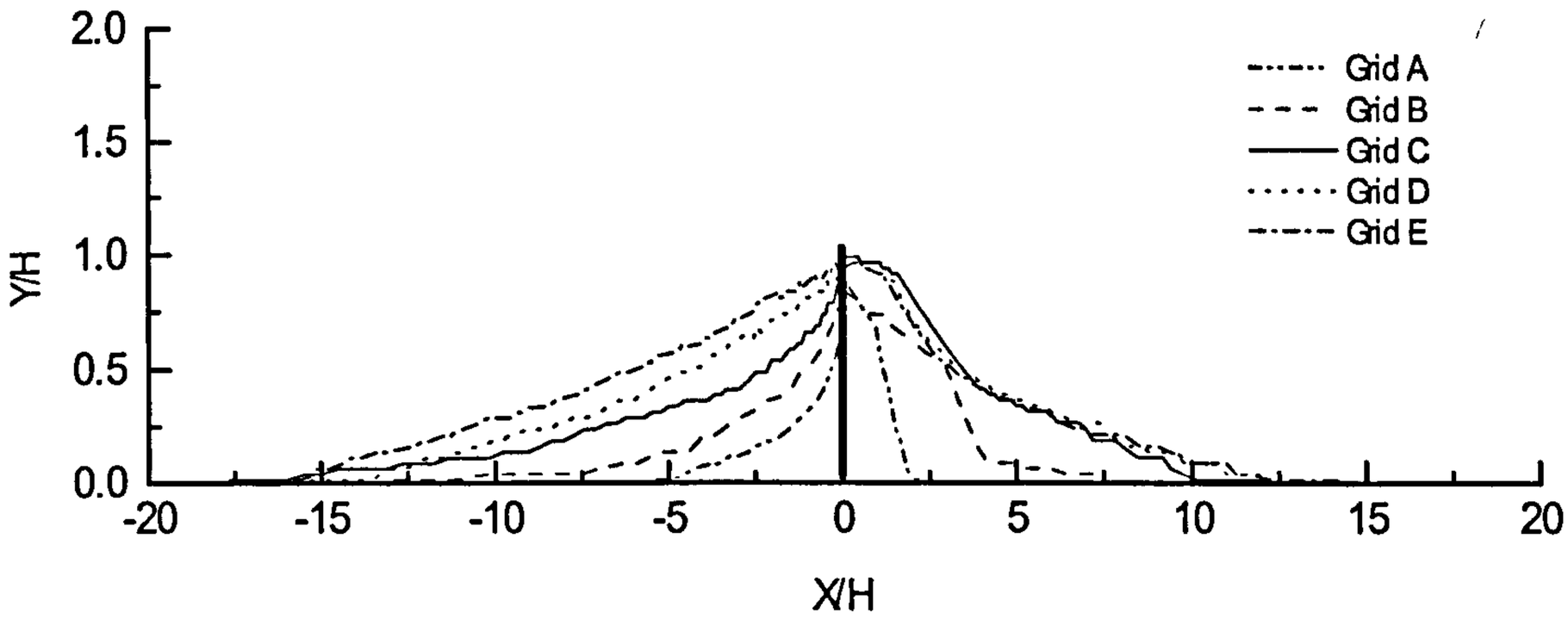

Figure 6.20: Particle deposition profiles for different grid distributions.

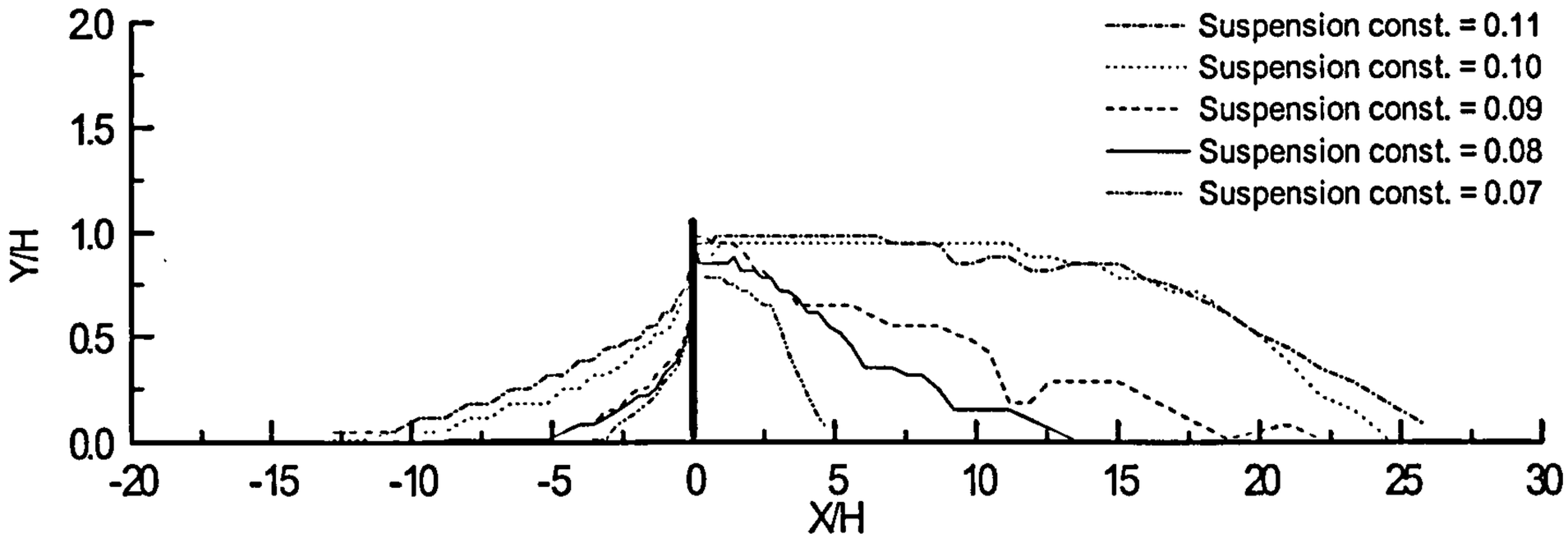

Figure 6.21: Particle deposition profiles for different values of suspension source term constant.

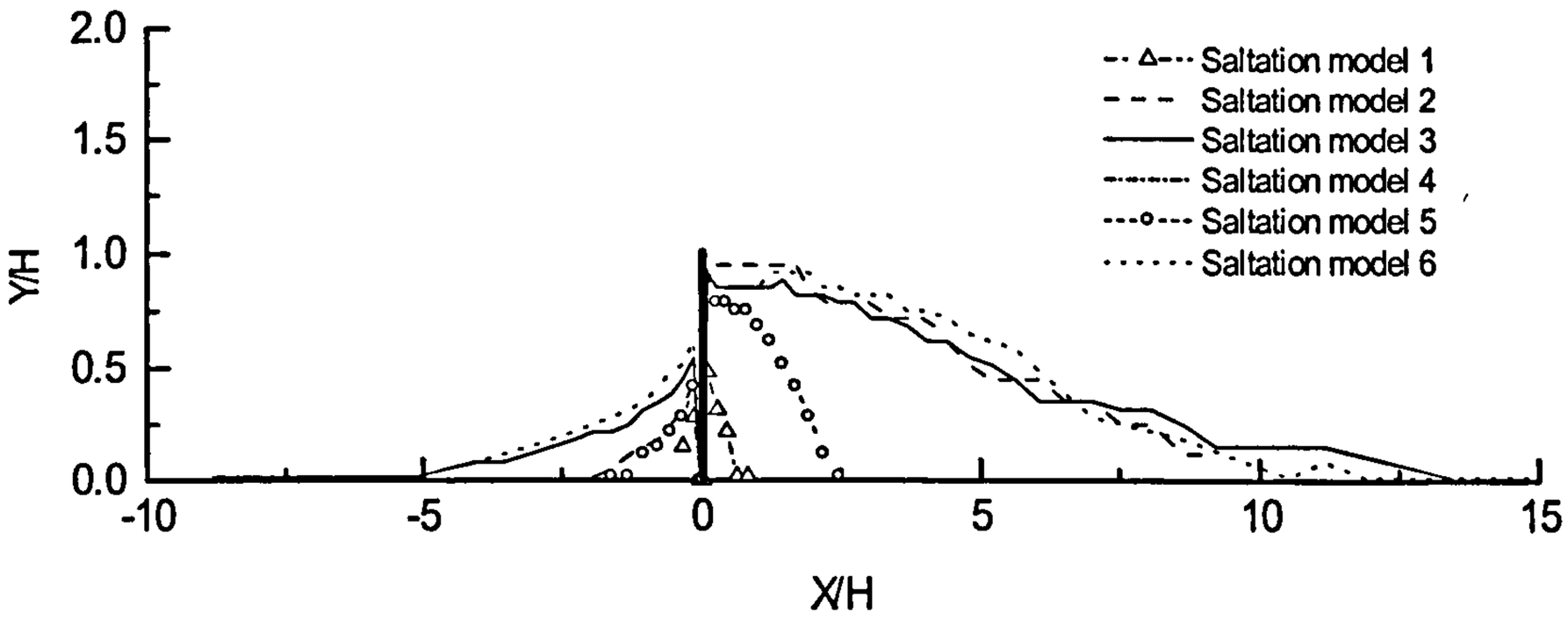

Figure 6.22: Particle deposition profiles using different saltation models.

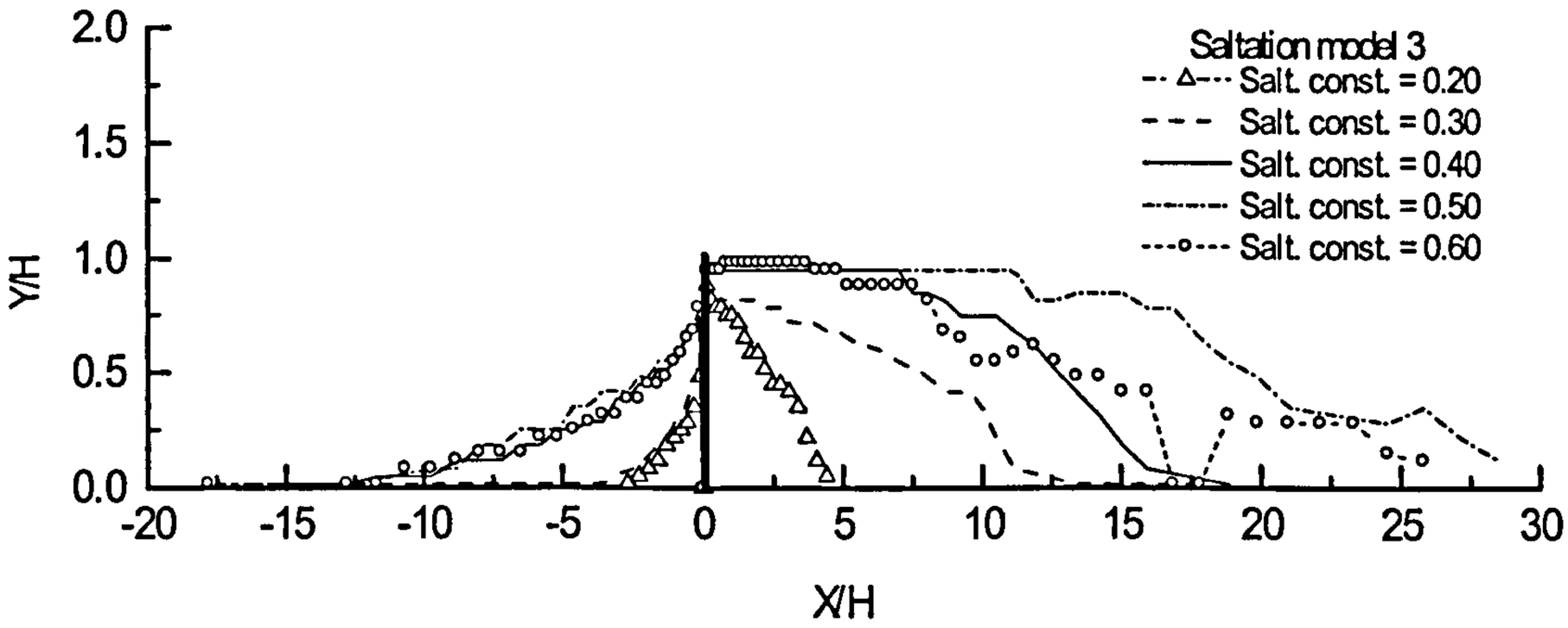

Figure 6.23: Particle deposition profiles using different saltation source term constant with saltation model 3.

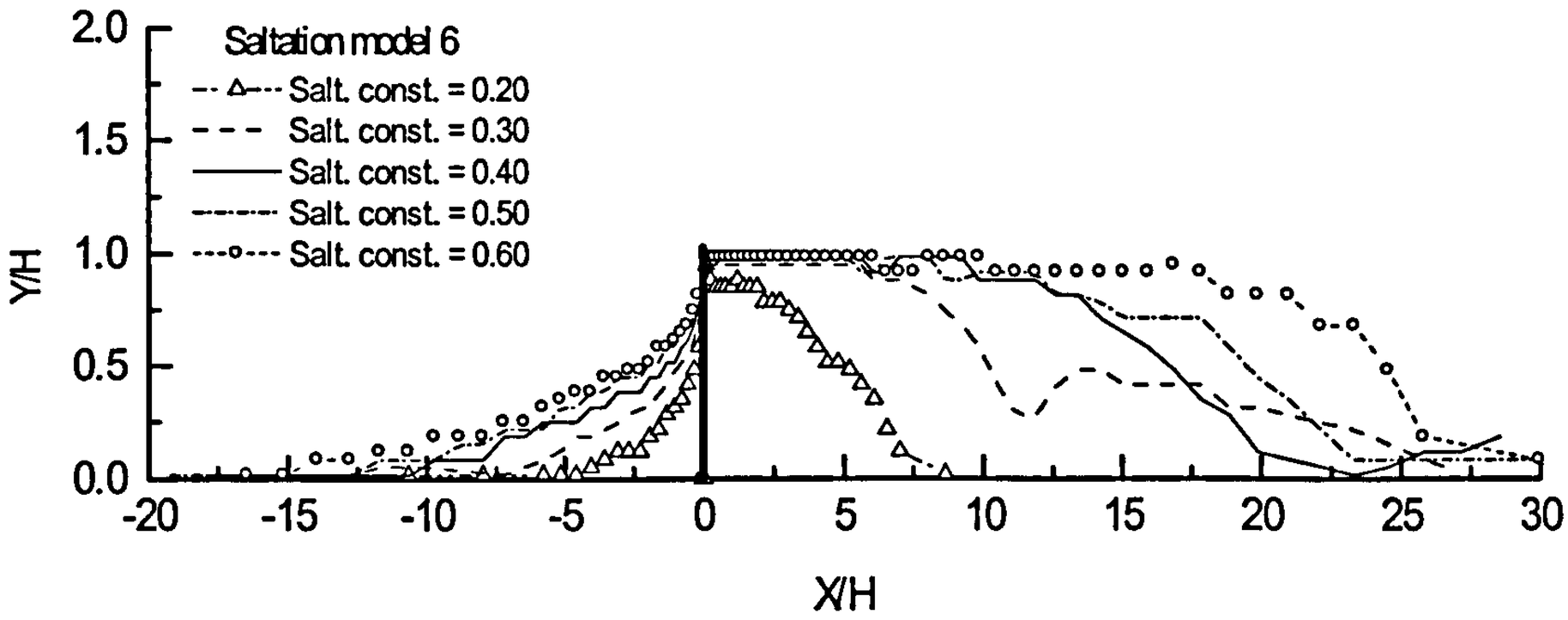

Figure 6.24: Particle deposition profiles using different saltation source term constant with saltation model 6.

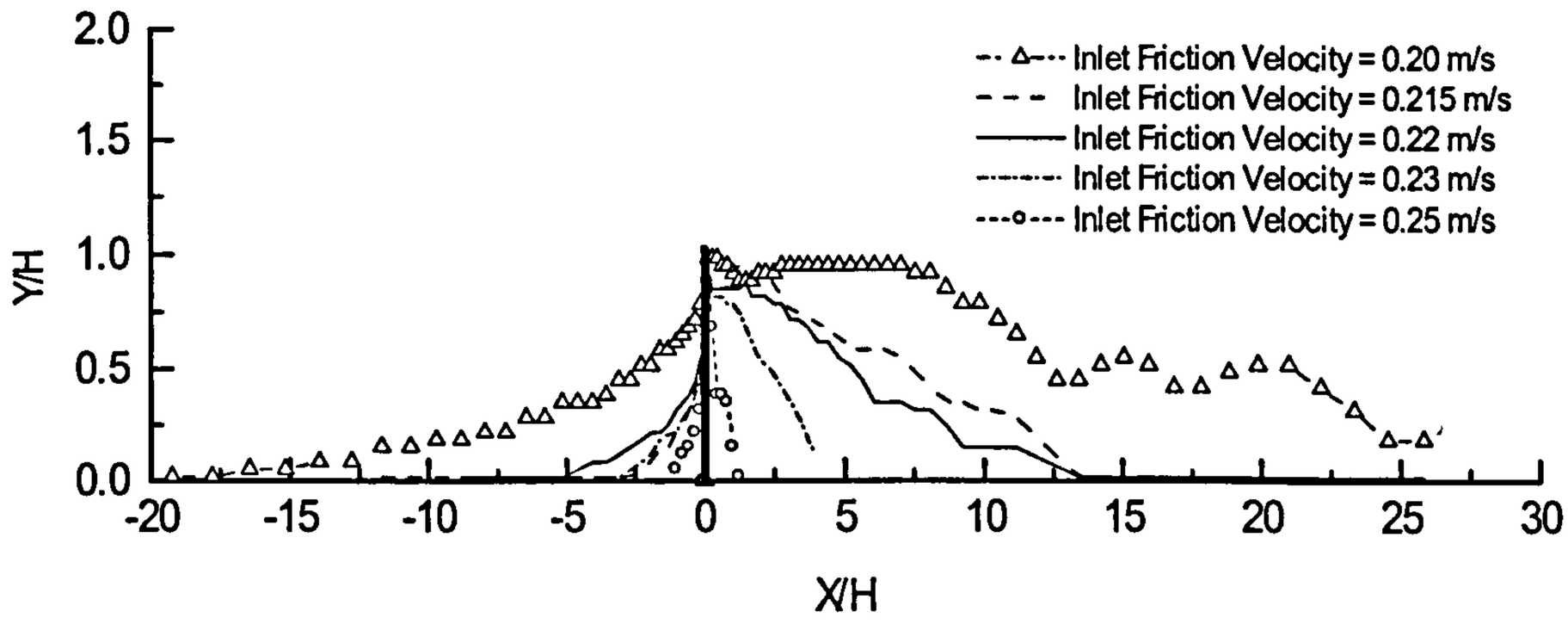

Figure 6.25: Particle deposition profiles using different inlet friction velocity.

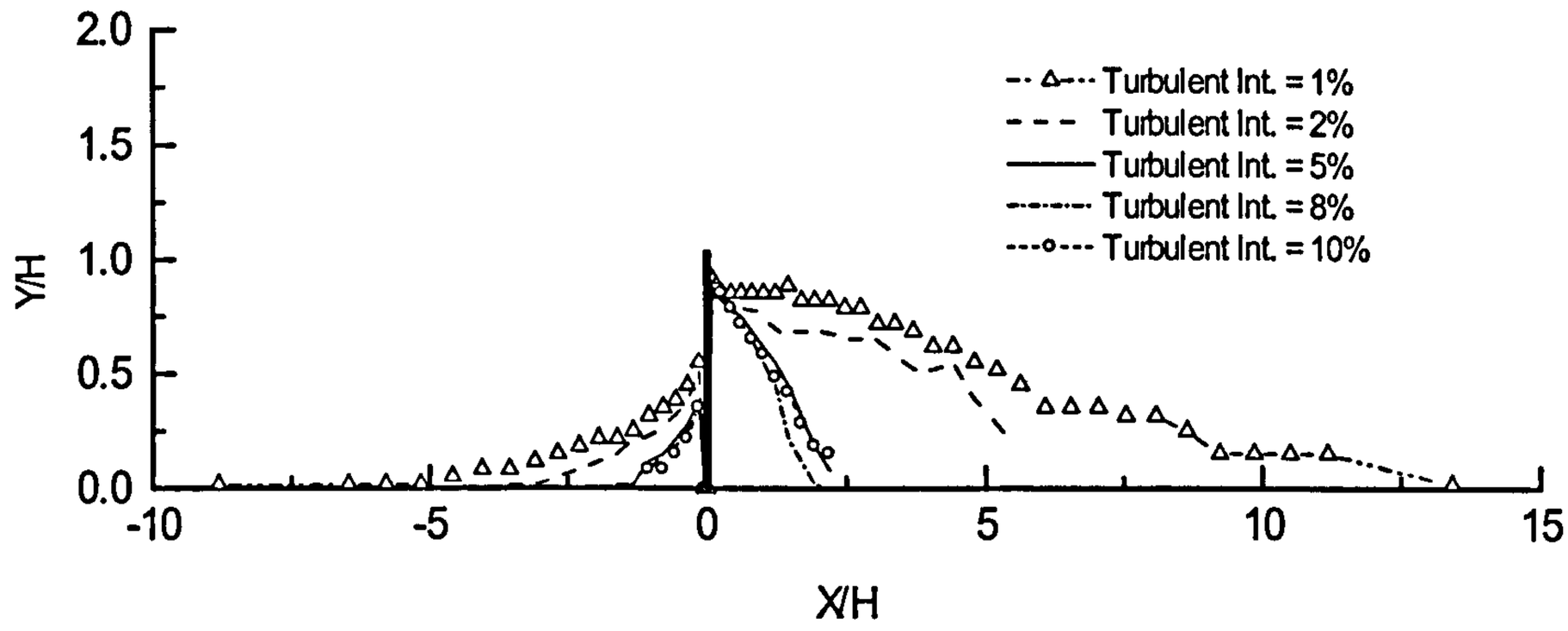

Figure 6.26: Particle deposition profiles using different inlet turbulent intensity.

6.11 Deposition around fences of different geometry

The wall geometry is an additional parameter that can influence the shape and the volume of the deposited particles. The previous sections examined the effects of the major controlling parameters on the deposition process, which were examined for flow around a single solid wall. In this section, the effect of changing the structure of the flow field, by varying the wall geometry, on the performance of the model will be examined. It will be demonstrated that a change in the wall geometry and hence the near wall flow field effects the location and the total amount of the deposition field.

Two different wall geometries were considered in this section. The first introduces a small gap underneath the wall through where the flow can pass. The effect of the gap size on the flow field and therefore the deposition process is analysed. In the second case, the wall is defined as having 50% porosity in addition to the small under-wall gap and the effect on the model behaviour of changing the suspension and saltation source term coefficient is examined.

6.11.1 Deposition at solid wall with different bottom gap heights

The introduction of the under-wall gap acts to eliminate the front recirculation zone while the eddy behind the wall expands further downstream pushing the reattachment point far downstream. Three different gap sizes were tested: 10%, 20% and 40% of the total wall height H. Initially the steady state solution using the homogenous model alone was employed for all cases. The FAVOR technique was then coupled with the homogenous solution to investigate the different stages of the development of the solid interface boundary representing the deposition profiles.

Figure 6.27 shows the steady state solution where the maximum particle concentration zone is generated behind the wall. This clearly demonstrates that an increase in the gap dimension moves the region of the high particle concentration downstream, this is a direct result of the increase in the flow velocity through the gap due to the nozzle effect.

The movement of the high concentration region will continue until the under-wall gap become large enough so that there is no significant variation in the particle volume fraction throughout the domain, as in the case for the 40% gap.

The inclusion of the FAVOR model in the calculation, as shown in figure 6.28 for the case of 20% gap, demonstrates that the particle deposition conditions are satisfied initially at a distance behind the wall location, at 5 to 6 times the wall height. Thus the first solid interface boundary created by FAVOR takes the form of a small dune as shown at T/Te = 15%.

After several accumulation steps, the deposition profile reaches the steady state situation where no more accumulation can be achieved by further calculations. This means that along the whole interface boundary, the friction velocity does not exceed the threshold value, and no erosion occurs. Equally the friction velocity does not drop below the threshold velocity simultaneously with an increase in the particle volume fraction so that further depositions may occur.

It can be noticed that the deposition profile has a sharp edge at the front. In real life this is what is known as the slip face of the dune where the particles slide down due to the high slope. This natural behaviour is beyond the capabilities of the FAVOR technique and it requires special treatment to maintain the slip face angle wherever it exists.

In figure 6.29, the Homogenous-FAVOR steady state solution is shown for the different gap sizes. It is clear that, in the case of the small gap the profile develops closer to the wall than the other cases. In the 40% gap, the effect of the wall on the deposition process is less and only a small dune develops far from the wall with a dune crest at a distance about 10 times the wall height H.

The 20% gap shows the largest amount of the deposited particles, which have a profile span over about 30 times the wall height H and dune crest height about 20% higher then the wall at a distance from the wall equal to 2H.

6.11.2 Deposition around 50% porous wall

Regular gaps are opened in the wall so that the solid wall becomes 50% porous, a weak flow region is generated behind the wall, which has different

characteristics than those of the weak region developed behind the solid walls with or without the gap. Figure 6.30a shows the wind velocity profiles at different distances across the domain comparing those of the solid wall to the 50% porous one. It is clear that the reverse flow found behind the solid wall no longer exists in the case of the porous wall but a significant reduction in the wind velocity is found in the area where the particles may satisfy the settling conditions.

Figure 6.30b shows higher values of the particle volume fraction close to the ground in the case of the porous wall than in the case of solid wall. These high values of the volume fraction are found near the surface even at large distances downstream, which gives an indication of the possible width of the deposition zone resulting from the wall porosity.

Using the same initial set-up conditions that have been used previously for the model controlling parameters, the homogenous model coupled with FAVOR was examined for the porous wall of different gap heights between the wall and the ground. The results are shown in figure 3.31, which clarify that due to the wall porosity, the majority of the deposition process occurs behind the wall while the gap size has the same effect on the deposition location as found when using the solid wall.

As the gap size increases the deposition area moves downstream with the flow direction whilst the largest area developed is found to be in the case of the 20% gap. Further increasing the gap height, such as the 40% case, results in a reduction in the size of the deposition profile, until a certain gap size greater than 40%, where no particles are able to settle in the flow field domain.

Figure 6.32 shows the subsequent stages of the profile development behind the porous wall with a 20% under-wall gap. It can be seen that the deposition process is initiated at a distance from the wall equal to 7H downstream. The profile then expands both up and downstream until reaching a steady state where the dune covers an area of about 35H in length with a maximum height about 20% above the wall height at 5H downstream.

Also, a small deposition profile is created just before the wall as a result of the modification in the flow field due to the large deposition solid surface developed behind the wall. The effects of the values of the suspension and saltation source term coefficients, β_{sus} and β_{Salt}, on the final deposition profile were examined for the case of porous wall with 20% gap. Figures 6.33 and 6.34 shows the steady deposition profiles as the coefficient values are changed alternately. Both coefficients are shown to be directly proportional to the deposition profiles.

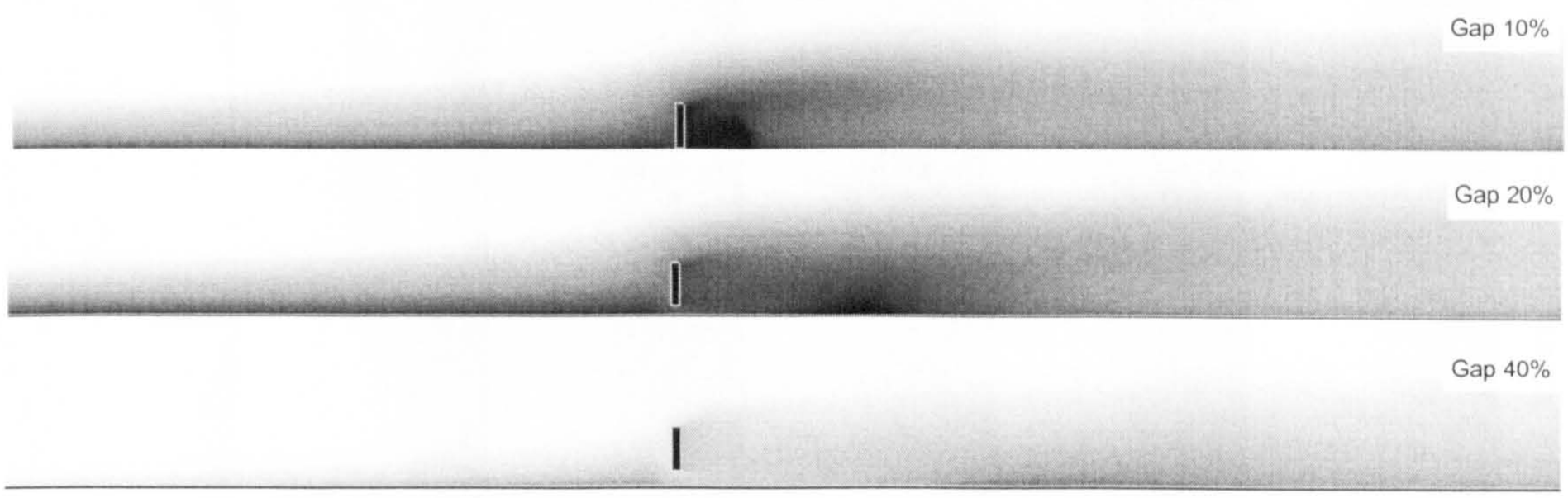

Figure 6.27: Particle concentration around solid walls with different gap heights.

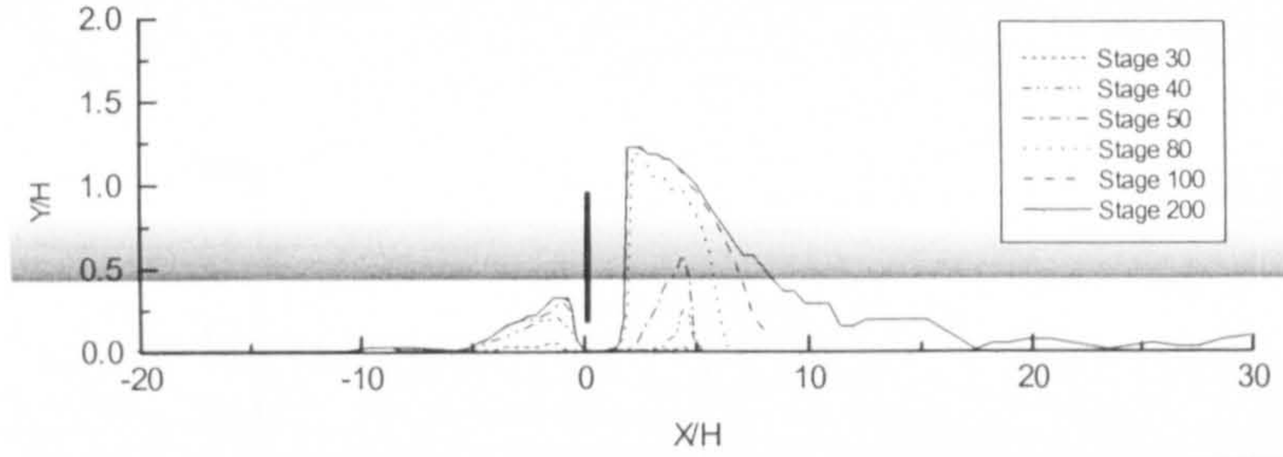

T/Te = 15%

T/Te = 20%

T/Te = 25%

T/Te = 40%

T/Te = 50%

T/Te = 100%

Figure 6.28: Stages of particle deposition profiles around solid walls with 20% gap.

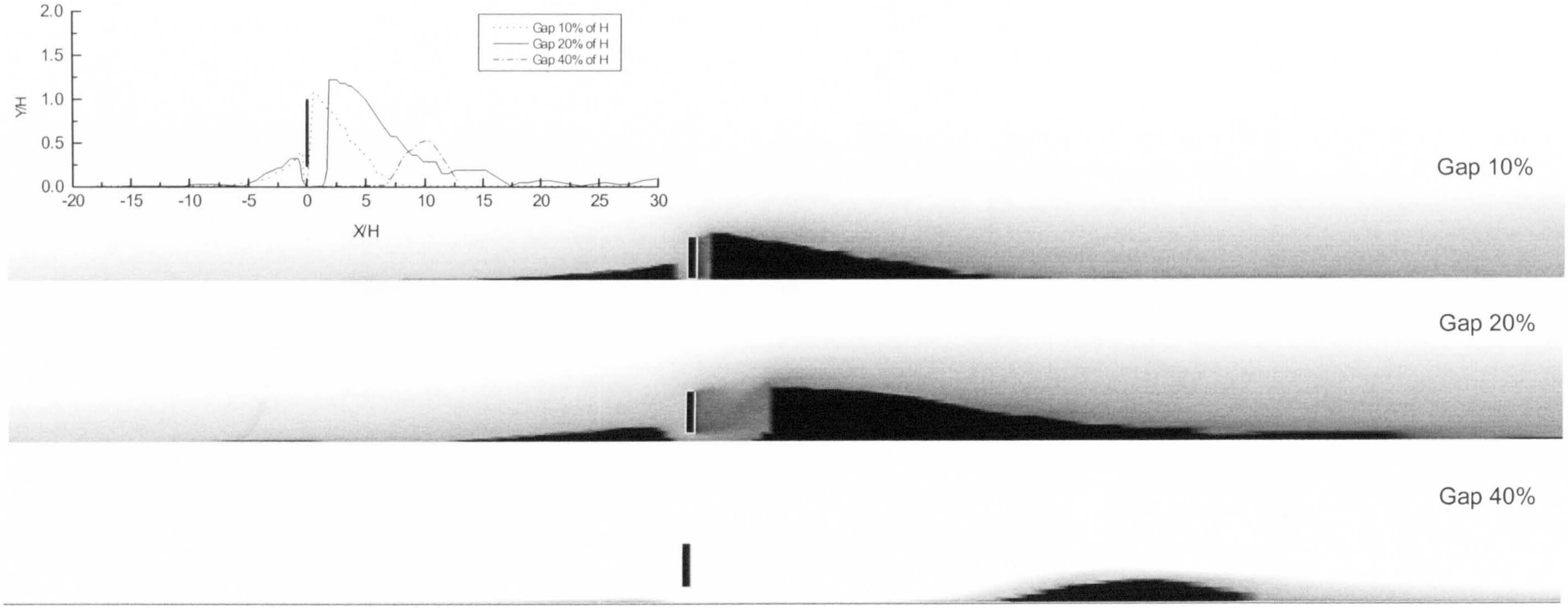

Figure 6.29: Particle deposition profiles around solid walls with different gap heights after including FAVOR.

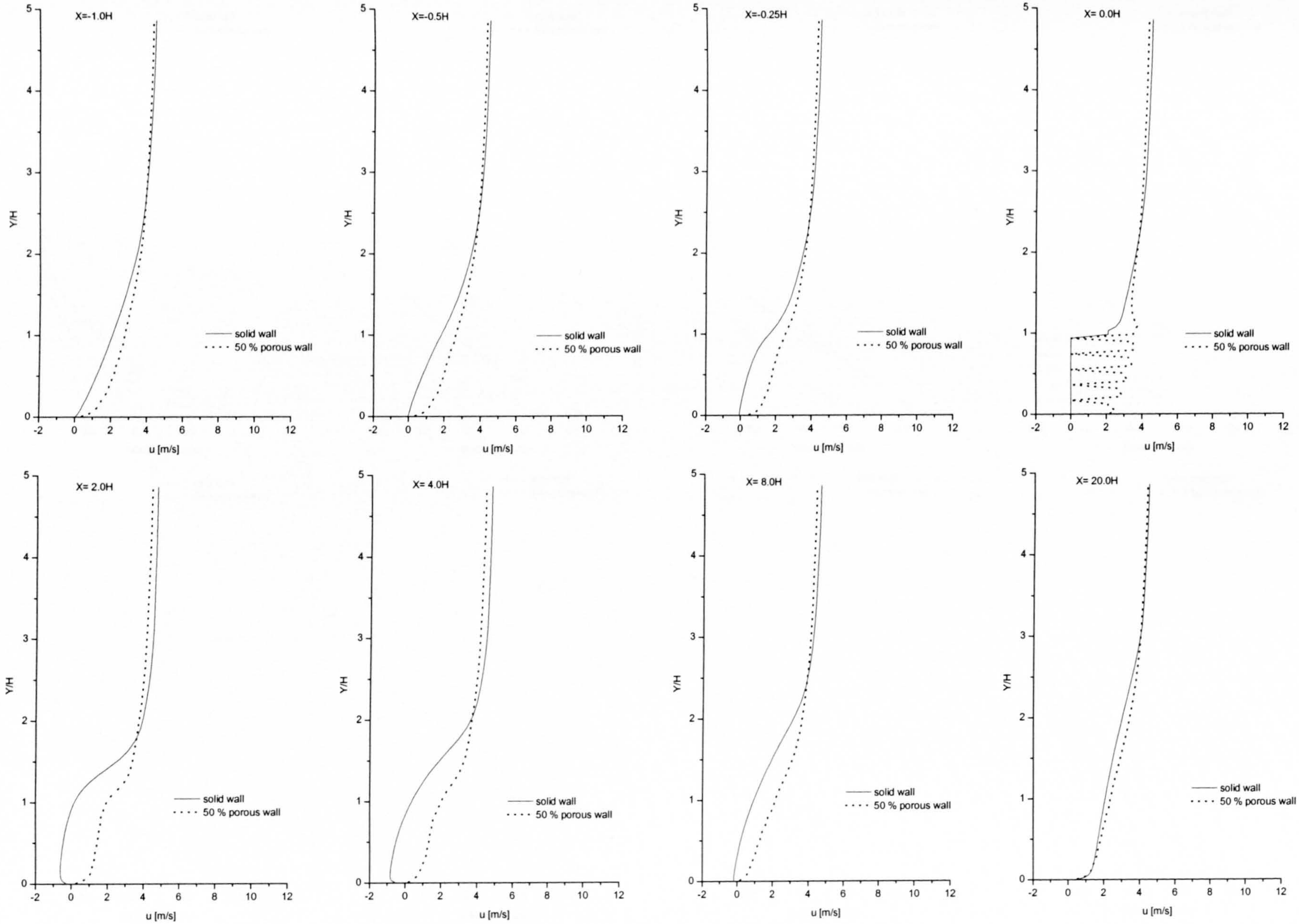

Figure 6.30a: Wind velocity profiles around solid and 50% porous walls.

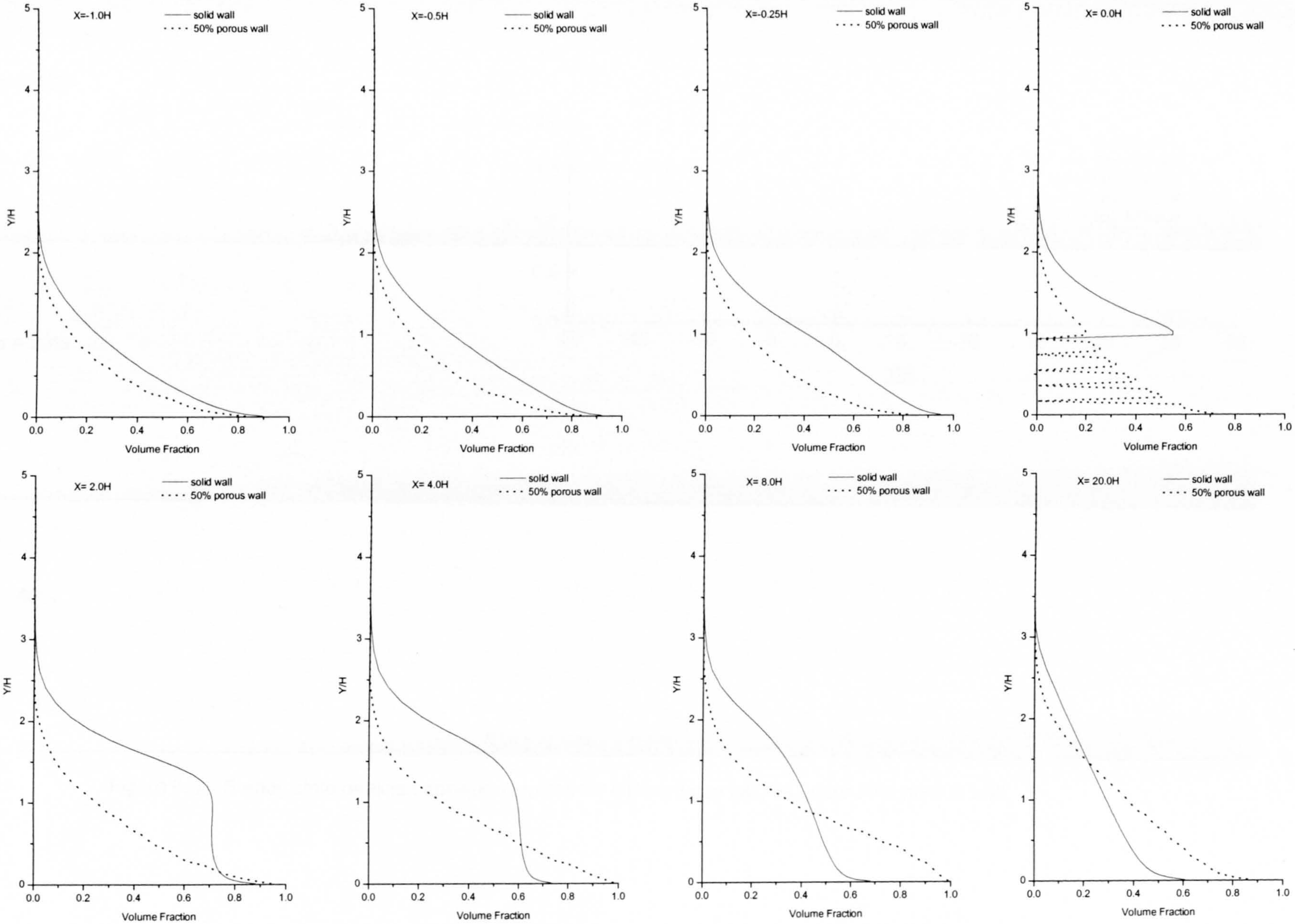

Figure 6.30b: Particle volume fraction around solid and 50% porous walls.

Gap = 10%

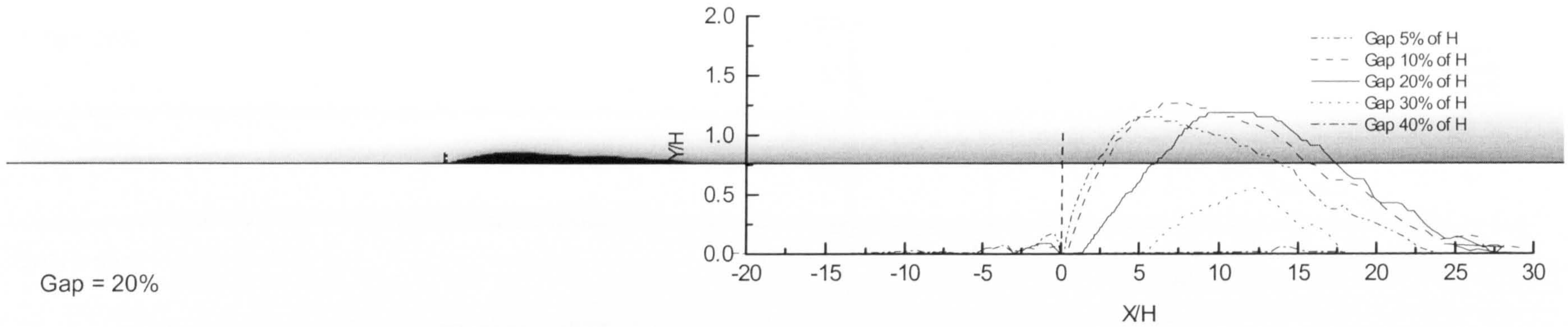

Gap = 20%

Gap = 40%

Figure 6.31: Steady state particle deposition profiles for different gap heights under 50% porous wall.

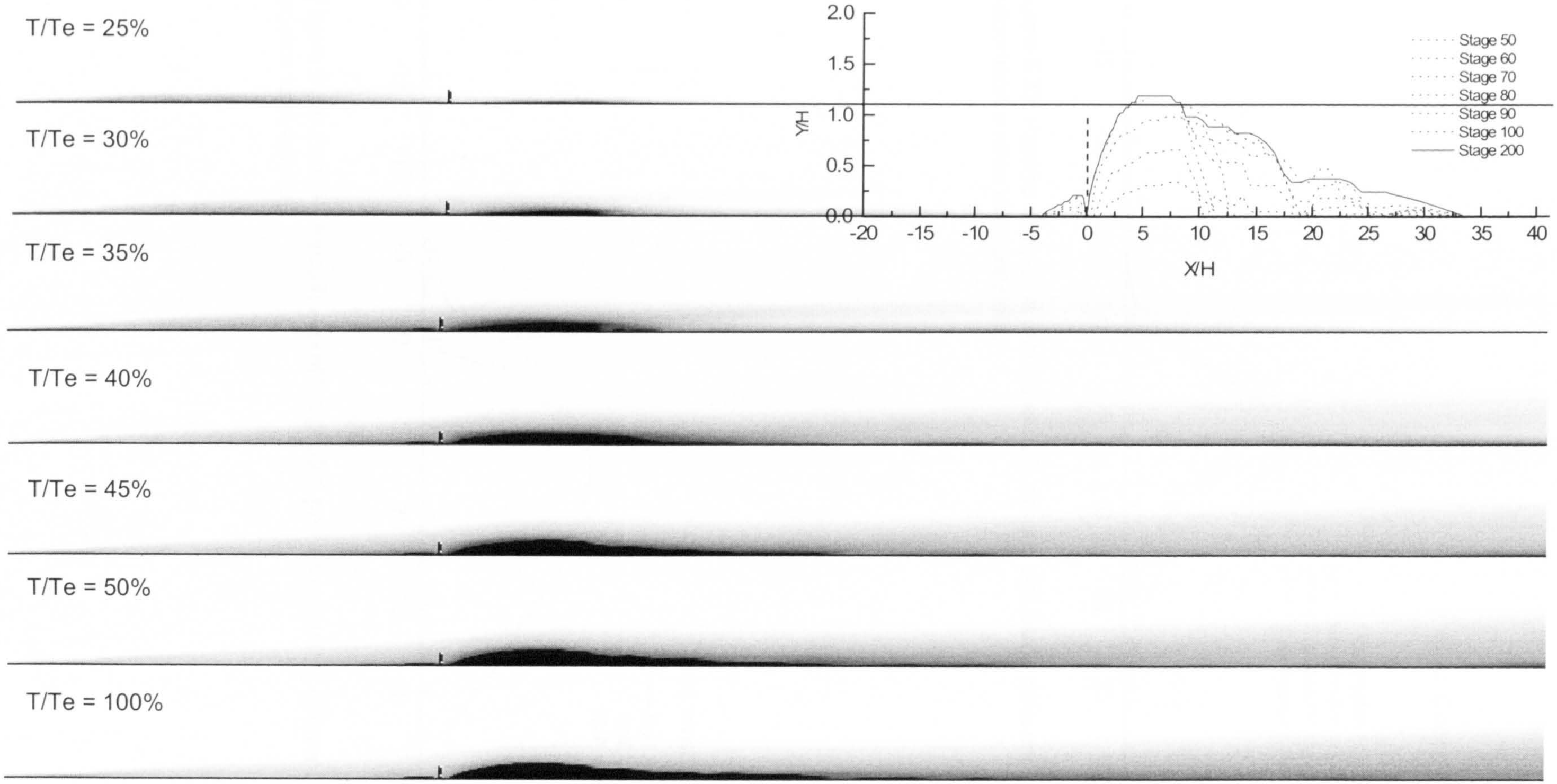

Figure 6.32: Transient particle deposition profiles at 50% porous wall. (saltation const. = 0.2 and suspension const. = 0.08)

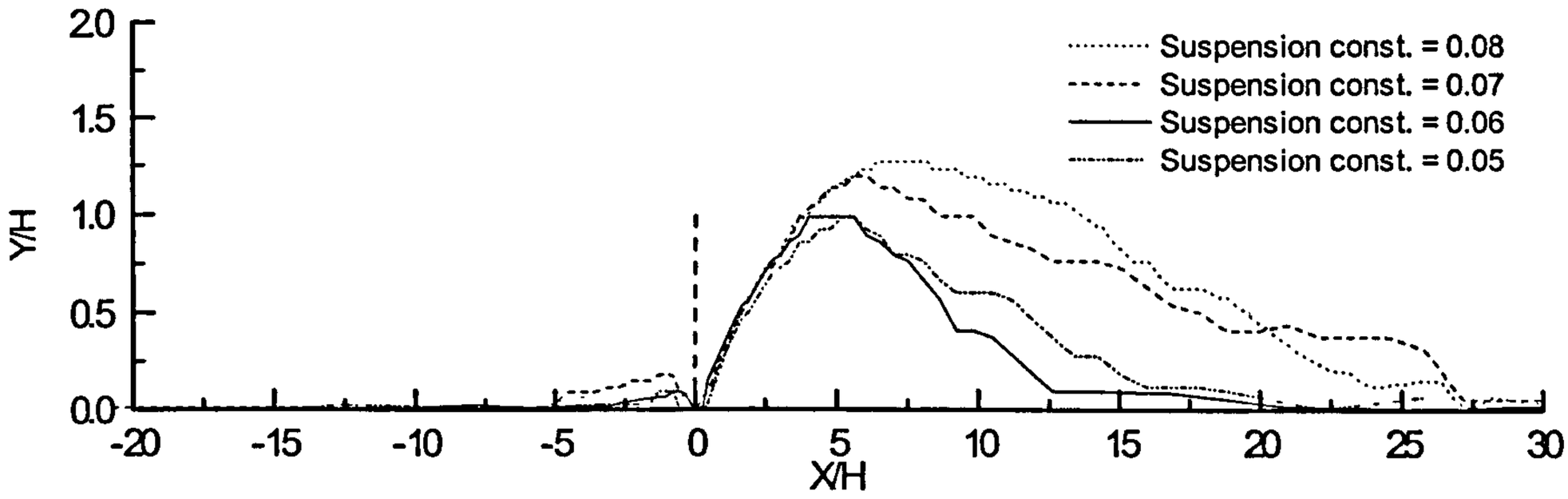

Figure 6.33: Particle deposition profiles at 50% porous wall using different suspension source term constant.

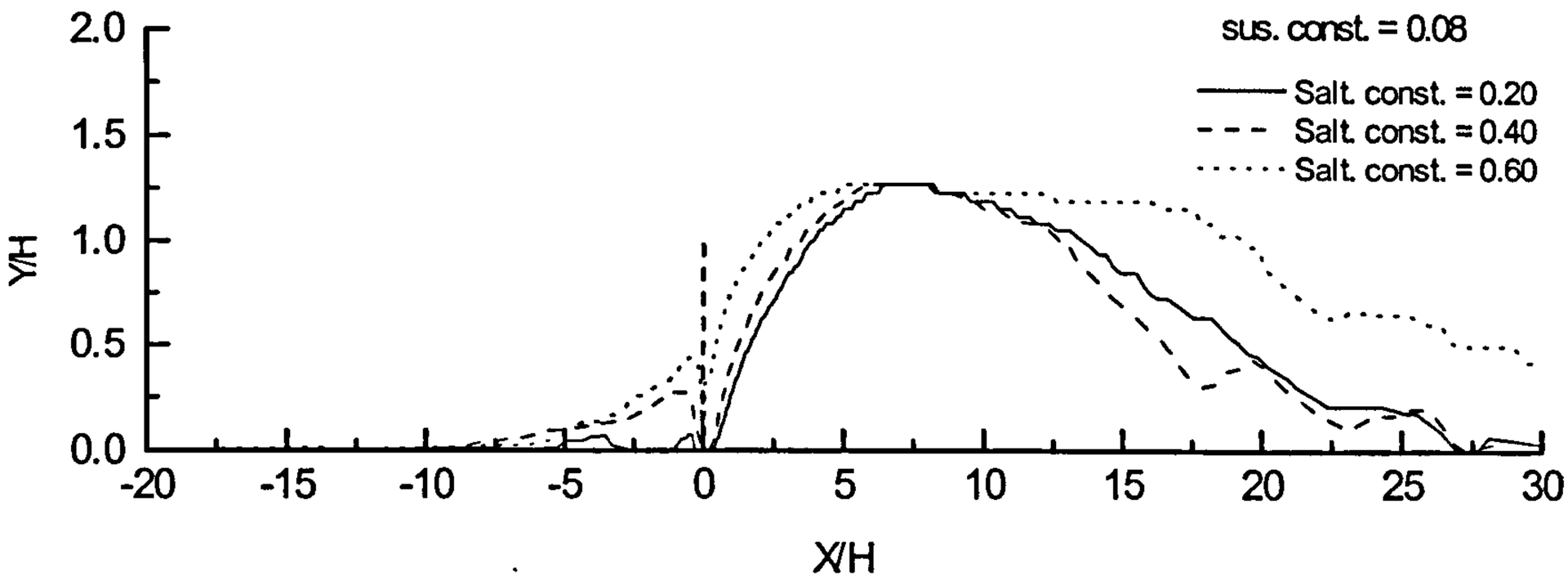

Figure 6.34: Particle deposition profiles at 50% porous wall using different saltation source term constant.

6.12 3-D deposition simulation around obstacles

In this section, the model is tested in a three-dimensional computational space. The axial and vertical dimensions used in the following cases are the same as those used in the above two-dimensional problems with the same grid distribution. The third dimension is the domain depth in the z-direction, which is chosen to be 0.25m with 50 uniformly distributed grid points, hence all control volumes in the domain have a uniform depth of 0.05m.

6.12.1 3-D deposition simulation around a solid wall

A series of steady state simulations were undertaken in which the depth of the solid wall was varied on the prediction of the flow around the solid wall. The wall was of height H and was located 40H from the inlet boundary. The wall depth was specified in terms of the wall height, 2H, 4H and 6H respectively.

Figure 6.35 shows the iso-surface of the particle concentration at a volume fraction equal to 0.75. The colour represents the values of the surface friction velocity shown in the legend, which varies between −0.25 and 0.25 m/s.

The particle threshold value was defined at 0.22 m/s hence the deposition area can be easily identified from the intermediate values where the friction velocity varies between −0.22 and 0.22.

The shape of the deposition area is seen to change with a change in the depth of the wall. A horseshoe deposition shape is formed around the small wall with two small eddies resulting from the wall ends effect, this is clarified by the streamlines.

The increase in the wall depth results in a symmetric flow field in which the deposition area along the centreline in front of the wall moves forward. The reverse flow sheet in front of the wall is stronger at the edges causing particle erosion to be greater at the edges than the centreline region of the wall.

At the middle of the wall this reverse flow becomes weaker due to the separation of the flow into two opposite directions towards the wall edges, which results in a small deposition area directly in front of the wall as shown in the case of the

4H wall. The front deposition area becomes even larger in the case of the 6H wall.

The FAVOR model was then coupled to the solution for the case of the 4H-wall depth allowing those regions, which satisfy the deposition conditions to form a solid interface boundary. The first 40 steps are shown in figure 6.36. The figure shows several flow features including the deposition areas as an iso-surface coloured by surface friction velocity and the flow streamlines.

In the early stages of the deposition process, the deposition conditions were satisfied in three regions. The first, as mentioned, due to the reverse flow in front of the wall, forming the horse shoe shape at a distance from the wall. Areas closer to the wall experience high reverse flow velocities, thus erosion of the particles occurs in the opposite direction, from near the wall to the upstream direction.

The other two deposition areas are at the eddy zone developed behind the ends of the wall forming two tongues of deposited particles. After several stages the deposition volume increases and the flow field changes according to the growth in the interface boundary, as can be seen from the flow streamlines in the different stages.

The irregularity of the deposition geometry at the ends of the deposition area, as seen in stage 40, is due to numerical errors associated with the large computational cell size defined far from the wall.

6.12.2 3-D simulation of Sand Accumulation an open Gate

The final case study in this assessment is to test the performance of the model for flow at a solid wall with an open gate in the middle. In this case the deposition behaviour at three gates of different widths, 2H, 4H and 6H, were simulated.

In this case both the homogenous and mixture models were used. Due to the limitations of the mixture model, a flow field with suspension source term coefficient of 0.025 and zero saltation source term were used.

Figure 6.37 shows the particle concentration surface represented by volume fraction equal to 1E-4, the surface velocity vectors and the flow streamlines are also shown as well. The surface colour represents the value of the surface friction velocity, which varies between -0.25 and 0.25 m/s.

The particle threshold velocity in this exercise was defined to be 0.22 m/s ,hence areas of possible deposition can be identified in regions of high particle volume fraction and friction velocity between −0.22 m/s and 0.22 m/s. As shown in the simulation of the 2-dimensional cases, both the homogenous and mixture models showed identical solutions for low particle volume fractions.

A set of simulations was undertaken in which the suspension source term coefficient was increased to 0.08 and the saltation effects were introduced with a source term coefficient of 0.2. The homogenous model was applied with these parameters to the various gate sizes. The steady state solutions for the particle concentration at a volume fraction of 0.75 are shown in figure 3.38. The results demonstrate that for a narrow gate the deposition is much higher than that of the wider gates. A long and thin deposition area is found downstream the gate. The depth of this area increases with the increase in the gate size.

The simulation was then repeated using the FAVOR model to represent the solid interface boundary for the gate size of 4H. Different deposition stages are shown in figure 3.39. The deposition process starts in front of the wall and moves forward along the gate centreline. Due to the nozzle effects near the gate sides, the flow velocity increases rapidly, which results in an increase in the friction velocity giving the erosion areas shown in the figure near the gate edges.

Additionally, the figure shows that the interface boundary increases as more deposition occurs and as it climbs both sides of the wall. The streamlines in the figure shows the change in the flow field as a result of the growth in the solid interface surface as deposition occurs on both sides of the wall. The velocity vectors show a strong recirculation zone just behind the gate edges, which results in more deposition at that specific zone.

6.13 Discussions and general remarks

Different two-phase flow models have been implemented and analysed for particle deposition around obstacles of different geometry. Lagrangian particle tracking model and Eulerian, homogenous and mixture, models were investigated for wind blown particles at different wall geometries.

The Lagrangian model provided a good description of the trajectories of individual particle within the flow field. The main weakness of this model is the requirement of very large numbers of particles to be tracked to satisfy the statistically significant condition. Moreover, in the case of wind blown sand or snow particles, millions of particle trajectories of different size and shapes are necessary to be tracked to form a small deposition zone. However, this model can give detailed information of how, when and where the initiation of the deposition process may begin and how these are related to the structure of the flow field around the area of interest.

Eulerian models show potential capabilities in simulating such problems by considering the particle phase as a pseudo-continuum flow phase. Eulerian models such as the homogenous and mixture models are cheaper from the computational point of view since information of individual particles is omitted and they appear in a form of particle concentration. The main weakness of these models is first the need of an extra transport equation to be solved every time a new particle of different physical properties such as size or density is involved.

Secondly, is the need for careful modelling of the different particle transport modes as well as the treatment of the interaction between the flow field and the solid interface boundary representing regions of high particle concentration.

The mixture model has the advantage of treating the mixture as a whole while the reduction in the flow velocity due to the existence of high concentration regions is taken into account through the diffusion stress introduced into the mixture momentum equations. However, the mixture model is found to be limited to diluted flow systems where, in the present study, the maximum possible particle concentration achieved is about 1E-4 and values higher than that result in computational instabilities, which lead to unrealistic results.

The homogenous model shows qualitatively reasonable results when coupled with the FAVOR technique as a mean of representing the solid deposition boundary. From the analysis above, it has been shown that the steady state deposition profiles are always dependent on the setting of the different controlling parameters such as the suspension and saltation source term coefficients, inlet boundary condition, surface roughness and the grid distribution.

A significant advantage however is that the models introduced above are independent of the empirical expressions employed in previous studies to predict the particle mass flow rate in the saltation layer.

In general, the coupled Homogenous-FAVOR model is adopted in the following chapter to validated the numerical model result against the field and wind tunnel measurements discussed in Chapter 3.

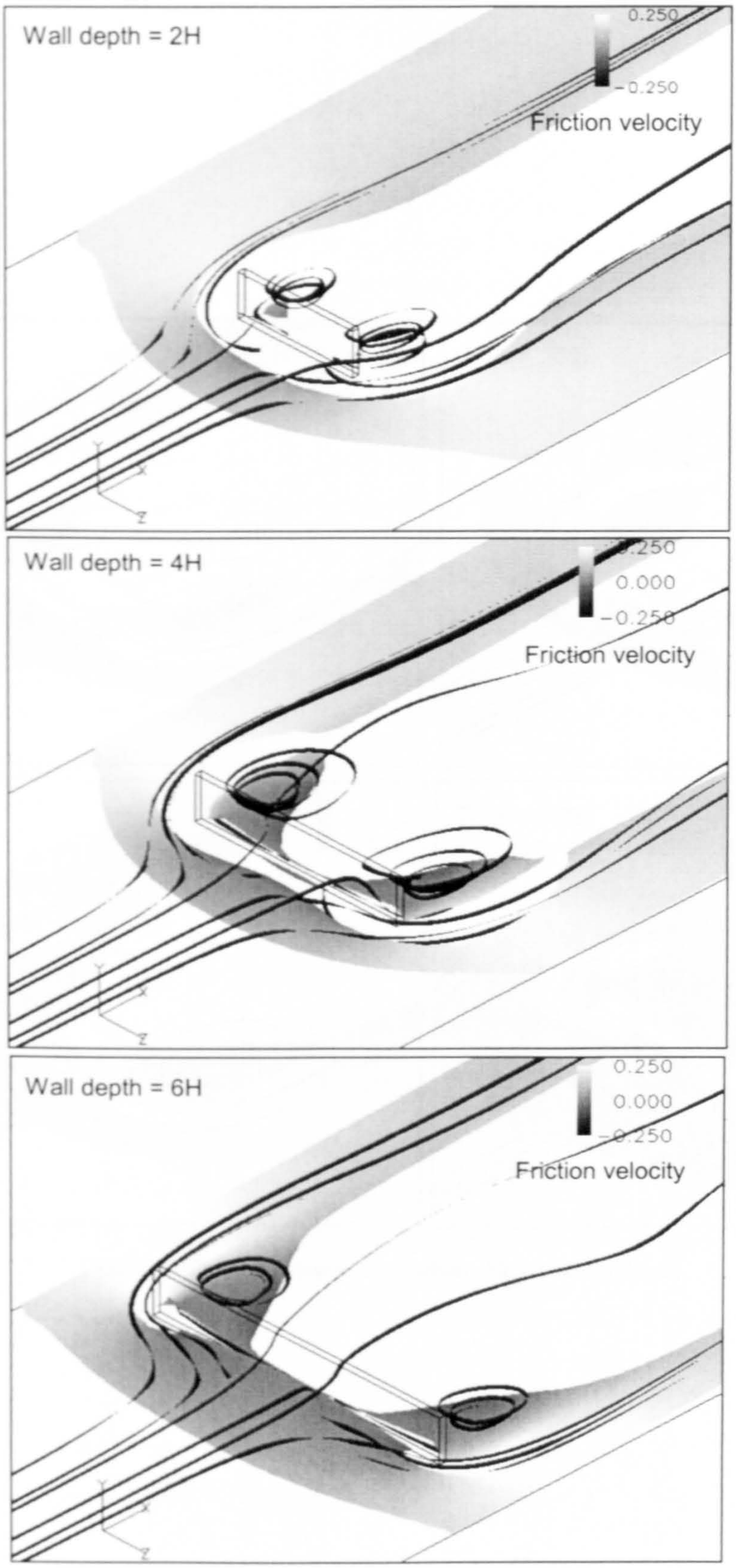

Figure 6.35: 3D particle volume fraction around solid walls with different depth in Z-direction. Iso-surface represents the surface flow friction velocity.

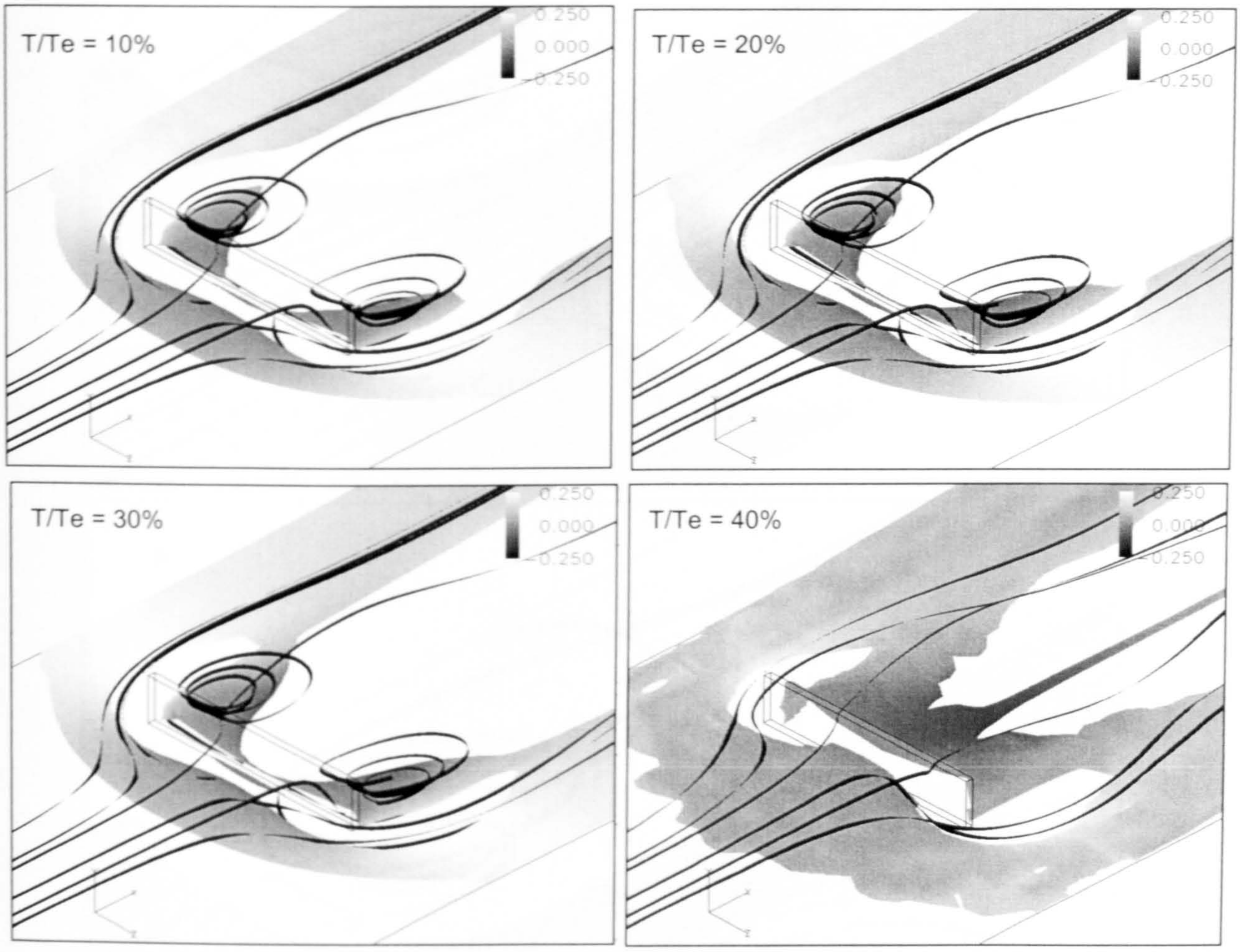

Figure 6.36: 3D transient deposition stages at solid wall.

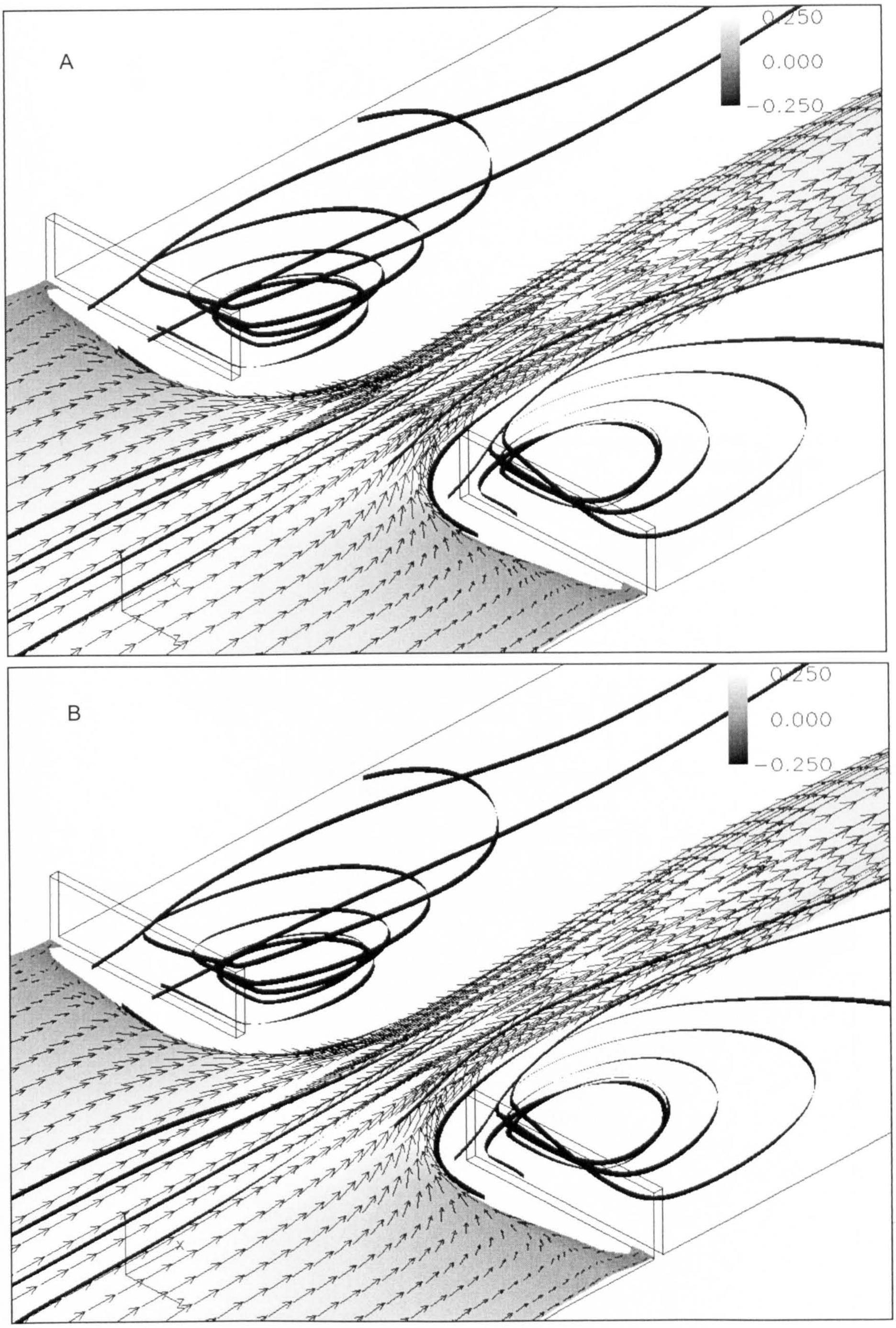

Figure 6.37: 3D steady state solution around gate. A) Homogenous model. B) Mixture model.

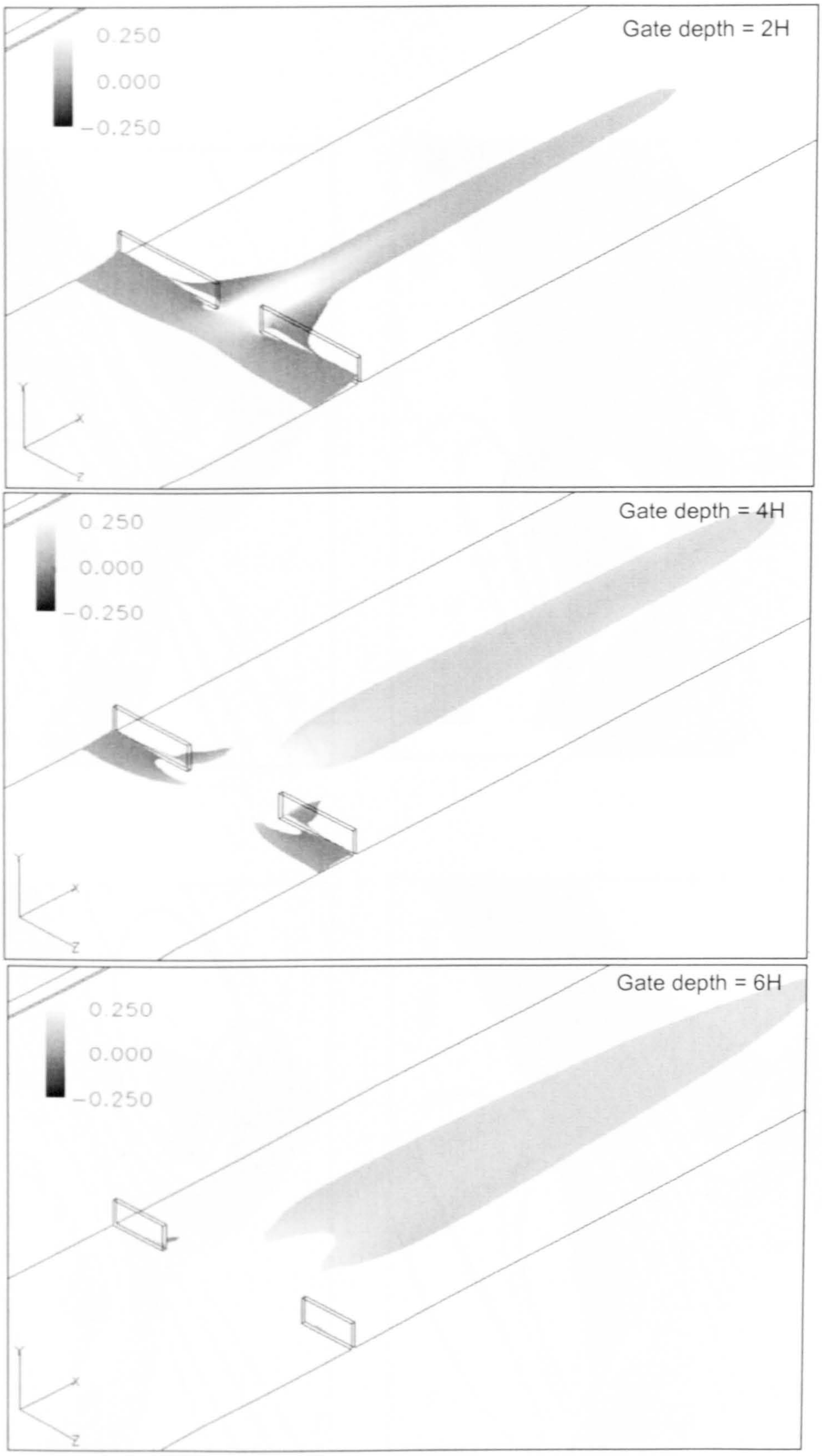

Figure 6.38: 3D steady state homogenous solution around gates of different sizes. (Iso_surface based on particle volume fraction 0.75)

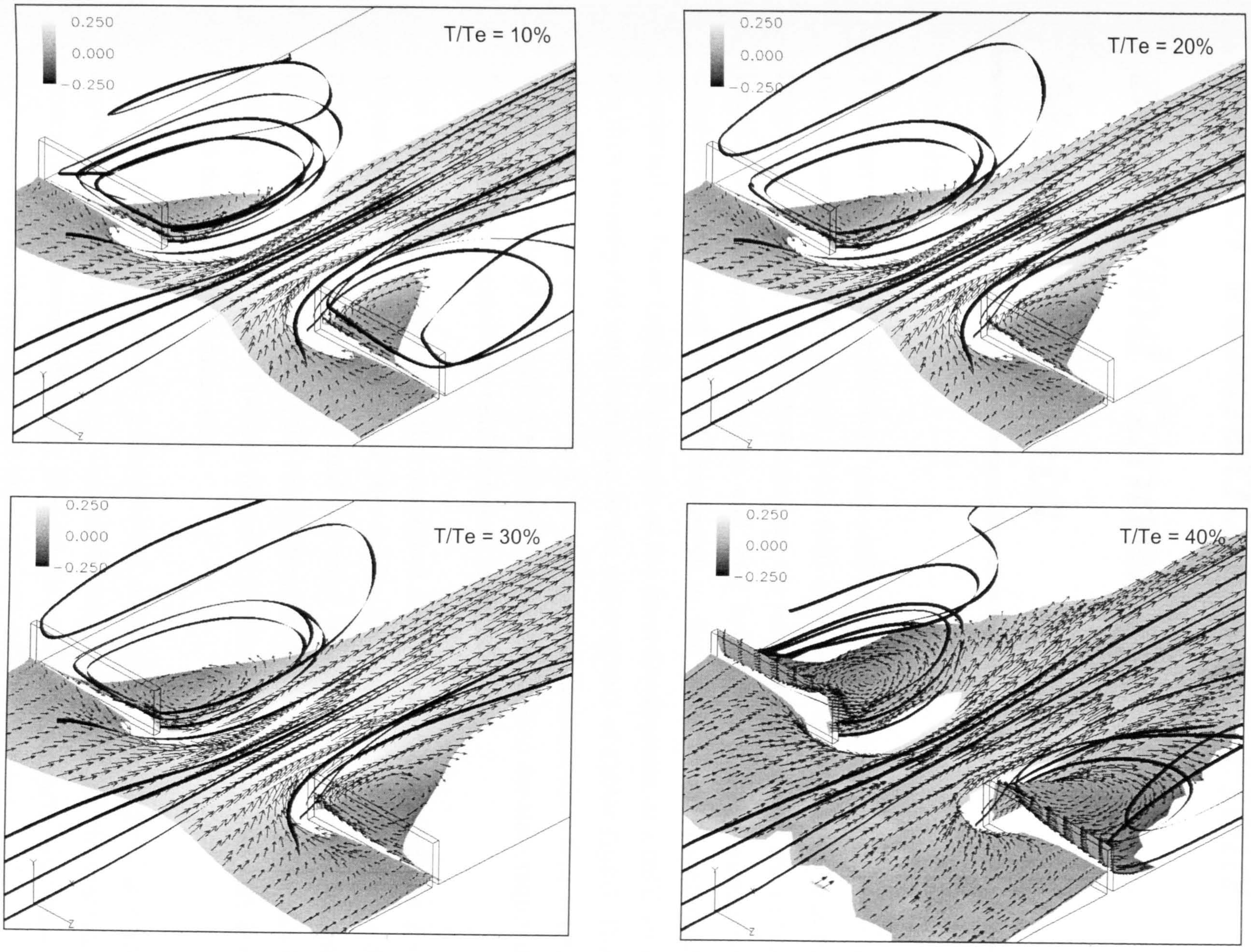

Figure 6.39: 3D transient deposition stages at open gate. Iso-surface colour represents the surface flow friction velocity.

Chapter 7

Model Validation with Field and Wind Tunnel Measurements

7.1 Introduction

This chapter covers four different case studies used to validate the numerical models presented and analysed in the field and wind tunnel studies given in Chapter 3. The first case study focuses on the relationship between the initial location of the deposition process and wall height, for this the numerical simulations are based on and compared to the wind tunnel experiment conducted by Tsoar (1983). The stages of the dune development at a solid wall are then investigated with reference to the observations of Tabler (1981). The deposition stages are presented as a function of the dimensionless time ratio, which is the ratio of the time at a specific deposition stage to the time required for the deposition process to reach the state of equilibrium.

The second case study covers the numerical simulation of snow drifts at the Wyoming 50% porous fence and the results are compared with both field measurements of Tabler (1981) and the wind tunnel experiment of Iversen (1981). In the third case study, the results from the full-scale simulation of sand drifting at multiple rows of porous fences is presented and compared with the Kuwaiti desert field measurements.

The final case study involves a 3-dimensional simulation of sand drifting around a gate facing the flow direction. The results are compared with observations from a field experiment held in the Kuwaiti desert. Finally, a general discussion and comments on the results of the numerical model are presented.

7.2 Case study I: Accumulation at a solid wall

7.2.1 Comparisons between predicted and wind tunnel measurements of the initial particle deposition at a solid wall

The homogenous model was employed to predict the initial deposition stages at a solid wall of different heights and the results were compared with the observations of Tsoar (1983) discussed in Chapter 3.

The dimensions of the wind tunnel test section were used to define the computational domain for the numerical experiments, 1m width, 0.82m height and 12.5m length. The wall in the wind tunnel experiment spanned the full width of the tunnel and therefore, ignoring the wall end-effects, it was possible to assume that the flow was 2-dimensional for the numerical simulations. A grid density of 150 by 80 in the axial and vertical directions respectively was used, figure 7.1.

Glass spheres of 49 μm diameter and a density equal to 3990 kg/m^3 were used in the simulation with an approximated threshold velocity of 0.215 m/s based on equation(2-1).

The velocity profile of the wind at the inlet boundary was set so that the inlet friction velocity was 2% above the particle threshold velocity with a surface roughness equal to 1.0e-4m. The turbulent inlet conditions were based on a turbulent intensity of 1% and a characteristic length equal to the wall height H.

The early stages of the deposition process at walls of different heights are shown in figure 7.2. It shows that the deposition always starts in front of the wall at a distance, d, which ranges between 30% and 40% of the wall height H. The dune crest is found to be at a distance that varies between 50% and 70% of the wall height.

Table 7-1 compares the predicted ratio of the distance d to the wall height H to those measured experimentally. It is clearly shown that the predicted values lie within the measured values if d is taken from the wall to the dune crest.

The initial stages of the deposition process are strongly related to the size of the eddy generated in front of the wall. Thus for a small eddy size the distance d is small and as the eddy size increases, by increasing the wall height, d increases and therefore the deposition process starts at increasing distances from the wall.

At the stagnation point, where the reverse flow meets the upstream flow, the velocity of the flow drops significantly, it is here that the first cells in the simulation satisfy the deposition conditions.

In these regions, the suspension and saltation source terms will have negative values, hence these cells become a particle sink and the particle volume fraction increases to values above the specified blocked value where the cell is assumed to be filled by particles. In this case study the blocked value was defined to be 75% of the total cell volume.

The stagnation point also causes a reduction in the friction velocity, which can reach values below the particle threshold velocity. Since these two conditions are first satisfied simultaneously at the stagnation point, the deposition process is initiated at this point. The blocked cells represent the interface boundary separating the flow field from the dune surface, figure 7.3a, which is comparable with Tsoar's observations shown previously in Chapter 3, figure 3.2.

The existence of this boundary will modify the entire flow field especially near the newly introduced surfaces resulting in a reduction in the friction velocity and an increase in the deposition area as shown in figure 7.3b.

Table 7-1: Measurements of the distance d as it varies with the wall height H after Tsoar (1983).

H [cm]	d [cm] Tsoar	d [cm] Predicted	Error %	d/H Tsoar	d/H Predicted	Error %
1.90	0.60	0.715	19.2	0.32	0.375	17.2
3.90	1.30	1.43	10.0	0.33	0.367	11.2
5.70	1.90	1.98	4.2	0.33	0.348	5.5
7.60	2.50	2.62	4.8	0.33	0.345	4.5
9.55	3.70	4.13	11.6	0.39	0.432	10.8
12.00	4.50	5.22	16.0	0.38	0.435	14.5

7.2.2 Steady state deposition profile at solid wall

In this section, the steady state solution of the stages of the dune development at solid wall of height 'H' by activating the FAVOR technique coupled with the homogenous model. At a solid snow fence, Tabler (1994) observed the different stages of the deposition process as previously shown in figure 3.3. After the first few stages, a cavity flow can be observed between the deposition profile and the wall. Progressively this cavity is filled by snow as the dune crest increases in height while snow particles slip towards the wall until the whole cavity is covered by particles and then the dune starts to climb the wall. At the steady state, Tabler observed that the dune that was developed as a result of the existence of a solid wall of height 'H' was found to extend over a distance equal to 15H both sides of the wall.

The numerical simulation was conducted using the wind tunnel scale dimensions used in the previous section for the wall height 9.55cm. Figure 7.3a shows the dune development stages, which are characterised by the current time normalised by the time required to achieve the steady state solution. It can be seen that after the first few stages, see figure 7.4, the height of the dune crest increases at the stagnation point where the highest deposition rate occurs.

The crest of the dune is found at a distance 'd' from the wall, while the cavity flow becomes clearer inside the eddy region between the wall and the crest of the dune. Similar to Tabler's observation, the distance 'd' decreases with time while the cavity decreases in size.

The cavity is characterised by a weak flow field velocity where the surface friction velocity drops to values well below the threshold value. The value of the particle volume fraction in the cavity is usually much lower than the maximum blocked value and as a result the deposition conditions are never met in this region.

Figure 7.3b shows the velocity vectors around the wall and in the accumulation region. It shows the growth of the interface boundary generated by the FAVOR technique, which represents the dune surface. It is clearly seen how the

existence of the interface boundary does effect the flow field by reducing the flow velocity as a result of the increase in the surface shear stress. Therefore the deposition conditions are satisfied along the dune boundary and progressively the dune increases in size with time as shown in figure 7.3b.

The existence of this cavity may cause numerical instability, especially for very small size of the cavity that might be captured by a small number of control volumes. In order to avoid such a cavity to be existed while surrounded by blocked cells, the deposition interface boundary was enabled to grow in a form of layers, one layer at a time, that is started from most lower surface. The layers are allowed to build on the top of each other starting from the bed surface or the old deposition boundaries in the outward direction as shown in figure 7.5a.

The steady state deposition profile shows that the dune expands upstream and downstream of the wall over a distance equivalent to 15 times the wall height H in each direction. This was found to be in good agreement with the observations of Tabler shown in figure 7.5b.

Another series of wind tunnel experiments were conducted by Iversen (1981) for the deposition around solid walls of different geometry, a simple solid wall, a hedgerow of 1.75 cm width and a hedgerow of 5.5 cm width. In all cases a gap was left underneath the objects equals to 0.1H. The deposition profiles shown in figure 7.6a,b and c provide a comparison between Iversen's measurements and the predicted profiles.

Although these measurements were taken at some intermediate stage of the deposition process, the numerical model shows fairly good comparisons. Since no equilibrium deposition profiles were provided from the experiments, this exercise shows the ability of the numerical model to predict some intermediate deposition stages. In addition, the steady state deposition profiles can be predicted even when the full experimental data is not available.

7.2.3 Case study I: Conclusion

The numerical model based on the homogenous model was employed to simulate air-particle flow and particle deposition patterns around solid walls of different heights 'H'. The model was then coupled with the FAVOR technique in order to take into account the effect of the dune interface boundary on the results. Additionally, the model was tested for solid walls with a gap at the bottom and for hedgerow of different width. The model shows a good qualitative agreement with the field observations especially at the early deposition stages, at which the shape and location of the initial depositions were captured successfully.

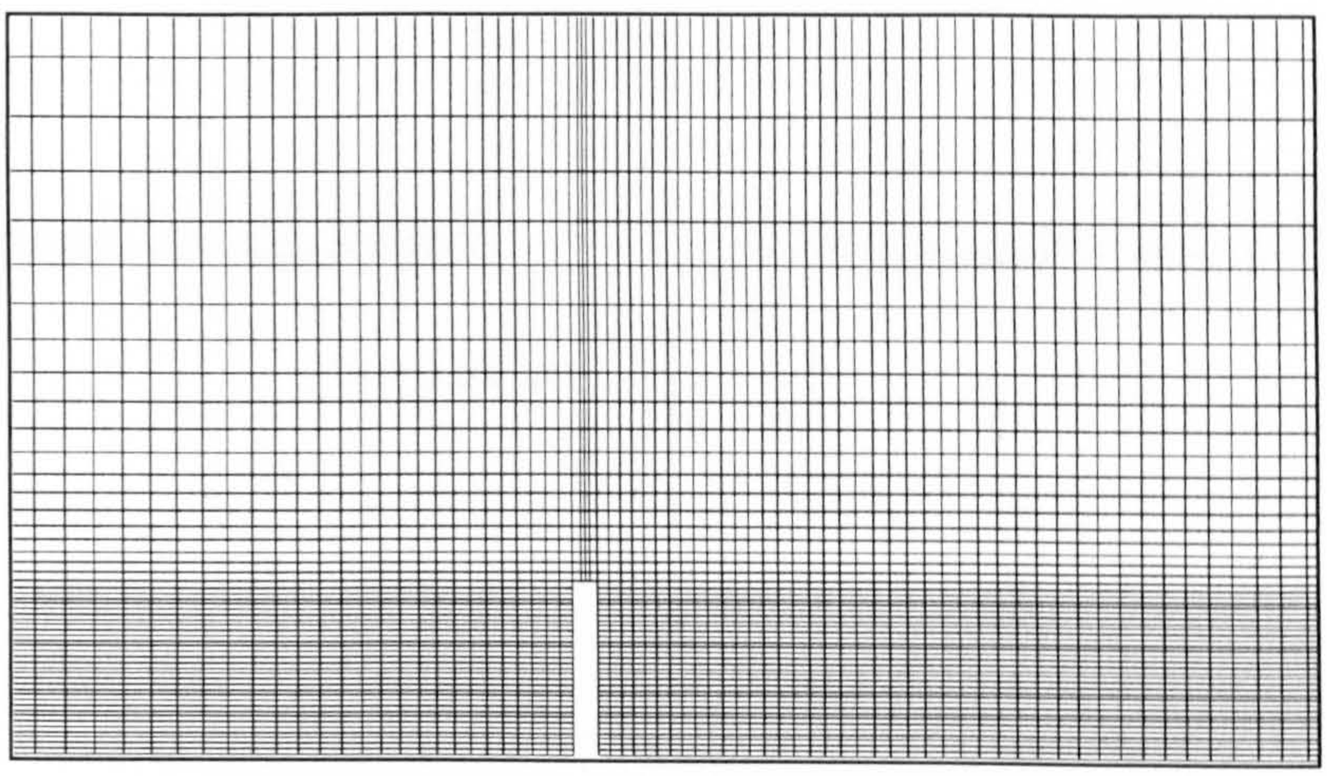

Figure 7.1: Grid distribution around solid wall.

7.2.3 Case study I: Conclusion

The numerical model based on the homogenous model was employed to simulate air-particle flow and particle deposition patterns around solid walls of different heights 'H'. The model was then coupled with the FAVOR technique in order to take into account the effect of the dune interface boundary on the results. Additionally, the model was tested for solid walls with a gap at the bottom and for hedgerow of different width. The model shows a good qualitative agreement with the field observations especially at the early deposition stages, at which the shape and location of the initial depositions were captured successfully.

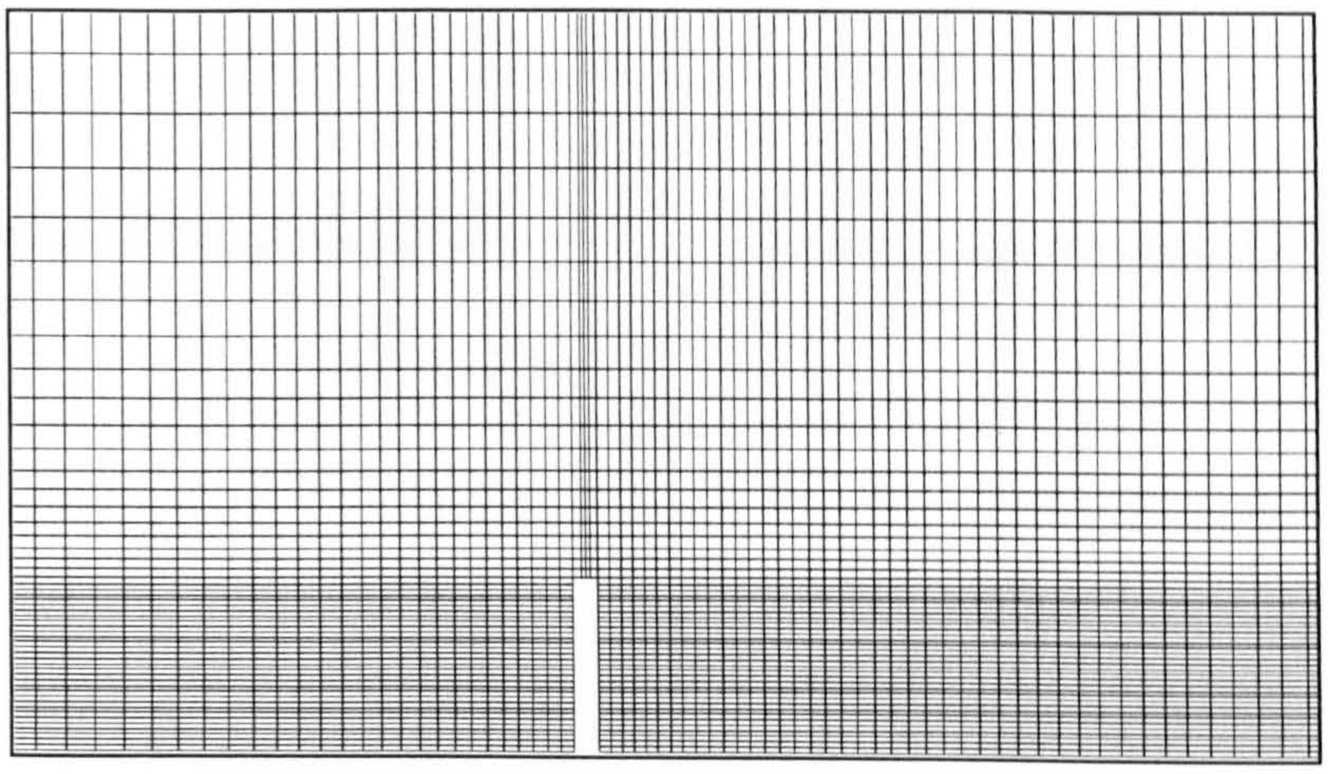

Figure 7.1: Grid distribution around solid wall.

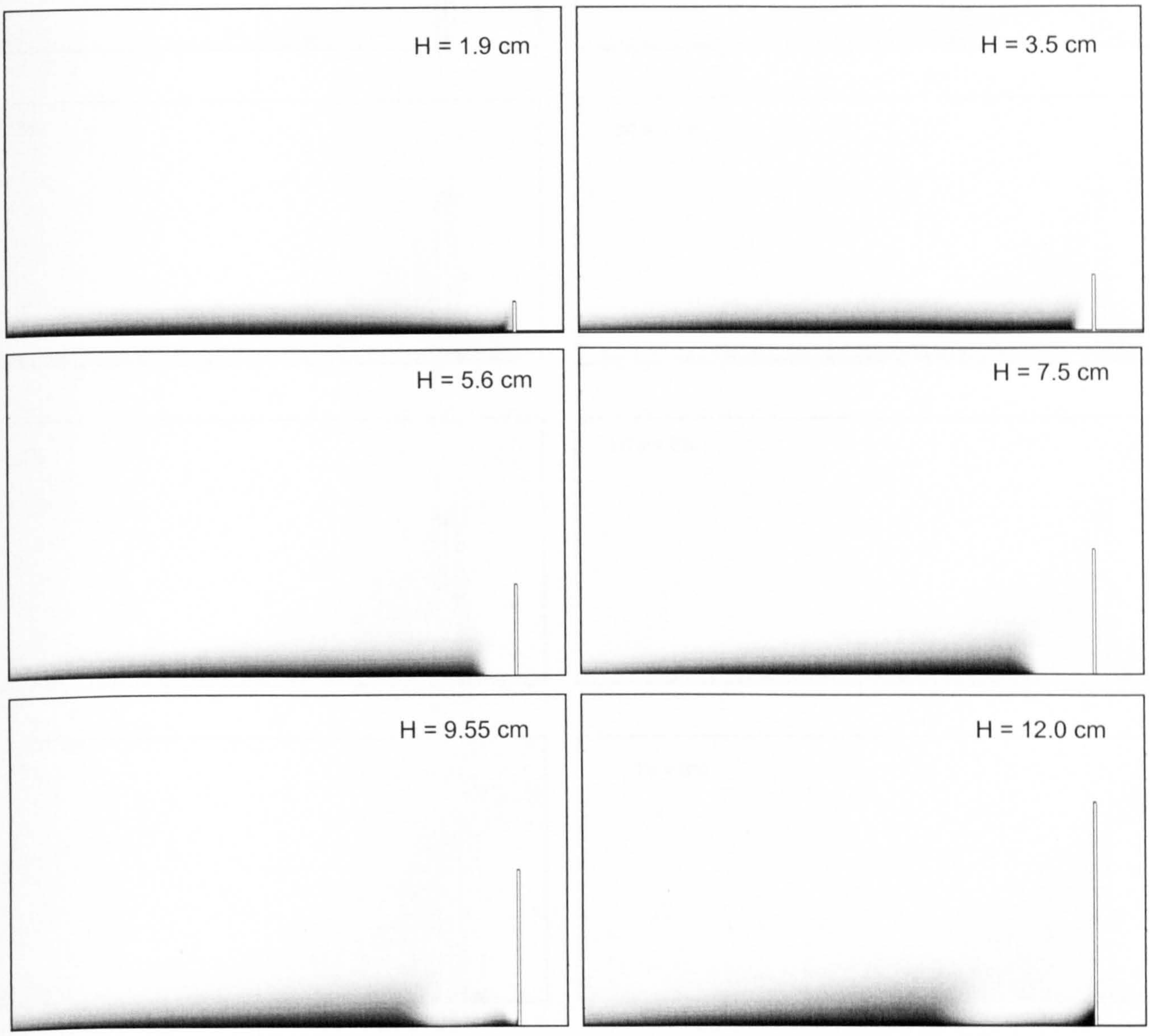

Figure 7.2: Early deposition stages in front of solid walls of different heights.

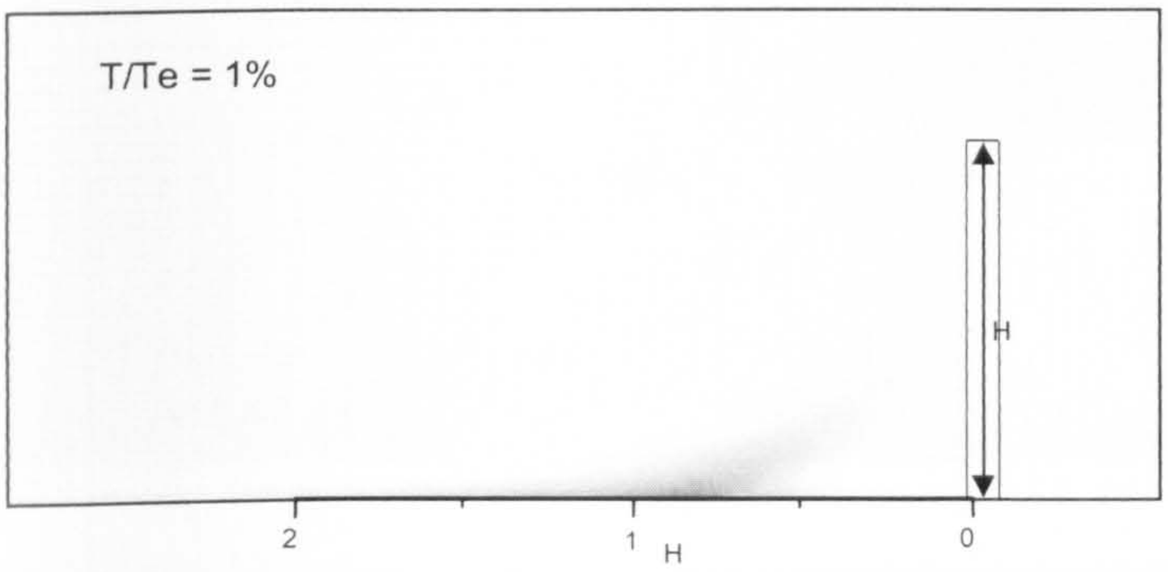

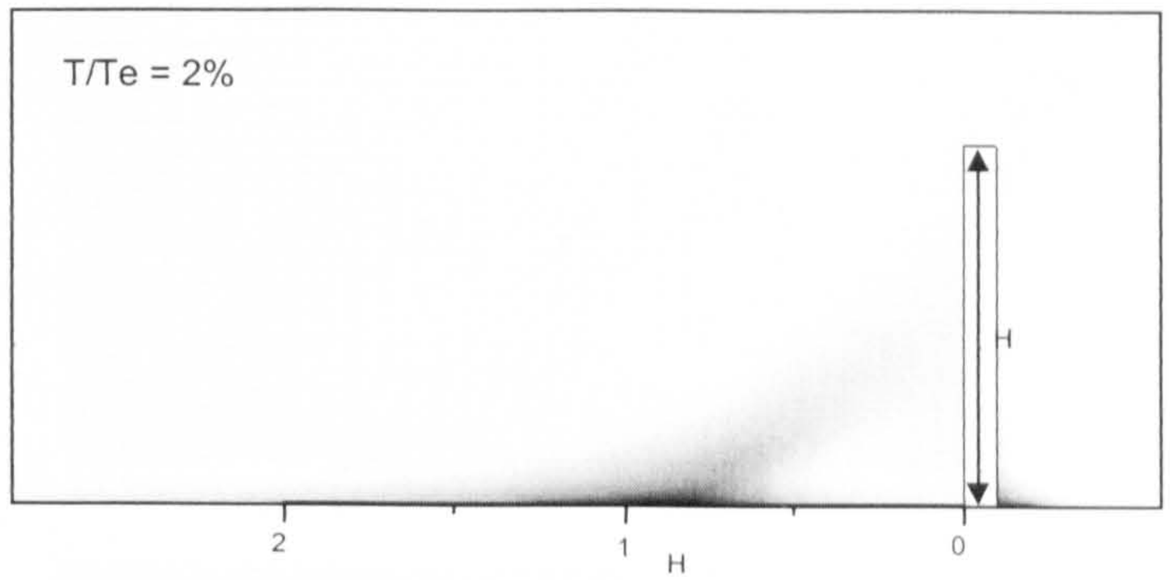

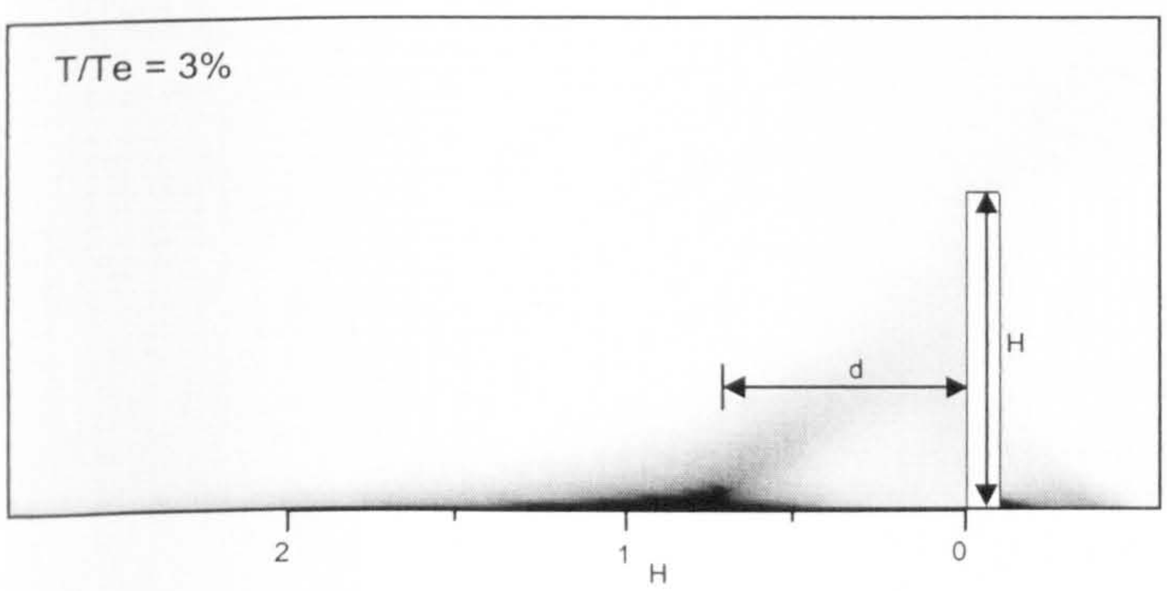

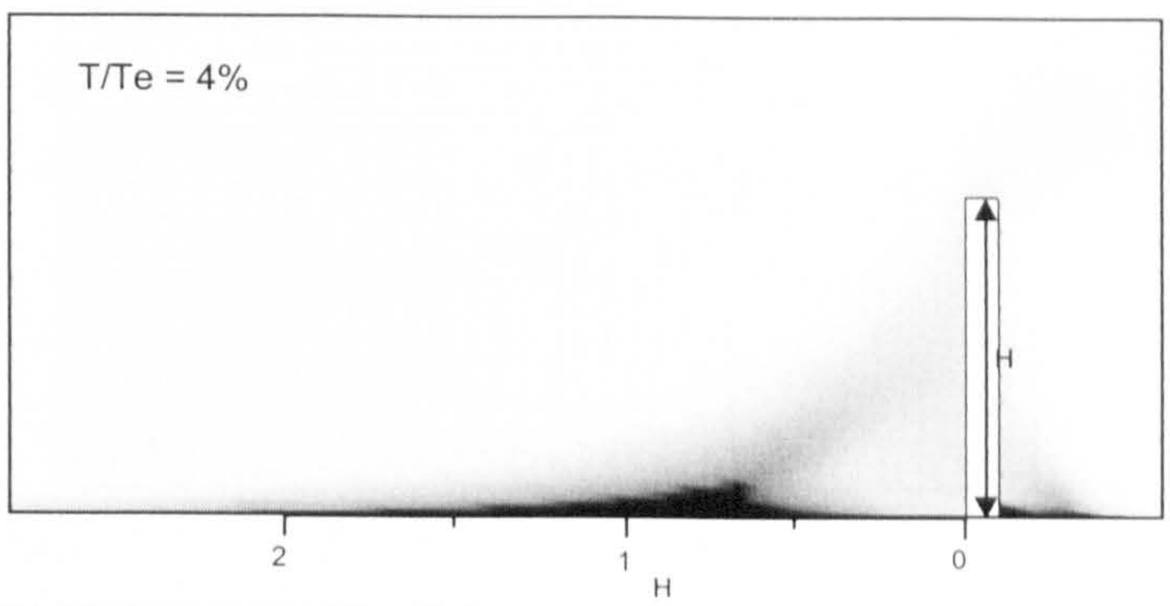

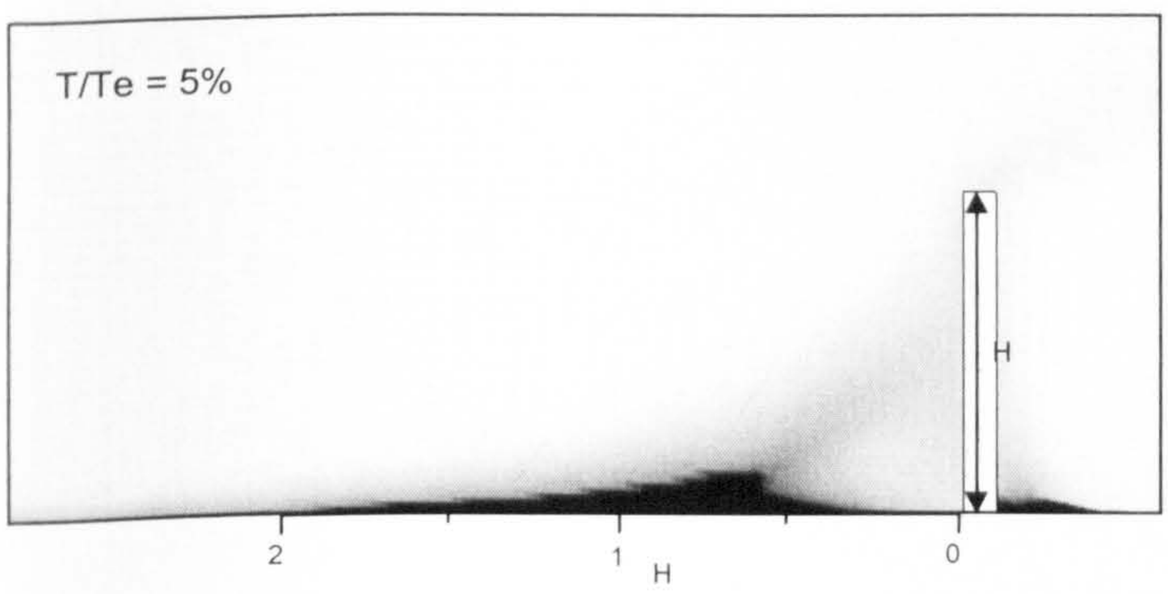

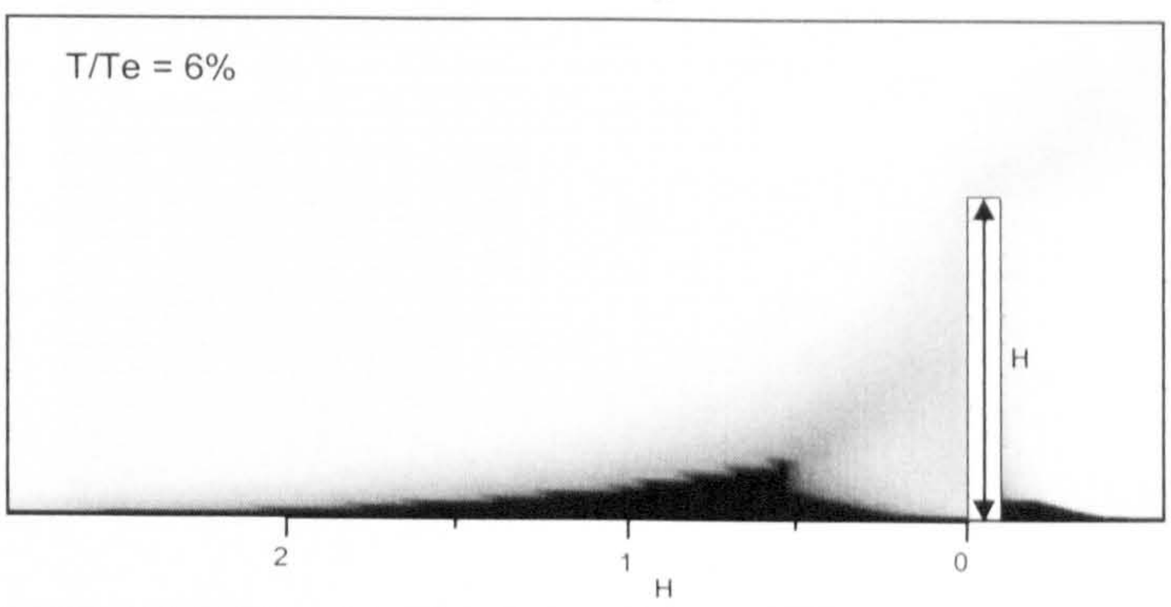

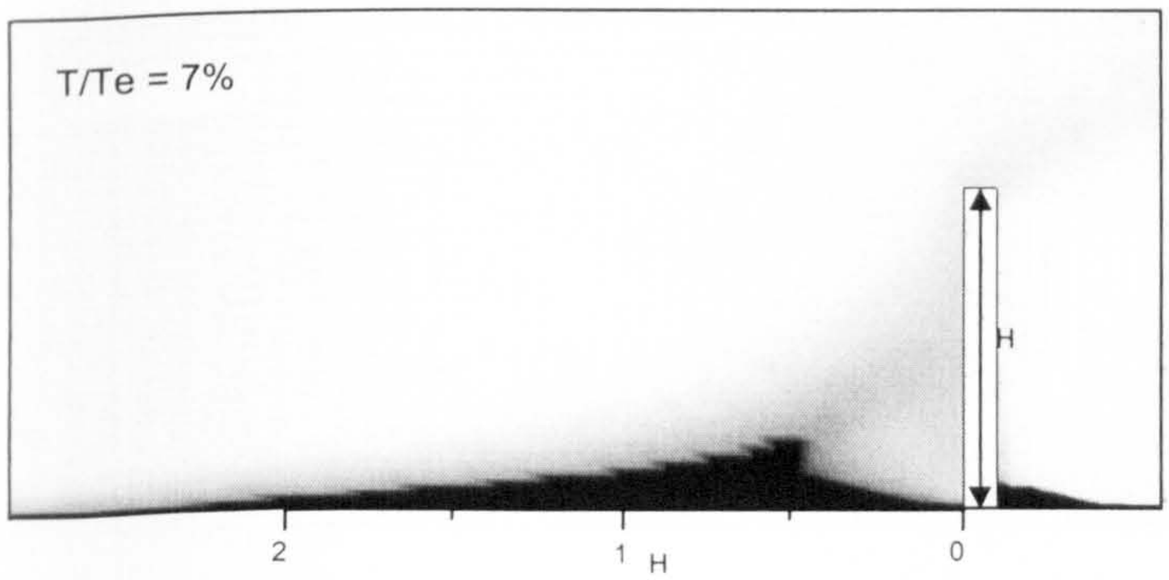

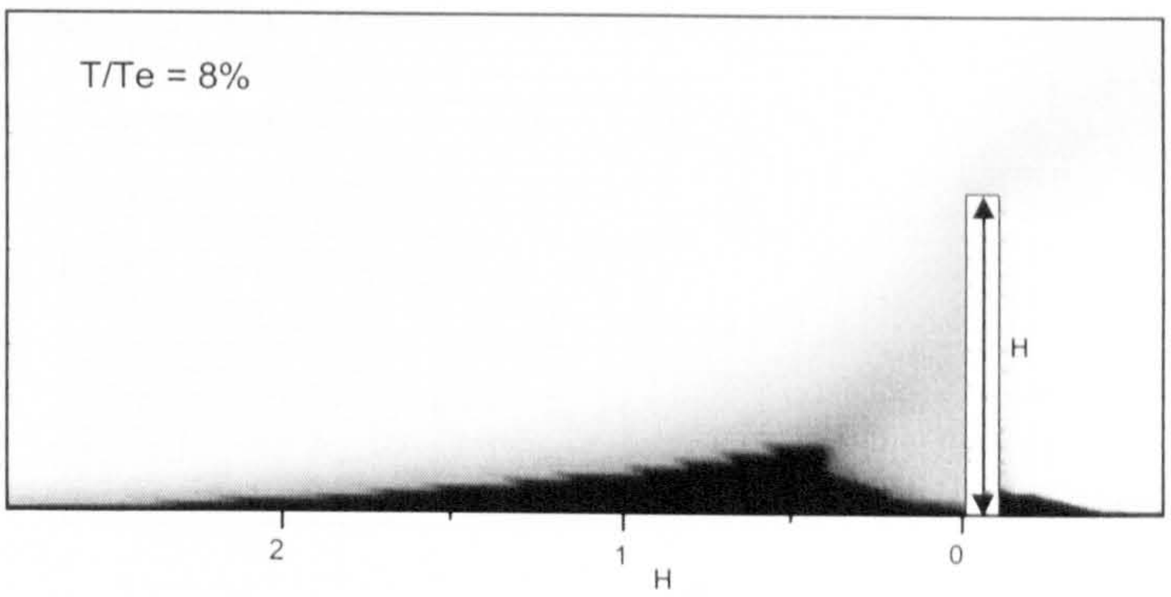

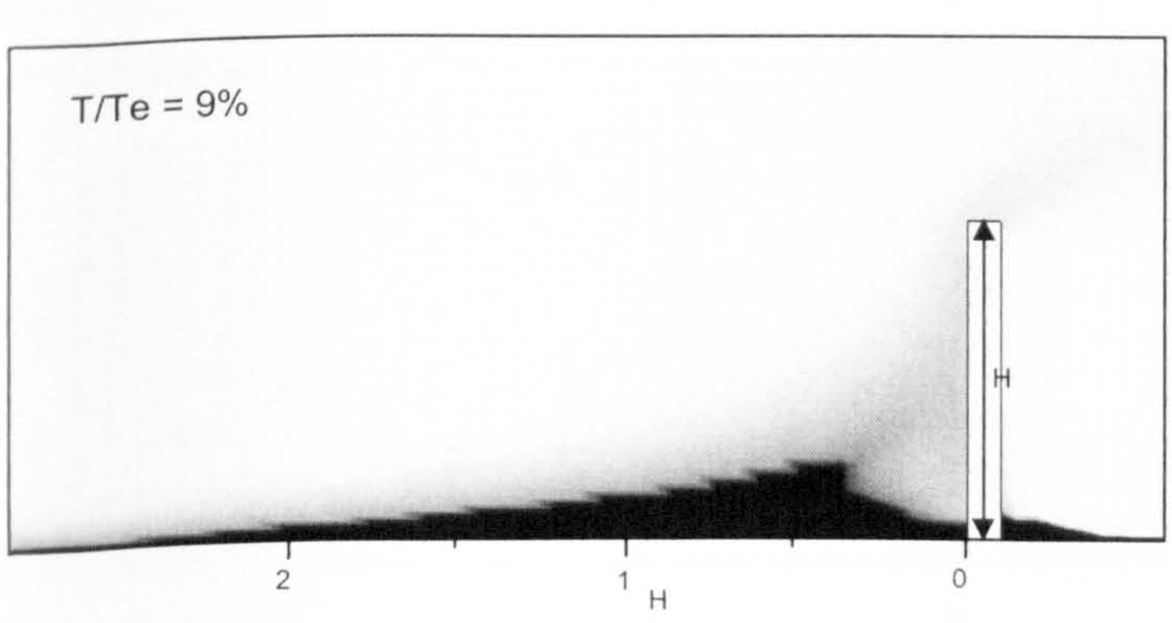

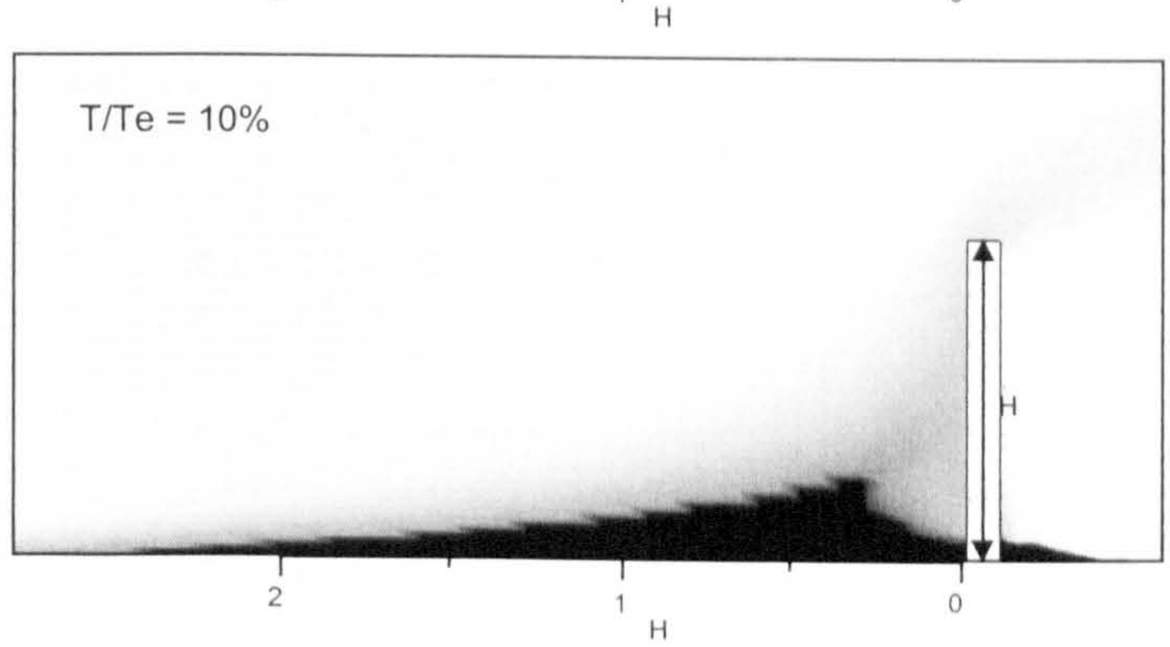

Figure 7.3a: Numerical prediction of particle deposition profile at a solid wall at different deposition stages.

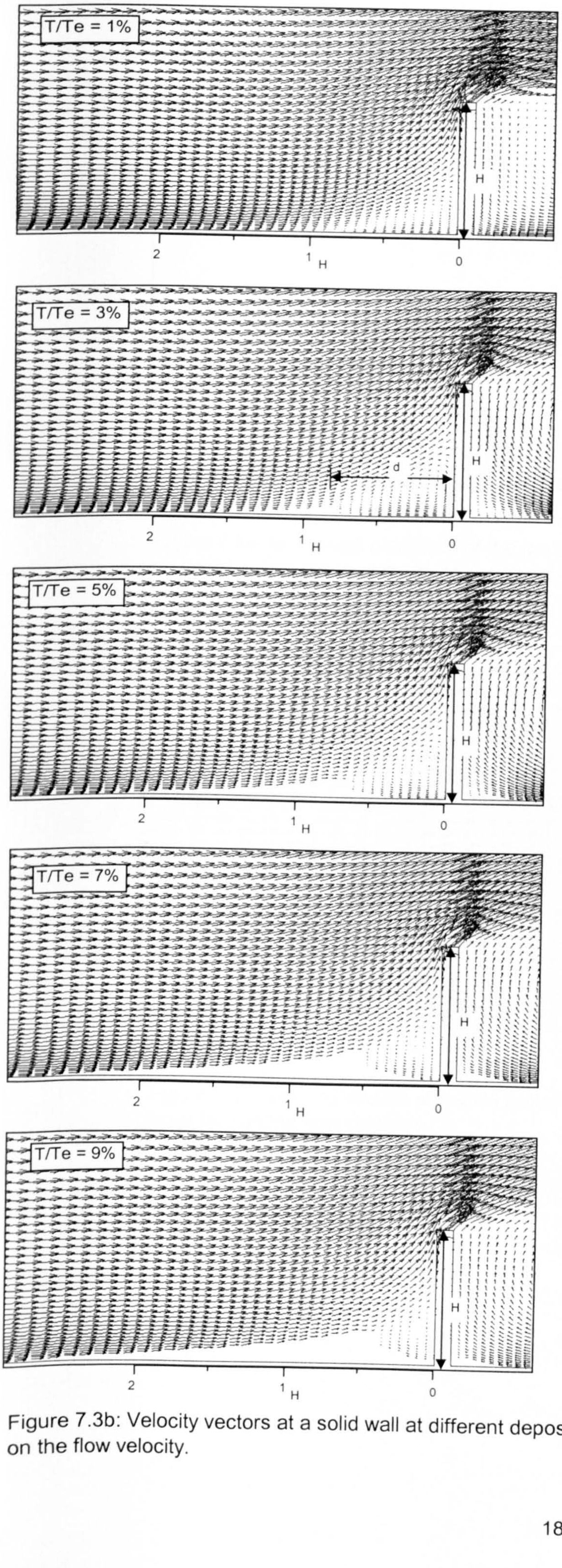

Figure 7.3b: Velocity vectors at a solid wall at different deposition stages showing the effect of the deposition boundary on the flow velocity.

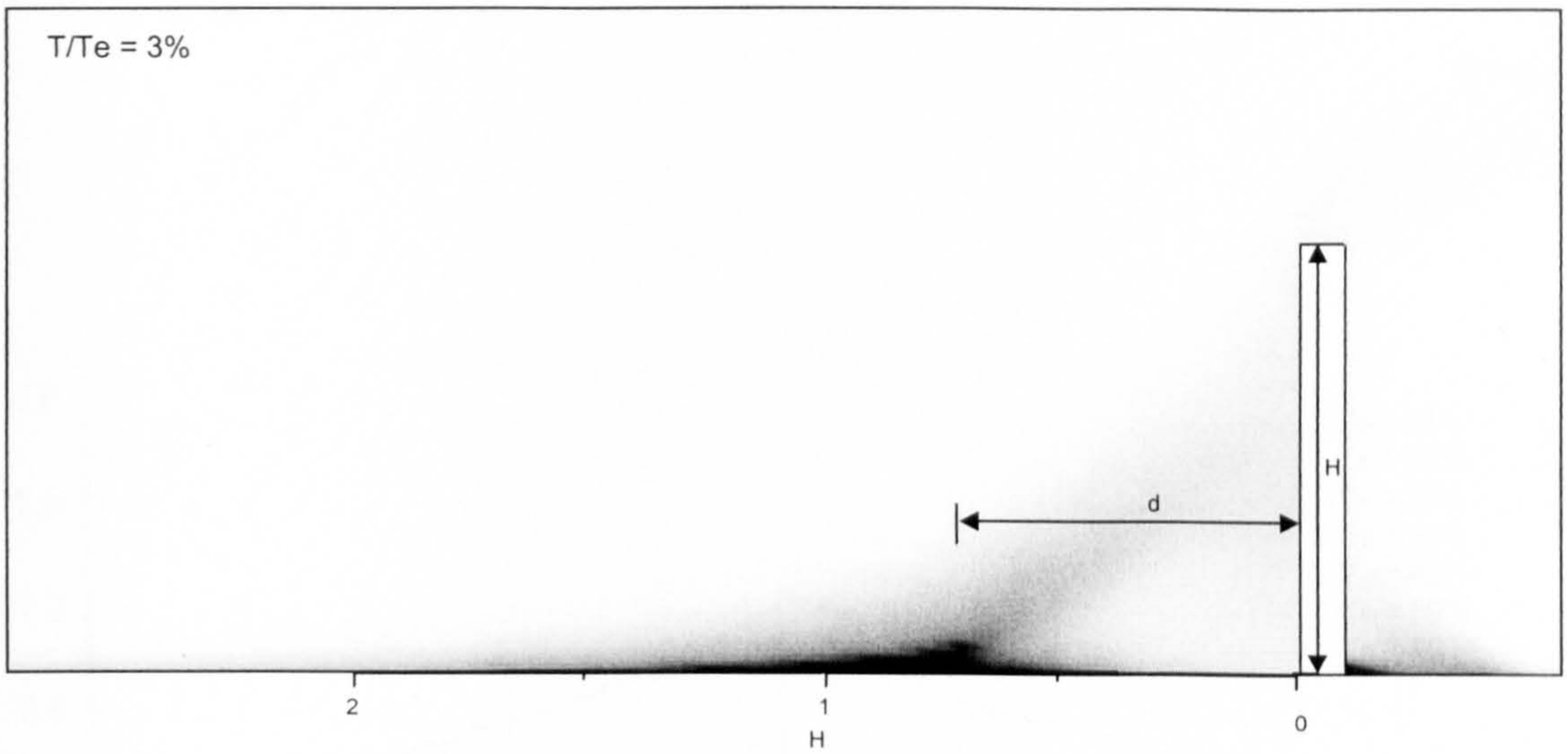

Figure 7.4a: Numerical prediction of the particle deposition profile at a solid wall showing an intermediate stage of the dune development.

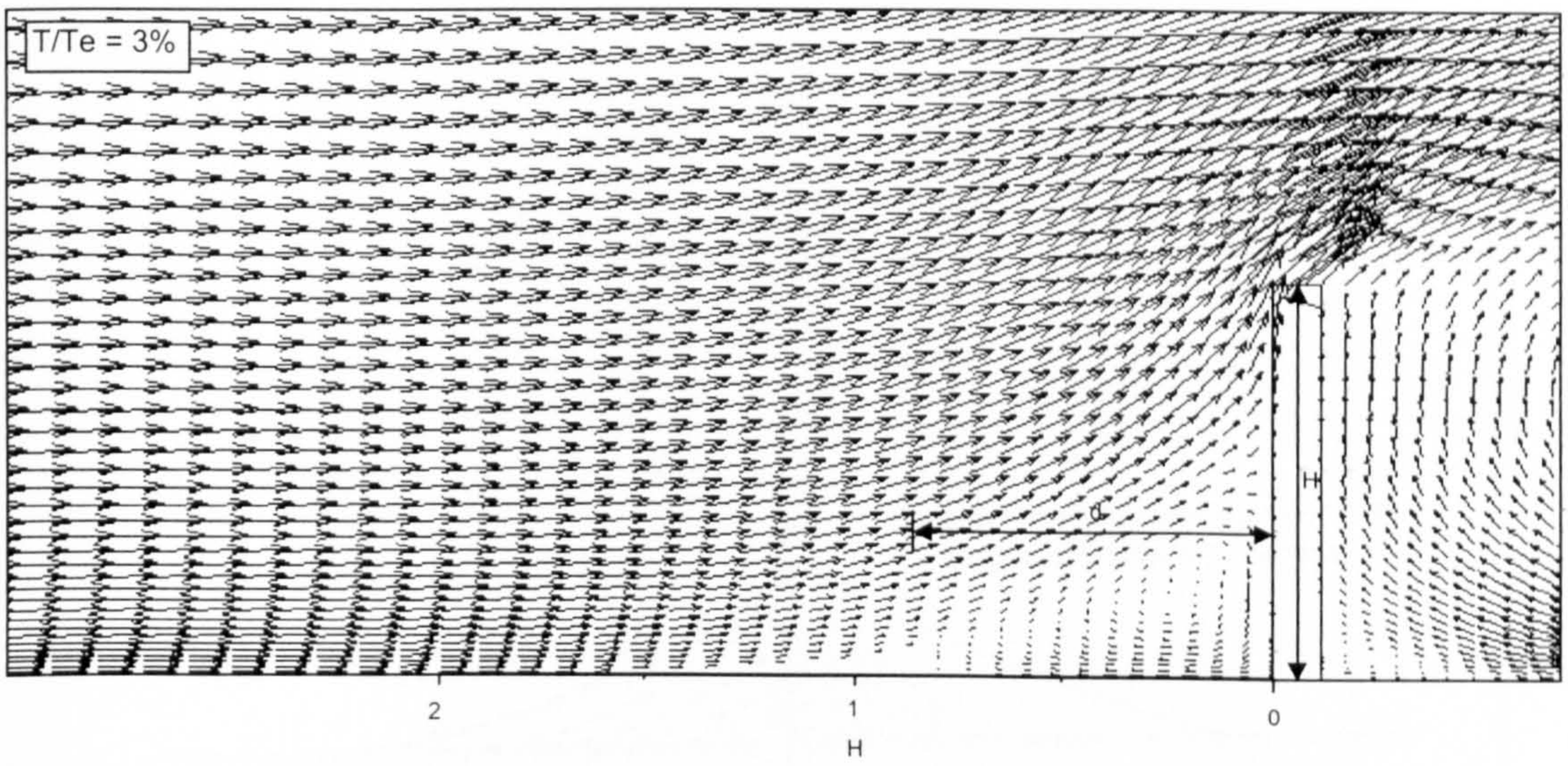

Figure 7.4b: Velocity vectors at a solid wall showing the effect of the interface solid boundary on the flow velocity.

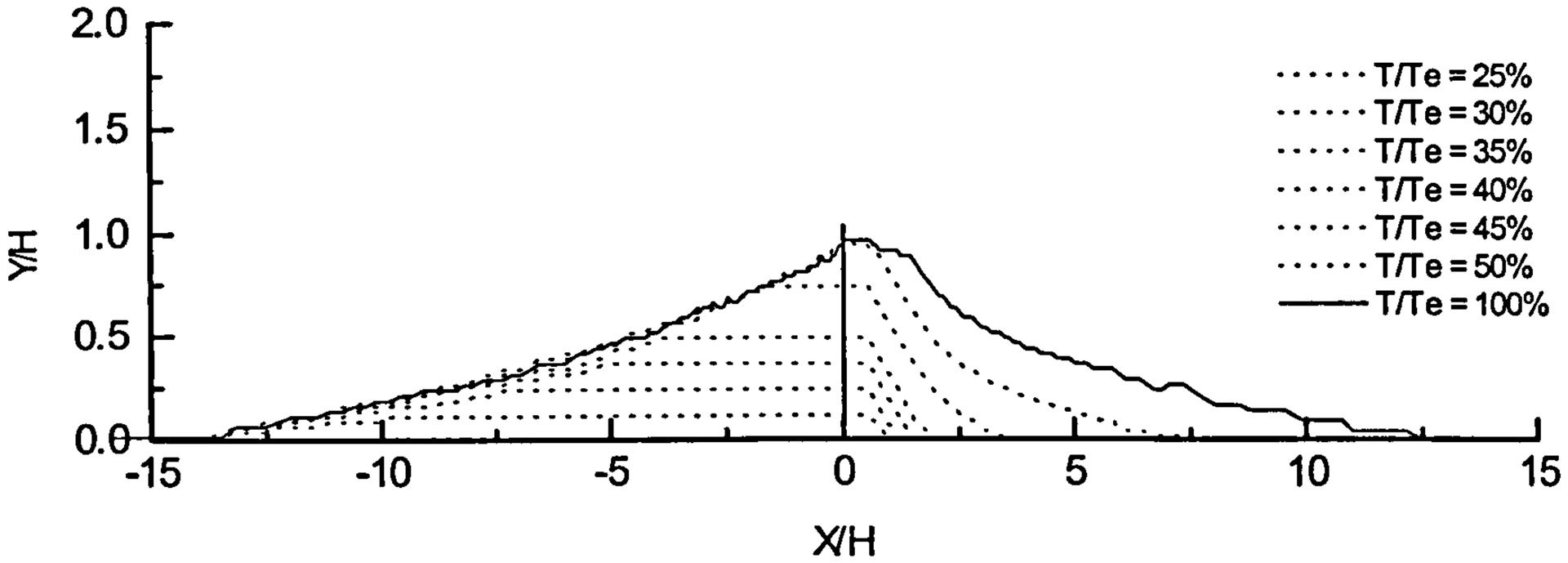

Figure 7.5a: Numerical prediction of the deposition stages at a solid wall of height H.

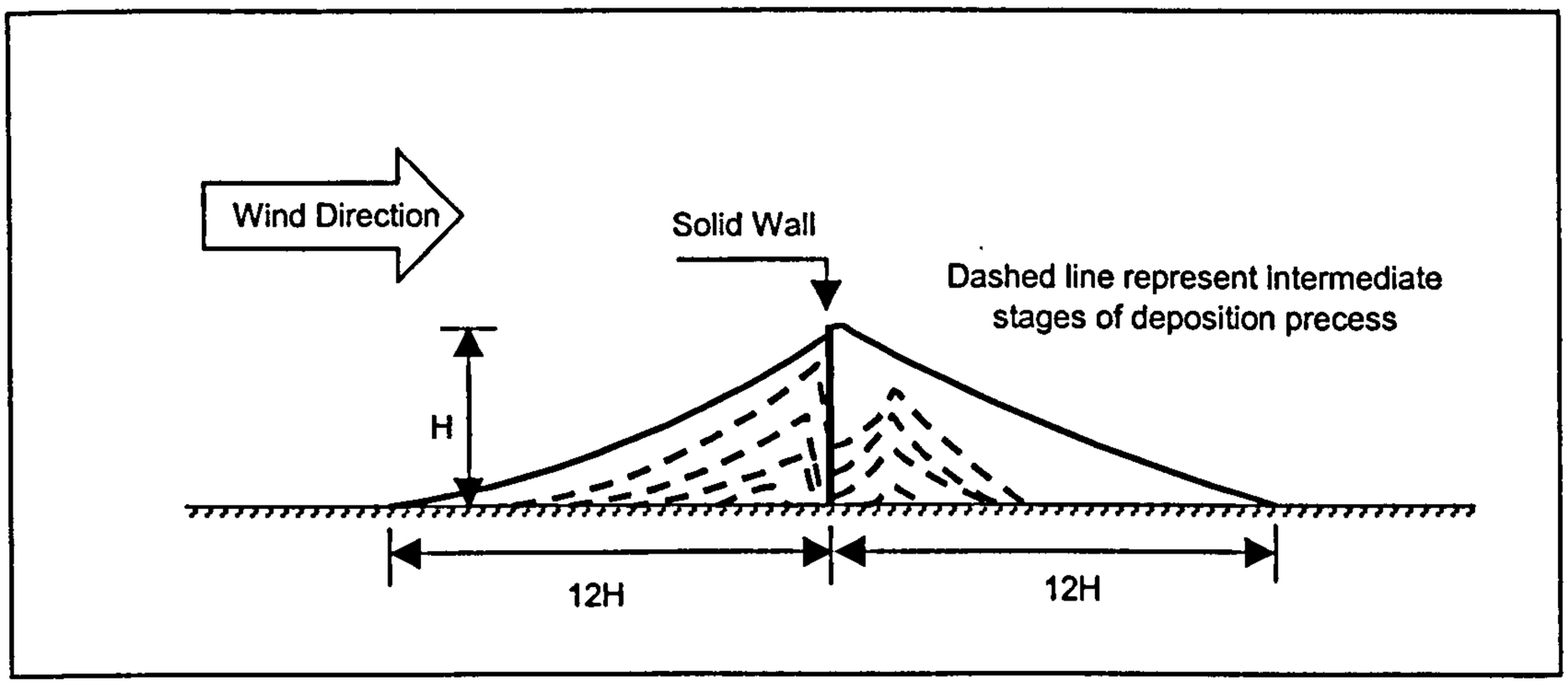

Figure 7.5b: Field observation of snow particles deposition stages at a solid wall of height H.
From Tabler (1994).

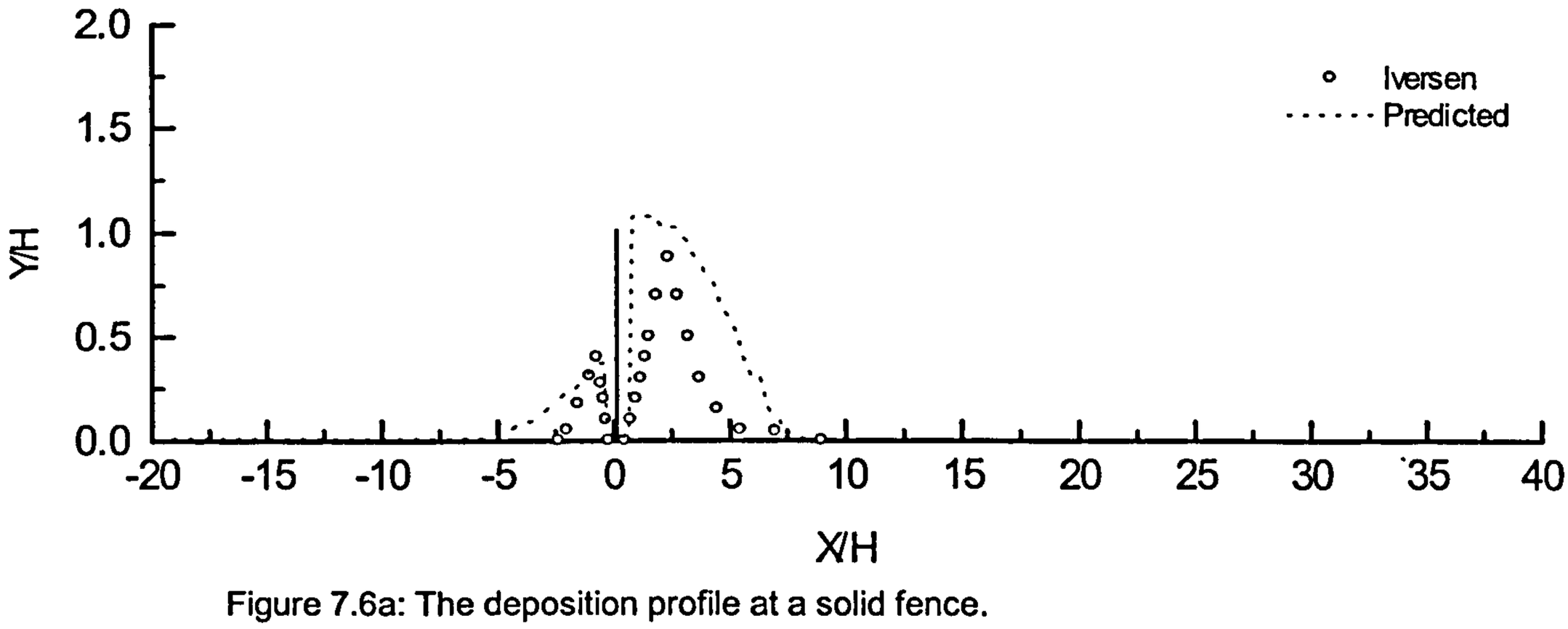

Figure 7.6a: The deposition profile at a solid fence.

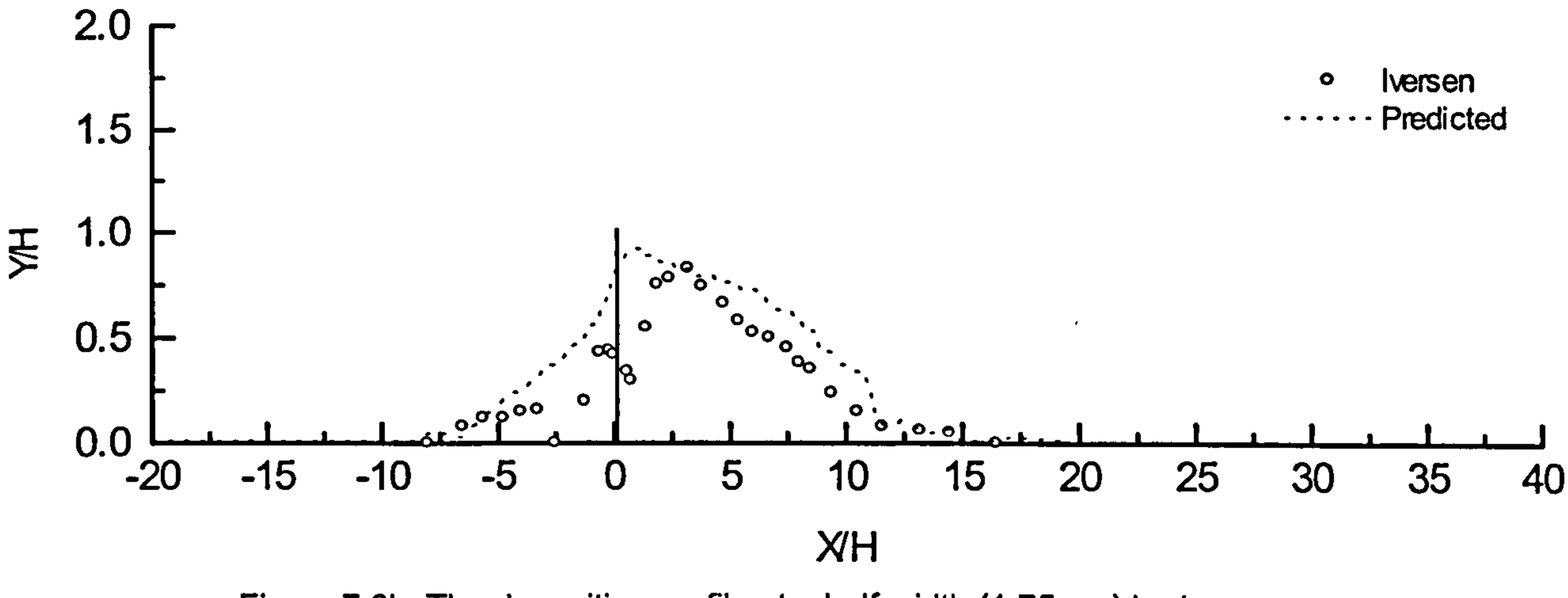

Figure 7.6b: The deposition profile at a half-width (1.75 cm) hedgerow.

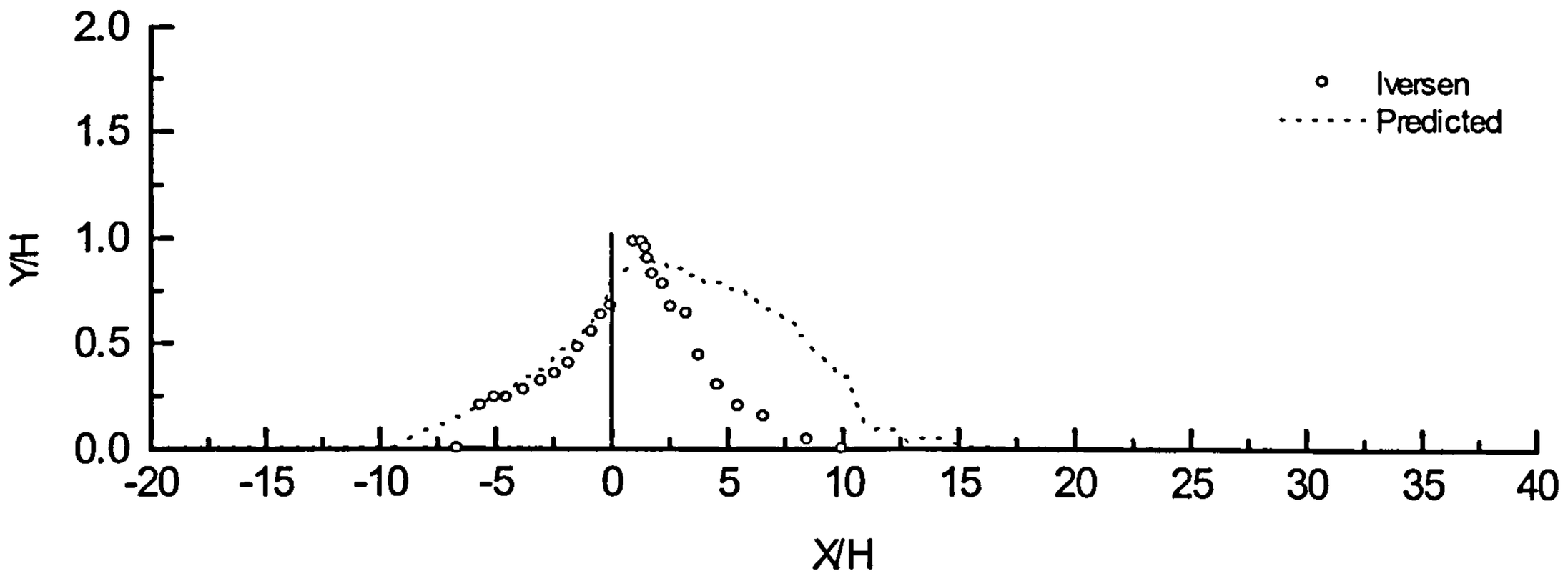

Figure 7.6c: The deposition profile at a full-width (3.5 cm) hedgerow.

7.3 Case study II: Drifting of snow particles at a single 50% porosity fence

In this section the results from the simulation of drifting particles at a 50% porous fence are compared with the field and wind tunnel observations. The first part includes the comparison between the field measurements of Tabler (1979), the wind tunnel experiment of Iversen (1981) and the numerical model.

7.3.1 Geometry and model set up

The wind tunnel test section of Iversen (1981) was used to define the numerical computational domain, 5m length and 1.1m by 1.1m cross section.

Since the fence spanned the tunnel width, a two-dimensional domain was considered using a 5m by 1.1m computational domain in the axial and vertical directions respectively with unit depth. A 50% porosity fence of 2.54cm height 'H' was placed in the computational domain perpendicular to the flow direction at a distance equal to 40 times the fence height H down stream from the inlet boundary of the domain.

The computational domain was divided into 303 by 72 grid points in the axial and vertical directions respectively. The grid resolution was increased close to the wall and in the regions of expected deposition as shown in figure 7.7.

The fence structures used in the simulation was similar to those used in both field and wind tunnel experiments. The porosity of the fence was represented by a series of horizontal strips placed on the top of each other. This was achieved by defining alternatively blocked and clear regions of the same height and 3x3 grid points, resulting in 50% of the total height open to the flow as shown in figure 7.7.

The height of the gap underneath the fence was set to be 10%H and was represented by 5 uniform grid points above the domain bed. The maximum cell height near the bed was defined to be at least equal to twice the particle diameter so realistic calculations of the surface roughness are assured.

The simulated snow particles were represented as, similar to Iversen's wind tunnel experiment, 4.9e-5 m diameter and 3990 kg/m^3 density, having a threshold velocity equal to 0.215 m/s. The homogenous model was employed to predict the particle volume fraction whilst the FAVOR model was used to represent the growth of the deposition interface boundary.

The suspension source term coefficient was set to 0.08 with 0.25 for the saltation source term. The normalised friction velocity defined in expression number 3 in table 5-1 was used to incorporate the saltation effect within the saltation source term.

At the inlet boundary, the wind profile was set using a friction velocity equal to 0.22 m/s, that is 2% above the threshold value and a surface roughness equal to 1.0e-4 m. The inlet turbulent kinetic energy and dissipation rate were set based on turbulence intensity and characteristic length of 1% and fence height H respectively.

The particle concentration profile at the inlet boundary was calculated from the vertical concentration profile equation proposed by Andersen (1983) using the same friction velocity applied for the wind profile at the inlet.

7.3.2 Results and discussions

The numerical computations were carried out until a steady state solution was achieved with the particle deposition profile reaching an equilibrium state. Figure 7.8a shows the different stages of the deposition process, which is comparable to the stages observed by Tabler (1986) shown in figure 7.8b. It shows that the majority of the deposition area is concentrated behind the fence with the crest of the dune found at a distance from the fence varying between 5 and 8 times the fence height H.

The maximum height of the dune was found to be similar to the observations, about 20%H over the height of the fence.

Figure 7.9a, shows the stages in the growth of the solid interface boundary representing the dune surface, while the change in the velocity vectors clarify the effect of the solid boundary surface of the dune on the flow field structure are shown in figure 7.9b.

The crest of the dune begins in the earlier stages at a distance downstream from the fence equal to about 6 to 8 times the fence height H. However, as more particles are deposited, the dune increases in size whilst the height of the crest point increases and moves backwards towards the fence. At the equilibrium state, the height of the crest point reaches 1.2H from the ground and 5H downstream from the position of the fence.

The full-scale, wind tunnel and numerical model deposition profiles are shown in figure 7.10a. The portion of the snow drift immediately downstream the fence in the wind tunnel experiment is just under the full-scale profile. Iversen (1981) explained this discrepancy by saying that the full-scale friction velocity is at times just above the particle threshold value while in the wind tunnel experiment it was set to some significant value above the threshold value. This is probably the reason for the lack of deposition in front of the fence in the wind tunnel experiment. It is also possible that the wind tunnel experiment had not reached the state of equilibrium.

The deposition profile predicted by the numerical model is shown to be comparable to those measured, figure 7.10a. The predicted profile shows fairly good agreement with the full-scale rather than the wind tunnel upstream and immediately down stream of the fence. Further down stream, from the crest of the dune to the trailing edge, the prediction and both measurements are shown to be in agreement.

The area of deposition in front of the wall was predicted as a result of the drop in the friction velocity to values below the particle threshold in the weak zone just upstream of the fence. This behaviour of the numerical model strengthens Iversen's explanation of the discrepancy between the full-scale and wind tunnel measurements.

In a further investigation of this behaviour, the same simulation was repeated under identical conditions with the exception of the inlet friction velocity, which was increased to a value 20% above the threshold value instead of 2% used in the previous exercise.

Figure 7.10b, shows that the increase in the inlet friction velocity does effect the amount and location of the depositing particles. As a direct result of the increase in the inlet wind strength, the predicted amount of deposited particles decreases and becomes closer to that of the wind tunnel experiment, which supports Iversen's explanation.

In addition, the deposition conditions are not satisfied in front of the fence, which results in no deposition in front of the fence similar to that observed in the wind tunnel.

The numerical model was then compared to the measurements of Tabler for the frozen-lake small-scale fence model and the wind tunnel measurements of Iversen. Figures 7.11a and b shows the comparison between the deposition profiles at an intermediate and equilibrium stage respectively. They show again that the numerical prediction gives closer profiles to the field measurements rather than to the wind tunnel and this again may be a direct result of the differences in the free stream wind conditions.

The prediction by the model at the steady stage shows a small accumulation zone just upstream the fence which is can also be seen from the photograph of the frozen lake, figure 7.11c, provided by Tabler (1994) but no measurement from that area were provided graphically. Generally, the model shows a good qualitative comparison with the observations.

The relationship between the properties of the different drift profiles were analysed and compared to those measured including the drift length L_{lee}, the maximum drift height D_{max}, the cross-sectional area under the deposition profile $A_{profile}$, the dune surface area and the total deposition volume, figure 7.12.

The relationship between the length of the lee drift and the maximum drift height is shown in figure 7.13. In the early stages of the deposition process, the vertical growth of the dune moves faster than the horizontal expansion of the lee drift. Moreover, as the process moves towards the equilibrium state the relationship becomes linear until halting when the lee drift and the maximum drift height become about 27H and 1.2H for the full-scale measurements, about 26H and 1.25H for the wind tunnel and 30H and 1.3H for the predictions respectively. Due to the fact that FAVOR at this stage deals only with open/blocked cells and that is why sharp edges appear in the relationship shown in the figure and this also is the reason of having poor prediction of the lee drift length at the final deposition stages.

Figures 7.14 and 7.15 show the relationship between the profile area of the lee drift and both the length of the lee drift and maximum height respectively. Similarly, both curves show good agreement with the measured data.

The volume and surface area of the deposition profiles are important parameters in the prediction of the maximum fence capacity; the ability of the fence to capture particles. Hence, a three-dimensional case of the 50% porosity fence was simulated. The total depth of the domain was chosen to be the tunnel depth, which is 1.1 m and divided in to 40 uniformly spaced grid points.

Figure 7.16(A) shows the deposition volume where the fence spanned the whole domain width and (B) where the fence depth is 0.762 metre placed in the middle of the flow domain. The simulation of the domain in which the fence spans the whole width produced a dune, which is symmetrical along the length of the domain. The prediction in the case of the centrally positioned fence produce a domal shape dune due to the effect of the change in the flow field at the fence edges, which is clarified by the flow streamlines.

The total volume was computed by summing the volume of all cells that were blocked when the solution reached the steady state. The surface area was calculated by summing the cell face areas of every cell on the interface boundary. Table 7-2, shows a comparison between full-scale, wind tunnel and

the model data for the lee drift length, profile and surface areas and the total volume. Following Iversen, the volume has been estimated using two different ways. First, by multiplying the surface area by the average profile height and second by multiplying the Tabler full-scale volume value by the ratio of the profile area to the Tabler profile area.

Table 7-2: Full-scale, wind tunnel and prediction model comparison of drift properties

Drift Parameter	Full Scale	Wind Tunnel	Predicted
Profile Area, $A_{profile}$	$18\,H^2$	$16.8\ H^2$	$15.2\ H^2$
Surface Area, $A_{Surface}$ (from 3D)	$693\ H^2$	$645\ H^2$	$581\ H^2$
Volume, $(465\,H^3 * A_{profile})/(18\,H^2)$	$465\ H^3$	$434\ H^3$	$393\ H^3$
Volume, $(A_{surface} * A_{profile})/L$ (from 3D)	$455\ H^3$	$406\ H^3$	$295\ H^3$
Length Maximum, L	$27.4\,H$	$26.7\,H$	$29.97\,H$
Length Average, $A_{surface}/L$ (from 3D)	$23.1\,H$	$21.5\,H$	$14.8\,H$

7.3.3 Case study II: Conclusion

In general the model shows fairly good agreement with measurements with an error of about 18% from the field measurements and 10% from the wind tunnel measurements for the two-dimensional comparison properties. The error increases in the three-dimensional simulations up to 50%. The majority of the error in the predictions can most liable be associated with the limited grid resolution used to keep the computational time and memory requirements of the simulation within practical ranges.

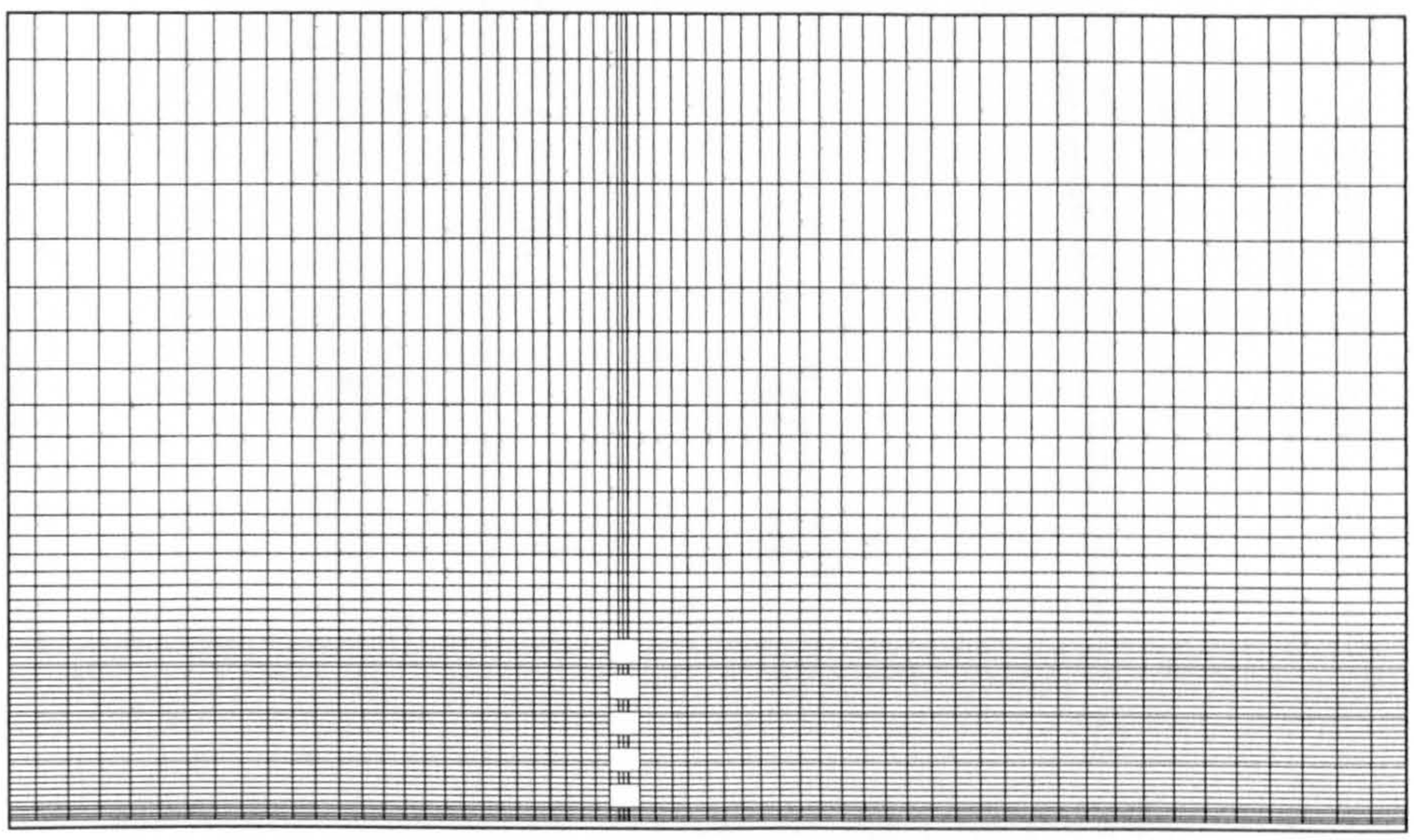

Figure 7.7: Grid distributions around 50% porous fence.

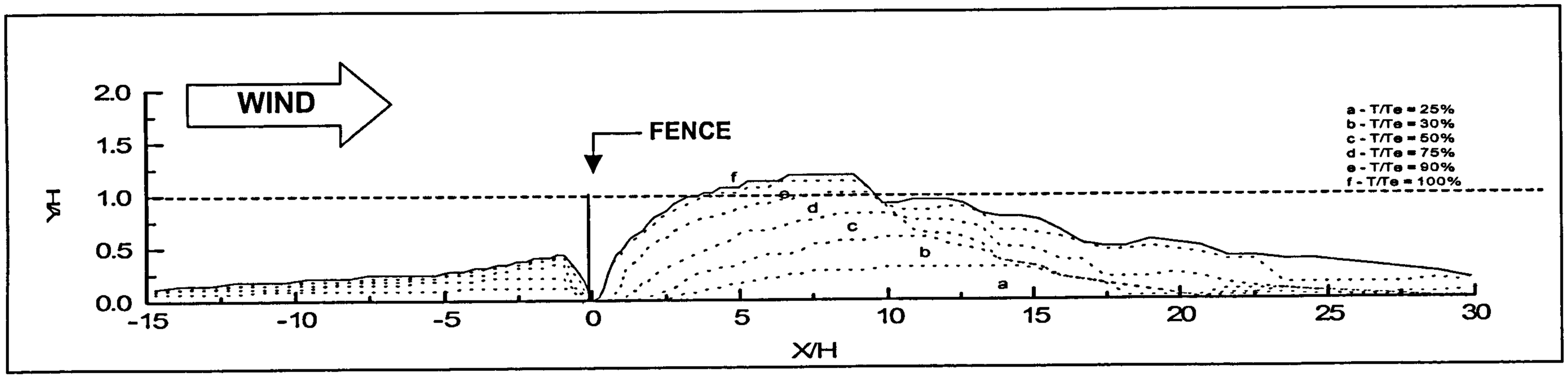

Figure 7.8a: Predicted stages of the snow deposition profiles at 50% porous fence.

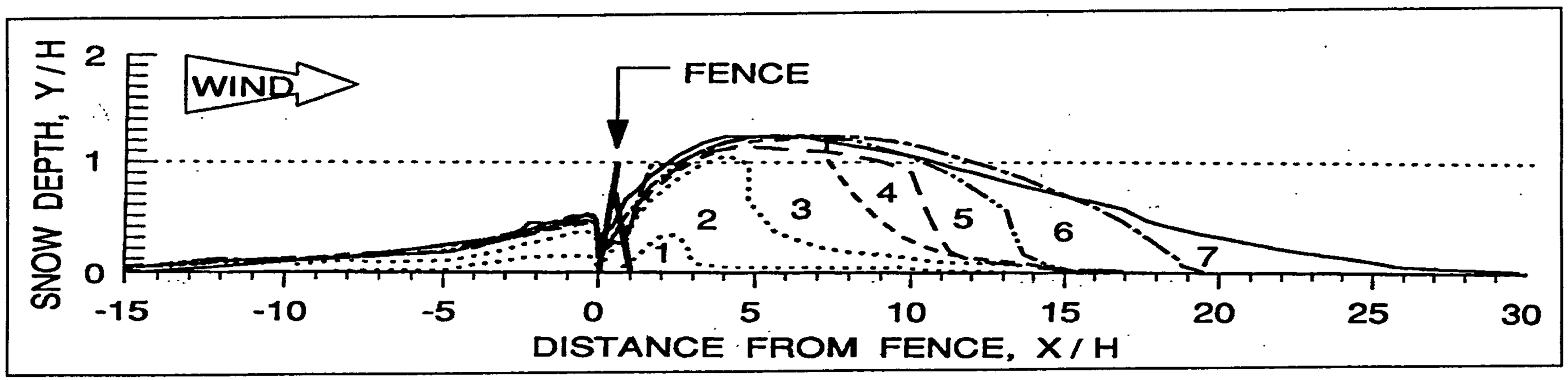

Figure 7.8b: Different deposition stages at Wyoming snow drift fence that is 3.66m height and 50% porous. From Tabler (1986).

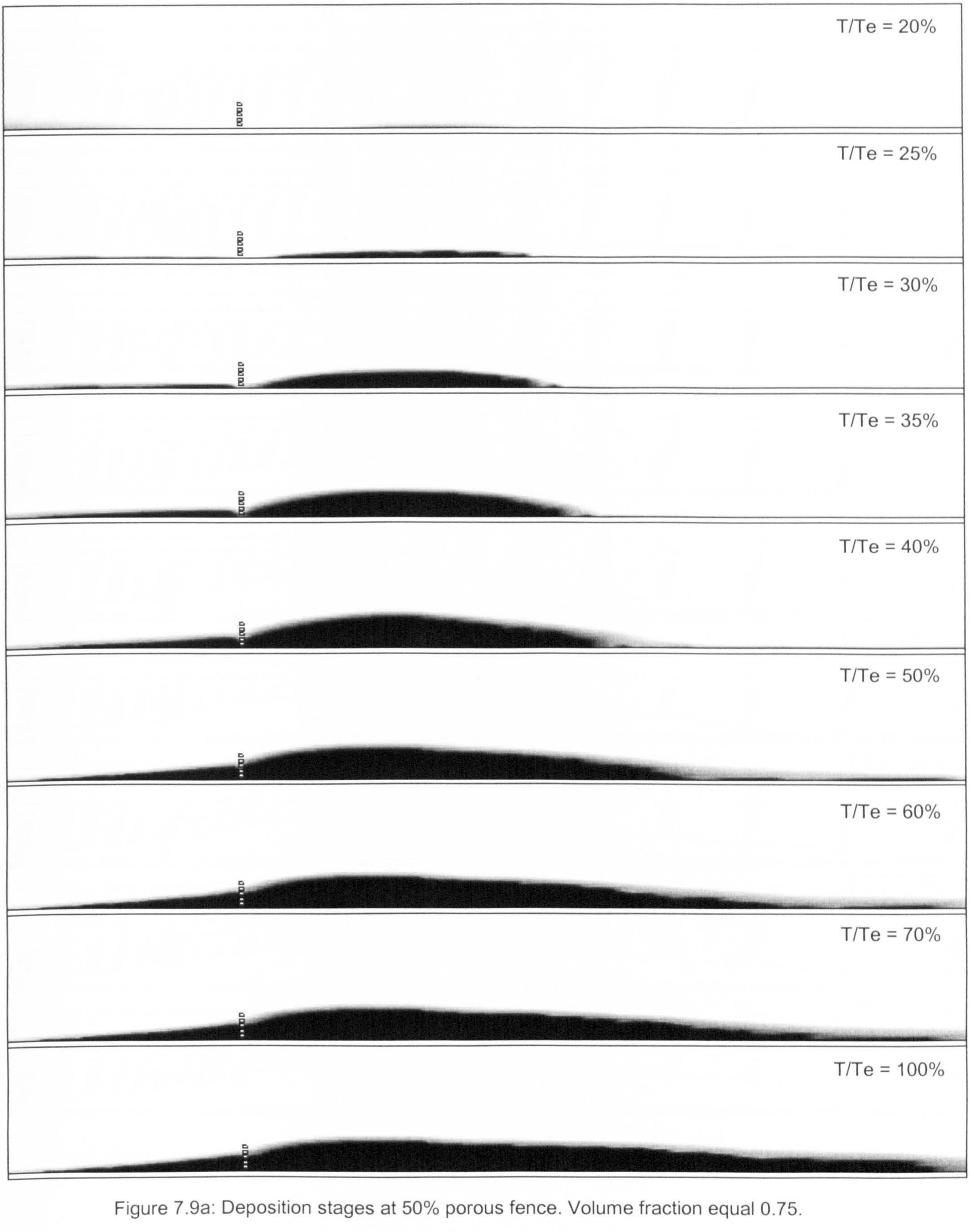

Figure 7.9a: Deposition stages at 50% porous fence. Volume fraction equal 0.75.

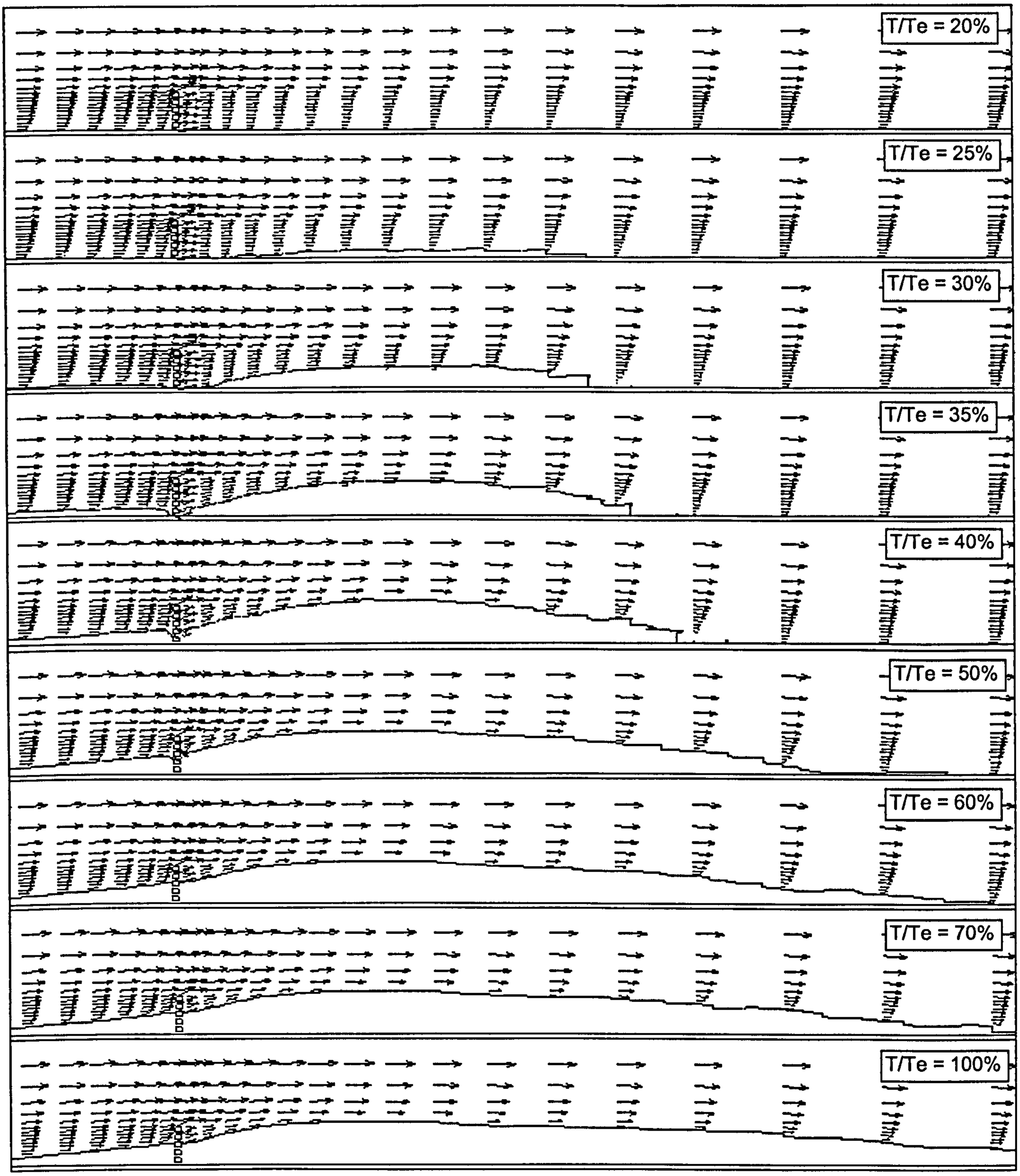

Figure 7.9b: Deposition stages at 50% porous fence showing velocity vectors on the interface boundary.

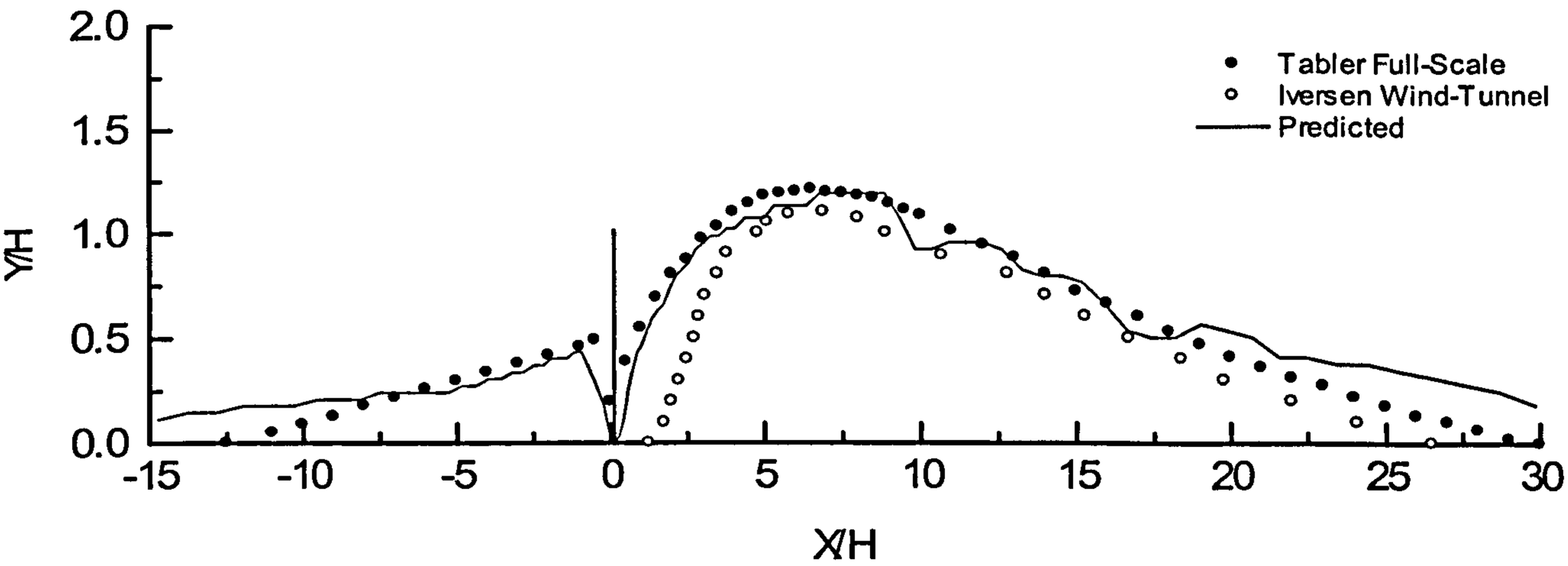

Figure 7.10a: Deposition profiles: Full -Scale measurements from Tabler (1981), Wind tunnel measurements from Iversen (1981) compared to the numerical prediction at 50% porous fence when the inlet friction velocity is 2% above the threshold value.

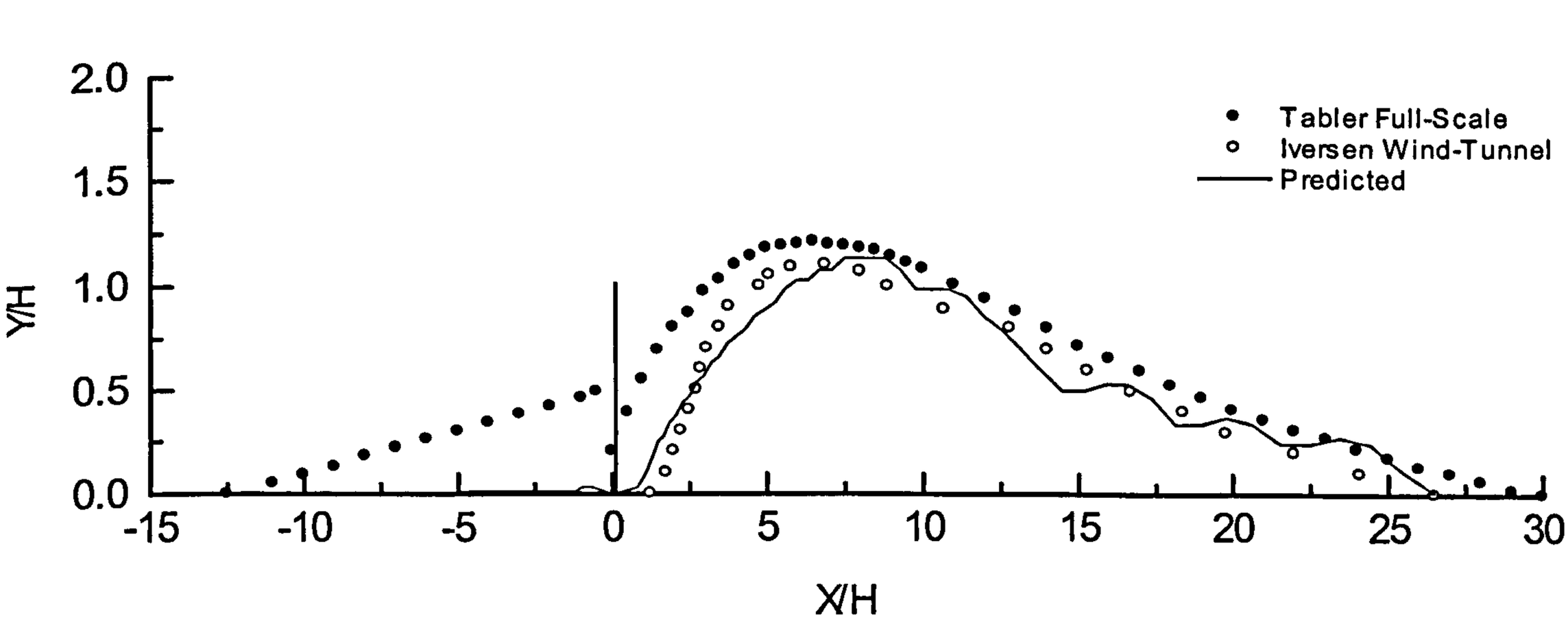

Figure 7.10b: Deposition profiles: Full -Scale measurements from Tabler (1981), Wind tunnel measurements from Iversen (1981) compared to the numerical prediction at 50% porous fence when the inlet friction velocity is 20% above the threshold value.

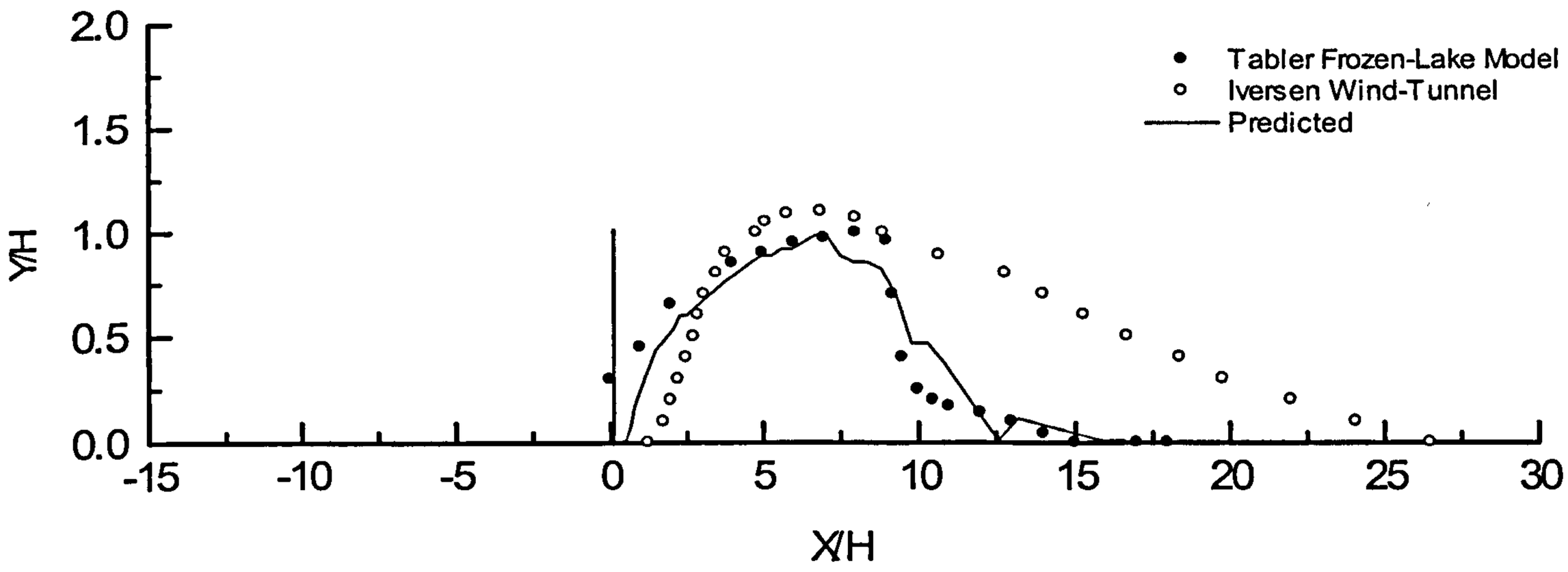

Figure 7.11a: Intermediate deposition profile at 50% porous fence. Comparing Tabler (1980) Frozen lake model and Iversen (1983) wind-tunnel model with the prediction.

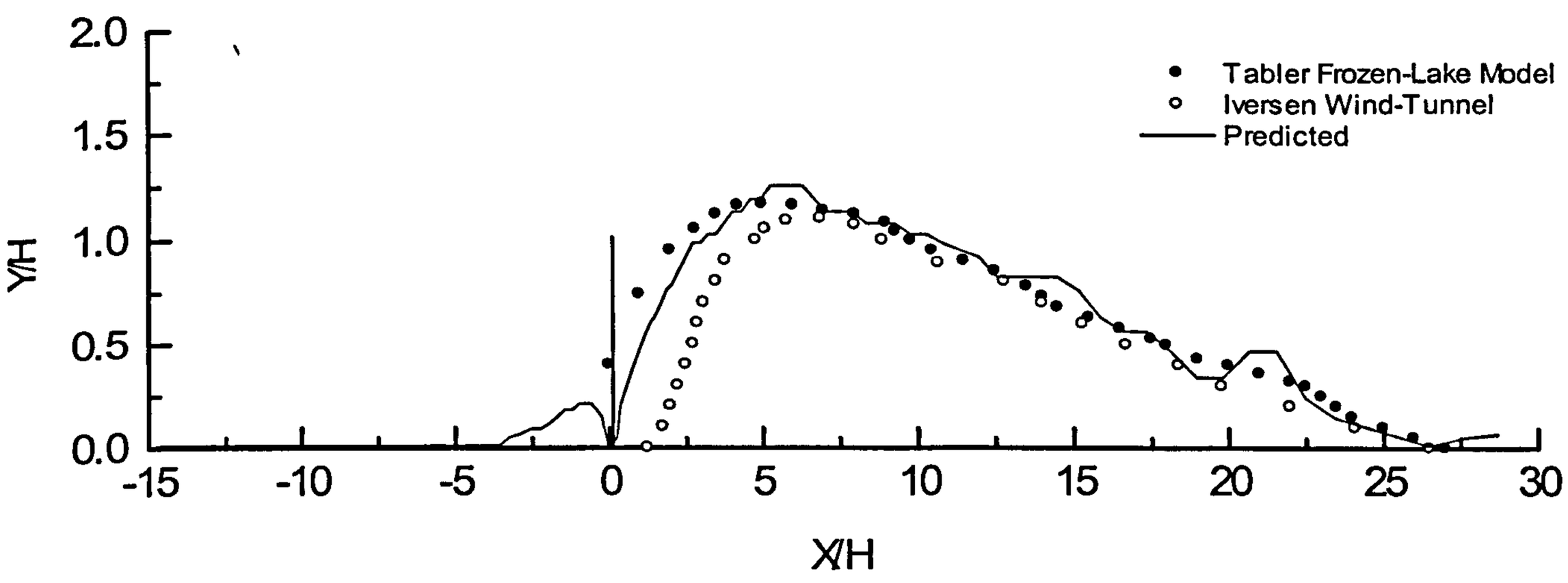

Figure 7.11b: Steady state deposition profile at 50% porous fence. Comparing Tabler (1980) Frozen lake model and Iversen (1983) wind-tunnel model with the prediction.

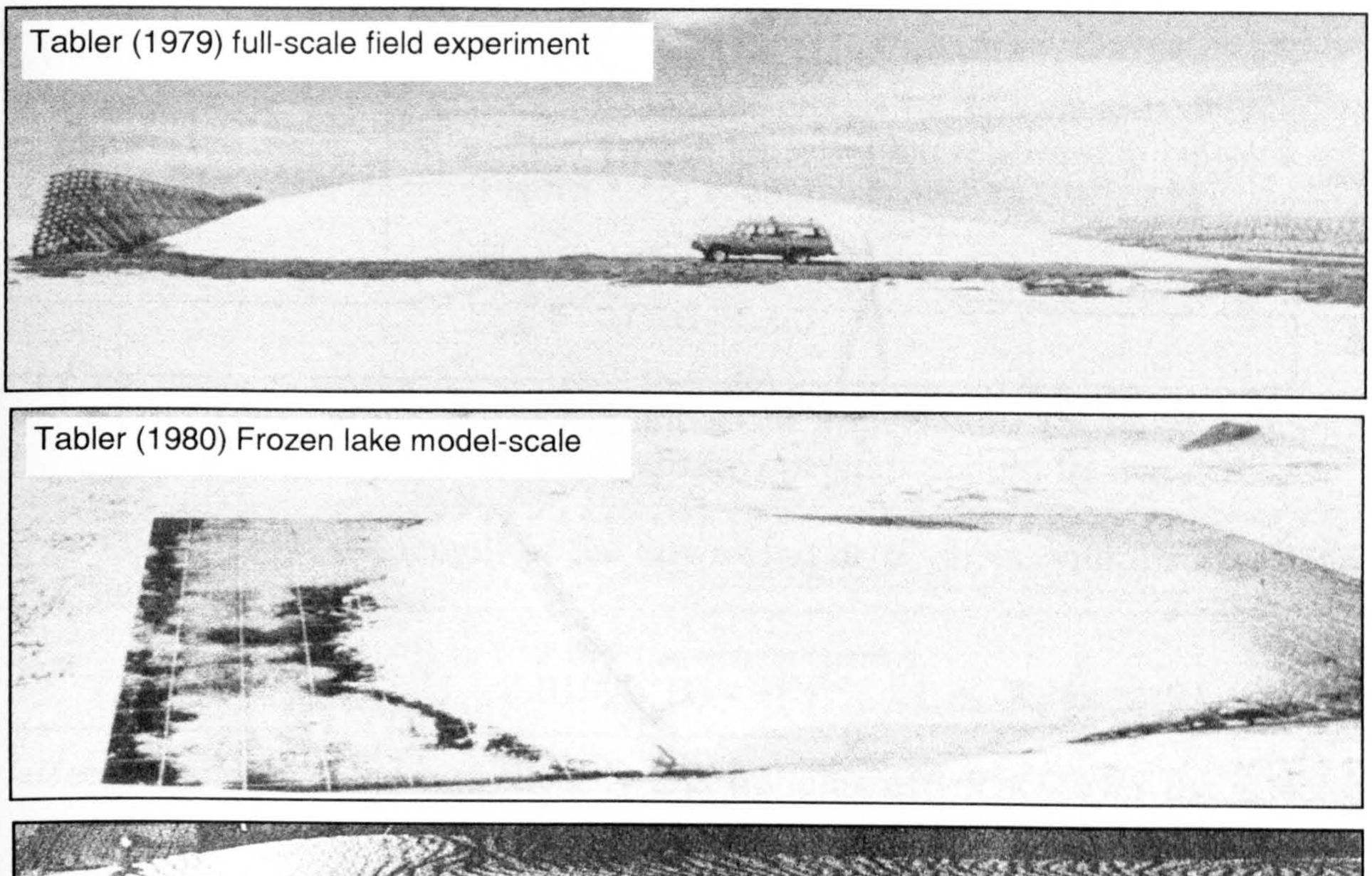

Figure 7.11c: Steady state deposition profiles at 50% porous fence. Comparing the different field and wind tunnel mesurements with the numrical predection.

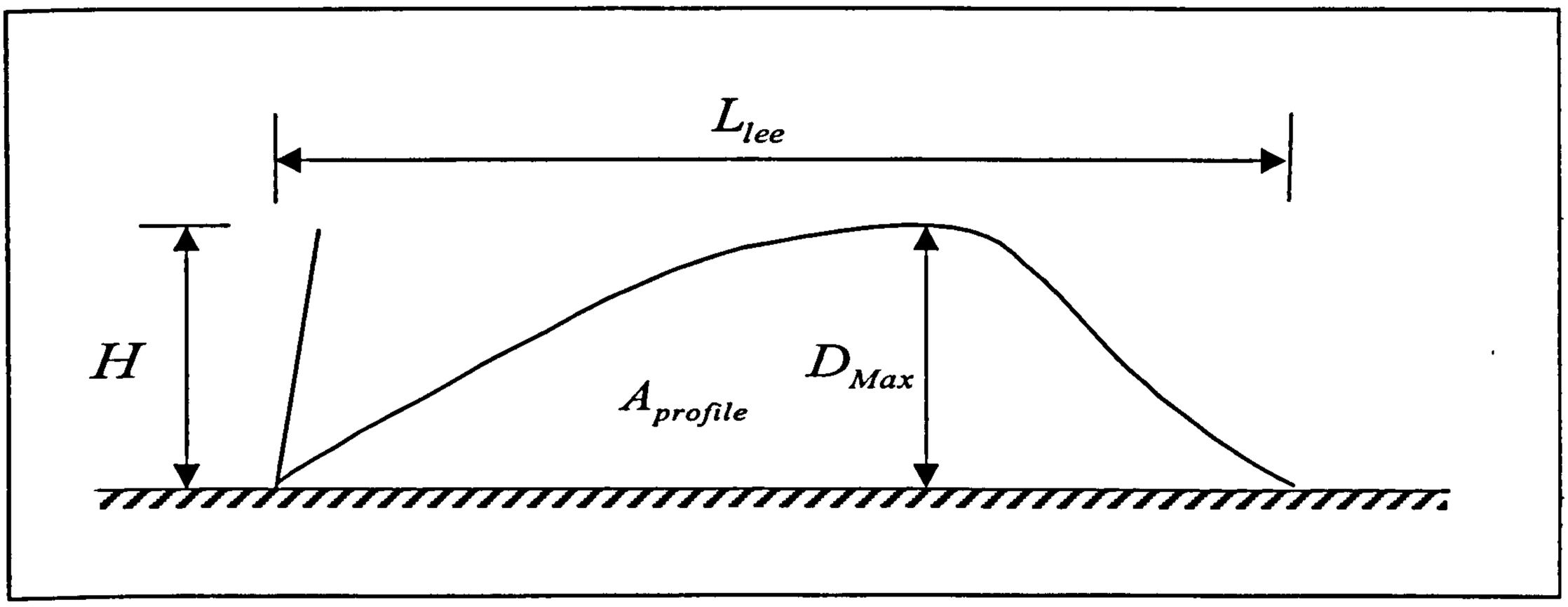

Figure 7.12: Drift geometry properties.

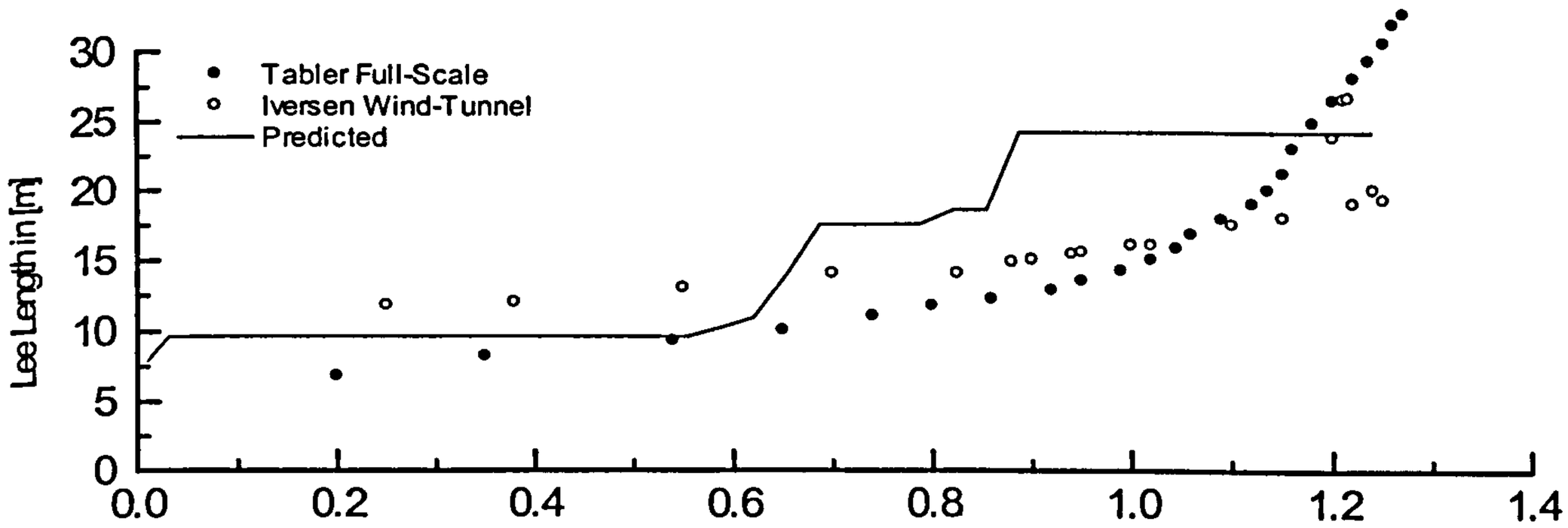

Figure 7.13: The relationship between the Lee drift length and the maximum dune height.

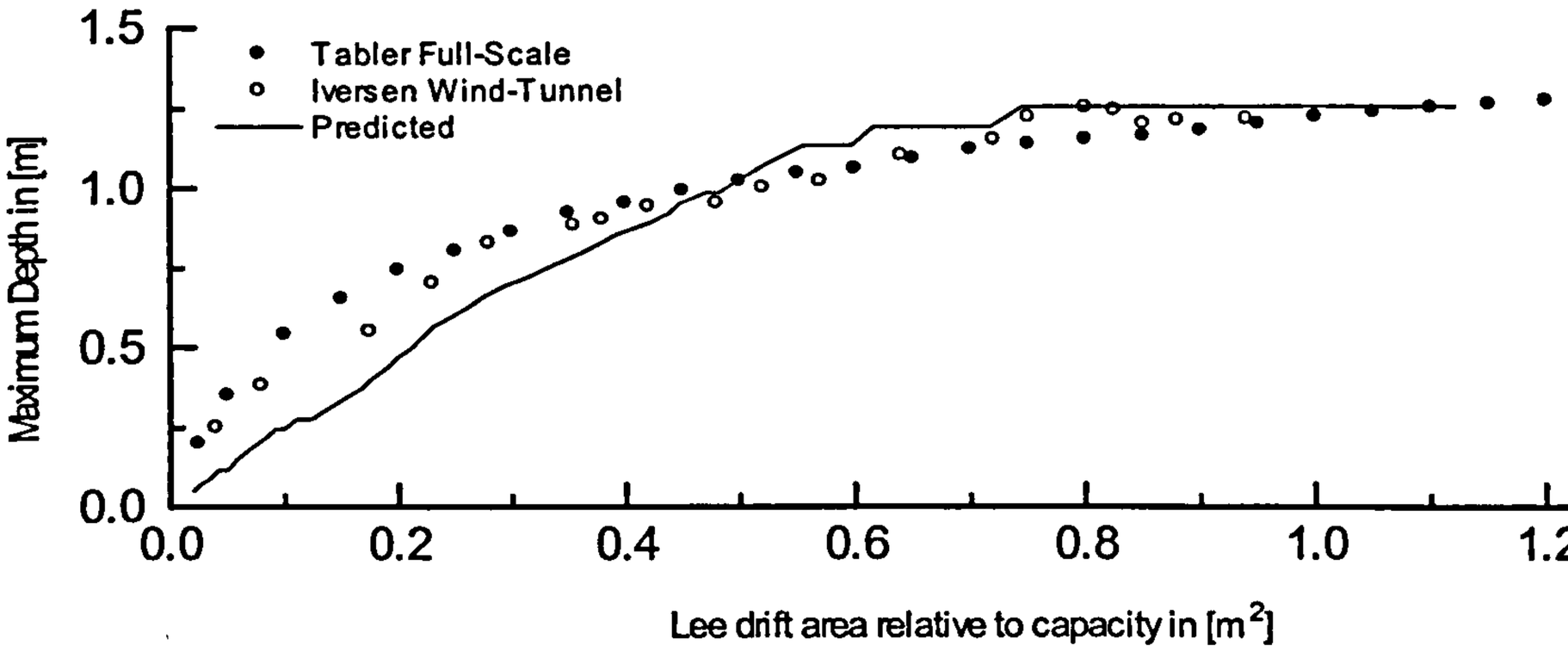

Figure 7.14: The relationship between the maximum dune height and the Lee drift area.

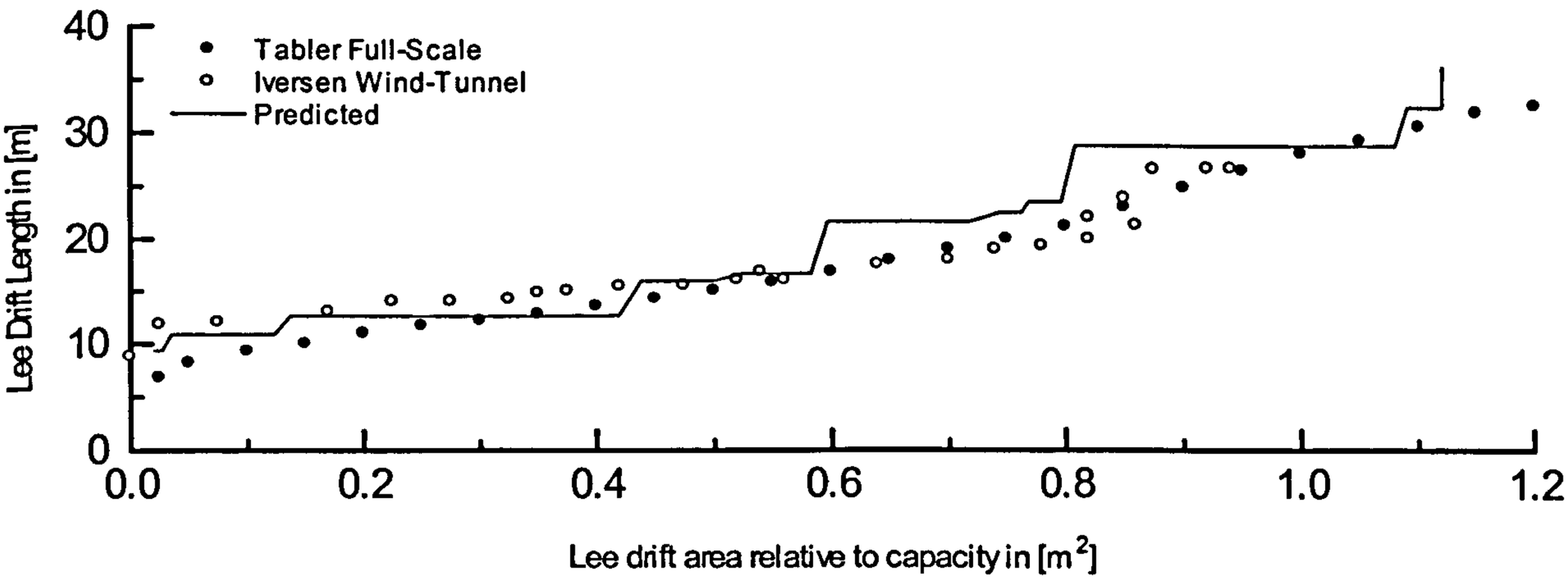

Figure 7.15: The relationship between the Lee drift length and the Lee drift area.

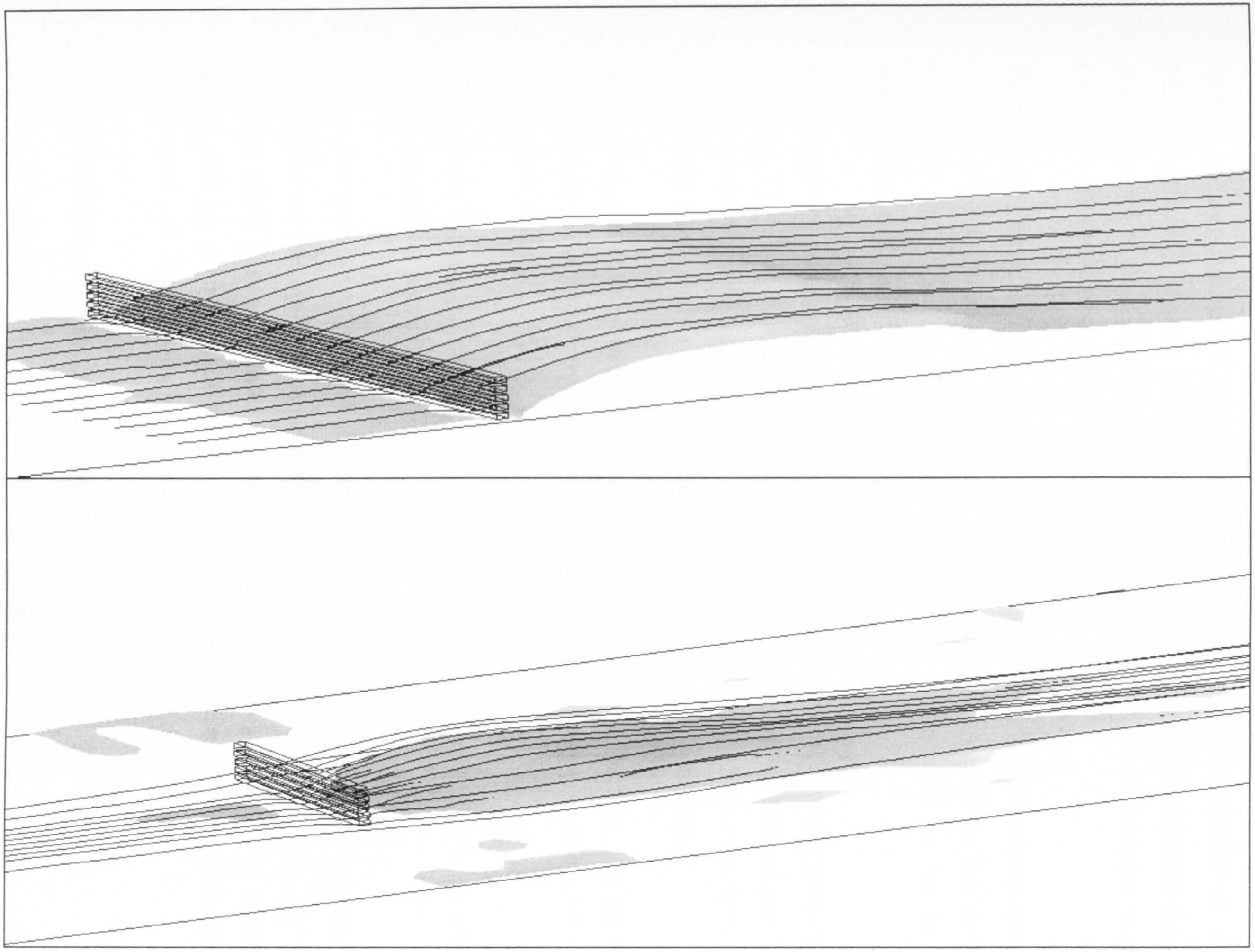

Figure 7.16: 3-dimentional simulation of the deposition dune behind 50% porous fence. Isosurface of volume fraction at 0.75. The colour shading for illustration purposes only.

7.4 Case study III: Drifting at a porous multiple row fence system

In this section, the model is used to simulate the deposition profiles of sand particles at a multiple row fence system. The results of the numerical simulation are compared to the data collected as a part of this study from field experiments conducted in the Kuwaiti desert. (See Chapter 3).

First of all, it must be known that the measurements were collected from fences, which had been installed in 1988 at the KISR station and in 1996 for the Burgan site. The deposition profiles measured are not considered to be in an equilibrium state due to the following reasons:

1. The wind strength applied on the field is never constant for long periods of time. Therefore strong winds may erode some of the pre-deposited particles around the fence whilst intermediate or calm wind may not even have the enough momentum to carry particles from the upstream sources.
2. Due to the change in the humidity ratio of the sand surface, the particle threshold conditions and therefore the sand flux never stay uniform for long periods of time.

Thus, these measurements were all considered as an intermediate stage of the entire deposition process.

Since the model simulations are performed under an idealised situation, the prediction of the deposition profiles might give an indication of the size and location of the deposition at the equilibrium state, which may never be achieved under real life situations. Hence, some of the intermediate predicted stages are monitored and discussed below in addition to the equilibrium state.

7.4.1 KISR double fence line system

The fence system at KISR station site discussed in Chapter 3 section 3.4.1, was assumed to be a two-dimensional case and simulated first using the full-scale dimensions.

The different stages of the deposition process are presented in figure 7.17. The development of the dune is observed first at the front fence line then some time later when the front dune has reached a certain level, a dune at the rear fence line is seen to grow. Similarly, the dune at the rear fence achieves its equilibrium state only after the front dune has already been at equilibrium for a period of time.

Figure 7.18 shows graphically the different stages of the deposition process, which clarifies that the dune, which developed at the front fence is wider than that developed at the rear one for the same deposition stage.

An intermediate and equilibrium state profiles are shown in figure 7.19 and are compared with the observations. It is shown clearly that the equilibrium state profile is larger than that which has been measured whilst the intermediate profile prediction provide more comparable results.

7.4.2 Burgan multiple fence line system

As discussed in section 3.4.1, the experiment at the Burgan site was conducted to investigate two principal deposition factors, firstly the effect of the number of the rows of fence on the amount and location of the deposition process. Secondly the effect of the distance separating these rows on the deposition process. The three zones defined in figure 3.13 were simulated in a two-dimensional domain assuming that every zone is infinitely wide.

Zone one with double fence lines and a space between them equal to 25 times the fence height 'H'. Zone two with three fence lines separated by 25H between each two consecutive rows. Zone three has double fence lines but with space equal to twice the one used in zone one.

Figures 7.20 to 7.22 show intermediate and equilibrium state deposition profiles as they are compared to those measured for all zones respectively. They all show fairly good predictions of the deposition at the front fence lines while at the rear fences the model shows predictions significantly different to the measurements at the early deposition stages. There are two possible reasons for that:

- The deposition profiles in the field might not be a result of a regular growth of the deposition process. Several erosion and deposition processes may be experienced under different environmental conditions before the measurements were actually made.

- Due to the significant effect of the value of the turbulent kinetic energy on the fluctuating velocity components and therefore on the prediction of the deposition conditions, the k-ε turbulence model might not be an adequate turbulence model to detect such detailed variances. This is a very well known drawback of the k-ε model especially in the prediction of flows including recirculation zones for example, the flow behind a backward facing step. However, the model is widely accepted and employed for many industrial applications, Thangam (1991).

Multiple fences of identical geometry must have identical capabilities for capturing the same amount and shape of depositing particles. The different deposition stages are shown in figures 7.23 to 7.25. It is clear from the figures that the deposition process begins at the front line and after a period of time commences at the following line, repeating for each consecutive line.

Similarly, the front fence reaches the equilibrium state first while the whole system of fences achieves that state when the downstream fence line has achieved its maximum capacity. In all cases, the final stages show a similar deposition amount and location at each fence line.

It is possible to simulate a severe sandstorm by increasing the particle mass flow rate. This can be achieved by increasing one or both of the suspension and saltation source term coefficients. There has been no detailed study that identifies which values correspond to specific storm strength, therefore for the purposes of simulation the saltation coefficient was increased from 0.25 to 0.27 and the above simulations of the multiple fence system were repeated.

The equilibrium state for all fence zones are shown in figure 7.26. It is clearly shown from this imaginary situation that, under some severe conditions the

trailing edge of the dune behind the front fence becomes attached to the dune developed around the following fence. Of course the speed of the merging of the dunes to form a single large dune is dependent on the distance separating the fence lines. Also it shows that the size of the largest dune increases with an increase in the number of lines.

7.4.3 Case study III: Conclusion

The numerical model based on the homogenous model was employed to simulate full-scale drifting sand flow and sand deposition around multiple row fence system in two-dimensional domain. The model shows a good qualitative agreement with the field observations especially at the first fence lines facing the prevailing wind. The model also shows a consecutive dune development at the different fence lines that were in a good agreement with the observations.

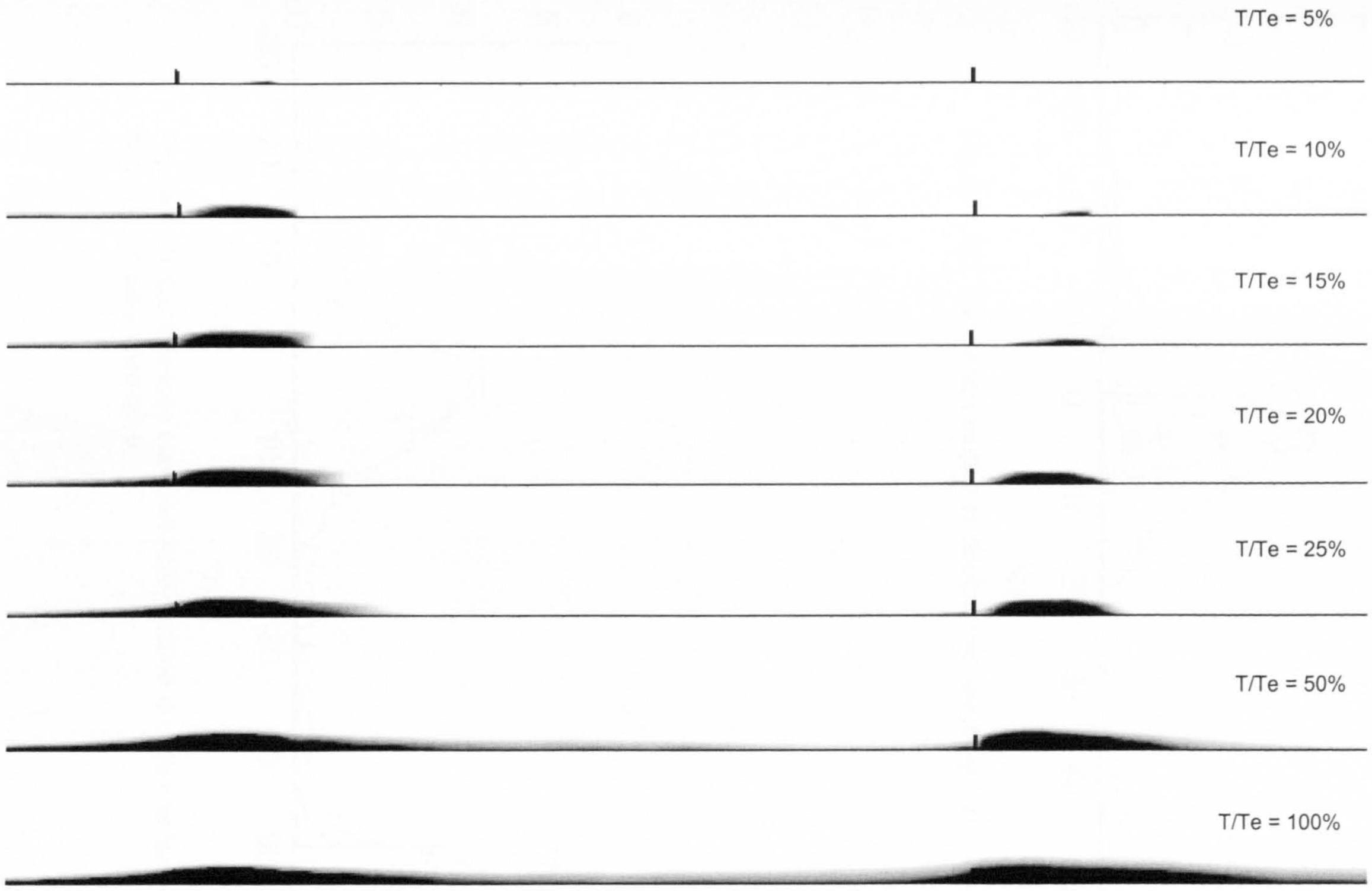

Figure 7.17: Deposition stages of double row fences system at KISR station.

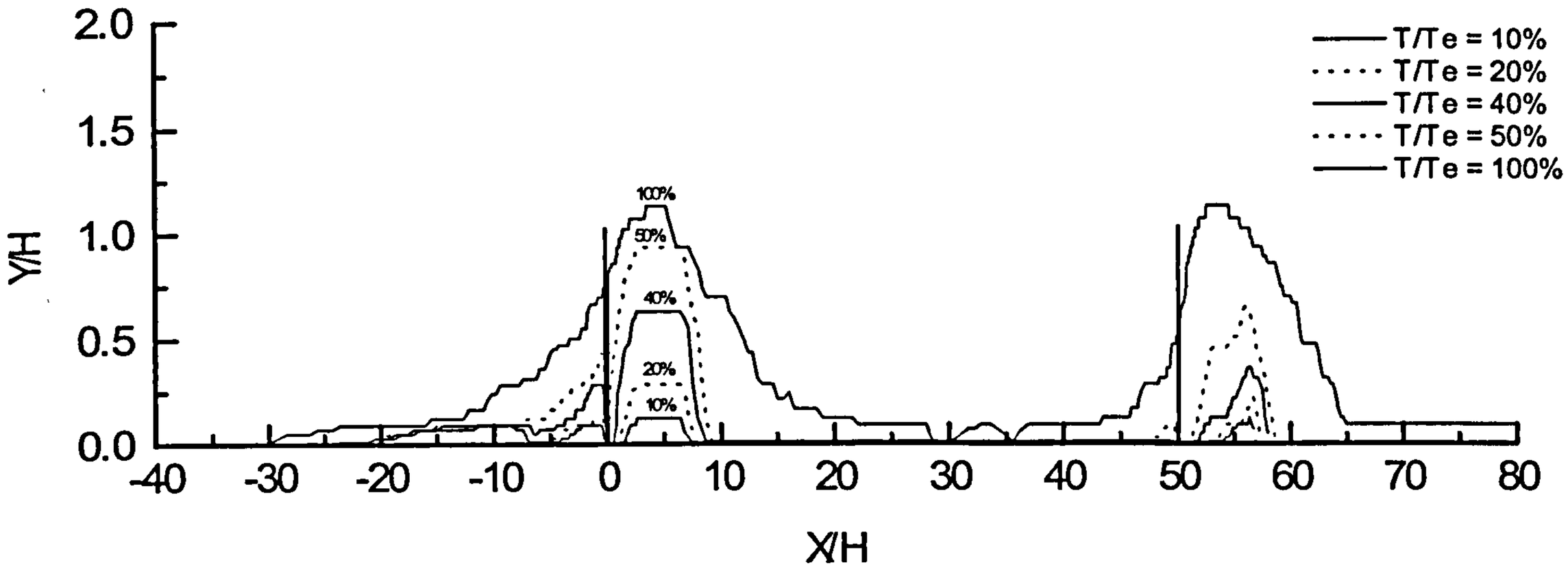

Figure 7.18: Deposition stages at double row fence system.

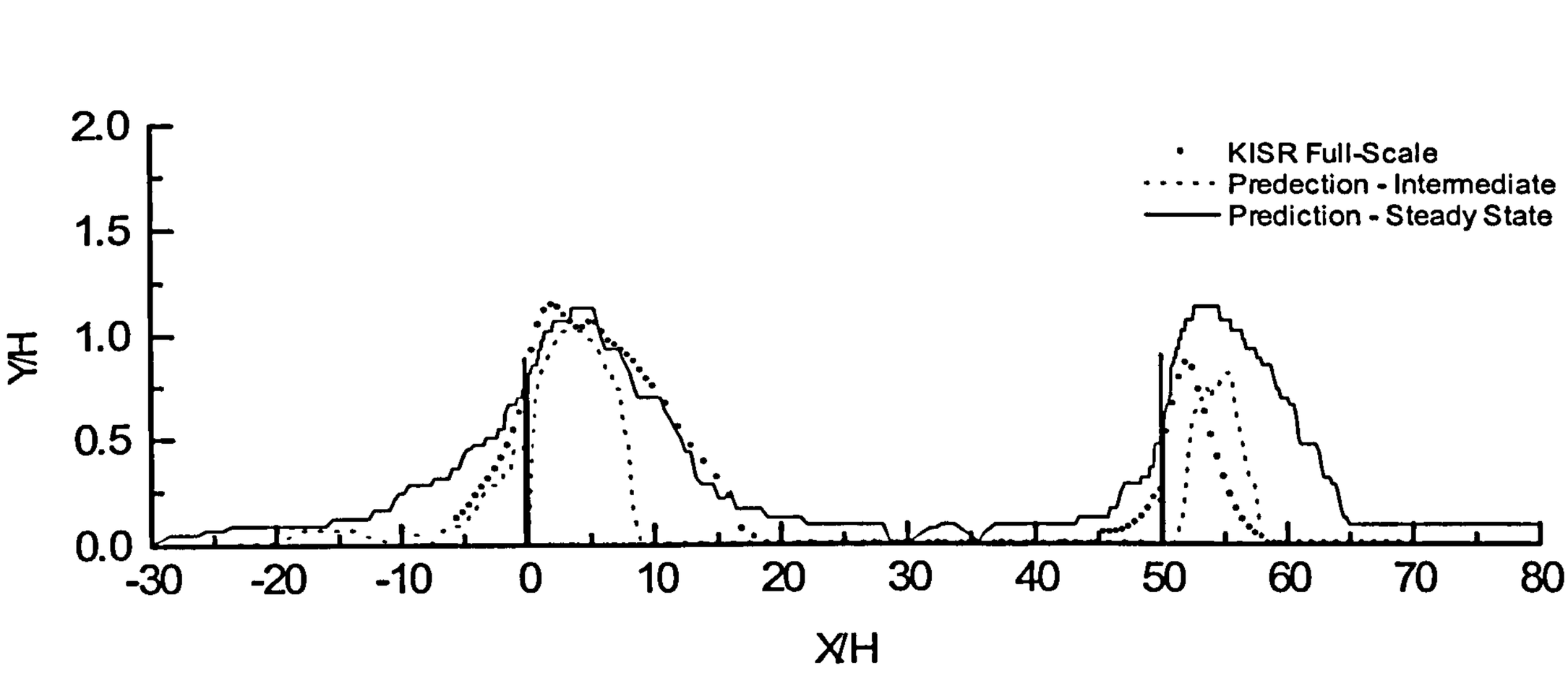

Figure 7.19: Comparison between KISR station double row fence system and the numerical model prediction.

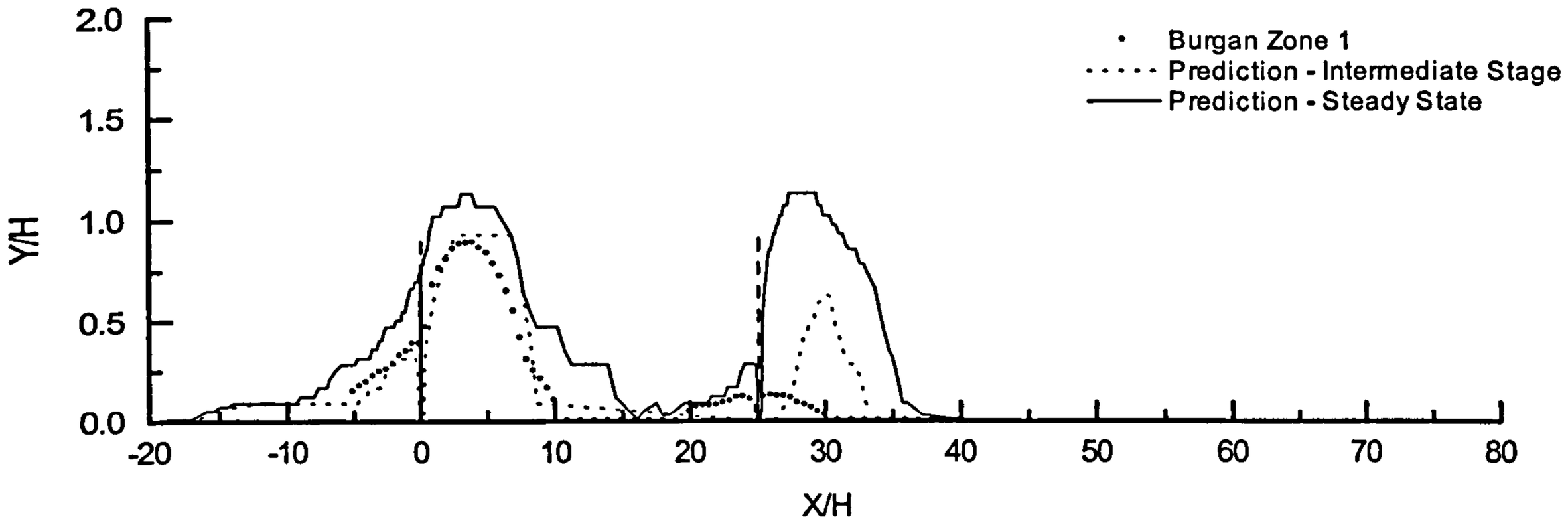

Figure 7.20: Comparison of the deposition profile at double row fence system in Burgan zone1.

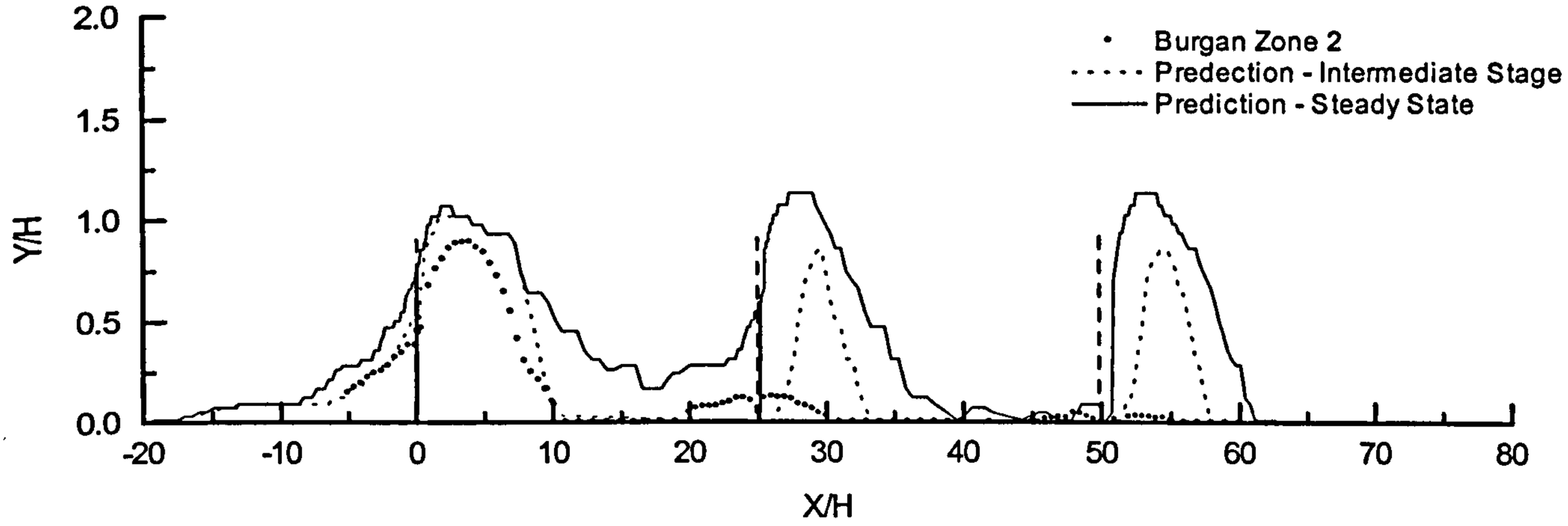

Figure 7.21: Comparison of the deposition profile at three row fence system in Burgan zone2.

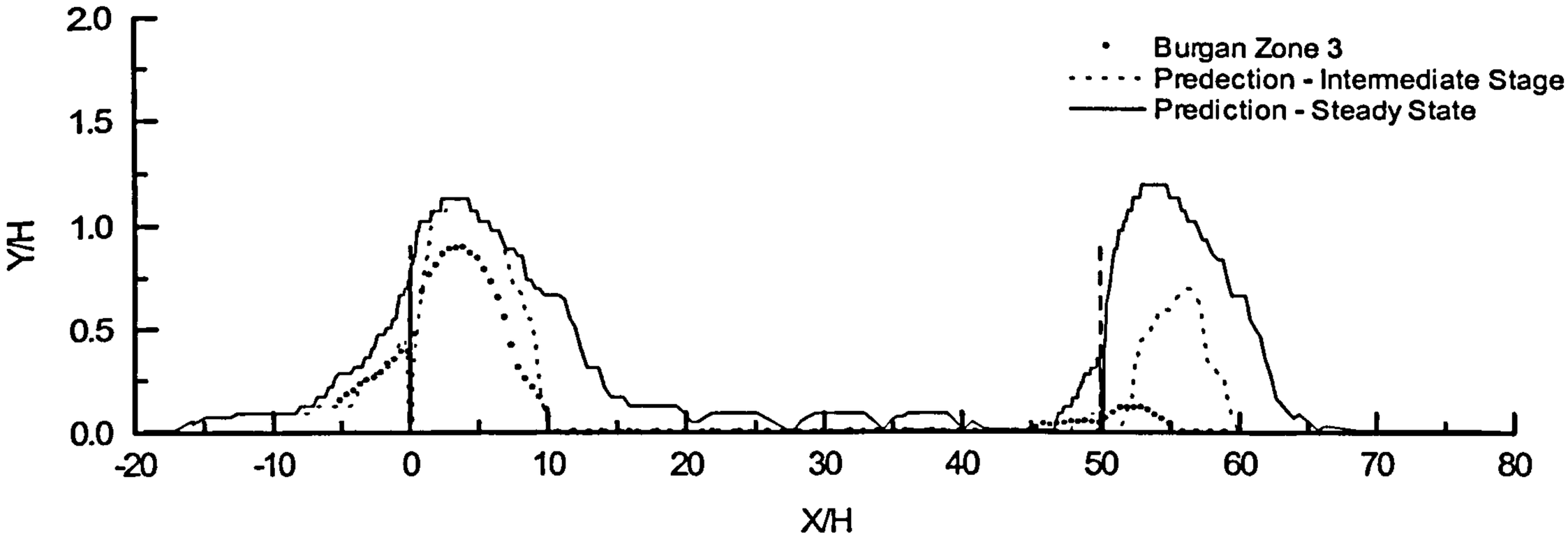

Figure 7.22: Comparison of the deposition profile at double row fence system in Burgan zone3.

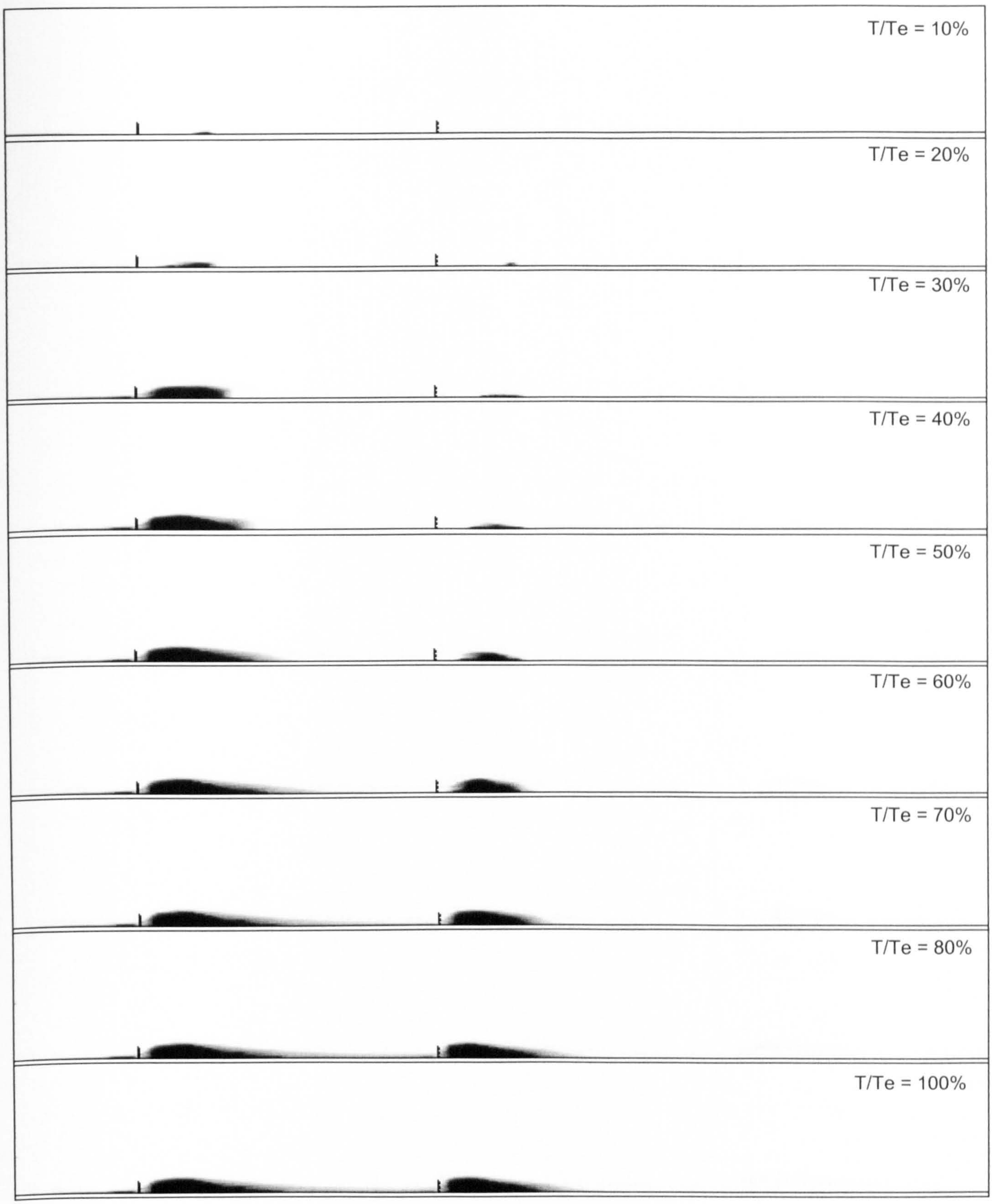

Figure 7.23: Deposition stages of multiple row fences system at Burgan zone1 using saltation coefficient 0.05.

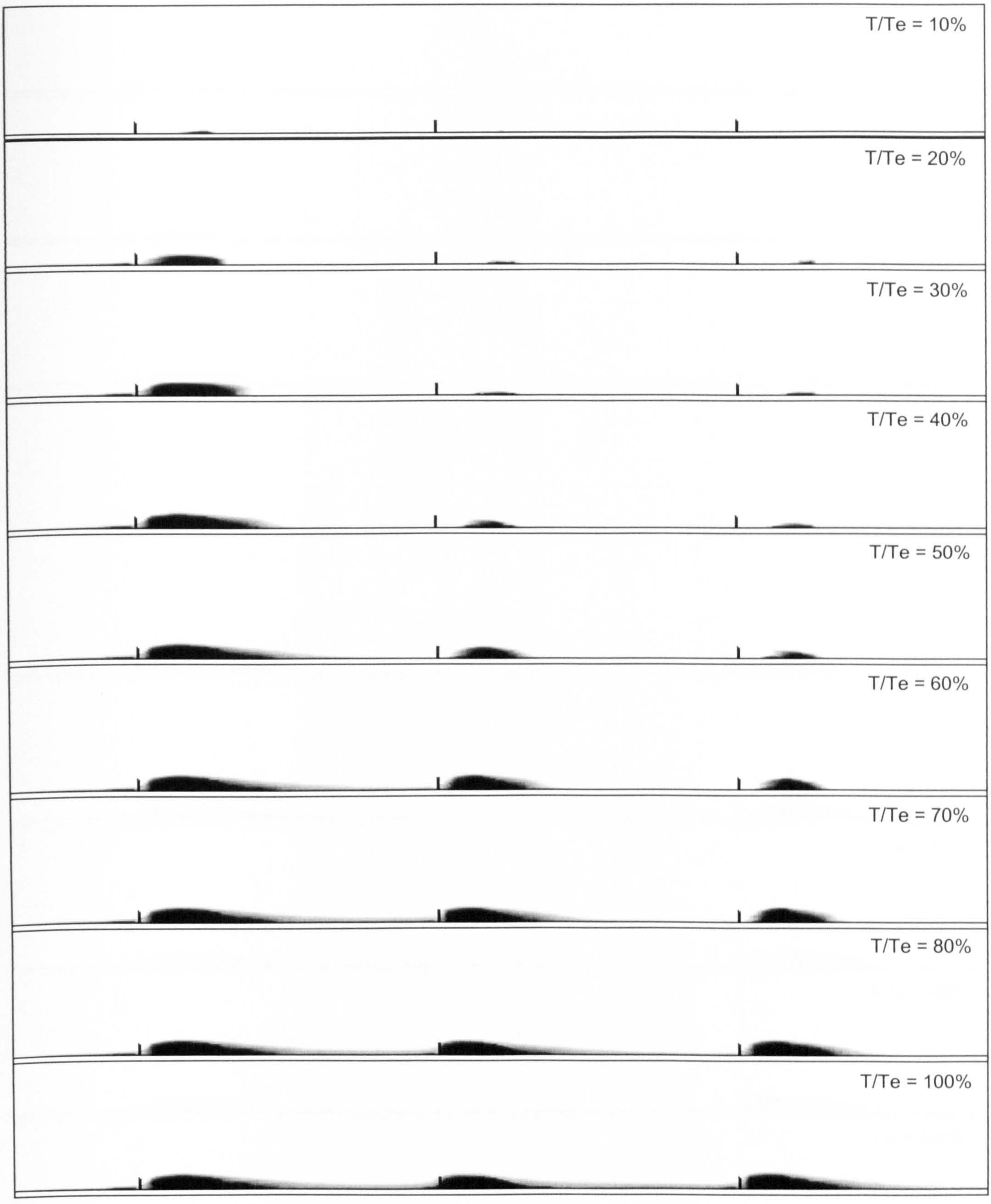

Figure 7.24: Deposition stages of multiple row fences system at Burgan zone2 using saltation coefficient 0.05.

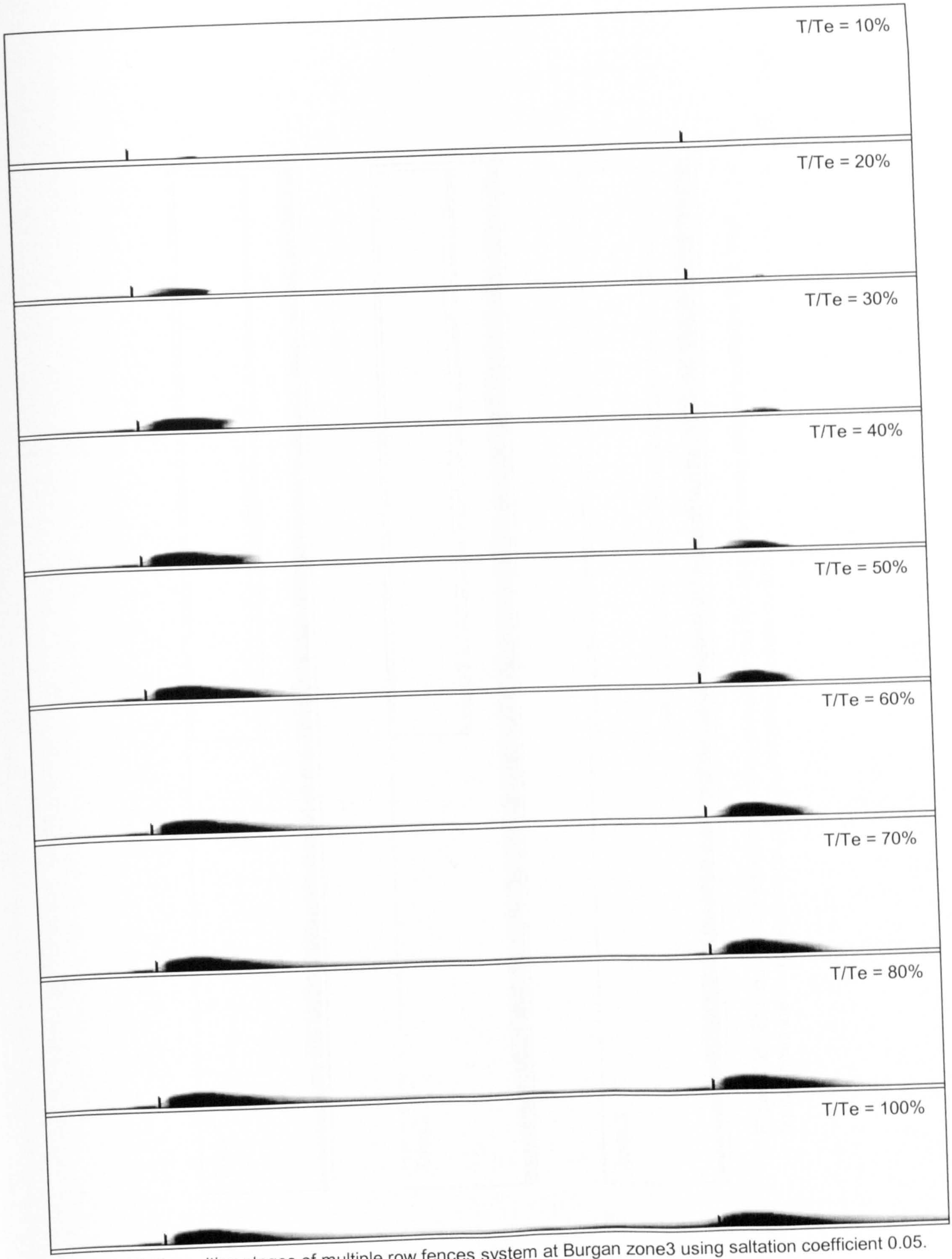

Figure 7.25: Deposition stages of multiple row fences system at Burgan zone3 using saltation coefficient 0.05.

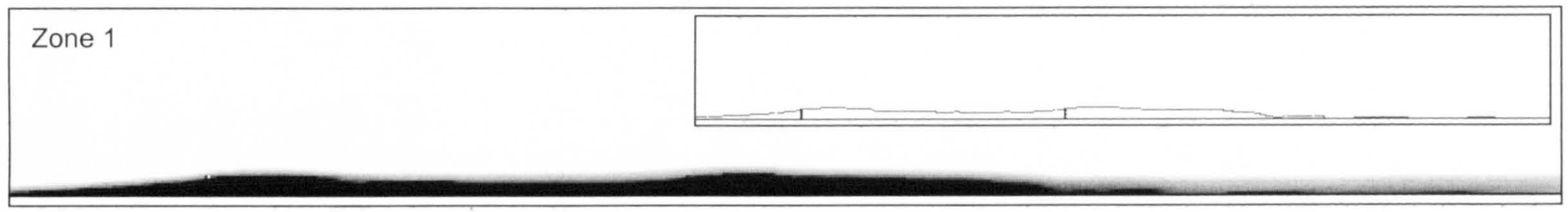

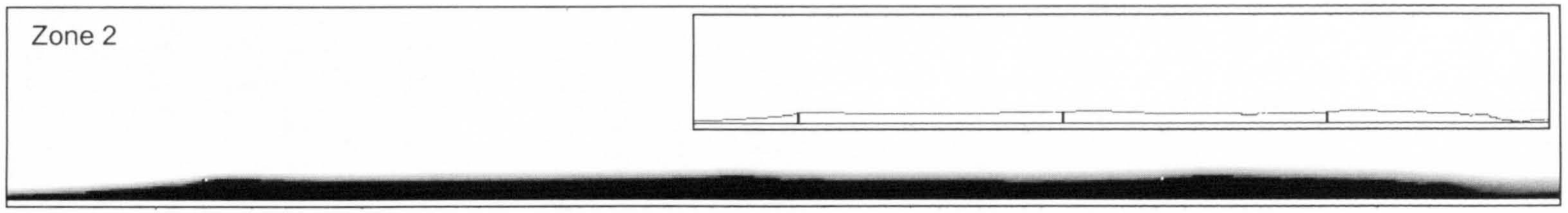

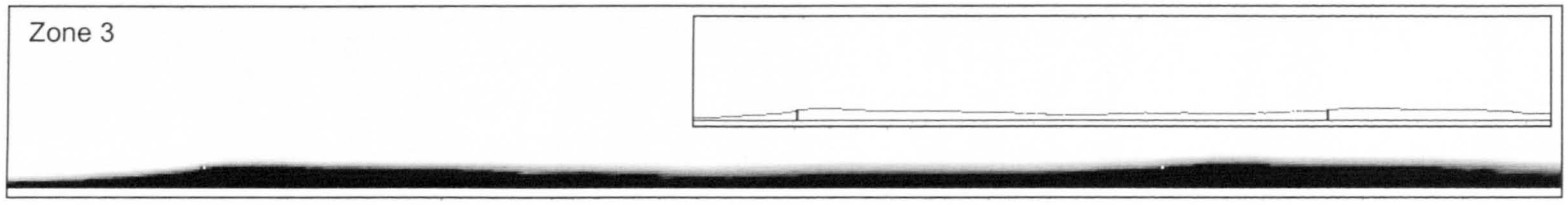

Figure 7.26: Equilibrium state deposition profiles at multiple row fences system using saltation coefficient 0.25. Inset figure shows the sharp interface boundary representing the dune surface.

7.5 Case study IV : Drifting sand at an open gate

The final case study is the simulation of drifting sand around an open gate facing the prevailing wind direction and comparison of the predicted drifts with those observed in the field experiment discussed earlier in Chapter 3.

7.5.1 Geometry and model set up

The gate geometry was defined as identical to that constructed in the full-scale field experiment and consists of two solid walls of 1.5 m height 'H' and 20m and 15 m length each as shown in figure 7.27.

The two walls were placed inside the computational domain separated by 4m, which represents the actual gate dimension. The inlet boundary was located upstream of the gate at a distance equal to 50H and the outlet boundary was 100H downstream from the wall. The side boundaries were set as a mirror boundary at 20H from the wall ends.

The domain was divided into 153 grid points in the axial direction, 75 grid points in the vertical direction and 80 grid points across the width. The distribution of these grid points took into account the requirement of finer grid resolution at areas of expected accumulation as well as around the wall and the gate where there is a significant change in the flow field as shown in the figure 7.27.

Quartz solid particles of 250μm diameter and 2650 kg/m^3 density were used to represent the average physical properties of typical sand particles. The inlet wind profile was set based on a friction velocity equal to 0.22 m/s and surface roughness equal to $D_p/30$. The turbulent intensity and length scale were set to be 1% and the wall height H respectively.

7.5.2 Results and discussions

The different stages of the dune development at the wall sides and through the gate are shown in figure 7.28. Similar to those observed in the field experiment,

figure 3.17, the dune initially started at a distance upstream from the wall where the reverse and the upstream flows meet.

The front edge of the dune forms according to the structure of the flow field, thus it is clearly shown at the early stages a very thin layer of particles are deposited through the gate centre line. As the dune increases in size, the reverse flow between the wall and the dune itself weakens and as a result the dune moves forward towards the wall until they meet and the dune starts climbing the wall.

It can be seen that the dune developed in front of the long wall is larger than the one formed in front of the smaller wall. This is a direct result of the ability of longer wall to reduce the flow velocity to a greater extent than the shorter wall, therefore a bigger dune develops in front of the longer wall.

The complex flow field immediately behind the wall and the gate is identified by the flow streamlines shown in figure 7.29. It is clearly shown that the flow field changes as a result of the presence of the interface solid boundary representing the dune surface. As expected, there is less disturbance of the flow field as the dune development reaches the steady state situation. This can be clarified by the streamlines in the later deposition stages where the flow streamlines passing the wall adopt a smoother shape than those passing the wall in the early stages.

Figure 7.30 shows the dune formed in front of the 20m wall from the upstream perspective for both field observation and numerical prediction. They are fairly comparable, both showing maximum heights of the dune at the wall centre line and minimum at the wall edges. This is a result of the flow separation at the centre of the wall and therefore a significant reduction in the flow velocity. As a consequence deposition conditions are more likely to be satisfied. The flow velocity increases when passing the ends of the wall, as a result increasing the friction velocity over the threshold value of the particles and therefore satisfying the erosion conditions, consequently particles are unlikely to be deposited.

Due to the occurrence of the flow diffusion zone just downstream of the gate, particles are deposited forming a dune with a dome shape as shown from the

field photograph in figure 3.19. The numerical model also captured this deposition behaviour at the same diffusion zone. Figure 7.31 shows the development of the diffusion zone dune from a downstream perspective. Due to the asymmetrical dimensions of the wall lengths, the dune is also shown to be of asymmetric shape at the early stages following the surrounding flow field structure. Similar to the observations, the dune then starts growing in all directions, as can be seen from the dune surface ripples in figure 3.19b and from the surface velocity vectors in figure 7.31.

The model provided predictions of later stages, which have been not yet achieved in the field showing that the dune may grow and expand in all directions until the dune completely blocks the gate. In the later stages, it can be observed that two side dunes are built within the weak flow zone created just behind the edges of the gate. These dunes grow up and start to climb the downstream side of the wall, which also may merge with the main dune and contribute to blocking the whole gate.

The last comparable behaviour that was captured by the model and clearly demonstrated in the field observation is the strong erosion area near the wall resulting from the acceleration of the flow as it passes through the gate, figure 3.19. Comparison of this photograph with the prediction at T/Te = 20% in figure 7.31, shows the erosion zones at the sides of the gate are clearly captured by the model wherever a high wind velocity occurs.

7.5.3 Case study IV: Conclusion

A numerical model based on the homogenous-FAVOR coupled model was employed to simulate air-sand flow and sand accumulation around a three-dimensional gate facing the prevailing wind direction. The model shows a good qualitative agreement with the field observations especially at the early deposition stages, at which the shape and location of the initial depositions were captured successfully.

7.6 Closure

The numerical model was validated against four distinct field and wind tunnel case studies. The predicted results were shown to be consistent with observations both in the two and three-dimensional computational space. The performance of the model shows qualitatively comparable results for the deposition shape, amount and location at solid and porous fences for the two dimensional applications and around an open gate for the three-dimensional applications.

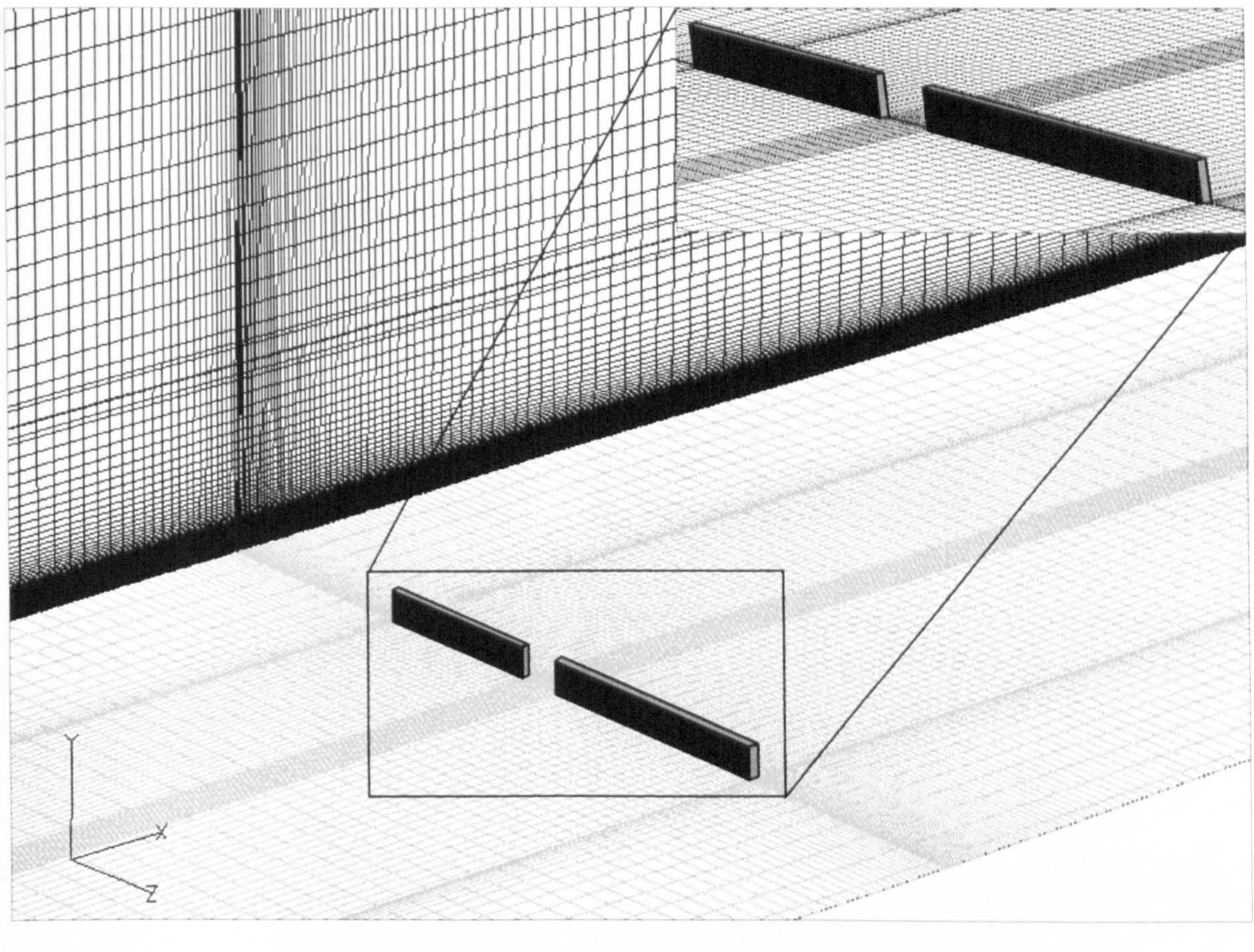

Figure 7.27: Computational domain showing the gate and wall geometry with the grid distribution.

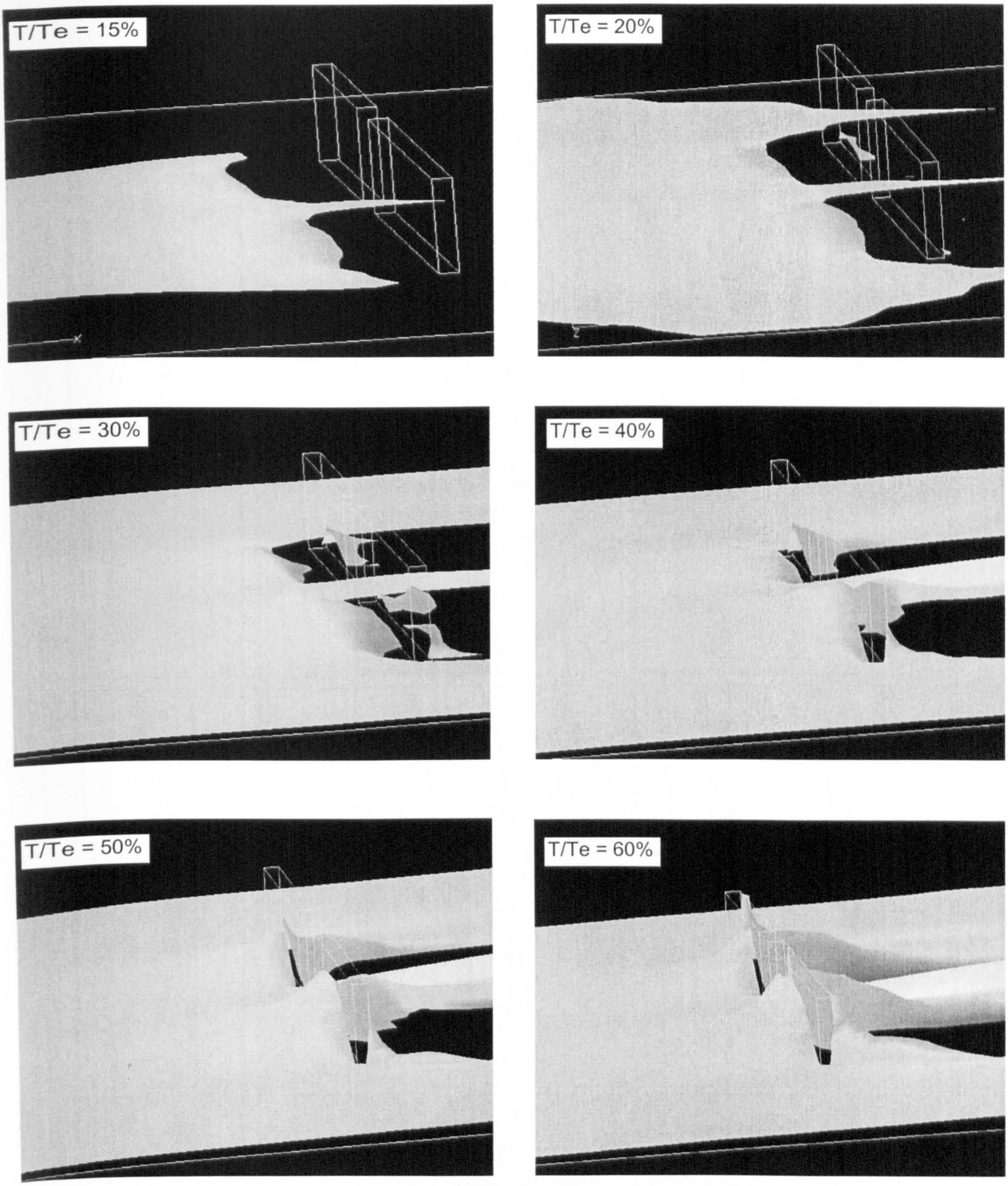

Figure 7.28: Simulation of the deposition stages around an open gate using the Homogenous model coupled with FAVOR. Isosurface of volume fraction at 0.75. Colour shading for illustration purposes only.

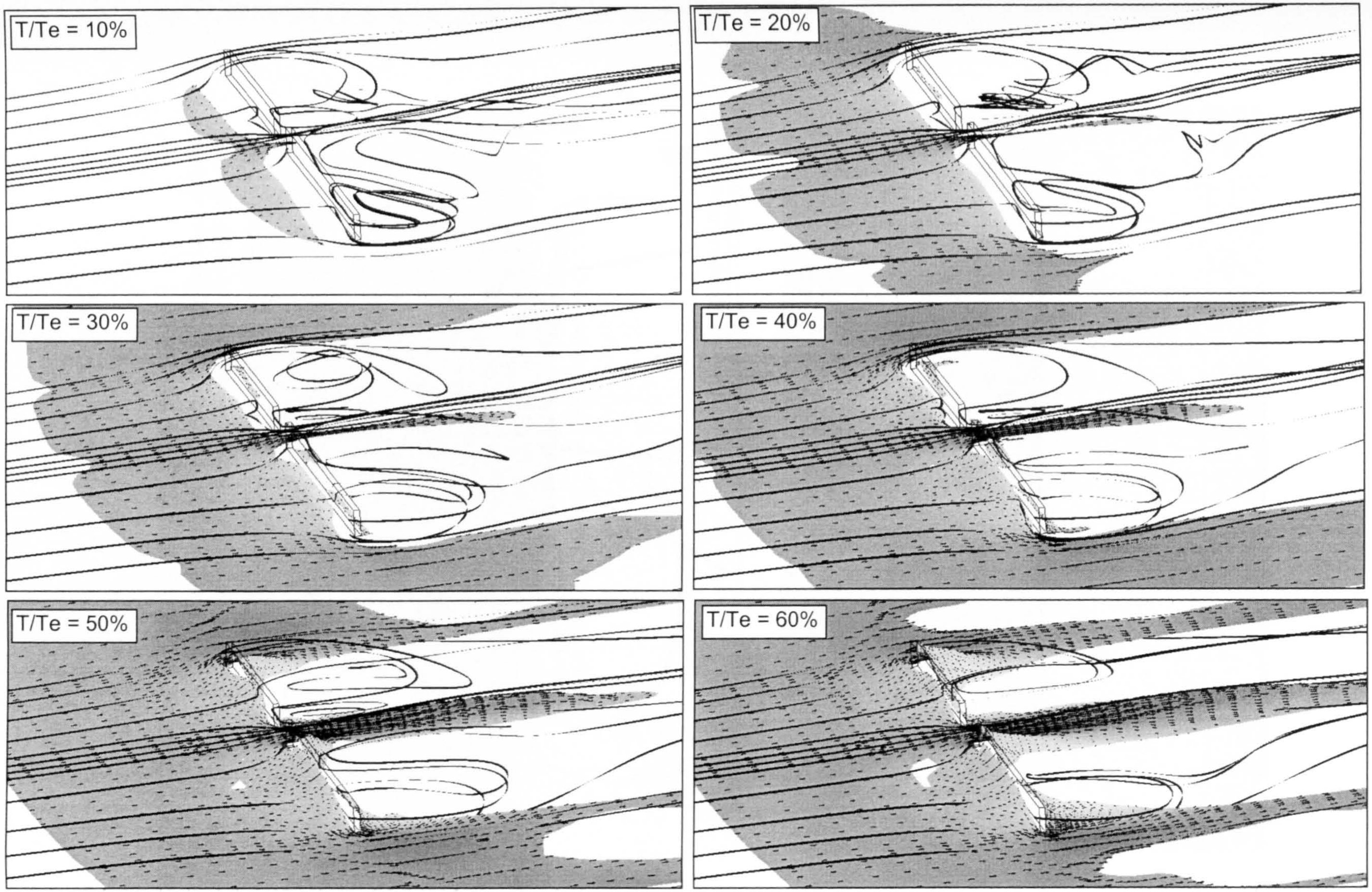

Figure 7.29: Deposition stages around an open gate showing the effect of the interface boundary on the flow field represented by surface velocity vector and flow streamlines. Isosurface of volume fraction at 0.75.Colour shading for illustration purposes only.

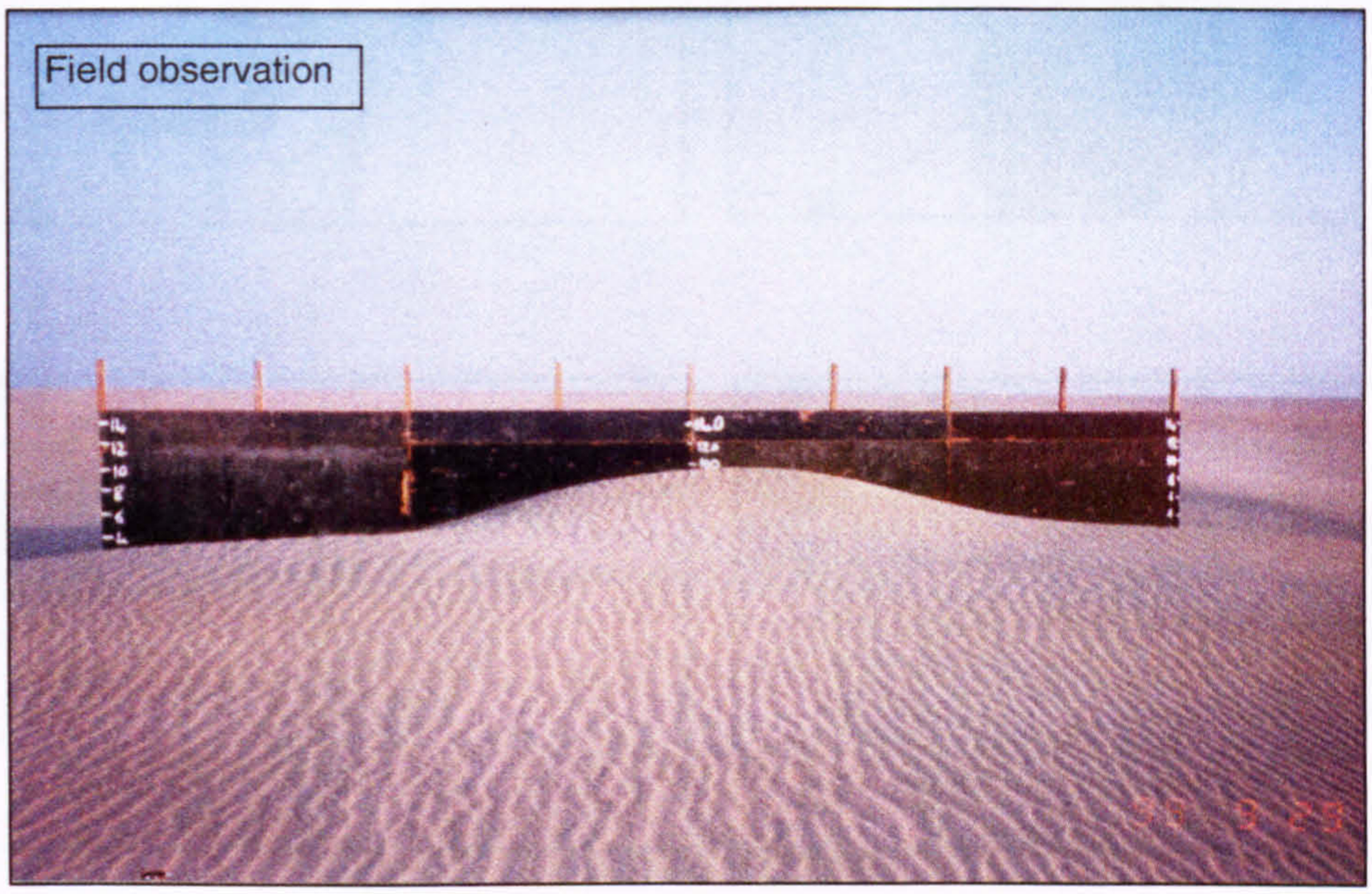

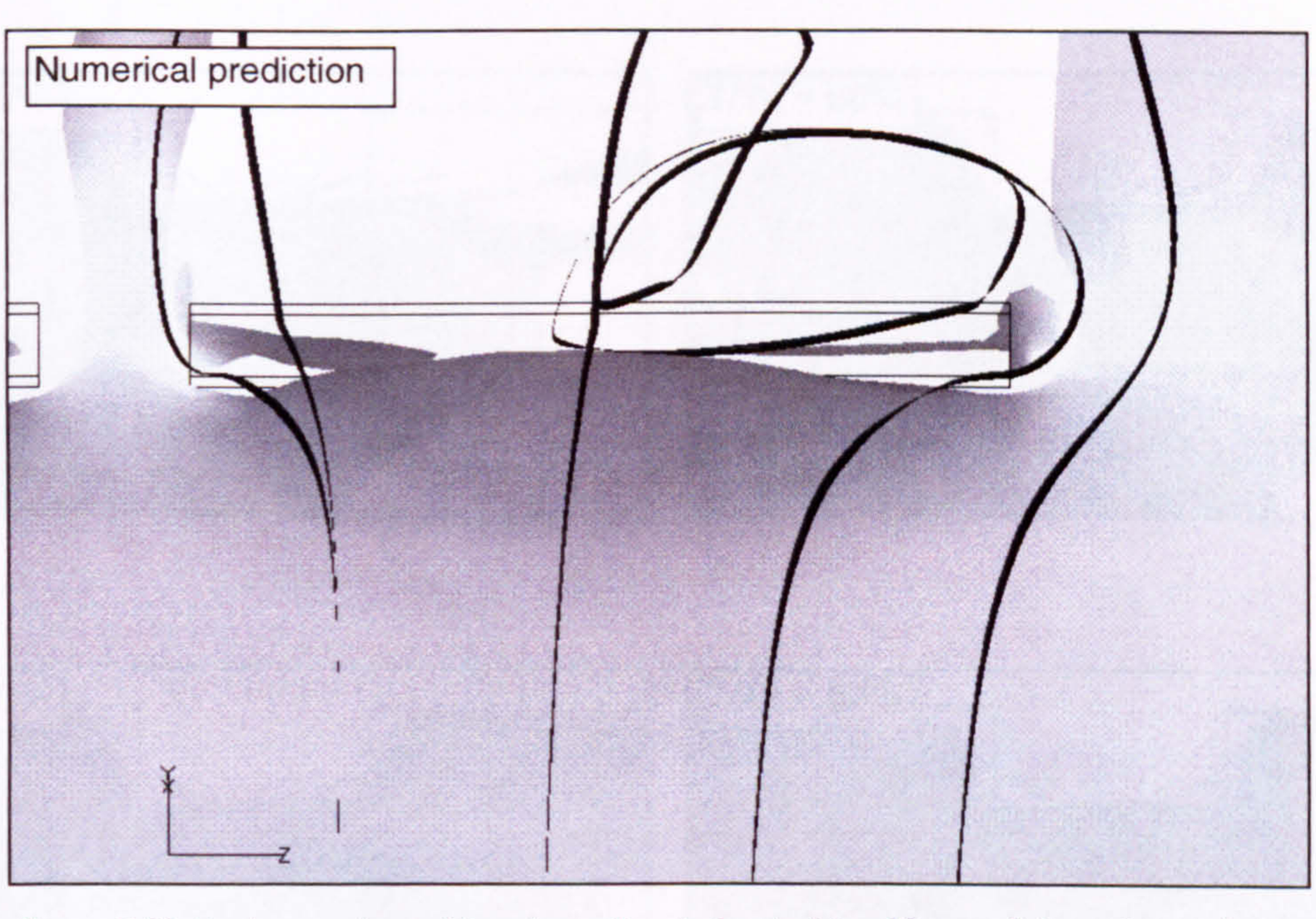

Figure 7.30: Upstream view of the deposition in front of the 20 m wall. Isosurface of volume fraction at 0.75. Colour shading for illustration purposes only.

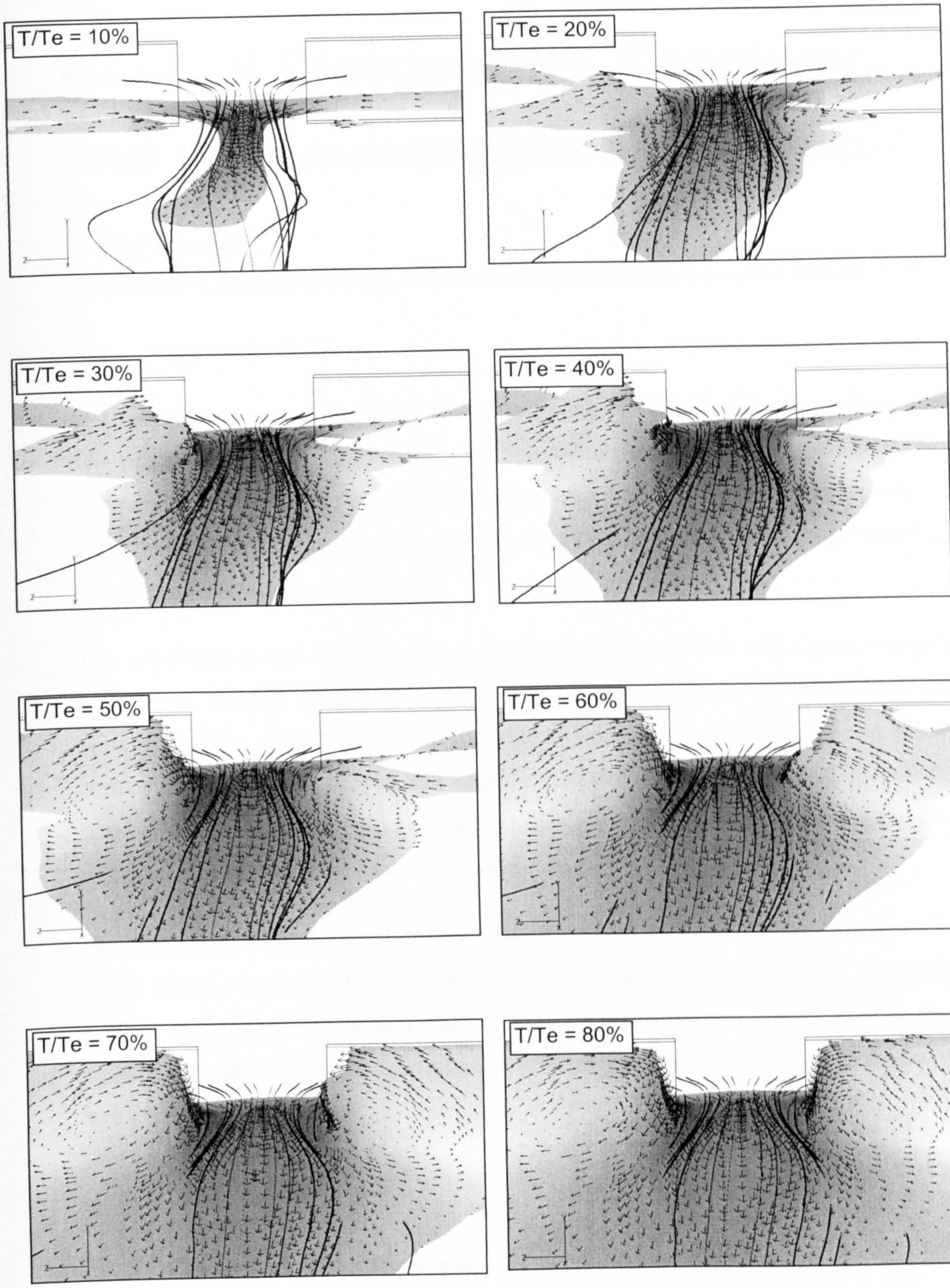

Figure 7.31: The Development stages of the diffusion dune downstream the gate showing the surface velocity vector and flow streamlines. Isosurface of volume fraction at 0.75. Colour shading for illustration purposes only.

Chapter 8

General Discussions, Conclusion and Recommendations for Future Studies

8.1 Introduction

In this chapter, some important points arising out of this study are discussed. The advantages and disadvantages of the numerical models implemented and examined in this work, using both Lagrangian and Eulerian approaches, are identified for environmental applications involving the drifting of sand (or snow) particles around obstacles.

The capabilities and limitations of employing the FAVOR technique, coupled with these models as a means of representing the interface solid boundary separating the flow field from the deposition areas, are identified. Model sensitivity issues related to the specification of the physical and numerical controlling parameters and the validation of the model against both field and wind tunnel observations are discussed.

Furthermore, the potential ability of the numerical model introduced in this work when employed for practical applications as an engineering designing tool or for purely scientific research is presented. Finally general comments, conclusion and recommendations for further possible extensions of this work are given.

8.2 General discussions

The work in this thesis reviewed the basic theoretical background of particle blown by wind including the three modes of transport and the threshold and

settlement conditions. The dune development and accumulation of particles, such as sand or snow, around obstacles of different geometry was reviewed. A field study was conducted during the work in this thesis at the Kuwaiti desert to observe the deposition patterns at multiple porous fences and at a full-scale gate model facing the prevailing wind.

Three different numerical approaches were investigated to simulate the erosion, transportation and then deposition of particles around obstacles in two and three dimensional computational space. The two-phase flow models developed during this work were incorporated into an existing, previously validated, single-phase CFD code. Modifications to the flow field governing equations were made in order to implement the FAVOR and the mixture two-phase flow models.

The Lagrangian particle tracking, and the Eulerian, homogenous and mixture, two-phase flow models show the potential capability to simulate flow regimes containing fluids of different physical properties such as either sand or snow particles and air.

The Lagrangian model has the advantage of computational simplicity, requiring only the solution of the particle equations of motion. The model can provide detailed information of individual particle trajectories and can be employed for a better understanding of the behaviour of particles in complex flow fields. Additionally, the model can represent flow fields containing particles with different physical properties such as size, density and with different initial conditions such as initial position or velocity. The distinction between suspended and saltated particles can be identified easily when the Lagrangian model is employed.

Although this model has many advantages, it is restricted to dilute flows where regions of high particle concentration are not expected. Additional terms must be incorporated into the particle equation of motion in order to take account of the contribution for other forces, which were ignored in the diluted flow, such as the particle-particle collision forces, the Basset Force and the Virtual mass Force.

Another significant drawback of the Lagrangian model is the computational cost involved in tracking a sufficiently large number of particles to obtain statistically stationary values that reflect the mean behaviour of the particles.

In contrast to the Lagrangian model, the Eulerian models represent the dispersed phase by transport of an additional continuum solved in a similar manner to that of the continuous phase governing equations.

The Eulerian models, such as the homogenous and mixture models, are computationally economical since the particle phase is treated as a continuum rather than a dispersed phase. The main weakness of Eulerian models is the computational complexity required to derive and implement terms involving the two-way coupling of momentum; the effect of the flow on the particles and the effect of the particles on the flow.

The homogenous model requires an additional transport equation for every particle phase with different physical properties, such as particle size or density.

The mixture model is more complicated where the mixture properties vary significantly. This is due to the need to solve the flow momentum equations for the mixture as a whole, where the mixture properties must include the contribution of every single secondary flow phase within the flow regime. Similar to the homogenous model, the mixture model requires an extra transport equation to be solved for each secondary flow phase within the flow.

The mixture model has an advantage over the homogenous model in its ability to incorporate the effect of high regions of particle concentration on the flow field. However, in practice the mixture model is limited to very small particle volume fractions by numerical instability. This was confirmed for high values of the particle volume fraction.

The major advantage of the homogenous model is that the flow field is not effected by the secondary phase flow even in regions of high particle concentration, thus it is in effect a one way coupled model. Therefore, the FAVOR technique can be employed efficiently and simply to take account of

the deposited particles on the flow field by developing an interface solid boundary surface whenever and wherever the particle deposition conditions are satisfied separating the entire flow field from the deposition zones.

Although FAVOR is relatively simple from the theoretical point of view, it shows potential capabilities to represent complicated solid surfaces such as the formation of sand dunes around obstacles, as an interface boundary within a fixed computational grid.

Additionally, the FAVOR technique performed well in response to the erosion and deposition process whenever the appropriate conditions were satisfied. The main weakness of FAVOR is the necessity of performing the simulation on a relatively fine grid especially near control volumes close to the interface boundary.

The model introduced in this work required tuning through many controlling parameters in order to simulate more realistic and practical applications as defined and analysed in Chapter 6. Through these parameters such as the particle suspension and saltation source term coefficients, the inlet wind and particle concentration condition and the surface roughness, specific flow conditions can be easily simulated.

The model has been validated against four distinct field and wind tunnel measurements and shows qualitatively good agreement and promising ability in the prediction of particle erosion-deposition phenomena around obstacles of different shapes. With the limited quantitative measurements available, the model shows good agreement with an acceptable degree of accuracy for engineering purposes. Generally, the model shows good qualitative comparisons of the deposition patterns in both two and three dimensional spaces.

8.3 Conclusion

A CFD code has been developed based on different two-phase flow computational theories such as particle tracking, homogenous and mixture models. These models were discussed, implemented and employed to simulate particle erosion, transportation and then accumulation around obstacles of different geometry.

Wind blown particles, accounting for both suspension and saltation were considered in two and three dimensions. The two modes of transport were represented in the model independently and no explicit empirical expressions were used to predict the particle flow rate.

The solid interface boundary between the flow field and the deposited particles was introduced successfully into the solution by rewriting the flow governing equations in a form suitable for the implementation of the FAVOR technique. In addition, an erosion-deposition algorithm was introduced based on the theory of the particle threshold and settlement conditions.

The homogenous model was found to be computationally efficient and theoretically simple to implement within an existing CFD code. The model was found to be even more versatile when coupled with the FAVOR technique for applications involving erosion, transportation and deposition of blown particles simultaneously.

Although the implementation can be considered to be in the preliminary stage of development, the models presented in this work already provide a practical CFD based tool for scientists and engineers. For scientists, the model can give a better and more detailed knowledge of particles blown by wind, knowledge which is either difficult or expensive to achieve in the field or with laboratory measurements.

For engineers the model can be considered to be a cheap and useful design tool that could assist in the preliminary design stage of roads, buildings, oil field installations, camps, farms etc that may built in such regions where sand or snow drift problems are a concern.

Also, the model can be applied to existing problems of sand drift by examining the effects of placing obstacles such as walls or fences upstream of the area of interest. The model can provide details regarding the aerodynamical structure of the flow field in general and on the location and amount of deposited particles.

In conclusion, a practical CFD tool has been developed and validated, incorporating novel physical and numerical models. The tool can be utilised by scientists and engineers to further understand the real world problem of drifting sand and snow in urban and industrial environments.

8.4 Recommendations for future studies

Further development of a number of key features in the model could be anticipated:

1. More detailed physical models of the different modes of particle transport by wind, suspension, saltation and surface creep, could be developed for the source terms in the particle transport. Additionally, the change in the surface shear stress due to saltating particles inside the flow boundary layer should be investigated and incorporated into the computations if more precise results are required.

2. The representation of the interface boundary by the FAVOR technique can be improved by a smoother surface definition, this can be achieved in two possible ways.

   - The first is by adapting the grid points around regions of an expected interface boundary to be finer allowing a smoother interface surface to be defined.

   - The second is by modelling the transport equation at cells crossed by the interface boundary so that they take into account the fraction of the cell blocked by the particle. This option was mentioned previously in Chapter 5.

3. The mixture model has produced promising results and has been employed successfully in many industrial applications. Yet special treatment to the governing equations and a careful treatment of the different mixture properties such as the mixture density, velocity and viscosity is required in order to apply it to practical applications involving drifting problems.

4. Expansion of the existing code could be undertaken to include the full multiphase flow model. This would enable a comprehensive numerical analysis of the potential and weakness of the existing two-phase flow based models in simulating flow fields involving drifting particles,

5. The models introduced in this work require continuous validation and calibration with as many field and laboratory measurement as possible. This will ensure that, in the future, reliable simulations may be obtained for as wide a variety of practical scenarios as possible.

References

Al-Ajmi, D.; F. Misak; F.I. Khalaf; M. Al-Sudairawi; and A.M. Al-Dousari. 1994. *Damage assessment of the desert and coastal environment of Kuwait by remote sensing* (VT001C). Kuwait Institute for Scientific Research, Report No. KISR4405, Kuwait.

Ahmadi, G. and D. Ma. 1990. A Thermodynamical Formulation for Dispersed Multiphase Turbulent Flows. I- Basic Theory. *Journal of Fluid Mechanics* 16, no. 2: 323-40.

Anderson, R. and P. K. Haff. 1988. Simulation of Eolian Saltation. *Science* 241: 820-3.

Anderson, R. and B. Hallet. 1986. Sediment Transport by Wind: Toward a General Model. *Geological Society of America Bulletin* 97: 532-5.

Anderson, Robert S. 1987. Eolian Sediment Transport as a Stochastic Process: The Effects of a Fluctuating Wind on Particle Trajectories. *Journal of Geology* 95: 497-512.

Bagnold, R. A. 1941. *The Physics of Blown Sand and Desert Dunes*, London: Methuen.

Berlemont, A., P. Desjonqueres, and G. Gouesbet. 1990. Particle Lagrangian Simulation in Turbulent Flows. *Int. J. Multiphase Flow* 16, no. 1: 19.

Blumberg, Dan G. and Ronald Greeley. 1996. A Comparison of General Circulation Model Predictions to Sand Drift and Dune Orientation. *Journal of Climate* 9: 3248.

Brookfield, M. E. and T. S. eds Ahlbrandt. 1983. *Eolian Sediments and Srocesses*, Amsterdam: Elsevier.

Budd, W. R., R. Dingle, and U. Radok. 1966. The Byrd Snowdrift Project: Outline and Basic Results. *In Studies in Antarctic Meteorology, American Geophysical Union, Antarctic Research Series.* 9: 71-134.

Burry, D. and G. Bergeles. 1993. *Int. J. Multiphase Flow* 19, no. 4: 651.

Cebeci, T. and P. Bradshaw. 1977. Momentum Transfer in Boundary Layers. London: McGraw-Hill.

Cermak, J. E Shen H. W. Peterka J. A. and L. F. Janin. 1982. *Wind-Tunnel Research for IAP Sand Study Project. Tech. Report 5-3-5684*. Colorado: Fluid Mechanics and Wind Engineering Program, Colorado State University.

Chen, X. Q. and J. C. F. Pereira. 1995. Prediction of Evaporating Spray in Anisotropiclly Turbulent Gas Flow. *Numer. Heat Transfer.* 27: 143.

Chepil, W. S. 1945b. Dynamics of Wind Erosion:II. Initiation of Soil Movement. *Soil Sci.* 60: 397-411.

Chepil, W. S. 1959. Equilibrium of Soil Grains at the Threshold Movement by Wind. *Proc. Soil Sci. Soc. Am.* 23: 422-8.

Cooke, R., Warren A. , and Goudie A. 1993. *Desert Geomorphology*. London: UCL.

Crowe, C. T., T. R. Troutt, and J. N. Chung. 1996. Numerical Models for Tow-Phase Turbulent Flows. *Annu. Rev. Fluid Mech.* 28: 11-43.

Dayou, Liu. 1997. A Further Discussion on Basic Equations for Two-Phase Flow. *Science in China* 41, no. 2: 216.

Dayou, Liu and Fie Dong. 1996. A Three-Fluid Model of the Sand Driven Flow. *Applied Mathematics and Mechanics* 17, no. 7: 647.

Dover, S. E. *Numerical Modelling of Blowing Snow*. PhD thesis, Dept of Applied Maths, University of Leeds, 1993.

Drew, D. A. 1983. Mathematical Modeling of Two-Phase Flow Equations. *Int. J. Multiphase Flow.* 5: 243-64.

Durst F. , Milojevic D. , and Schonung B. 1984. Eulerian and Lagrangian Predictions. *AIAA J.* 23: 396-404.

El-Baz, F. and M. H. A. eds Hassan. 1986. *Physics of Desertification.* Dordrecht: Martinus Nijhoff.

Faeth, G. M. 1983. Recent Advances in Modeling Particle Transport Properties and Dispersion in Turbulent Flow. *Proc. ASME-JSME Therm. Engng. Conf.* 2: 517-34.

Gidaspow, D. 1994. *Multiphase Flow and Fluidization. Continuum and Kinetic Theory Descriptions.* San Diego: Academic Press.

Gillette, D. A. 1981. Production of Dust that may be Carried Great Distances. In Desert Dust, T.L. Pewe (eds), 11-26. *Geol. Soc. Am. Spec. Pap. 186* .

Gosman, A. D. 1999. Developments in CFD for Industrial and Environmental Applications in Wind Engineering. *Jornal of Wind Engineering and Industrial Aerodynamics* 81: 21-39.

Gosman, A. D. and E. Ioannides. 1983. Aspects of Computer Simulation of Liquid-Fuelled Combustors. *Combustors. J. Energy* 7: 482.

Greeley, R. and J. D. Iversen. 1986. *Wind as a Geological Process,* Cambridge: Cambridge University Press.

Hirt, C. W. 1993. Volume-Fraction Techniques: Powerful Tools for Wind Engineering. *Journal of Wind Engineering and Industrial Aerodynamics* 47: 327-38.

Hirt, C. W. and J. M. Sicilian. 1985. A Porosity Technique for the Definition of Obstacles in Rectangular Cell Meshes. *4th. Int. Conf. Ship Hydro.*

Horikawa, K., S. Hotta, and N. C. Kraus. 1986. Literature Review of Sand Transport by Wind on a Dry Sand Surface. *Coastal Engineering* 9: 503-26.

Hutchinson, P. ; Hewitt, G.F. and Dukler, A.E., 1971, Deposition of liquid or solid suspensions from turbulent gas stream : A Stochastic Model, *Chem. Eng. Sci*. Vol. 26, pp. 419.

Ishii, M. 1975. *Thermo-Fluid Dynamics Theory of Two-Phase Flow*. Eyrolles.

Ishii, M. and K. Mishima. 1984. Two-Fluid Model and Hydrodynamic Constitutive Relations. *Nucl. Eng. & Des.* 82: 843-54.

Iversen, J. D. 1981. Comparison of Wind-Tunnel Model and Full-Scale Snow Fence Drifts. *Journal Wind Eng. Industrial Aerodynamics* 8: 231-49.

Iversen, J. D. 1983. Saltation Threshold and Deposition Rate Modelling. *Eolian Sediments and Processes*. Edited M.E. Brookfield and T.S. Ahlbrandt, Amsterdam, Elsiver : 103-13.

Iversen, J. D. and others. 1987. Aeolian Saltation Threshold: The Effect of Density Ratio. *Sedimentology.* 34: 699-706.

Iversen, J. D. and K. R. Rasmussen. 1999. The Effect of Wind Speed and Bed Slope on Sand Transport. *Sedimentology* 46: 723-31.

Iversen, James D. and Rasmussen Keld R. 1999. The Effect of Wind Speed and Bed Slope on Sand Transport. *Sedimentology* 46: 723-31.

Jensen, J. L. and M. SØrensen. 1983. *On the Mathematical Modeling of Aeolian Saltation. In Mechanics of Sediment Transport*, B.M. Sumer and A. Muller (eds). Rotterdam: Balkema.

Joseph, D. D. and others. 1990. Ensemble Average and Mixture Theory Equations for Incompressible Fluid-Particle Suspensions. *Int. J. Multiphase Flow* 16, no. 1: 35-42.

Kawamura, R. 1951. Study on Sand Movement by Wind. *Reports of Physical Sciences Research Institute of Tokyo University*, 5, no. 3: 95-112, [Translated from the Japanese by National Aeronautic and Space Administration (NASA), Washington DC, 1972].

Kawamura, Tetuya, Kan Makiko , and Tsutomu Hayashi. 1999. Numerical Study of the Flow and the Sand Movement Around a Circular Cylinder Standing on the Sand. *JSME Int. Journal* 42, no. 4: 605-11.

Kind, R. J. 1976. A Critical Examination of the Requirements for Model Simulation of Wind-Induced Erosion/Deposition Phenomena Such as Snow Drift. *Atmospheric Environmrnt* 10: 219-27.

Kind, R. J. 1990. Mechanics of Aeolian Transport of Snow and Sand. *Journal of Wind Engineering and Industrial Aerodynamics.* 36: 855-66.

Kind, R. J. 1992. one-dimensional Aeolian Suspension above Beds of Loose Particles- A New Concentration-Profile Equation. *Atmospheric Environment* 26, no. 5: 927-31.

Kwarteng, A.Y., V. Singhroy, R. Saint-Jean, and D. Al-Ajmi. 1997. RADARSAT SAR data assessment of the oil lakes in the Greater Burgan oil field, Kuwait, *Proceedings, International Symposium on Geomatics in the Era of RADARSAT*, Ottawa, Canada, May 24-30.

Lettau K. and Lettau H.H. 1977. Experimental and Micro-meteorological Field Studies of Dune Migration. In Exploring the World's Driest Climate, Lettau K. and Lettau H.H. (eds). 110-147. Wisconsin: *Institute for Environmental Studies*, University of Wisconsin-Madison.

Loth, E. 2000. Numerical Approaches for Motion of Dispersed Particles, Droplets and Bubbles. *Progress in Energy and Combustion Science*, 26: 161–223.

Masselot, A. and B. Chopard. 1998. A Lattice Boltzmann Model for Particle Transport and Deposition. *Europhysics Letters* 42, no. 3: 259-64.

McEwan, I. K. 1991. *The Physics of Sand Transport by Wind*. Ph.D. Thesis. 1991: University of Aberdeen.

Melaaen, M. C. 1990. *Analysis of Curvilinear Non-orthogonal Coordinates for Numerical Calculation of Fluid Flow in Complex Geometries*. Norway: PhD Thesis, University of Trondheim.

Mikko Manninen , Veikko Taivassalo , and Sirpa Kallio. 1996. Finland: Technical Research Center of Finland, VTT Puplications, 288.

Minato, Akihiko and Ryuhei Kawabe. 1988. Numerical Analysis Method for Two-Dimensional Two-Fluid Model using Control Volume Formulation. *Journal of Nuclear Scince and Technology* 25, no. 12: 901-13.

Monin, A. S. and A. M. Yaglom. 1965. *Statistical Fluid Mechanics: Mechanics of Turbulence*. Cambridg, MA: MIT Press.

Moodie, T. B., J. P. Pascal, and G. E. Swatres. 1998. Sediment Transport and Deposition from a Two-Layer Model of Gravity Currents on Sloping Bottoms. *Studies in Applied Mathematics* 100, no. 3: 215-44.

Mostafa, A. A. and H. C. Mongia. 1987. On the Modelling of Turbulent Evaporation of Sprays: Eulerian vs Lagrangian Approach. *Int. J. Heat Mass Transfer* 30, no. 12: 2583.

Murata, Shigeto, Minato Akihiko, and Osamu Yokomizo. 1991. Development of Three-Dimensional Analysis Code for Two-Phase Flow using Two-Fluid Model. *Journal of Nuclear Scince and Technology* 28, no. 11: 1029-40.

Nickling, W. G. 1988. The Initiation of Particle Movement by Wind. *Sedimentology*, 35: 499-511.

Nordstrom, K. F., N. P. Psuty, and R. W. G. eds Carter. 1990. *Coastal Dunes*, Chichester: Wiley.

Ormancey, A. and Martinon J. 1984. Prediction of Particle Dispersion in Turbulent Flows. *J. PCH PhysicoChemical Hydrodynamics* 5: 229.

Owen, P. R. 1964. Saltation of Uniform Grains in Air. *Journal of Fluid Mechanics*, 20: 225-42.

Peric, M. 1985. *Finite Volume Method for the Prediction of Three-Dimensional Fluid Flow in Complex Duct*. London: PhD. Thesis: Imperial College.

Phillips, C. J. and B. Willetts. 1979. Predicting Sand Deposition at Porous Fences. *J. Am. Soc. Civ. Eng., Waterway, Port, Costal & Ocean Eng. Div.* 105: 15-31.

Picart, A., A. Berlemont, and G. Gouesbet. 1986. Modeling and Predicting Turbulent Fields and

the Dispersion of Discrete Particles Transported by Turbulent Flows. *Int. J. Multiphase Flow* 12, no. 2: 237-61.

Pomeroy, J. W. 1988. Ph.D. Thesis, Saskatoon: University of Saskatchewan.

Pye, K. and Tsoar H. 1990. *Aeolian Sand and Sand Dunes*. London: Unwin Hyman.

Rubini, P.A. "SOFIE - Simulation of Fires in Enclosures", *Proceedings of 5th International Symposium on Fire Safety Science*, Melbourne, Australia, March 1997, International Association for Fire Safety Science, ISBN 4-9900625-5-5.

Schmidt, R. A. 1980. Threshold Wind-Speeds and Elastic Impact in Snow Transport. *Journal of Glaciology* 26: 453-67.

Schmidt, R. A. 1985. Transport Rate of Drifting Snow and the Mean Wind Speed Profile. *Boundary Layer Meteorology* 34: 312-241.

Sheun, J. S. and others. 1985. Structure of Particle-Laden Jets: Measurements and Predictions. *AIAA J.* 23: 396-404.

Shirolkar, J. S., C. F. Coimbra, and M. Queiroz McQuay. 1996. Fundamental Aspects of Modeling Turbulent Particle Dispersion in Dilute Flows. *Prog. Enrgy Combust. Sic.* 22: 363-99.

Simonin, O. 1990. Eulerian Formulation for Particle Dispersion in Turbulent Two-Phase Flows. *Proc. 5th workshop two-phse flow pred.*: Erlangen.

Soo, S. L. 1990. *Multiphase Fluid Dynamics*. Science Press and Grwer Technical.

SØrensen, M. 1991. An Analytical Model of Wind-Blown Sand Transport. O.E. Barndorff-Nielsen and B.B. Willetts (eds). Acta Mechanica, Suppl. 1: 67-81.

SundsbØ, Per-Arne and Ernst W.M. Hansen. 1997. Modeling and Numerical Simulation of Snow Drift Around Snow Fences. *Snow Engineering*: 353.

Tabler, R. D. 1980. Geometry and Density of Drifts Formed by Snow Fences. *Journal of Glaciology* 26, no. 94: 405-19.

Tabler, R. D. 1986. *Snow Fence Handbook (Releas 1.0).* Laramie, Wyoming.: Tabler & Associates.

Tabler, R. D. 1989. Snow Fence Technology: State of the Art. *First International Confrence on snow Engineering*USA: Army Corps of Engineering, Cold Regions Research Laboratory.

Tabler, R. D. 1994. *Design Guidelines for the Control of Blowing and Drifting Snow*. Washington: National Research Council.

Tabler, R. D. and R. L. Jairell. 1980. Studying Snowdrifting Problems with Small-Scale Models Outdoors. *In Westren Snow Conference.* 1-13Wayoming.

Takeuchi, M. 1980. Vertical Profile and Horizontal Increase of Drift-Snow Transport. *Journal of Glaciology* 26, no. 94: 481-92.

Thangam, S. and C.G. Speziale. Turbulent separated flow past a backward-facing step: a critical evaluation of two-equation turbulence models. ICASE Report 91-23, *Institute for Computer Applications in Science and Engineering*, NASA Langley Research Center, Hampton, Virginia, 1991.

Toorman, E. A. and J.E. Berlamont. 1992. Free Surface Flow of a Dense, Natural Cohesive Sediment Suspension. *Computational Fluid Dynamics* 2: 1005.

Tsoar, H. 1983. Wind Tunnel Modelling of Echo and Climbing Dunes. Eolian Sediments and Processes. *Edited M.E. Brookfield and T.S. Ahlbrandt*, Amsterdam, Elsiver : 247-59.

Uematsu, T. and others. 1991. Three-Dimensional Numerical Simulation of Snowdrift. *Cold Region Science and Technology* 20: 65-73.

Ungar, J. E. and P. K. Haff. 1987. Steady State Saltation in Air. Sedimentology 34: 289-99.

Ungarish, M. 1993. *Hydrodynamics of Suspensions: Fundamentals of Centrifugal and Gravity*

Separation. Berlin: Springer.

Van Dijk, P. M., S. M Arens, and Van Boxel J.H. 1999. Aeolian Processes Across Transverse Dune. II: Modelling the Sediment Transport and Profile Development. *Earth Surface Processes and Landforms* 24: 319-33.

Warner, B. T. and P. K. Haff. 1988. The Impact Process in Aeolian Saltation: Two Dimensional Simulations. *Sedimentology* 35: 189-96.

Wei Shyy and others. 1996. *Computational Fluid Dynamics with Moving Boundaries.* London: Taylor & Francis Ltd.

White, B. R. and J. C. Schulz. 1977. Magnus Effect in Saltation. *Journal of Fluid Mechanics.* 81: 497-512.

Willetts, B. B. and M. A. Rice. 1985. Inter-saltation Collisions. *Proceeding of the International Workshop on the Physics of Blown Sand.*

Wipperman, F. K. and G. Gross. 1986. The Wind Induced Shaping and Migration of an Isolated Dune - A Numerical Experiment. *Boundary-Layer Meteorology* 36: 319-34.

Yoon, J. Y. and V.C. Patel. 1996. Numerical Model to Turbulent Flow Over Sand Dune. *Journal of Hydrulic Engineering* 122, no. 1: 10.

Yuan, Y. and C. T. Crowe. 1989. *Particulate Sci. Technol.* 7: 129.

Zingg, A. W. 1953a. Wind Tunel Studies of the Movement of Sedimentary Material. *Proceedings of the 5th Hydraulics Conf. Bull.* 34: 111-35.

Appendix A

Optimum Particle Searching Algorithm

It is a time-consuming procedure in Lagrangian trajectory computations to determine the location of a particle inside a Eulerian control volume. The simplest but most computationally expensive way of locating a particle in the computational domain is to check all the Eulerian control volumes. Note that this procedure has to be repeated along all the trajectories at each time step.

Figure A.1, shows how a particle moves from its old position at time "t" to a new position at time "t+Δt" after a Lagrangian time step Δt. Two questions should be answered quickly and efficiently for each particle at each time step:

- *Is the particle still inside the control volume or not?*
- *If not. In which control volume is the particle?*

The answer to these questions is simple when viewed on a piece of paper or graphically on the computer screen, but it can cost a lot of computer CPU time to do this computationally if a short way of finding the new particle location is not introduced. An efficient way of answering these questions has been introduced by Chen (1997) . It is untended to enhance the computational efficiency by reducing the number of trial-and-error sweeping searches at each Lagrangian time step.

Locating a particle in a control volume

When orthogonal Cartesian grids are used to solve a problem with a simple geometry, the location of a particle position can be performed simply by comparing the particle co-ordinates with those of the control volume surfaces. This is due to the fact that the co-ordinates of the control volume surfaces are all parallel to the axes of the Cartesian co-ordinates. This procedure cannot be extended to non-orthogonal grids.

Given the general Cartesian co-ordinates at four vertices, a Eulerian control volume can be uniquely determined. In figure A.2, the Cartesian co-ordinates for four vertices are $A(x_a,y_a)$, $B(x_b,y_b)$, $C(x_c,y_c)$, and $D(x_d,y_d)$. To judge whether

a particle, at position $P(x_p,y_p)$, lies within the boundaries of the considered control volume (ABCD), a reference point, $O(x_o,y_o)$, is defined at the centre of the quadrangle. This reference point is given by averaging the co-ordinates at the four vertices as:

$$x_o = \frac{x_a + x_b + x_c + x_d}{4} \quad , \quad y_o = \frac{y_a + y_b + y_c + y_d}{4} \tag{A-1}$$

This corresponds to the main node of a Eulerian control volume described by Patankar (1980). This reference point always lies in the interior of the quadrangle, therefore it is a good reference point to be used to ensure whether or not a particle lies inside the control volume.

In the case of a 2D control volume as in figure A.2, the judgement of whether a particle is inside or outside the boundaries, can be divided into four sub-checks for each side of the quadrangle. For example, if we take the west surface (AB), the reference point O and the particle locations P_1 and P_2. Four vectors are defined based on the starting point of defining the control volume side moving around the boundaries surfaces in a clockwise direction so based on this the starting point for the west surface is point (A). Therefore the following auxiliary vectors are defined as :

$$r_w = [x_b - x_a]i + [y_b - y_a]j$$

$$r_0 = [x_0 - x_a]i + [y_0 - y_a]j \tag{A-2}$$

$$r_{p1} = [x_{p1} - x_a]i + [y_{p1} - y_a]j$$

$$r_{p2} = [x_{p2} - x_a]i + [y_{p2} - y_a]j$$

where i and j represent two unit vectors along the x and y directions respectively, in the Cartesian co-ordinates. The normal of the vector r_w can be derived from the orthogonal conditions of two vectors. Since the dot product of two orthogonal vectors is zero then the normal of vector r_w can be defined as:

$$N = -[y_b - y_a]i + [x_b - x_a]j \tag{A-3}$$

To determine whether the particle lies on the correct side of the line AB which is the side of the central point 0, the angles at which the other vectors intersect with N can be determined from:

$$COS[r_0,N] = \frac{r_0 . N}{|r_0||N|} \quad , \quad COS[r_p,N] = \frac{r_p . N}{|r_p||N|} \tag{A-4}$$

Based on the vectorial analysis of the right hand rule, the particle lies in the correct direction (the direction of the central point) if and only if both angles have the same sign. And the particle cross the side AB if the signs of the angles are different figure A.3.

By applying this analysis to all sides of the control volume, we can judge whether the particle lies inside the control volume or not. From a programming point of view, at least four "if" statements are necessary to complete the above check procedure, and it will be very complicated in the case of three-dimensional domain. To avoid this Chen (1997) proposed an alternative approach, which only requires to count the sign of the following test variable for each of the control volume sides:

$$\Omega = [r_0 . N][r_p . N] \tag{A-5}$$

Ω is positive when the particle and the reference point lie on the same side with respect to line AB, otherwise it is negative. Therefore a unit integer variable can be computed in terms of the sign of Ω:

$$I_w = Sign[1,\Omega] \tag{A-6}$$

where;

$I_w = 1 \implies \Omega \geq 0$ *(the particle and centre points lie on the same side)*

$I_w = -1 \implies \Omega < 0$ *(the particle and centre points lie on the opposite side)*

Repeating the forgoing procedure for the other three surfaces enables the unit integer variables of I_e, I_s, I_n to be determined. By summing all unit integer variables, the particle can be examined if it is lies inside or outside the control volume as follows:

$$I=I_w+I_e+I_s+I_n=\begin{cases}4\\Othervalues\end{cases} \tag{A-7}$$

The particle lie inside the control volume if and only if I = 4, otherwise it is outside (In the case of three-dimensional domain I = 6, means the particle lie inside the control volume)

In such a way only one "if" statement is required in programming the model instead of the four required in the two-dimensional domain and much complicated statements in the three-dimensional domain.

Optimised Searching Path

Due to the refined grids used to resolve the flow field, it is likely that in one Lagrangian time step, particles can jump over more than one control as in figure A.3.

It is possible and easy to locate the new particle position by checking computations, described in the previous section, for all Eulerian control volumes, such a blind search is undoubtedly time consuming. Frank and Schulze (1994), developed what is called a "circular-search" by suggesting that the search path should go around the particle's old control volume (Γ_0) figure A.4. It is shown that, this method requires a total number of 16 trial-and error computations to locate the control volume (Γ_{15}) whereas the optimal search path needs only three trial-and error computations (Γ_0, Γ_2, Γ_3 then Γ_{15}), (Γ_0, Γ_4, Γ_{16}, then Γ_{15}) or (Γ_0, Γ_4, Γ_3 then Γ_{15}) which needs five time less trial-and-error than the trial-and-error required by the circular-search approach. Note that the third way is a critical one since it follow the particle trajectory as it move from one control volume to another.

By using the unit integer values of the four sides of the control volume calculated in the previous section, we can judge whether the particle is still

inside the control volume or if it has crossed one of its boundaries. Also from this information it is possible to determine from which cell faces the particle exit the control volume. The optimal search path introduced by Chen (1997), is based on the fact that the first trial-and-error search for the new particle position should be in one of the control volumes which are joined with the initial control volume figure A.5, presents an example of how this works on a two-dimensional grid.

If the particle migrates from the control volume Γ_o from the east surface "e" then I_e must be equal to -1. On the other hand, the search procedure usually starts with the initial control volume with the numbering combination of (I_{old} ,J_{old}). To determine the optimal search path, an appropriate increment of ΔI and ΔJ should be assigned to the indices of I_{old} and J_{old}, respectively. These increments are determined in terms of the available unit integer values of I_w, I_e, I_s and I_n as follows:

$$\Delta I=\frac{1-I_e}{2}\frac{1-I_W}{2} \quad , \quad \Delta J=\frac{1-J_n}{2}\frac{1-J_s}{2} \tag{A-8}$$

Note that the right-hand side of the above equation follows the convention of integer operations in FORTRAN. It can be verified that $\Delta I = 1$ (Search toward the east) when $I_e = -1$, and that $\Delta I = -1$ (Search toward the west) when $I_w = -1$. Bearing in mind that I_e and I_w never take the same value of -1 simultaneously unless the control volume is probably zero which is not the case being considered. Similarly the step in the other direction, ΔJ, can be explained. If both ΔI and ΔJ are known, the new control volume (I_{new} , J_{new}) for the next trial-and-error computation is determined by :

$$I_{new}=I_{old}+\Delta I\,,J_{new}=J_{old}+\Delta J \tag{A-9}$$

By repeating the above procedure, the new location of the particle can be reached with a minimum number of trials, which it could be one of the three paths mentioned above.

As was mentioned, one of these three paths is the path, which follows the particles trajectory. This critical path could be determined by the addition of

one further simple step to the above procedure. This is of significant importance in the calculation of other particle properties such as the fluid-particle momentum exchange at each control volume crossed by particle.

It is clear from figure A.6, that two sides out of the four sides will return the sign of establishing that the particle is outside the control volume, these are the south and east sides. Following either one will take us to the new particle position by the same number of trials but only one will follow exactly the particle trajectory which is in this case the east side.

To do this mathematically, it is possible to work out the intersection point between the line representing the particle trajectory between time t and $t+\Delta t$, and the lines representing each of the control volume edges south (AB) and east (BC). One of these intersection points will lie on the control volume edge while the other will lie on the other line but not on the part of the line which represent the control volume edge but on its extension, as shown in figure A.6.

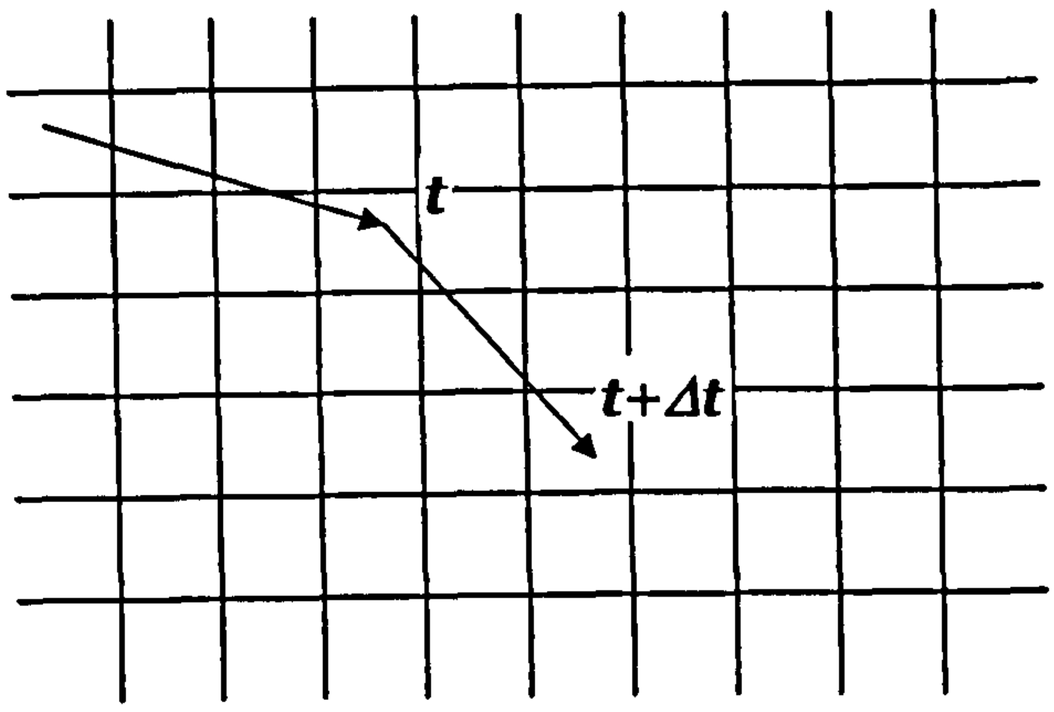

Figure A.1: Movement of a particle in a two-dimensional.

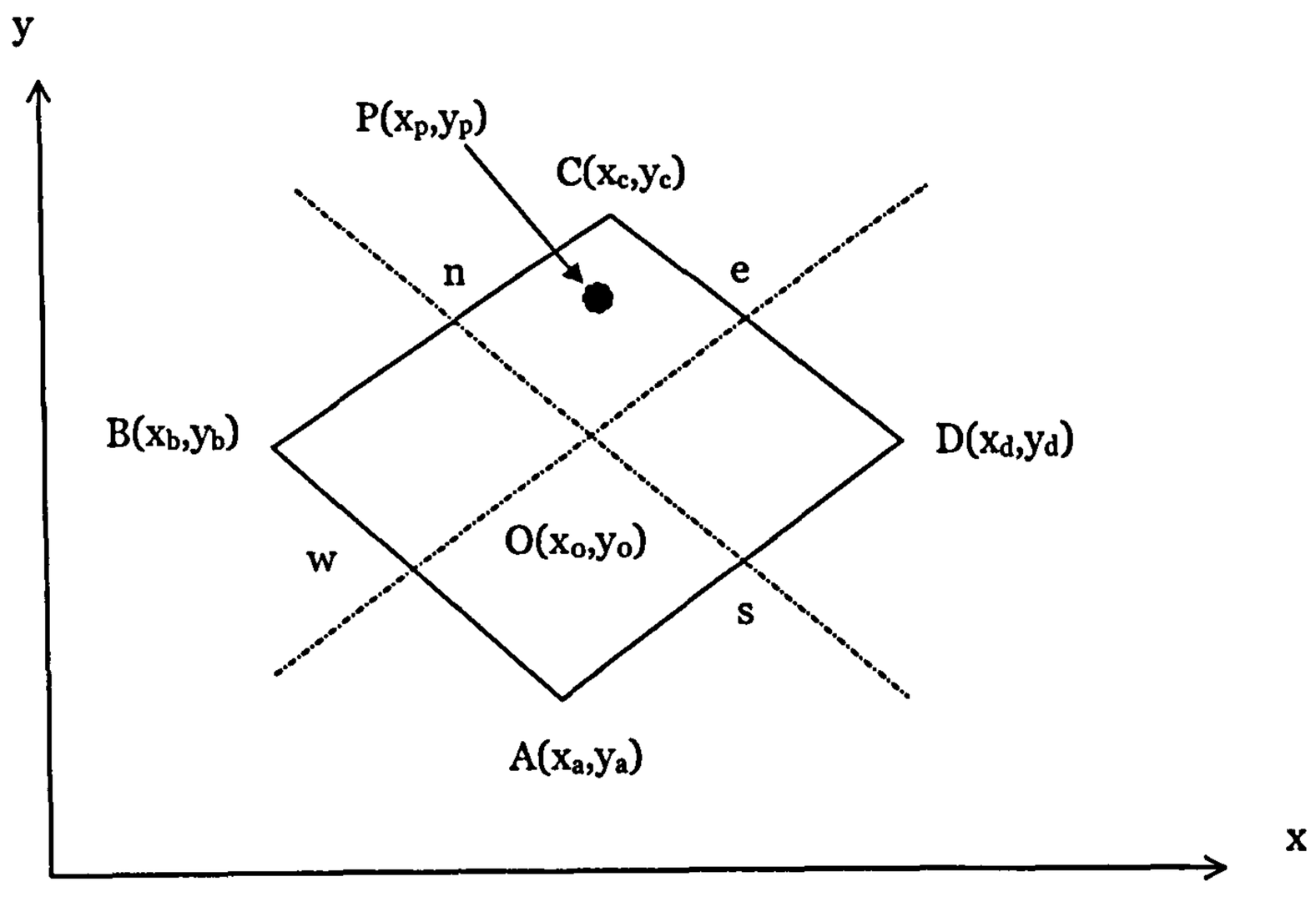

Figure A.2: Definition of an arbitrary 2D Eulerian control volume.

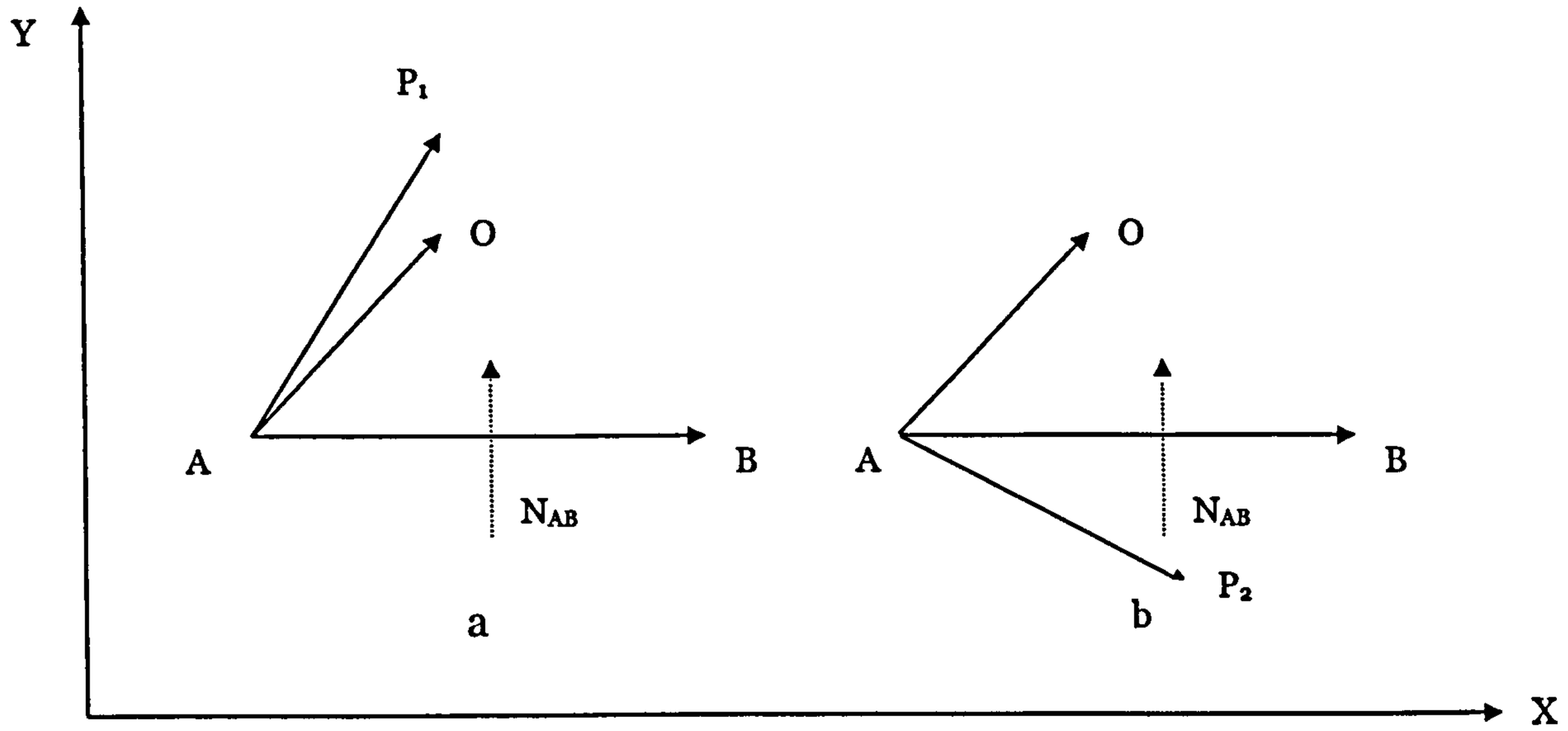

Figure A.3: a) Both particle and cell centre point are on the same side with respect to line AB.
b) Particle and cell centre point are on the opposite sides with respect to line AB.

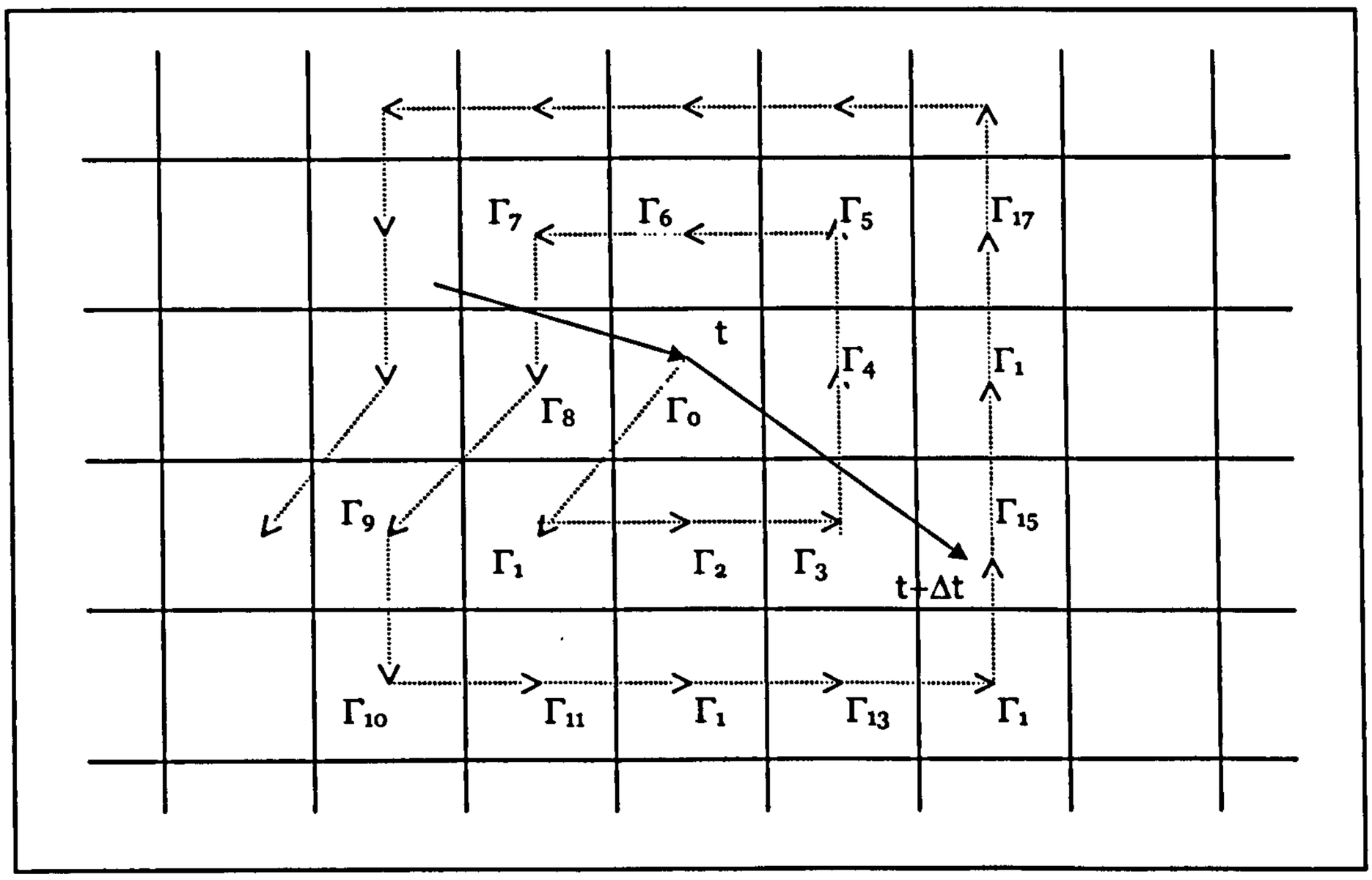

Figure A.4: Definition of Eulerian control volume and conceptual circular-search path.

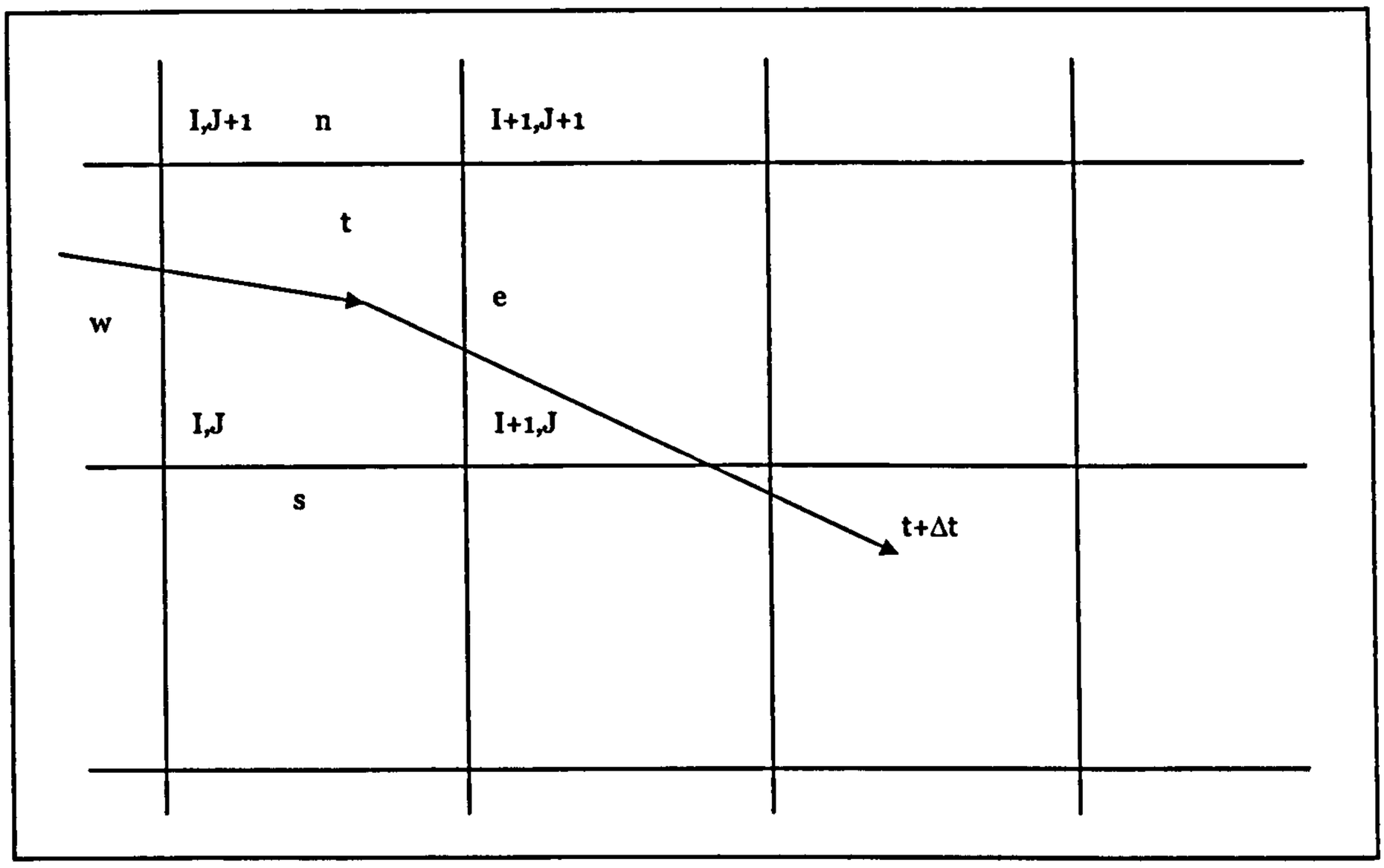

Figure A.5: Numbering of an Eulerian control volume (I,J).

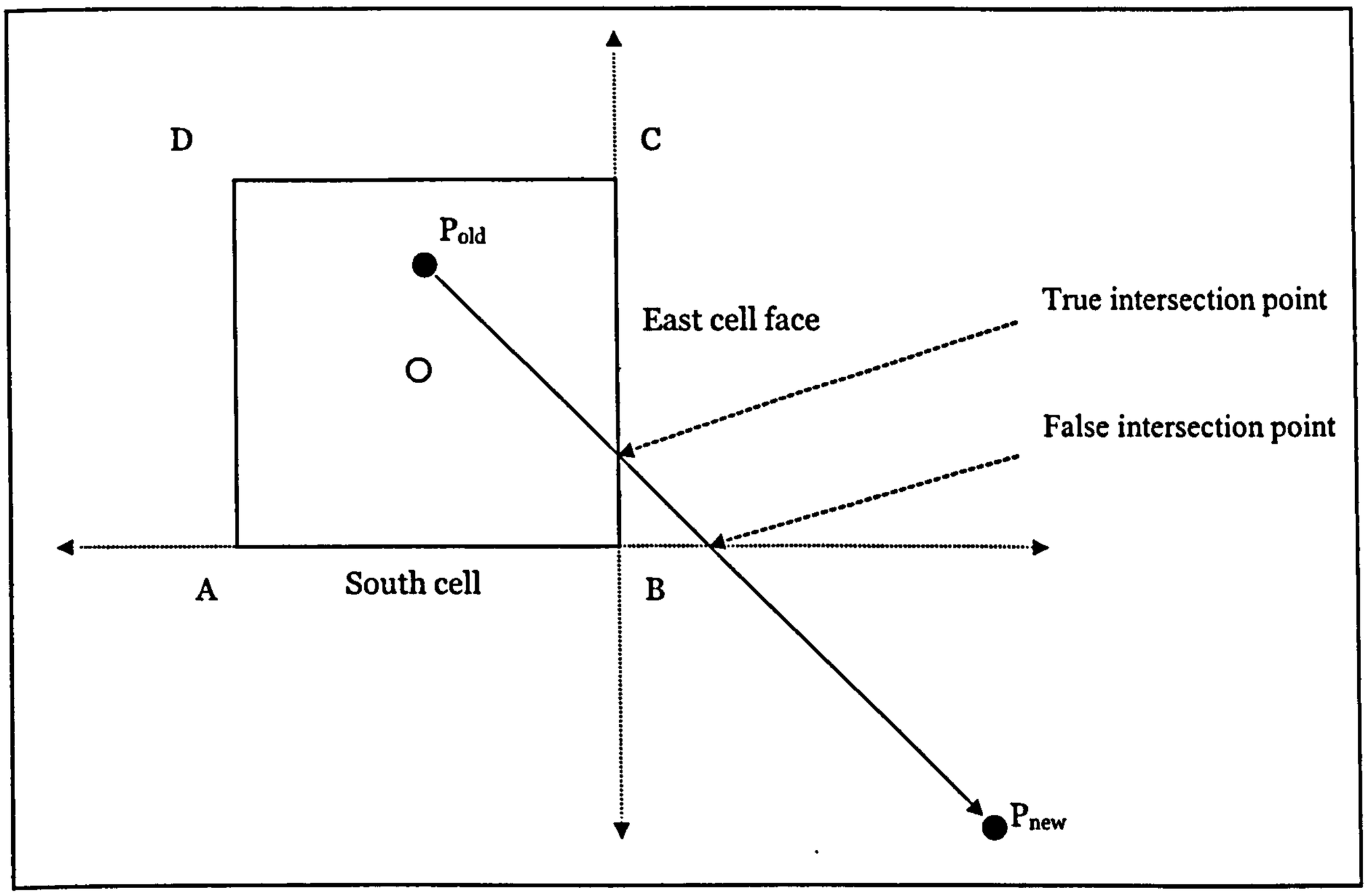

Figure A.6: Particle-cell intersection points.

Appendix B

Single-phase flow governing equation

The FAVOR suitable compacted form of the governing equations (5-43), (5-44) and (5-45) may be expanded in terms of the orthogonal and non-orthogonal contributions. For Cartesian orthogonal grid, the terms involving non-orthogonal contributions equate to zero resulting in the following set of equations:

Continuity equation

$$\frac{\partial \rho}{\partial t}+\frac{1}{V_f}\frac{\partial(\rho u A_x)}{\partial x}+\frac{1}{V_f}\frac{\partial(\rho v A_y)}{\partial y}+\frac{1}{V_f}\frac{\partial(\rho w A_z)}{\partial z}=0 \qquad \text{(B-1)}$$

Momentum equation (Navier-Stokes equation)

$$\frac{\partial(\rho u)}{\partial t}+\frac{1}{V_f}\frac{\partial(\rho u u A_x)}{\partial x}+\frac{1}{V_f}\frac{\partial(\rho v u A_y)}{\partial y}+\frac{1}{V_f}\frac{\partial(\rho w u A_z)}{\partial z}=$$
$$-\frac{\partial P A_x}{\partial x}+\frac{1}{V_f}\frac{\partial \tau_{xx} A_x}{\partial x}+\frac{1}{V_f}\frac{\partial \tau_{yx} A_y}{\partial y}+\frac{1}{V_f}\frac{\partial \tau_{zx} A_z}{\partial z}+\rho f_x \qquad \text{(B-2)}$$

$$\frac{\partial(\rho v)}{\partial t}+\frac{1}{V_f}\frac{\partial(\rho u v A_x)}{\partial x}+\frac{1}{V_f}\frac{\partial(\rho v v A_y)}{\partial y}+\frac{1}{V_f}\frac{\partial(\rho w v A_z)}{\partial z}=$$
$$-\frac{\partial P A_y}{\partial y}+\frac{1}{V_f}\frac{\partial \tau_{xy} A_x}{\partial x}+\frac{1}{V_f}\frac{\partial \tau_{yy} A_y}{\partial y}+\frac{1}{V_f}\frac{\partial \tau_{zy} A_z}{\partial z}+\rho f_y \qquad \text{(B-3)}$$

$$\frac{\partial(\rho w)}{\partial t}+\frac{1}{V_f}\frac{\partial(\rho u w A_x)}{\partial x}+\frac{1}{V_f}\frac{\partial(\rho v w A_y)}{\partial y}+\frac{1}{V_f}\frac{\partial(\rho w w A_z)}{\partial z}=$$
$$-\frac{\partial P A_z}{\partial z}+\frac{1}{V_f}\frac{\partial \tau_{xz} A_x}{\partial x}+\frac{1}{V_f}\frac{\partial \tau_{yz} A_y}{\partial y}+\frac{1}{V_f}\frac{\partial \tau_{zz} A_z}{\partial z}+\rho f_z \qquad \text{(B-4)}$$

Where: u, v, w are the velocity components in the coordinate directions x, y, z.

A_x, A_y, A_z are the area volume fractions defined in FAVOR model for the coordinate directions x, y, z.

V_f The FAVOR model cell volume fraction.

f_i The body forces

τ_{ij} The stress tensors

There are nine viscous stress terms three for each equation; two shear stresses and one normal stress components. The stress tensor, τ_{ij}, is represented by:

Normal stresses:

$$\tau_{xx} = 2\mu\frac{\partial u}{\partial x} - \frac{2}{3}\mu D$$

$$\tau_{yy} = 2\mu\frac{\partial v}{\partial y} - \frac{2}{3}\mu D \qquad \text{(B-5)}$$

$$\tau_{zz} = 2\mu\frac{\partial w}{\partial z} - \frac{2}{3}\mu D$$

Shear stresses:

$$\tau_{xy} = \tau_{yx} = \mu\left(\frac{\partial u}{\partial y} + \frac{\partial v}{\partial x}\right)$$

$$\tau_{xz} = \tau_{zx} = \mu\left(\frac{\partial u}{\partial z} + \frac{\partial w}{\partial x}\right) \qquad \text{(B-6)}$$

$$\tau_{yz} = \tau_{zy} = \mu\left(\frac{\partial v}{\partial z} + \frac{\partial w}{\partial y}\right)$$

The term D is defined as:

$$D = \frac{\partial u}{\partial x} + \frac{\partial v}{\partial y} + \frac{\partial w}{\partial z} \qquad \text{(B-7)}$$

Turbulence modelling

The k-ε turbulence model is a two-equation model since it requires the solution of two additional transport equations one for the turbulent kinetic energy k and another for the kinetic energy dissipation rate ε.

The turbulent shear stress is related to the mean velocity gradients through a turbulent viscosity defined as:

$$\tau_{ij} = -\rho\overline{u_i u_j} = \mu_t\left(\frac{\partial U_i}{\partial x_j} + \frac{\partial U_j}{\partial x_i}\right) - \frac{2}{3}\rho k\,\delta_{ij} \qquad \text{(B-8)}$$

where μ_t is the turbulent or eddy viscosity and defined in terms of k and ε:

$$\mu_t = C_\mu\,\rho\frac{k^2}{\varepsilon} \qquad \text{(B-9)}$$

The transport equation for k and ε are:

$$\frac{\partial(\rho k)}{\partial t} + \frac{\partial}{\partial x_j}(\rho u_j k) = \frac{\partial}{\partial x_j}\left[\frac{\mu_t}{\sigma_k}\frac{\partial k}{\partial x_j}\right] + \left[-\rho\overline{u_i' u_j'}\frac{\partial U_j}{\partial x_i}\right] + \varepsilon \qquad \text{(B-10)}$$

$$\frac{\partial(\rho\varepsilon)}{\partial t} + \frac{\partial}{\partial x_j}(\rho u_j \varepsilon) = \frac{\partial}{\partial x_j}\left[\frac{\mu_t}{\sigma_\varepsilon}\frac{\partial \varepsilon}{\partial x_j}\right] + C_{1,\varepsilon}\frac{\varepsilon}{k}\left[-\rho\overline{u_i' u_j'}\frac{\partial U_j}{\partial x_i}\right] - C_{2,\varepsilon}\,\rho\frac{\varepsilon^2}{k} \qquad \text{(B-11)}$$

The five empirical closure constants in the above equations are taken as a standard values from Launder and Spalding (1974).

C_μ	$C_{1,\varepsilon}$	$C_{2,\varepsilon}$	σ_k	σ_ε
0.09	1.44	1.92	1.0	1.3

The general form of the transport equation

The conservation equations can be expressed in a general transport form as:

$$\frac{\partial(\rho\phi)}{\partial t}+\frac{\partial(\rho u\phi)}{\partial x}+\frac{\partial(\rho v\phi)}{\partial y}+\frac{\partial(\rho w\phi)}{\partial z}= \frac{\partial}{\partial x}\left[\Gamma\frac{\partial\phi}{\partial x}\right]+\frac{\partial}{\partial y}\left[\Gamma\frac{\partial\phi}{\partial y}\right]+\frac{\partial}{\partial z}\left[\Gamma\frac{\partial\phi}{\partial z}\right]+S_\phi \quad \text{(B-12)}$$

Or in even shorter form:

$$\frac{\partial(\rho\phi_i)}{\partial t}+\frac{\partial}{\partial x_j}(\rho u_j\phi_i)=\frac{\partial}{\partial x_j}\left[\Gamma_\phi\frac{\partial\phi_i}{\partial x_j}\right]+S_\phi \quad \text{(B-13)}$$

Where ϕ represent the variable need to be expressed. Thus following the different expression of ϕ it is possible to form any of the above equations as shown in table B-1:

Table B-1: Formulation of the general transport equation variables.

	ϕ	Diffusion Coeff. Γ_ϕ	Source Term S_ϕ
Continuity	1	0	0
Momentum	U	Γ_U	$-\frac{\partial P}{\partial X_j}+S_U$
Kinetic energy	k	μ_T/σ_k	S_k
Kinetic energy dissipation	ε	μ_T/σ_ε	S_ε

Where: $S_k=\tau_{ij}\frac{\partial U_i}{\partial X_j}-\varepsilon$, $S_\varepsilon=C_{1,\varepsilon}\frac{\varepsilon}{k}\left(\tau_{ij}\frac{\partial U_i}{\partial X_j}\right)-C_{2,\varepsilon}\rho\frac{\varepsilon}{k}$,

Appendix C

Finite volume discretization of general transport equation

First of all it is important to notice that the notations used in this section are not consistent with those used in the previous sections.

The compact form of differential equations which describe the transport of mass, momentum and an arbitrary scalar quantity over general coordinate system can be written for steady, viscous and incompressible flow as:

$$\frac{\partial}{\partial X^j}\left(\rho u_m \alpha^{mj}\right)=S_m \tag{C-1}$$

$$\frac{\partial}{\partial X^j}\left[\left(\rho u_m u_i - T_{mi}\right)\alpha^{mj}\right]=S_i^u \tag{C-2}$$

$$\frac{\partial}{\partial X^j}\left[\left(\rho u_m \phi - q_m\right)\alpha^{mj}\right]=S_\phi \tag{C-3}$$

The coefficient α^{ji} can be expressed as:

$$\alpha^{ji}=\alpha_j^i=\frac{1}{J}\beta_j^i \tag{C-4}$$

Where:

The Jacobian 'J' is the volume of the control volume in general coordinate system and is defined in 3-dimentional computational domain as:

$$J=\begin{vmatrix} \frac{\partial y^1}{\partial x^1} & \frac{\partial y^1}{\partial x^2} & \frac{\partial y^1}{\partial x^3} \\ \frac{\partial y^2}{\partial x^1} & \frac{\partial y^2}{\partial x^2} & \frac{\partial y^2}{\partial x^3} \\ \frac{\partial y^3}{\partial x^1} & \frac{\partial y^3}{\partial x^2} & \frac{\partial y^3}{\partial x^3} \end{vmatrix} \tag{C-5}$$

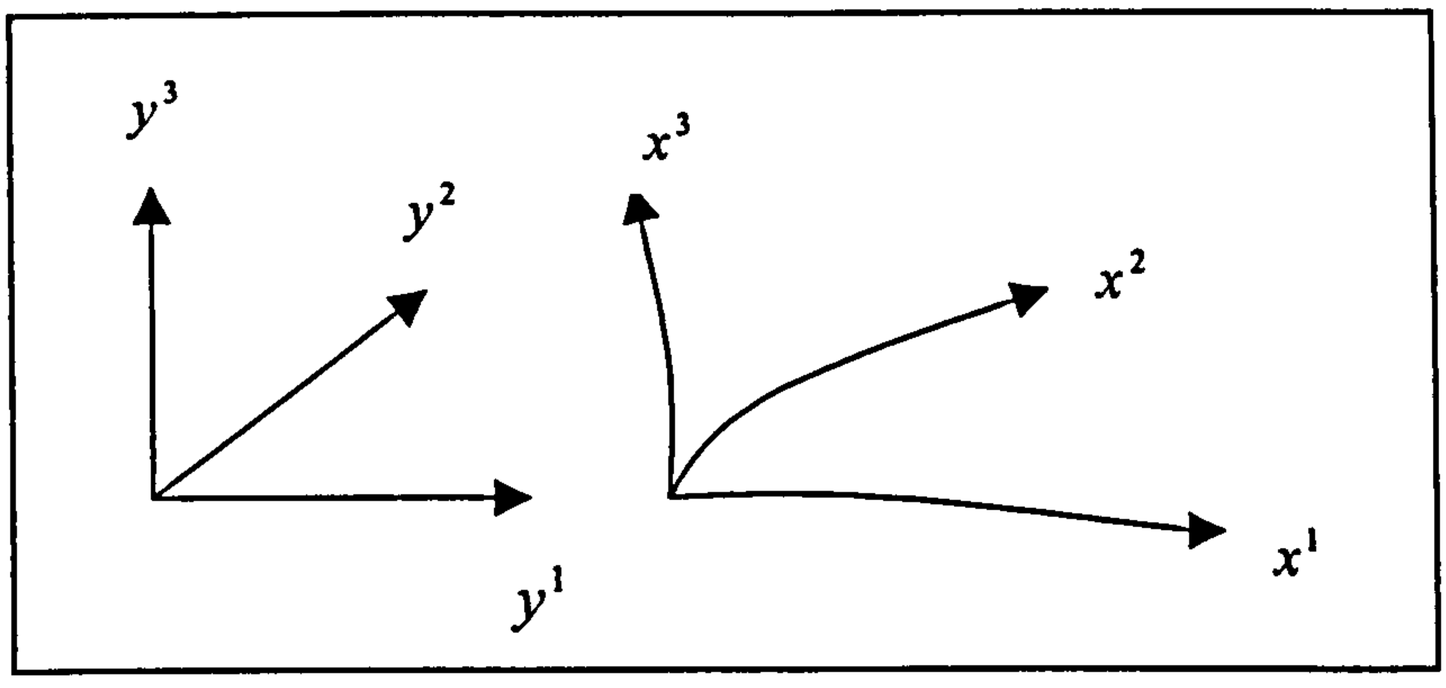

Figure C.1: The cartisian and general coordinat system componenets.

And the area vector as β_j^i given as:

$$\beta_1^1 = A_{x^1y^1} = \left[\frac{\partial y^2}{\partial x^2}\ \frac{\partial y^3}{\partial x^3} - \frac{\partial y^2}{\partial x^3}\ \frac{\partial y^3}{\partial x^2}\right]$$

$$\beta_2^1 = A_{x^1y^2} = -\left[\frac{\partial y^1}{\partial x^2}\ \frac{\partial y^3}{\partial x^3} - \frac{\partial y^1}{\partial x^3}\ \frac{\partial y^3}{\partial x^2}\right]$$

$$\beta_3^1 = A_{x^1y^3} = \left[\frac{\partial y^1}{\partial x^2}\ \frac{\partial y^2}{\partial x^3} - \frac{\partial y^1}{\partial x^3}\ \frac{\partial y^2}{\partial x^2}\right]$$

$$\beta_1^2 = A_{x^2y^1} = -\left[\frac{\partial y^2}{\partial x^1}\ \frac{\partial y^3}{\partial x^3} - \frac{\partial y^2}{\partial x^3}\ \frac{\partial y^3}{\partial x^1}\right]$$

$$\beta_2^2 = A_{x^2y^2} = \left[\frac{\partial y^1}{\partial x^1}\ \frac{\partial y^3}{\partial x^3} - \frac{\partial y^1}{\partial x^3}\ \frac{\partial y^3}{\partial x^1}\right] \qquad \text{(C-6)}$$

$$\beta_3^2 = A_{x^2y^3} = -\left[\frac{\partial y^1}{\partial x^1}\ \frac{\partial y^3}{\partial x^3} - \frac{\partial y^1}{\partial x^3}\ \frac{\partial y^3}{\partial x^1}\right]$$

$$\beta_1^3 = A_{x^3y^1} = \left[\frac{\partial y^2}{\partial x^1}\ \frac{\partial y^3}{\partial x^2} - \frac{\partial y^2}{\partial x^2}\ \frac{\partial y^3}{\partial x^1}\right]$$

$$\beta_2^3 = A_{x^3y^2} = -\left[\frac{\partial y^1}{\partial x^1}\ \frac{\partial y^3}{\partial x^2} - \frac{\partial y^1}{\partial x^2}\ \frac{\partial y^3}{\partial x^1}\right]$$

$$\beta_3^3 = A_{x^3y^2} = \left[\frac{\partial y^1}{\partial x^1}\ \frac{\partial y^2}{\partial x^2} - \frac{\partial y^1}{\partial x^2}\ \frac{\partial y^2}{\partial x^1}\right]$$

When using FAVOR, the area fractions of the cells and the cell volume fraction are the fractions of the area and volume of the cell open to the flow. These fractions take the values from 0 to 1. If it is 1, no flow passes through that

specific cell or cell side, whereas if it is 0, the area or volume is fully open to the flow.

For a 3-dimensional computational domain in a general coordinate system, it requires 10, 3-dimensional arrays to represent these fractions in the governing equations, 3 area fractions, (one for each flow direction), and one for the volume fraction.

Area fraction in vector form can be expressed as:

$$\begin{aligned} A_{f1} &= \lfloor A_{f11} \quad A_{f12} \quad A_{f13} \rfloor \\ A_{f2} &= \lfloor A_{f21} \quad A_{f22} \quad A_{f23} \rfloor \\ A_{f3} &= \lfloor A_{f31} \quad A_{f32} \quad A_{f33} \rfloor \end{aligned} \tag{C-7}$$

V_f = *Is the volume fraction of a specific cell*

Since the area fraction is the ratio of the cell face closed to the total area, then we could assume that it is constant for each flow direction. In this case the required arrays to represent the area fractions will be reduced from 9 to 3 only. Thus

$$\begin{aligned} A_{f1} &= A_{f11} = A_{f12} = A_{f13} \\ A_{f2} &= A_{f21} = A_{f22} = A_{f23} \\ A_{f3} &= A_{f31} = A_{f32} = A_{f33} \end{aligned} \tag{C-8}$$

The compact form of the governing equations can be rewritten as follow:

$$\frac{1}{J}\frac{\partial}{\partial X^j}\left(\rho u_m \beta^{mj} A_{fj}\right) = S_m \tag{C-9}$$

$$\frac{1}{J}\frac{\partial}{\partial X^j}\left[\left(\rho u_m u_i - T_{mi}\right)\beta^{mj} A_{fj}\right] = V_f S_i^u \tag{C-10}$$

$$\frac{1}{J}\frac{\partial}{\partial X^j}\left[\left(\rho u_m \phi - q_m\right)\beta^{mj} A_{fj}\right] = V_f S_\phi \tag{C-11}$$

Each of these equations will be expanded taking into account the area/volume fractions:

1: Continuity Equation

$$\frac{\partial}{\partial X^1}U_1+\frac{\partial}{\partial X^2}U_2+\frac{\partial}{\partial X^3}U_3=J\,S_m$$

Where:

$$U_1=\rho\left(u_1\,\beta_1^1+u_2\,\beta_2^1+u_3\,\beta_3^1\right)A_{f1}$$

$$U_2=\rho\left(u_1\,\beta_1^2+u_2\,\beta_2^2+u_3\,\beta_3^2\right)A_{f2} \qquad \text{(C-13)}$$

$$U_3=\rho\left(u_1\,\beta_1^3+u_2\,\beta_2^3+u_3\,\beta_3^3\right)A_{f3}$$

2: General Scalar Equation

The flux vector q can be written as:

$$q_m=\Gamma_\phi\frac{\partial\phi}{\partial x^n}\frac{1}{J}\beta_m^n \qquad \text{(C-14)}$$

Where in expanded form:

$$q_1=\frac{1}{J}\Gamma_\phi\left[\frac{\partial\phi}{\partial x^1}\beta_1^1+\frac{\partial\phi}{\partial x^2}\beta_1^2+\frac{\partial\phi}{\partial x^3}\beta_1^3\right]A_{f1}$$

$$q_2=\frac{1}{J}\Gamma_\phi\left[\frac{\partial\phi}{\partial x^1}\beta_2^1+\frac{\partial\phi}{\partial x^2}\beta_2^2+\frac{\partial\phi}{\partial x^3}\beta_2^3\right]A_{f2} \qquad \text{(C-15)}$$

$$q_3=\frac{1}{J}\Gamma_\phi\left[\frac{\partial\phi}{\partial x^1}\beta_3^1+\frac{\partial\phi}{\partial x^2}\beta_3^2+\frac{\partial\phi}{\partial x^3}\beta_3^3\right]A_{f3}$$

When these expressions introduced into equation 10 taking into account equation 12, it will take the following form:

$$\frac{\partial}{\partial X^j}\left[\left(U_j\,\phi-\frac{\Gamma_\phi}{J}\frac{\partial\phi}{\partial x^m}B_m^j\,A_{jj}\right)\right]=V_f\,J\,S_\phi \qquad \text{(C-16)}$$

Where in expanded form:

$$\frac{\partial}{\partial X^1}\left[U_1\phi-\frac{\Gamma_\phi}{J}\left(\frac{\partial\phi}{\partial x^1}B_1^1+\frac{\partial\phi}{\partial x^2}B_2^1+\frac{\partial\phi}{\partial x^3}B_3^1\right)A_{f1}\right]+$$

$$\frac{\partial}{\partial X^2}\left[U_2\phi-\frac{\Gamma_\phi}{J}\left(\frac{\partial\phi}{\partial x^1}B_1^2+\frac{\partial\phi}{\partial x^2}B_2^2+\frac{\partial\phi}{\partial x^3}B_3^2\right)A_{f2}\right]+ \qquad \text{(C-17)}$$

$$\frac{\partial}{\partial X^3}\left[U_3\phi-\frac{\Gamma_\phi}{J}\left(\frac{\partial\phi}{\partial x^1}B_1^3+\frac{\partial\phi}{\partial x^2}B_2^3+\frac{\partial\phi}{\partial x^3}B_3^3\right)A_{f3}\right]=V_f\,J\,S_\phi$$

In equation 16, $B's$ represent the following products:

$$B_j^i=\beta_k^j\,\beta_k^i \qquad \text{(C-18)}$$

Which take the following expanded form:

$$\begin{aligned}
B_1^1 &= \beta_1^1\,\beta_1^1+\beta_2^1\,\beta_2^1+\beta_3^1\,\beta_3^1\\
B_2^1=B_1^2 &= \beta_1^2\,\beta_1^1+\beta_2^2\,\beta_2^1+\beta_3^2\,\beta_3^1\\
B_3^1=B_1^3 &= \beta_1^3\,\beta_1^1+\beta_2^3\,\beta_2^1+\beta_3^3\,\beta_3^1\\
B_2^2 &= \beta_1^2\,\beta_1^2+\beta_2^2\,\beta_2^2+\beta_3^2\,\beta_3^2\\
B_3^2=B_2^3 &= \beta_1^2\,\beta_1^3+\beta_2^2\,\beta_2^3+\beta_3^2\,\beta_3^3\\
B_3^3 &= \beta_1^3\,\beta_1^3+\beta_2^3\,\beta_2^3+\beta_3^3\,\beta_3^3
\end{aligned} \qquad \text{(C-19)}$$

3: Momentum Equation

The stress tensor can be written in the following form:

$$T_{mi}=-P\delta_{mi}+\frac{\mu}{J}\left[\frac{\partial u_i}{\partial x^n}\beta_m^n+\frac{\partial u_m}{\partial x^l}\beta_i^l\right] \qquad \text{(C-20)}$$

In the expanded form:

$$T_{11}=-P+\frac{2\mu}{J}\left[\left(\frac{\partial u_1}{\partial x^1}\beta_1^1+\frac{\partial u_1}{\partial x^2}\beta_1^2+\frac{\partial u_1}{\partial x^3}\beta_1^3\right)\right]$$

$$T_{12}=T_{21}=\frac{\mu}{J}\left[\begin{array}{l}\left(\frac{\partial u_2}{\partial x^1}\beta_1^1+\frac{\partial u_2}{\partial x^2}\beta_1^2+\frac{\partial u_2}{\partial x^3}\beta_1^3\right)+\\ \left(\frac{\partial u_1}{\partial x^1}\beta_2^1+\frac{\partial u_1}{\partial x^2}\beta_2^2+\frac{\partial u_1}{\partial x^3}\beta_2^3\right)\end{array}\right]$$

$$T_{13}=T_{31}=\frac{\mu}{J}\left[\begin{array}{l}\left(\frac{\partial u_3}{\partial x^1}\beta_1^1+\frac{\partial u_3}{\partial x^2}\beta_1^2+\frac{\partial u_3}{\partial x^3}\beta_1^3\right)+\\ \left(\frac{\partial u_1}{\partial x^1}\beta_3^1+\frac{\partial u_1}{\partial x^2}\beta_3^2+\frac{\partial u_1}{\partial x^3}\beta_3^3\right)\end{array}\right] \qquad \text{(C-21)}$$

$$T_{22}=-P+\frac{2\mu}{J}\left[\left(\frac{\partial u_2}{\partial x^1}\beta_2^1+\frac{\partial u_2}{\partial x^2}\beta_2^2+\frac{\partial u_2}{\partial x^3}\beta_2^3\right)\right]$$

$$T_{23}=T_{32}=\frac{\mu}{J}\left[\begin{array}{l}\left(\frac{\partial u_3}{\partial x^1}\beta_2^1+\frac{\partial u_3}{\partial x^2}\beta_2^2+\frac{\partial u_3}{\partial x^3}\beta_2^3\right)+\\ \left(\frac{\partial u_2}{\partial x^1}\beta_3^1+\frac{\partial u_2}{\partial x^2}\beta_3^2+\frac{\partial u_2}{\partial x^3}\beta_3^3\right)\end{array}\right]$$

$$T_{33}=-P+\frac{2\mu}{J}\left[\left(\frac{\partial u_3}{\partial x^1}\beta_3^1+\frac{\partial u_3}{\partial x^2}\beta_3^2+\frac{\partial u_3}{\partial x^3}\beta_3^3\right)\right]$$

Then the momentum equation in its compact form can be written as:

$$\frac{\partial}{\partial X^j}\left[U_j u_i-\frac{\mu}{J}\left(\frac{\partial u_i}{\partial x^m}B_m^j+\frac{\partial u_k}{\partial x^m}\beta_i^m\,\beta_k^j\right)A_{fj}+P\beta_i^j A_{fj}\right]=V_f J S_i^u \qquad \text{(C-22)}$$

Three equations can be written from the above equation for velocity components, one for each Cartesian velocity component as follow:

A. u_1-Momentum equation

$$\begin{aligned}&\frac{\partial}{\partial X^1}\left[U_1 u_1-\frac{\mu}{J}\left\{\begin{array}{l}\left(\frac{\partial u_1}{\partial x^1}B_1^1+\frac{\partial u_1}{\partial x^2}B_2^1+\frac{\partial u_1}{\partial x^3}B_3^1\right)A_{f1}+\\ \left(W_1^1\beta_1^1+W_1^2\beta_2^1+W_1^3\beta_3^1\right)A_{f1}\end{array}\right\}+P\beta_1^1 A_{f1}\right]+\\ &\frac{\partial}{\partial X^2}\left[U_2 u_1-\frac{\mu}{J}\left\{\begin{array}{l}\left(\frac{\partial u_1}{\partial x^1}B_1^2+\frac{\partial u_1}{\partial x^2}B_2^2+\frac{\partial u_1}{\partial x^3}B_3^2\right)A_{f2}+\\ \left(W_1^1\beta_1^2+W_1^2\beta_2^2+W_1^3\beta_3^2\right)A_{f2}\end{array}\right\}+P\beta_1^2 A_{f2}\right]+ \qquad \text{(C-23)}\\ &\frac{\partial}{\partial X^3}\left[U_3 u_1-\frac{\mu}{J}\left\{\begin{array}{l}\left(\frac{\partial u_1}{\partial x^1}B_1^3+\frac{\partial u_1}{\partial x^2}B_2^3+\frac{\partial u_1}{\partial x^3}B_3^3\right)A_{f3}+\\ \left(W_1^1\beta_1^3+W_1^2\beta_2^3+W_1^3\beta_3^3\right)A_{f3}\end{array}\right\}+P\beta_1^3 A_{f3}\right]=V_f J S_1^u\end{aligned}$$

B. u_2 **-Momentum equation**

$$\frac{\partial}{\partial X^1}\left[U_1 u_2 - \frac{\mu}{J}\left\{\begin{array}{c}\left(\frac{\partial u_2}{\partial x^1}B_1^1 + \frac{\partial u_2}{\partial x^2}B_2^1 + \frac{\partial u_2}{\partial x^3}B_3^1\right)A_{f1} + \\ \left(W_2^1\,\beta_1^1 + W_2^2\,\beta_2^1 + W_2^3\,\beta_3^1\right)A_{f1}\end{array}\right\} + P\,\beta_2^1\,A_{f1}\right] +$$

$$\frac{\partial}{\partial X^2}\left[U_2 u_2 - \frac{\mu}{J}\left\{\begin{array}{c}\left(\frac{\partial u_2}{\partial x^1}B_1^2 + \frac{\partial u_2}{\partial x^2}B_2^2 + \frac{\partial u_2}{\partial x^3}B_3^2\right)A_{f2} + \\ \left(W_2^1\,\beta_1^2 + W_2^2\,\beta_2^2 + W_2^3\,\beta_3^2\right)A_{f2}\end{array}\right\} + P\,\beta_2^2\,A_{f2}\right] + \qquad \text{(C-24)}$$

$$\frac{\partial}{\partial X^3}\left[U_3 u_2 - \frac{\mu}{J}\left\{\begin{array}{c}\left(\frac{\partial u_2}{\partial x^1}B_1^3 + \frac{\partial u_2}{\partial x^2}B_2^3 + \frac{\partial u_2}{\partial x^3}B_3^3\right)A_{f3} + \\ \left(W_2^1\,\beta_1^3 + W_2^2\,\beta_2^3 + W_2^3\,\beta_3^3\right)A_{f3}\end{array}\right\} + P\,\beta_2^3\,A_{f3}\right] = V_f\,J\,S_2^u$$

C. u_3 **-Momentum equation**

$$\frac{\partial}{\partial X^1}\left[U_1 u_3 - \frac{\mu}{J}\left\{\begin{array}{c}\left(\frac{\partial u_3}{\partial x^1}B_1^1 + \frac{\partial u_3}{\partial x^2}B_2^1 + \frac{\partial u_3}{\partial x^3}B_3^1\right)A_{f1} + \\ \left(W_3^1\,\beta_1^1 + W_3^2\,\beta_2^1 + W_3^3\,\beta_3^1\right)A_{f1}\end{array}\right\} + P\,\beta_3^1\,A_{f1}\right] +$$

$$\frac{\partial}{\partial X^2}\left[U_2 u_3 - \frac{\mu}{J}\left\{\begin{array}{c}\left(\frac{\partial u_3}{\partial x^1}B_1^2 + \frac{\partial u_3}{\partial x^2}B_2^2 + \frac{\partial u_3}{\partial x^3}B_3^2\right)A_{f2} + \\ \left(W_3^1\,\beta_1^2 + W_3^2\,\beta_2^2 + W_3^3\,\beta_3^2\right)A_{f2}\end{array}\right\} + P\,\beta_3^2\,A_{f2}\right] + \qquad \text{(C-25)}$$

$$\frac{\partial}{\partial X^3}\left[U_3 u_3 - \frac{\mu}{J}\left\{\begin{array}{c}\left(\frac{\partial u_3}{\partial x^1}B_1^3 + \frac{\partial u_3}{\partial x^2}B_2^3 + \frac{\partial u_3}{\partial x^3}B_3^3\right)A_{f3} + \\ \left(W_3^1\,\beta_1^3 + W_3^2\,\beta_2^3 + W_3^3\,\beta_3^3\right)A_{f3}\end{array}\right\} + P\,\beta_3^3\,A_{f3}\right] = V_f\,J\,S_3^u$$

Where the expression $W_j^k = \frac{\partial u_k}{\partial x^m}\beta_j^m$ or in the expansion form as:

$$W_1^1 = \frac{\partial u_1}{\partial x^1}\beta_1^1 + \frac{\partial u_1}{\partial x^2}\beta_1^2 + \frac{\partial u_1}{\partial x^3}\beta_1^3$$

$$W_2^1 = \frac{\partial u_1}{\partial x^1}\beta_2^1 + \frac{\partial u_1}{\partial x^2}\beta_2^2 + \frac{\partial u_1}{\partial x^3}\beta_2^3$$

$$W_3^1 = \frac{\partial u_1}{\partial x^1}\beta_3^1 + \frac{\partial u_1}{\partial x^2}\beta_3^2 + \frac{\partial u_1}{\partial x^3}\beta_3^3$$

$$W_1^2 = \frac{\partial u_2}{\partial x^1}\beta_1^1 + \frac{\partial u_2}{\partial x^2}\beta_1^2 + \frac{\partial u_2}{\partial x^3}\beta_1^3$$

$$W_2^2 = \frac{\partial u_2}{\partial x^1}\beta_2^1 + \frac{\partial u_2}{\partial x^2}\beta_2^2 + \frac{\partial u_2}{\partial x^3}\beta_2^3 \qquad \text{(C-26)}$$

$$W_3^2 = \frac{\partial u_2}{\partial x^1}\beta_3^1 + \frac{\partial u_2}{\partial x^2}\beta_3^2 + \frac{\partial u_2}{\partial x^3}\beta_3^3$$

$$W_1^3 = \frac{\partial u_3}{\partial x^1}\beta_1^1 + \frac{\partial u_3}{\partial x^2}\beta_1^2 + \frac{\partial u_3}{\partial x^3}\beta_1^3$$

$$W_2^3 = \frac{\partial u_3}{\partial x^1}\beta_2^1 + \frac{\partial u_3}{\partial x^2}\beta_2^2 + \frac{\partial u_3}{\partial x^3}\beta_2^3$$